School of Molecular and Life Sciences

The Application of Chiral Resorcinarenes As Modifiers of Crystallization and Inhibitors of Corrosion

Munna Ali Mohamed Bertata

This thesis is presented for the degree of

Doctor of Philosophy

of

Curtin University

October 2018

Declaration

To the best of my knowledge and belief this thesis contains no material previously published by any other person except where due acknowledgment has been made. This thesis contains no material which has been accepted for the award of any other degree or diploma in any university.

Signature: 

Data: 09/10/18

Acknowledgements

O Allah, praise be to you always at every blink of an eye and breath, thank you as is must be for your Majesty and your great sultan.

I am indebted to my supervisors A/Prof. Mauro Mocerino, Dr. Franca Jones, and Dr. Katerina Lepkova, for their guidance, patience and enthusiastic throughout this project.

I would also like to thank all my colleagues in the laboratory especially the past members of the synthesis labs for their advice.

My thanks go extend my sincere gratitude to staff members of chemistry department.

Most thanks definitely to my Father, the fountain that did not tire of giving, to instilling the meaning of patience in me and who supports me in life, and I wish him speedy recovery.

My thanks to my Mother, whose perfume has fragranced my life, and whose prayers and blessings lightened my way.

Finally, I would like to thank my brothers and sisters especially Ihmid for his support and patience.

Abstract

The application of chiral calixarenes and resorcinarenes have attracted considerable interest and consequently many syntheses of chiral calixarenes and resorcinarenes have been developed over the last decade. During this work, 19 previously unreported compounds have been synthesised and characterised. Resorcinarenes functionalized at the upper rim with aspartic acid or diethylethyleneamine were synthesized by Lewis acid catalysed cyclocondensation of 3-methoxyphenol with aliphatic aldehydes. The resulting racemic resorcinarene derivatives were alkylated with ethyl bromoacetate, then the product used to form two different compounds. One way was hydrolysis of the ester to give acid, which was then coupled with dimethyl *L*-aspartic acid hydrochloride to give the tetra-amino acid functionalised tetramethoxyresorcinarenes. The diastereomers of the chiral resorcinarenes were separated by fractional crystallization. The other way was to react this ester with *N*,*N*-diethylethyleneamine to give tetra-diethylenediamine tetramethoxyresorcinarenes. Also, an alkyl amide with aspartic acid was synthesised by reaction of dimethyl *L*-aspartic acid hydrochloride with dodecanoyl chloride. Similarly, *N*,*N*-diethylethyleneamine reacted with dodecanoyl chloride to give *N*-(2-diethylaminoethyl)dodecanamide. The structures of the new compounds were elucidated by nuclear magnetic resonance (NMR), infrared (IR) spectroscopy and mass spectrometry (MS).

The new resorcinarene derivatives were used in investigations to determine their impact on crystallisation processes and corrosion inhibition. To study their role as crystal growth modifiers, the aspartic acid derivatives were applied to model mineral systems (calcium carbonate, barium sulfate, calcium oxalate) and compared with an undecyl amide model, and with previously investigated lower rim calixarene derivatives. The study found that the upper rim aspartic acid functionalized resorcinarenes had an impact on the morphology of calcium carbonate, barium sulfate and calcium oxalate. The propyl aspartic acid resorcinarene (**10**) was the potent inhibitor of calcium carbonate, barium sulfate and calcium oxalate crystallization. In comparison with the lower rim calixarenes, the upper rim aspartic acid resorcinarenes had high impact on the calcium carbonate and calcium oxalate and less impact on barium sulfate crystallization.

Amino acid functionalized resorcinarenes were also investigated as corrosion inhibitors on carbon steel in brine media under CO_2. The results indicate that all the aspartic acid resorcinarene derivatives inhibited the corrosion process more than the diethylethylenediamine resorcinarene derivatives. At high concentrations, the dodecyl amide is more potent than the amino acid functionalized resorcinarenes.

List of Presentations

Munna Bertata, Franca Jones and Mauro Mocerino. Crystal Growth Applications o Aspartic acid functionalised methoxy resorcin[4]arene. Crystallisation Downunder workshop at Curtin university, Perth. 11-12 January, 2016.

Munna Bertata, Ding-Yi Fu, Adam Tinker, Mauro Mocerino and Yuqing Wu. The synthesis of amino acid functionalised calixarenes and their interactions with surfaces. 14th International Conference on Calixarenes at Tianjin, China. 20 – 24 August, 2017.

Table of Contents

List of Figures

List of Schemes

List of Tables

1.0 Introduction

1.1 Overview

This chapter will provide a brief overview of the structure of the thesis. It will very briefly introduce the field of supramolecular chemistry with a focus on macrocyclic compounds, particularly calixarenes and resorcinarenes, and their applications as inhibitors in the crystallization and corrosion fields. The aim and scope of the thesis will also be introduced along with a description of the chapter topics.

1.2 A brief introduction to supramolecular chemistry

Supramolecular chemistry refers to the area of chemistry interested in non-covalent interactions between molecules. Jean-Marie Lehn was the first to define supramolecular chemistry as "*Chemistry of molecular assemblies and of the intermolecular bond"* or as *"Chemistry beyond the molecule."*[1] Another definition is "*The synthetic molecular system that are held together by intermolecular forces (non-covalent interactions)".*[2] These include ionic and dipolar interaction, hydrogen bonding, π-interactions and van der Waal interactions.[1-2] These intermolecular forces are weak separately but produce very stable molecular complexes when they are used together to form a new structure/complex.[3-4]

There are several concepts that have been addressed by supramolecular chemistry. For instance, molecular self-assembly,[5-6] host-guest compounds,[1-2, 7] molecular recognition,[8-10] molecular machinery,[11-12] macrocycles[1-2]…. etc. Moreover, supramolecular chemistry as a broader field can be applied in various fields including chemistry, physics and biology and because of that, it has been rapidly expanding.[1-2] Figure 1.1 shows the development of a supramolecular system from molecular building blocks.[2]

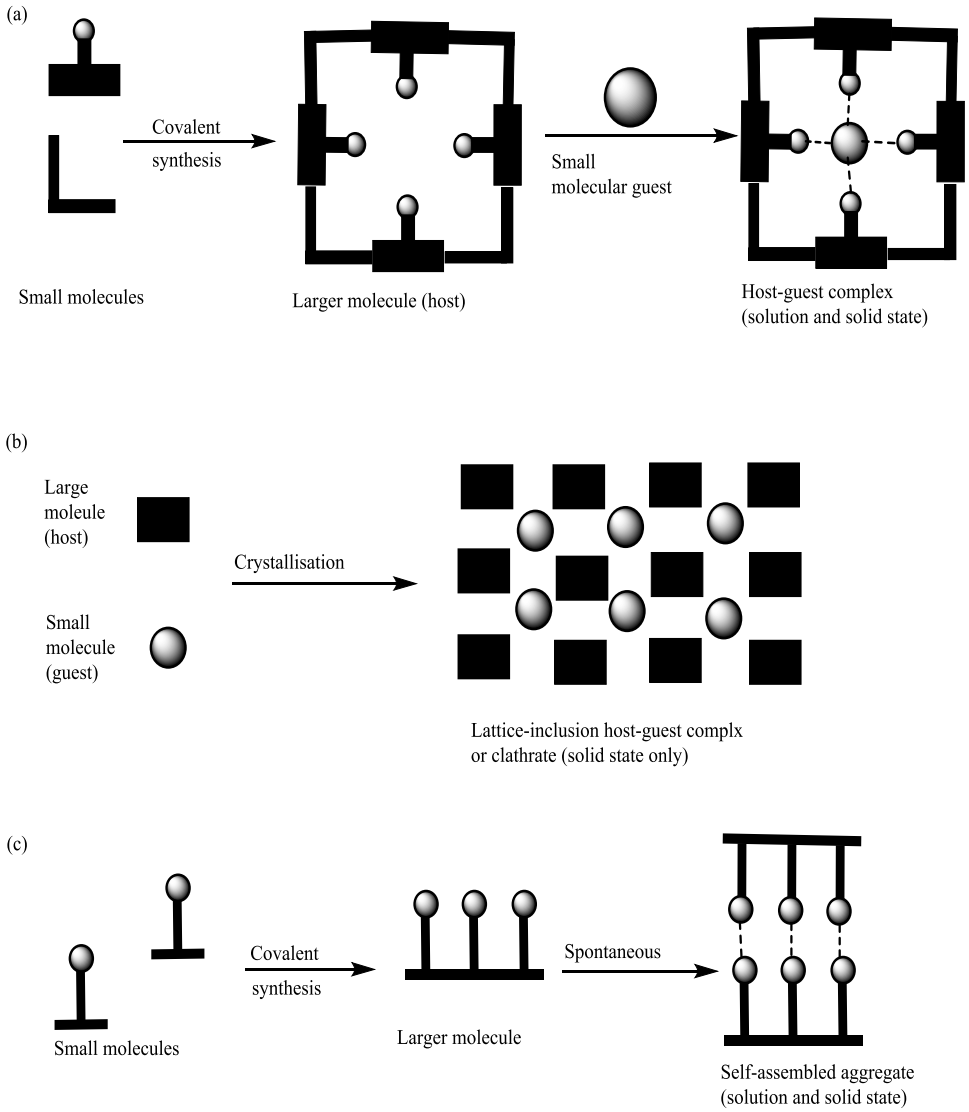

Scheme 1.1: Schematic illustrates three types of supramolecular systems from molecular building blocks. Adapted from Steed et al.2

Macrocyclic compounds are common in supramolecular chemistry[1-2] and include cyclodextrins, crown-ethers and calixarenes and resorcinarenes as shown in Figure 1.2. This thesis will focus on the calixarenes and resorcinarenes.[13-14]

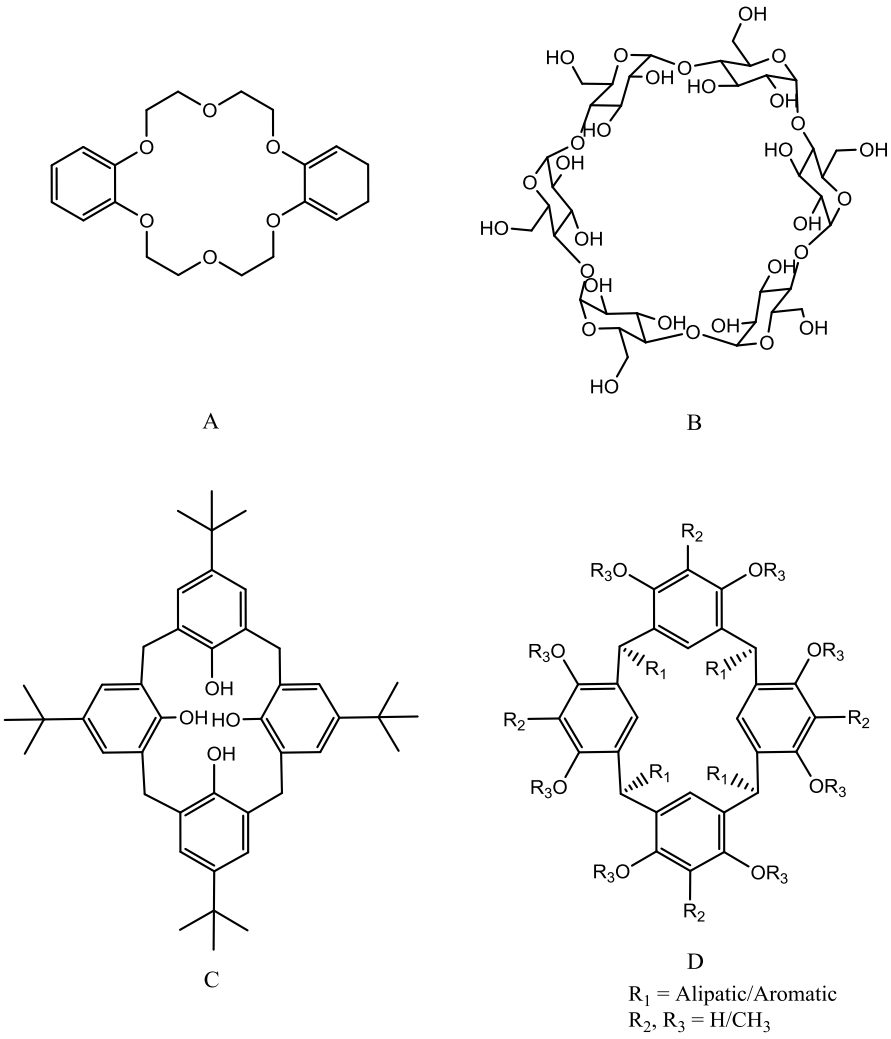

Figure 1.1: Structure of a crown ether (A), cyclodextrins(B), calix[4]arenes(C), resorcinarenes(D).

1.3 Brief background of calixarenes and resorcinarenes

Calix[n]arene, where n is the number of benzene rings, is the term that describes a novel class of phenolic metacylcophanes derived from the condensation of phenols and aldehydes.[15-16] The name was suggested by Gutsche and was derived from the Latin word "calix" due to the vase-like structure that these macrocyclic compounds take when all phenyl rings are arranged in the same direction.[17-18] In these molecules two different areas are available for functionalization: the lower (narrow) rim, where the phenolic oxygen atoms are arranged and the upper (wide) rim characterized by the *para*-positions of the aromatic rings as shown in Figure 1.2. As the calixarenes are large molecules, many representation styles have been used to show their structures. Figure 1.3 shows some of the different structural representations of

calixarenes.[19] Calixarenes can be synthesized in one step from the condensation of formaldehyde with *p-tert*-butylphenol under alkaline conditions,[16, 20] as is shown in Scheme 1.2. By carefully controlling the conditions and base, high yields of calixarenes with 4, 6 or 8 aromatic rings can be obtained.[16]

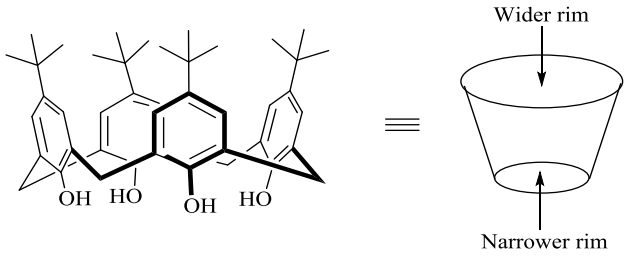

Figure 1.2: Structure of p-tertbutyl calix[4]arene.

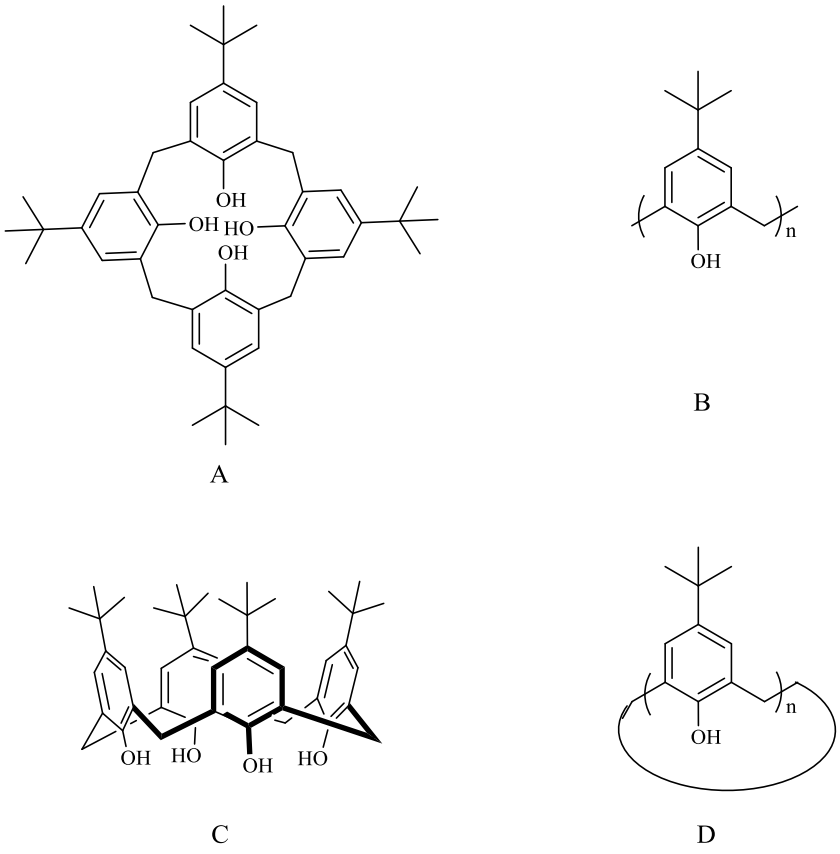

Figure 1.3: Some representation styles of calixarenes.

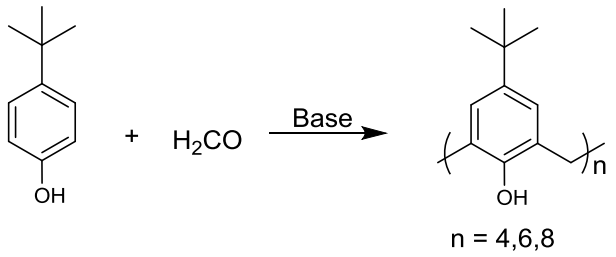

Scheme 1.2: Calixarenes synthesis.

Resorcin[n]arenes belong to the class of calix[n]arene.[21] These are also [1_4] metacylcophanes.[22-23] They were generated in 1872 by von Baeyer. In 1940, Niederl and Vogel suggested the resorcinarene structure and in 1968, Erdtman used single crystal X-ray analysis to prove their structures.[18, 24] Moreover, like the Calixarenes, they can be viewed as a basket with the two different rims as given in the Figure 1.2. However, unlike the calixarenes, resorcinarenes form almost exclusively the tetramer (n = 4).[19] A general structures of resorcinarenes are given in Figure 1.4 and this is the representation style of resorcinarenes that will be used most commonly in this thesis. **Chapter 2** will give more details on resorcinarene chemistry.

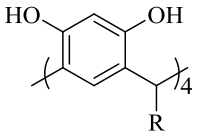

Figure 1 4: Representation of resorcinarenes.

1.4 Applications of macrocyclic compounds

As calixarenes and resorcinarenes are easily synthesized and modified, this prompted research into their applications in biological[14, 25] and industrial fields.[18, 26] In the past three decades, calixarenes have been investigated for biological activities such as antiviral, antifungal, antibacterial, antiangiogenic and anticancer activities.[21] Calixarenes have also been used in various applications, including decontamination of wastewater,[27] as medical diagnostics,[28] selective sensors in analytical applications,[29] electrodes[26, 30] and in the solvent extraction of metal ions.[31] For example, calixarene derivatives showed a good selectivity of thallium(I) ion over other ions in ion- selective electrodes.[32-33] Two other applications of calixarenes and

resorcinene are in the area of crystallization control and corrosion inhibition, which will be included in this study and they will be discussed briefly here and in more detail in the next chapters.

1.4.1 Crystal growth modifier

The control of crystallisation in industry is important for several reasons including the controls of scale,[34] product formation[35] and morphology.[36] A vast amount of literature has been published about a variety of biomineral systems such as mollusk shells,[37-38] bone,[39] and shells of cephalopods.[40] Each one of these studies found that a small amount of organic material or inorganic ions can have a large impact on the mineral formation and properties. The protein components of the organic matrices within the biomineral, particularly those associated with calcium carbonate, have been found to be rich in the acidic amino acids, aspartic and glutamic acids.[41] Gotliv et al. has studied aspartic acid rich (asprich) proteins and has suggested these may take part in Ca^{2+} transportation limiting the superstauration of calcium carbonate.[42] Hence, the focus of the crystallization literature is on the impact of acidic amino acid on the crystallization of inorganic minerals. Calcium carbonate and barium sulfate are also common components of industrial scale and they are important minerals in industry.[43-44] Calixarenes and resorcinarenes have been used as modifiers of crystal growth of calcium carbonate and barium sulfate.[45] There are many reports of functionalization of calixarenes and resorcinarenes on the lower and upper rims. For example, Volkmer *et al*. have utilized the calixarene and resorcinarene derivatives shown in Figure 1.5, as monolayers on an aqueous surface to study the crystallization of calcium carbonate.[46-47] They found that by changing the charge densities of the monolayer, crystallisation of calcium carbonate could be controlled.[48]

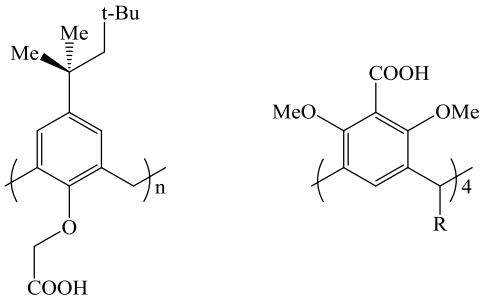

n = 4, 6 R = $(CH_2)_{10}CH_3$

A B

Figure 1.5: Examples of calixarenes (A) and resorcinarenes (b) used as Langmuir monolayers on calcium carbonate crystallization.

1.4.2 Corrosion inhibition

Internal corrosion of carbon steel pipelines is a major problem in the oil and gas industry. Therefore, the control of corrosion by using inhibitors is an effective way to reduce the corrosion attack on metal surfaces.[49] Inorganic compounds such as chromates have been employed as inhibitors of corrosion, but they are toxic and can promote corrosion if their concentrations drop below critical levels.[50] Calixarene derivatives have been used as inhibitors of corrosion of steel and many of its alloys in acidic media. The compound shown in Figure 1.6 has been used as a corrosion inhibitors on steel and it was found that inhibitor efficiency increased with concentration but their efficiency decreased with increasing temperature.[49]

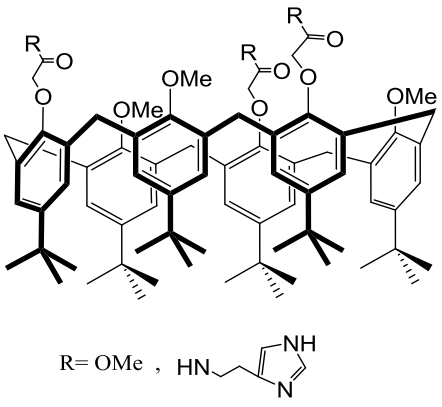

Figure 1.6: An example of corrosion inhibitor.

1.5 Aim and scope

The aim of this PhD project is to synthesise and characterize functionalized resorcinarene derivatives and evaluate their efficacy as crystal growth modifiers and corrosion inhibitors.

1.6 Structure of this thesis

This thesis is organized as follows. **Chapter 2** deals with the chemistry of resorcinarenes. It commences with a brief literature review and introduction of resorcinarene chemistry relating to their synthesis methodology and functionalization. This is followed by the experimental details of the synthetic work carried out during this PhD. Finally, a discussion of the results of this work is provided which includes the spectroscopic characterisation of the molecules synthesised.

Chapter 3 provides a brief overview on the theory of crystallization and the role of an additive on the growth process. The experimental work and results of this study, which focuses on the impact of the synthersised resorcinarene compounds on calcium carbonate, barium sulfate and calcium oxalate crystallisation are discussed. Scanning electron microscopy (SEM), Fourier-transform infrared spectroscopy (FT-IR) and ultraviolet spectroscopy (UV) were used to assess the impact of the new additives.

Chapter 4 gives a brief introduction on corrosion science and explains CO_2 corrosion, the types of inhibitors used to prevent corrosion and electrochemical techniques that have been used to measure the corrosion rate. This is followed by the experimental study and a discussion of the results obtained.

Chapter 5 outlines general conclusions of this thesis as well as directions for future work

2.0 Resorcinarenes

2.1 Outline

This chapter will provide a brief background of the nomenclature and conformation of resorcinarenes, the chirality aspect of these compounds, a summary on different synthesis routes that have been used, and some examples of the functionalization of these resorcinarenes. The chapter will then present the synthesis research carried out in this PhD.

2.2 Resorcinarenes

Resorcinarenes are the subclass of the calixarene family and are sometimes referred to as calixresorcarenes.[24] Adolph Van Baeyer was the first to create a resorcinarene by the condensation of benzaldehyde and resorcinol under acidic conditions, although, the structure of this crystalline compound was not determined. Sixty years later, Vogel and Niederl investigated the condensation of resorcinol and a variety of aliphatic aldehydes and proposed the cyclic tetrameric structure of resorcinarenes. Resorcinarene synthesis was further improved by Cram, *et al*.[51] Resorcinarenes are easily synthesized and functionalized,[52] and, have been employed in different fields such as supramolecular recognition,[53] inhibition of scale formation,[54] and biological applications.[1]

2.2.1 The nomenclature of resorcinarenes

There are a various names given to these compounds such as Hogberg compounds,[22] resorcinarenes,[24] and calix[4]resorcinarenes.[55-56] Prior to 2002, the International Union of Pure and Applied Chemistry [57] recommended that the nomenclature for resorcinarenes describe them as macrocyclic polyhydroxy-polyenes (see Figure 2.1(A)). In 2002, a new IUPAC recommendation for naming cyclophanes was developed, according to the following rules:[57]

1. *numbering of the phane parent hydride*
2. *heteroatoms introduced by skeletal replacement (‘a’) nomenclature*
3. *indicated hydrogen*
4. *nondetachable ‘hydro- ‘/’dehydro- ‘prefixes*
5. *principal characteristic group (named as suffix)*
6. *unsaturation (‘-ene’/ ‘-yne’ ending and ‘hydro-’/ ‘dehydro-’prefixes)*
7. *substituents named as prefixes (alphabetised substituents)*

Figure 2.1 shows an example of a resorcin[4]arene which is named by using the pre-2002 preferred method and the 2002 phane nomenclature rules. The older naming convention is 2,8,14,20-tetramethylpentacyclo[l9.3.1.1^{3,7}.1^{9,13}.1^{15,19}]octacosa-1(25),3,5,7^{58},9,11,13(27),15,-17,19(26),21,23-dodecaene-4,6,10,12,16,18,22,24-octol. The current IUPAC preferred name is 2,4,6,8-tetramethyl-1,3,5,7(1,3)-tetrabenzenacyclooctaphane-1^4,1^6,3^4,3^6,5^4,5^6,7^4,7^6-octol, which is a lengthy name to be applied in text. In this thesis the name has been shortened by replacing the ‘‘1,3,5,7(1,3)-tetrabenzenacyclooctaphane” with ‘‘resorcin[4]arene” and the name will be resorcin[4]arene-1^4,1^6,3^4,3^6,5^4,5^6,7^4,7^6-octol.[57]

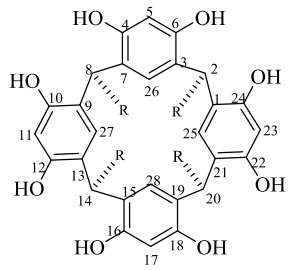

A

2,8,14,20-tetramethylpentacyclo[l9.3.1.1^{3,7}.1^{9,13}.1^{15,19}]octacosa-1(25),3,5,7^{11},9,11,13(27),15,17,19(26),21,23-dodecaene-4,6,10,12,16,18,22,24-octol
(Old system)

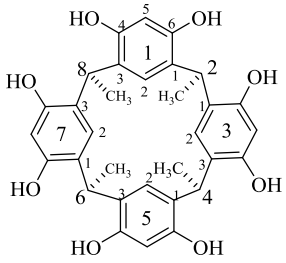

B

2,4,6,8-tetramethyl-1,3,5,7(1,3)-tetrabenzenacyclo-octaphane-1^4, 1^6, 3^4, 3^6, 5^4, 5^6, 7^4 ,7^6 - octol (IUPAC system)
Or
2,4,6,8-tetramethylresorcinarene-1^4, 1^6, 3^4, 3^6, 5^4, 5^6, 7^4 ,7^6 - octol
(Phane nomenclature rules)

Figure 2. 1: Resorcinarene nomenclature showing the old and new systems.

2.2.2 The conformation of resorcinarenes

Resorcinarenes are non-planar three-dimensional compounds and therefore have several conformations[22-23] as shown in Figure 2.2. Högberg was the first to isolate and identify two of the conformational isomers of the resorcinarenes, namely the chair and the boat.[23] Timmerman *et al*. have explained that, there are five conformations (isomers) of the resorcinarenes, which are Crown, Chair, Boat, Diamond and Saddle but only four have been found experimentally (Boat, Chair, Diamond, and Saddle). These conformations can be arranged symmetrically as follows: C_{4v} symmetry can be formed in the crown conformer, where the resorcinol units are orientated in a bowl-like shape. C_{2v} symmetry is observed in the boat

isomer, it contains two rings lying in a perpendicular position with two resorcinol rings in an upward position. C_{2h} symmetry can be found in the chair conformer, here one resorcinol is orientated in an upward position with the other resorcinol ring in a downward position and two rings are in perpendicular position to them. C_s symmetry is observed in the diamond isomer, where two adjacent rings orientated downwards and other two adjacent upwards. Finally, C_{2d} symmetry is seen in the saddle conformer, where two opposite rings face down and the other opposite two faces upwards.

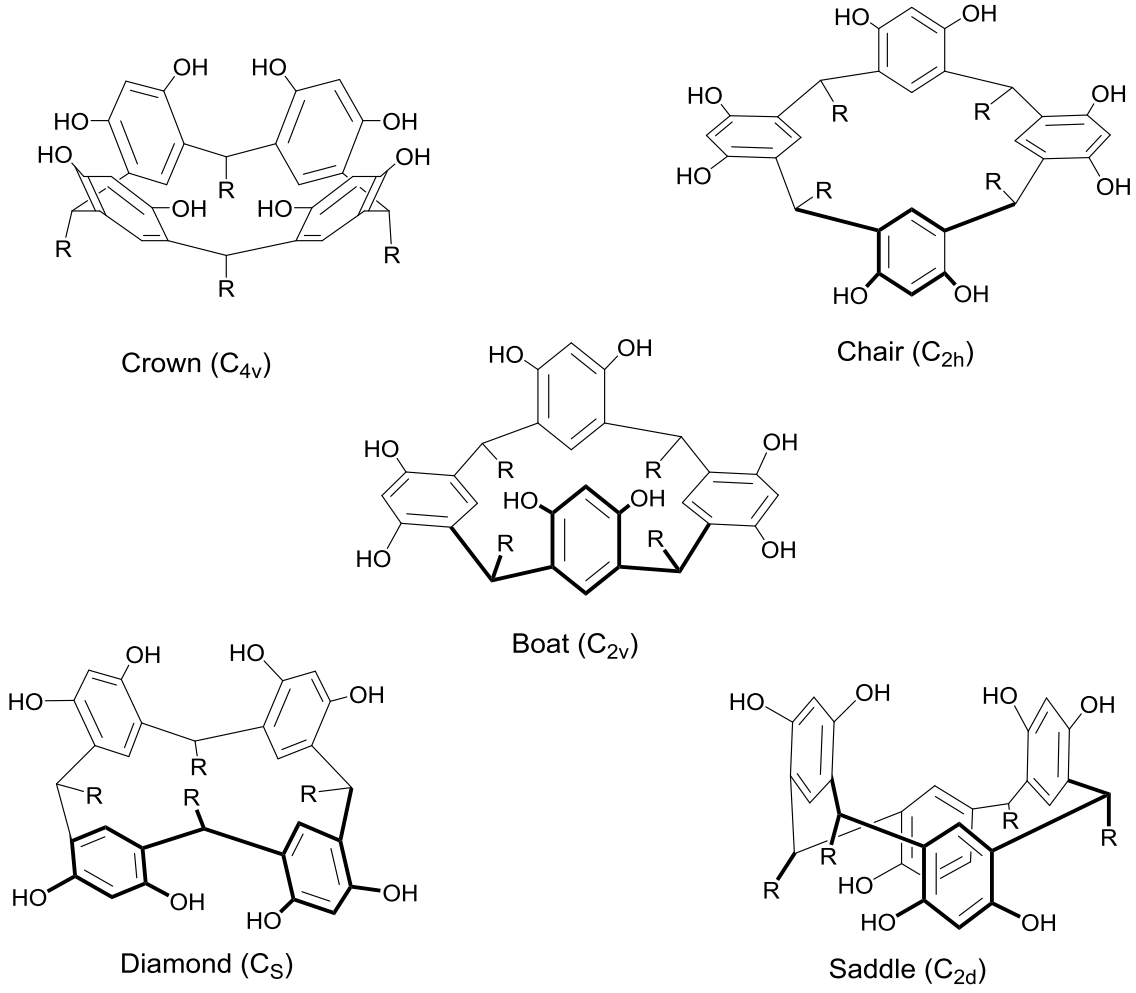

Figure 2. 2: Resorcinarenes conformations.

The other stereochemical element to consider is the relative configurations. In resorcinarenes, at the bridging carbon atoms (Ar-C-Ar), there are four prochiral centres and due to that four different stereoisomer arrangements can be formed.

These are, firstly, all-*cis* (rccc), where all groups are attached in same direction in a *cis*- relation to a reference (r), the *cis*-*cis*-*trans* (rcct), here one group is in the opposite orientation to the other three (in a trans-relationship). The third is the *cis*-*trans*-*trans* (rctt), this configuration contains two groups opposite to the other two (including the reference group) and finally, the *trans*-*cis*-*trans* (rtct), this configuration contains two groups (including reference group) in *cis*-relationship opposite to the other two (in a *trans*-relationship). See Figure 2.3.

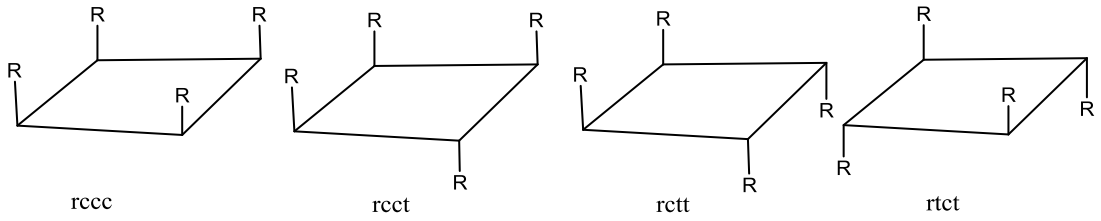

Figure 2. 3: Relative configuration at methylene bridges.

The last stereochemical element is the individual configuration, this is the individual stereochemistry of substituents on the carbon atoms at the benzylic position of the resorcinarenes which may be in an axial or equatorial position on the macrocycle *C* symmetry.[24]

2.3 Chirality of resorcinarenes

McIldowie has described the chirality of calixarenes and resorcinarenes in a review.[59] Here a brief description of the concept of resorcinarene chirality will be presented. Resorcinarene can be made chiral by substituting some of the hydroxy groups and some examples will be briefly discussed below. The chiral resorcinarenes can be described as either attachment chiral or chiral by asymmetric functionalization. Attachment chirality is obtained by linking a chiral molecule at the upper or lower rims. Asymmetric functionalization can be obtained by attaching moieties on the non-planar resorcinarene skeleton. In asymmetric functionalization, the C_{4v} symmetry may be lost and lower C_1 or C_2 symmetry formed. Figure 2.4 shows an example of a resorcinarene that formed by chiral attachment (A),[60] and the resorcinarene formed by asymmetric functionalization (B).[61]

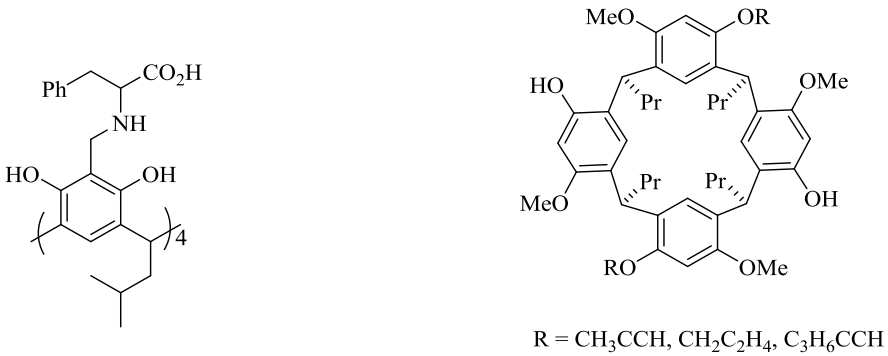

A B

Figure 2. 4: Figure 2.4: An example of chiral resorcinarenes formed by (A) attachment chiral, (B) asymmetric functionalization.

The chiral resorcinarenes from asymmetric functionalization can have three C_n symmetry types which are C_1, C_2 and C_4 dissymmetry. The C_1 symmetry in resorcinarene can be achieved by alkylation of one of the resorcinarene phenols. Scheme 2.5 introduces an example of forming the C_1 symmetry by monobenzylation.[62]

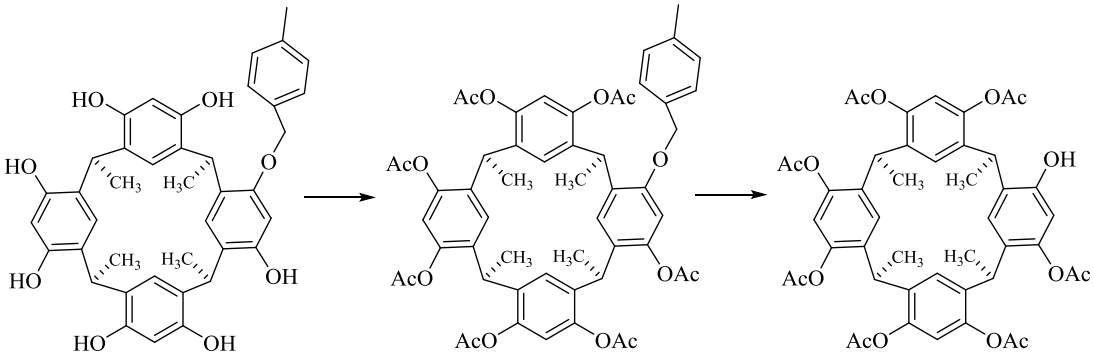

Figure 2. 5: An example for formation *C*1 symmetry resorcinarenes.

Bohmer has synthesized the 1,3-bisbenzoxazine compounds which have been used to prepare the C_2 dissymmetry resorcinarenes. Figure 2.6 presents an example of the distal tetratosylates that have been utilized for preparing a variety of derivatives.[63]

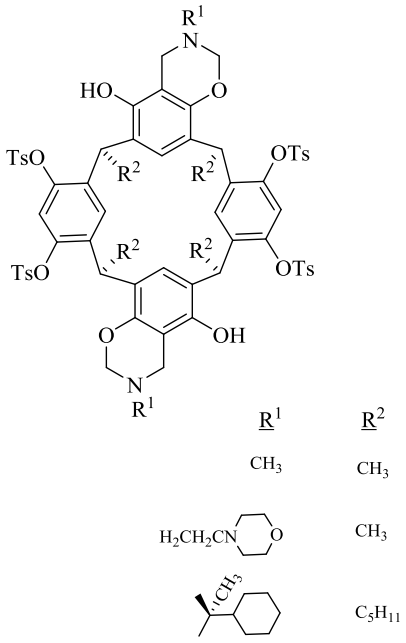

Figure 2. 6: An example of the C2 dissymmetric resorcinarenes.

The *C4* dissymmetric resorcinarenes can be achieved by two ways, selective functionalization at the upper rim, or from the resorcinol mono-ether. The achiral amines were used by Bohmer *et al*. to prepare the benzoxazine derivative is an example of selective functionalization at the upper rim is shown in Figure 2.7.[64]

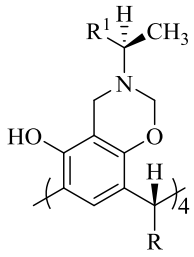

R^1	R
$C_{11}H_{23}$	C_6H_5
$C_{11}H_{23}$	naphthyl

Figure 2. 7: The benzoxazine derivative as an example of selective functionalization.

The use of resorcinol mono-ethers to synthesise the *C4* dissymmetric resorcinarene has been reported.[65] Figure 2.8 illustrates an example of the resorcinarene skeleton from resorcinol mono-ethers by condensation of resorcinol mono-ethers and alkyl aldehydes in the presence of boron trifluoride etherate. This gave the *C4* dissymmetric resorcinarene as a racemate.[65]

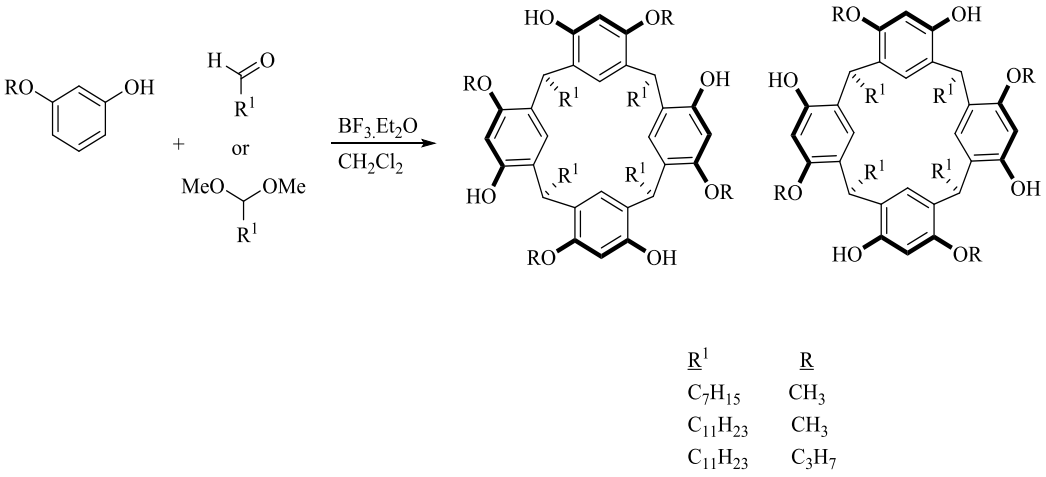

Figure 2. 8: Synthesis of C4 dissymmetric resorcinarene by using mono ethers.

Also, the resorcinarenes have four stereogenic centers which makes it easy to describe the chirality.[59] Buckley and his co-workers *have* described how to distinguish between the absolute C_4 dissymmetric resorcinarene enantiomers using the *M*/*P* notation and the CIP *R*/*S* system. An example of chirality of resorcinarene is illustrated in Figure 2.9, which explains this system to describe the C_4 dissymmetric resorcinarene in Figure 2.9A as *M* or 2*R*,4*R*,6*R*,8*R*- and in Figure 2.9B as *P* or 2*S*,4*S*,6*S*,8*S*-.[66]

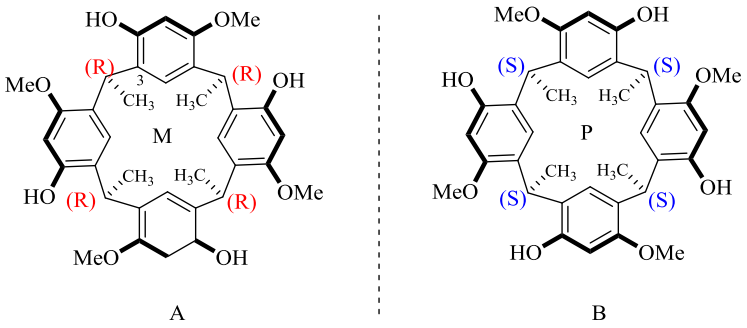

Figure 2. 9: The absolute C4 dissymmetric resorcinarenes enantiomers via using M/P notation and the CIP R/S.

Figure 2.10 represents the four different ways of depicting the structures of a single chiral resorcinarene enantiomer where Figure 2.10c shows an outside view of the resorcinarene and Figure 2.10d shows the inside view of the resorcinarene. The best and simplest representation of the racemate of a chiral resorcinarene is in a mirror view, as shown in Figure 2.11.

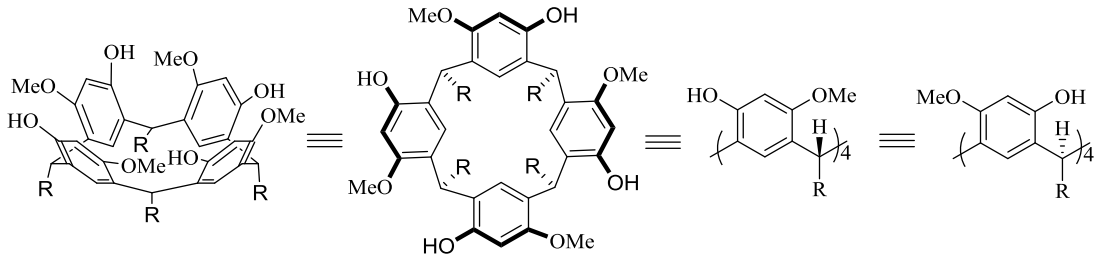

Figure 2. 10: The four-depicted structures of a single chiral resorcinarene enantiomer.

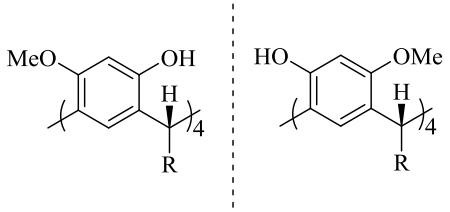

Figure 2. 11: A mirror view of chiral resorcinarenes.

2.4 Synthesis of resorcinarenes

Different synthetic routes have been used for the synthesis of resorcinarenes by employing different catalysts and conditions. The first report of the synthesis of resorcinarene was by Bayer, who obtained the resorcinarene by the condensation of resorcinol with an aldehyde under acidification.[67] This one-pot reaction has been used with a wide variety of aldehydes ranging from aliphatic to aryl aldehydes.[56, 68-69] The original procedure reacted resorcinol with various aldehydes in the presence of ethanol under acidic conditions then heated the mixture under reflux for several hours to give reasonable to excellent yields.[56, 70] Also, Bronsted acid catalysis has been utilized in the resorcinarene synthesis, typically using hydrochloric acid. Lewis acid catalysts have been also used to generate efficient yields of resorcinarene, and provide selectivity as to which resorcinarene is formed.[71] Recently, a green synthesis route has been developed and proven to form resorcinarene under solvent free conditions.[72] Another development in resorcinarene synthesis is using a 1,3,5-trioxane instead of aldehydes.[73]

2.5 Mechanism of resorcinarenes formation

Determining a mechanism of a reaction is an important aspect of understanding and optimizing the chemical reaction involved. In 1991, Weinelt and Schneider proposed a mechanism for the formation of resorcinarene by acid-catalyzed condensation between resorcinol and acetaldehyde (in the cyclic trimer form) in methanol/HCl.[74] The proposed mechanism is shown in Scheme 2.1, and starts with protonation of the acetal, **B.** This serves as the initial electrophile and adds to the resorcinol to form the compound, **C.** After that, the addition of another resorcinol unit to **C** leads to the displacement of the methoxy group of **C.** This forms a second molecule of methanol and **D** is formed. A sequential addition of acetaldehyde acetal and resorcinol units to **D** leads to **E** followed by F. Finally, addition of the final aldehyde group and cyclisation forms tetramer **G** or, if more than four monomers are added, oligomer units are generated by the sequential coupling of the dimer with other resorcinol molecules. In the last step, the rapid cyclisation is a result of two main factors; hydrogen bonding between adjacent hydroxyls of resorcinol units and the lack of conformational strain.[24, 74]

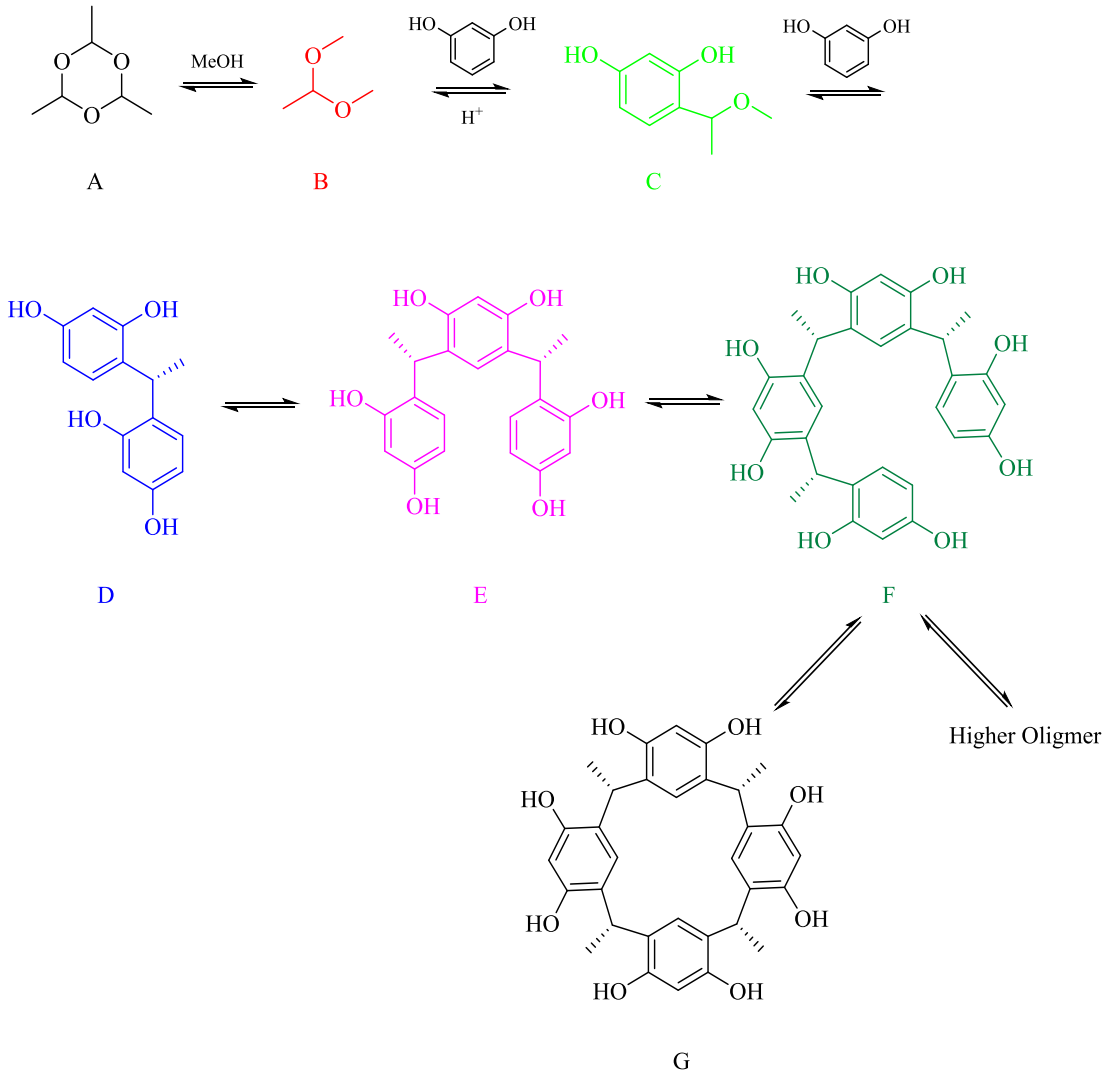

Scheme 2. 1: Mechanism of resorcinarenes formation.

2.6 Functionlisation of resorcinarenes

Over the years, many methodologies have been developed to modify the resorcinarene framework in an assortment of ways and some examples will be provided here. These methodologies allow the preparation of various resorcinarenes. Resorcinarenes have a cavity and this provides a site for the binding of guest molecular species. Therefore, the methodologies for the functionalization of resorcinarenes have focused on the modification of the peripheral substituted groups. The modification is manly performed at the three positions (R^1, R^2, $R^{2'}$, R^3), see Figure 2.12. The first position (R^1), namely the one *ortho* to both the hydroxyl groups, is highly activated and can readily undergo electrophilic aromatic substitutions reactions.[75] The second position (R^2 and $R^{2'}$), namely the phenolic

hydroxyl groups can be readily functionalized by acylation or *O*-alkylation.[68] These two positions relate to the upper or wider rim. Resorcinarenes can be also modified at the R^3 position, namely the lower rim or narrower rim. This position arises from the aldehyde used in the synthesis of the resorcinarenes.[19]

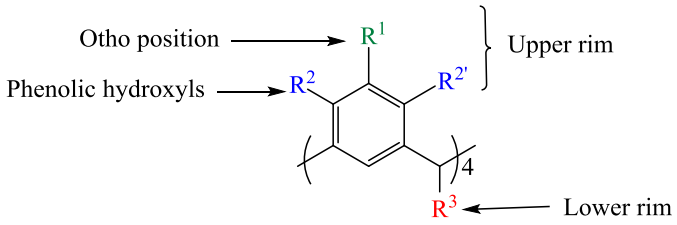

Figure 2. 12: Functionalization positions of resorcinarenes.

There is a great deal of literature examples relating to the modifications of resorcinarenes, so only a few examples will be provided here focusing on the resorcinarenes at these different positions listed above. As has been discussed before, at the upper rim, electrophilic substitution is preferred. A Mannich reaction is an example of an electrophilic substitution reaction, that has been applied successfully on resorcinarenes.[76-79] Konishi et al,[75] have demonstrated how the resorcinarene can be modified at the R^1 position by using Mannich reaction under different conditions. Scheme 2.2 illustrates an example of a Mannich reaction.

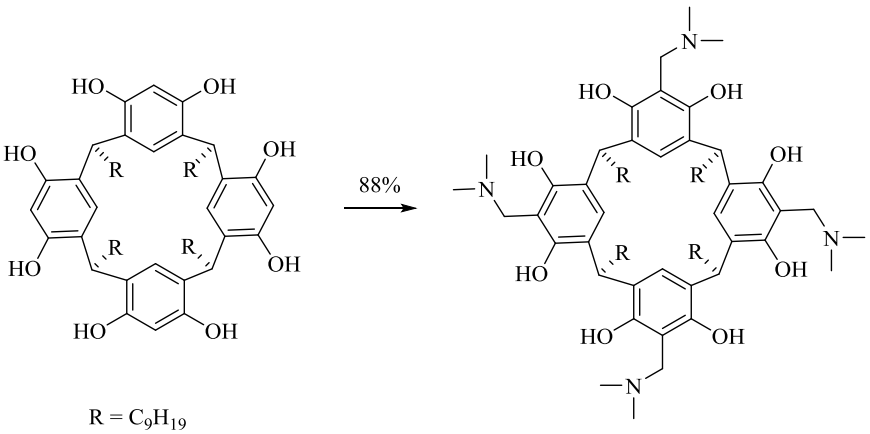

Scheme 2. 2: An example of Mannich reaction.

Also, functionalized resorcinol derivatives have been used as starting materials to form resorcinarenes. These react with aldehydes in a one-pot reaction under basic conditions. (see scheme 2.3).[80-81]

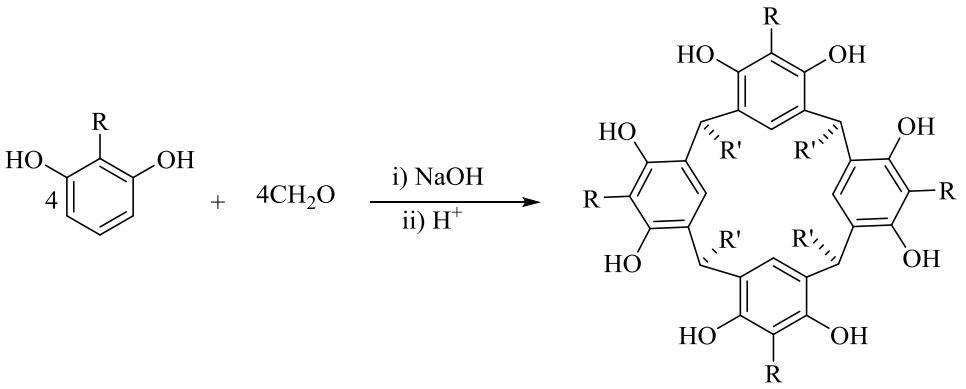

R'	Yield %
NO_2	60
Ac	37
CO_2H	50
H	16

Scheme 2. 3: Reaction of resorcinol with aldehyde under acidic condition.

Another functionalization of the resorcinarene can occur at the upper rim in the R^2 and $R^{2'}$ positions. The resorcinarene has the phenolic hydroxyl groups which allows the usual reactions of alcohols and phenols to be applied, *e.g*. etherification and esterification.[68, 81-84] For example, Moore and Matthews have published a review on *O*-alkylation of the resorcinarene in which a wide variety of examples and strategies has been described. [81]

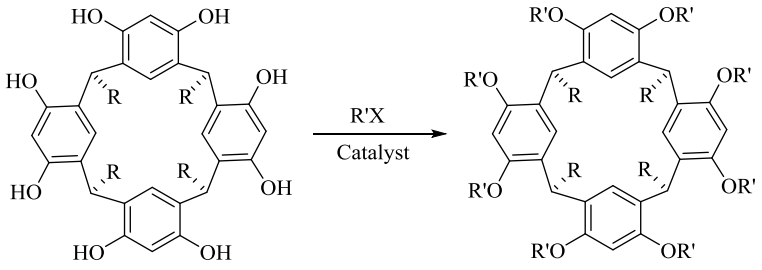

R'
p-TolSO_2
PO(Oi-Pr)
Bn
Ph_2P

Scheme 2. 4: O-alkylation of resorcinarenes.

Moreover, cavitand compounds have been formed by the functionalization at this position. Cavitands are bridged resorcinarenes and can be formed by reaction of groups bearing two leaving groups with resorcinarenes under basic conditions.[68]

These compounds are used as receptors[55, 85] or rigid scaffolds for large molecules[57, 86] (see Figure 2.13).

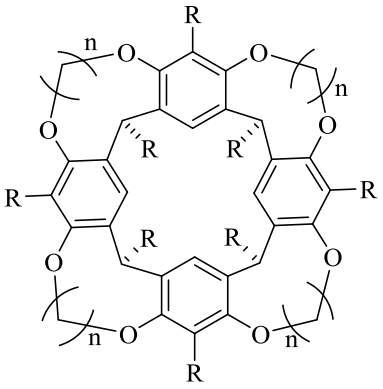

R = H, CH_3, Br, I
n = 1, 2, 3

Figure 2. 13: Example of resorcinarene cavitands.

Functionalization of the lower rim position (R^3) has also been well reported. For example, Ghaedi *et al*. have synthesized new a resorcinarene under acidic conditions as shown in Scheme 2.5 and used it as a ligand to separate specific ions (Co^{2+}, Ni^{2+}, Cu^{2+}, and Cd^{2+}).[87]

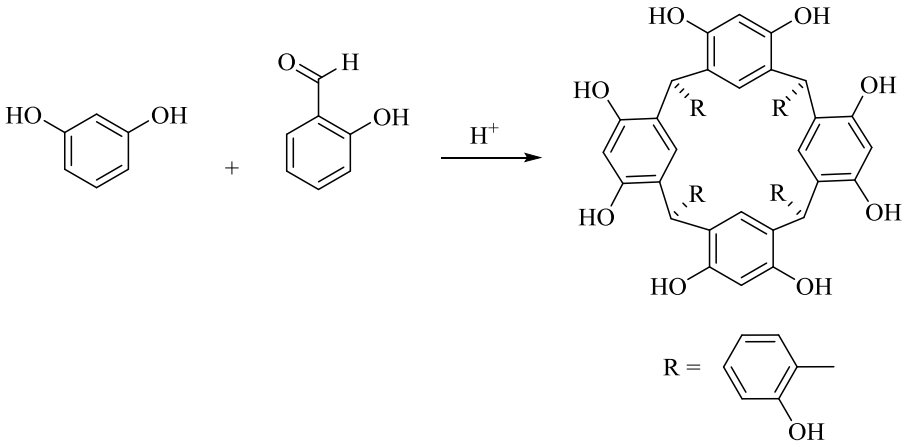

Scheme 2. 5: Synthesis of new resorcinarene derivatives.

Furthermore, various catalysts have been utilized with efficiency as environmentally friendly, recyclable and inexpensive catalysts for the synthesis of resorcinarenes such as molecular iodine,[88] Fe_3O_4 nanoparticles,[89] bismuth[90,91] lanthanide[92] ions.

2.7 Functionalisation of resorcinarene in this thesis

All the chemistry of the resorcinarenes of interest in this work occurs on the tetramethoxy-resorcinarene. The synthesis of this kind of resorcinarene was reported by McIldowie in 2000,[65] by Lewis acid catalyzed condensation of 3-alkoxyphenol with aliphatic aldehydes. A wide variety of aldehydes, whether saturated or unsaturated alkyl aldehydes,[68, 71, 93-94] have been utilized successfully to synthesise variants at the R^3 position. Scheme 2.6 provides some examples where an aldehyde is used to attach different R groups to the lower rim of the functionalized resorcinarenes.[59] In the synthesis of these chiral resorcinarenes only the crown conformation was obtained. Consequently, the crown conformer was used for all the studies described in this thesis. Furthermore the crown is best suited for our studies as all the substituent groups are on the same face of the macrocycle.

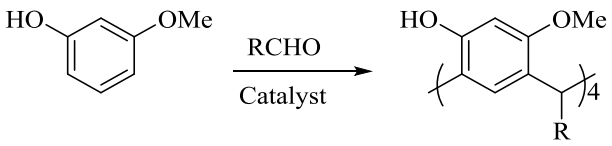

R	Yield %
CH_3	60
C_2H_5	88
$C5H_{11}$	77
$C_{11}H_{23}$	68

Scheme 2. 6: Synthesis of resorcinarenes.

The tetramethoxy resorcinarene is characterized by the presence of four hydroxyl groups, making it easy to modify and use in different areas such as supramolecular chemistry.[65] Scheme 2.7 provides an overview of the synthesis pathway in this thesis. The first step is the synthesis of the three alkyl- tetramethoxy resorcinarene derivatives followed by introduction of the linker group at the position $R^{2'}$. Hydrolysis and then coupling the resulting acids with protected *L*-aspartic acid provides a diastereoisomeric mixture of the protected target compounds. Final deprotection should produce the octa-acid derivatives (Section A). The synthesis of amino functionalized derviatives will be prepared by amidation of the ester intermediate produced previously (Section B). Reference compounds based on dodecanoic acid will also be prepared to investigate any synergistic effect of the macrocycle (Section C).

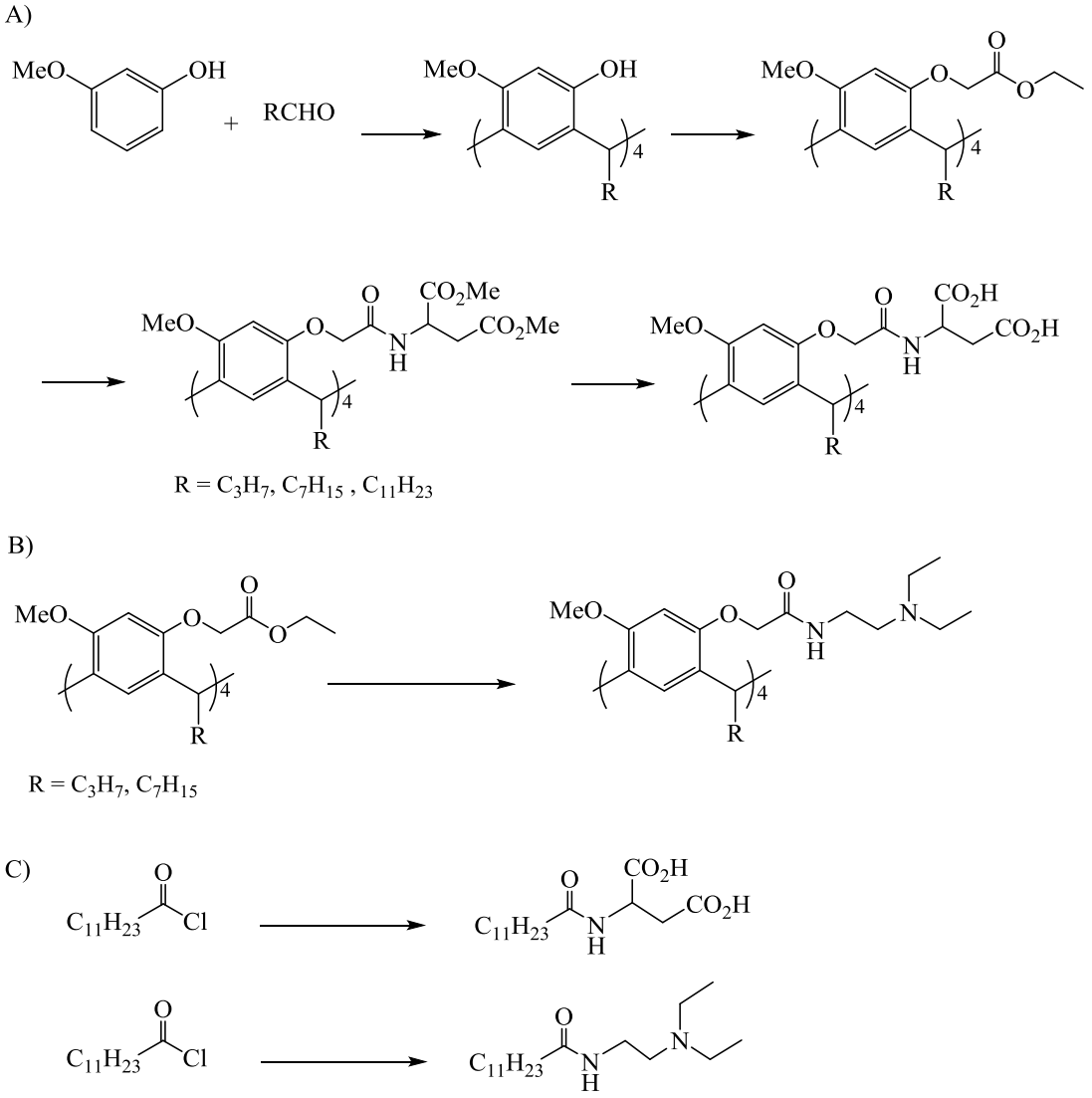

Scheme 2. 7: The synthesis pathway.

2.8 Results and Discussion

The synthetic pathway for the desired tetramethoxytetraalkylresorcinarene tetra-*L*-aspartic acid derivatives is shown in **Scheme 2.7**. The first step was to prepare the resorcinarene scaffolds using the one step Lewis acid catalysed condensation of an aliphatic aldehyde with 3-methoxyphenol as described by McIldowie.[59] This produced the desired tetramethoxyresorcinarenes (**2a-c**), as shown in scheme 2.8, in moderate yields. Three different tetramethoxyalkylresorcinarenes were synthesised to investigate the effect of the alkyl chain length on crystallization and corrosion inhibition.

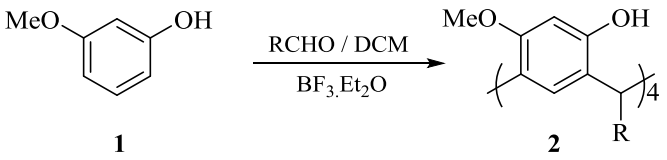

1 **2**

Compound	R
2a	C_3H_7
2b	C_7H_{15}
2c	$C_{11}H_{23}$

Scheme 2. 8: Synthesis of alkyl tetramethoxy resorcinarene derivatives.

The propyl resorcinarene derivative, **2a** was obtained in 44 % yield as white crystals after crystallisation from methanol. The ^{1}H NMR spectrum showed the distinct signals due to the aromatic protons at δ 6.27 and 7.16, one singlet for the methoxy protons at δ 3.75 and a triplet at δ 4.30 corresponding to the methine proton between the two aromatic rings. The propyl signals appeared at δ 2.18, 1.31 and 0.98 ppm integrating for a total of 7 protons. Similarly, **2b** and **2c** showed the appropriate signals in the region δ 3.85-3.6 for the heptyl **2b** and undecyl **2c** derivatives, with difference being the integration due to the methylene protons in alkyl chain, as shown in Figure 2.14. These data support the conformation of the derivatives with the suggested structure.

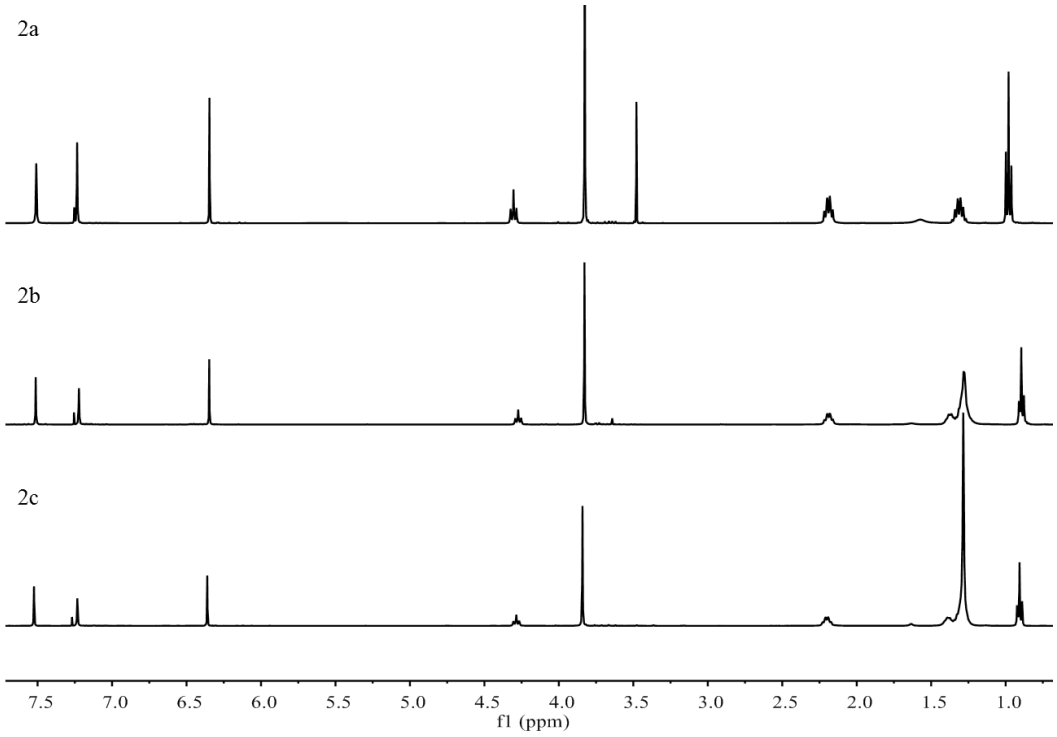

Figure 2. 14: The 1H NMR spectra of **2a**, **2b**, **2c**.

In order to introduce the amino acid groups, it is necessary to introduce a linker group onto the tetramethoxyresorcinarene derivatives. The methyleneoxycarboxylic acid group has already been used with calixarenes[36, 95] and resorcinarenes,[96] is easy to introduce and functionalise, so this was chosen as the target linker. The linker was synthesised according to the procedure described by McIldowie.[59] The tetramethoxyresorcinarene was treated with ethyl bromoacetate and anhydrous potassium carbonate in dry acetonitrile for 24 hours. Workup gave light-yellow oil which crystallized from a minimum amount of cold methanol to gain a colourless powder without the need for further purification (Scheme 2.9).

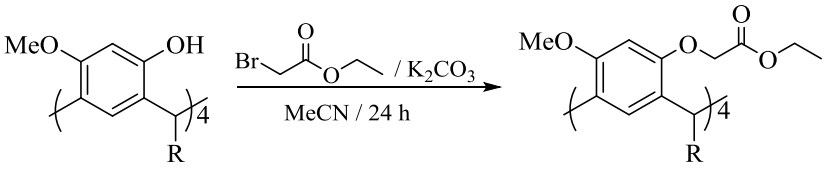

2 **3**

Compound	R
3a	C_3H_7
3b	C_7H_{15}
3c	$C_{11}H_{23}$

Scheme 2. 9: Synthesis of ester alkyl tetramethoxy resorcinarenes derivatives.

The ^{1}H NMR spectrum of compound **3a** (Figure 2.15) showed the expected signals for the resorcinarene protons as well as the signals for the attached linker group with the appropriate integration ratios. In particular, the signals for the methyleneoxy protons appeared as an AB system at δ 4.28 and 3.97 as would be expected of methylene protons attached to a chiral resorcinarene.[59] The ^{13}C NMR spectrum showed the appropriate number of signals including three in the region δ 70 - 55 corresponding to the aliphatic carbon atoms bonded to oxygen atom. The derivatives **3b** and **3c** were synthesised in a similar manner and their NMR spectra showed similar signals varying only in those for the alkyl chains.

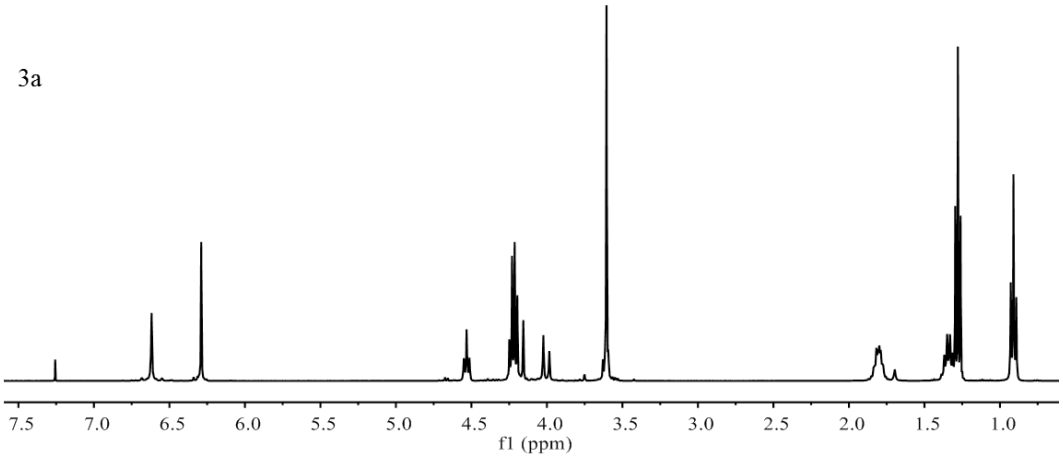

Figure 2. 15: The 1H NMR spectrum of **3a**.

This alkylation reaction is a nucleophilic substitution where the carbonate ion deprotonates the oxygen atom of the hydroxyl group, generating the nucleophile which adds to the electrophilic carbon atom of ethyl bromoacetate, displacing the bromide ion leaving group as shown in Scheme 2.10.

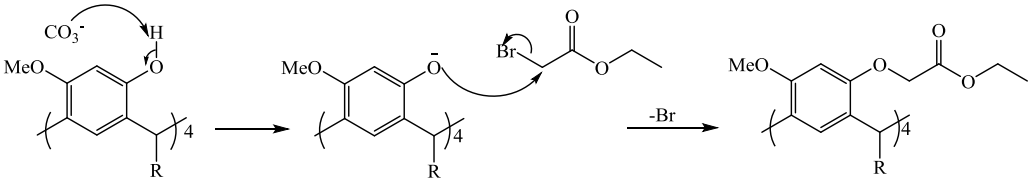

Scheme 2. 10: Mechanism of formation of the ester alkyl tetramethoxy resorcinarenes.

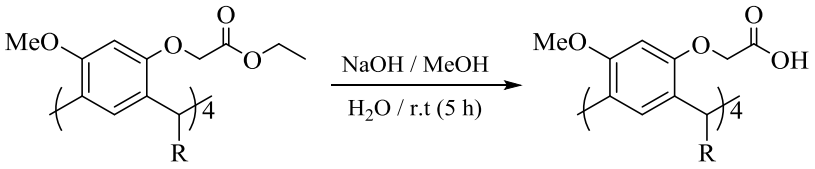

3 **4**

Compound	R
4a	C_3H_7
4b	C_7H_{15}
4c	$C_{11}H_{23}$

Scheme 2. 11: Hydrolysis of the esteralkyltetramethoxy resorcinarenes to form the acid derivatives (4a-c).

The acids (**4a-c)** were formed by the reaction of the corresponding esters with sodium hydroxide in aqueous methanol followed by acidification with hydrochloric

acid (5 M). These hydrolysis reactions produced the desired acids as white powders which did not require further purification. The ^{1}H NMR spectrum (Figure 2.16) of the acid (**4a**) showed the key expected signals, along with the disappearance of the methyl and methylene protons of the ethyl ester. The ^{13}C NMR spectra also gave more evidence where the three signals in the region δ 70 - 55 corresponding to carbon atoms bonded to oxygen atoms were reduced to two signals.

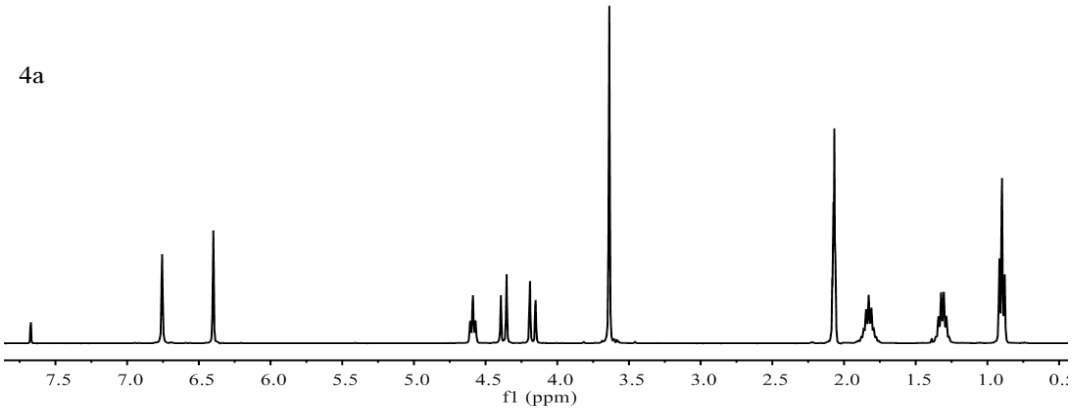

Figure 2. 16: The 1H NMR Spectrum of the acid **4a**.

The formation of an amide by using a peptide coupling reagent was reported.[36, 95, 97] The amino acid can be attached on the calixarene or resorcinarene scaffold *via* many strategies and a few will be briefly described here. The acid halide method requires that the carboxylic acid is first converted into the acid halide (usually chloride) before coupling with an amino group. Common reagents used for preparing the acid halides includes oxalyl chloride,[97-98] *N*,*N*-diethylaminosulfur trifluoride (DAST)[99] and thionyl chloride.[100-101] Another strategy is to prepare activated esters by using coupling reagents like *N*,*N'*-dicyclo-hexylcarbiimide (DCC)[102-103] with *N*-hydroxy-succinimide (HOSu)[104] or 1-hydroxybenzotrizole (HOBt),[105-106] then the activated ester reacts with the amino acid to give the amide product. A third method combines the carbodiimide and hydroxytriazole units. For example, *N*,*N*,*N*',*N*'-tetramethyl-*O*-(1*H*-benzotriazol-1-yl)uronium hexafluorophosphate (HBTU)[36, 107] or tetramethyl-*O*-(benzotriazol-1-yl)uronium tetrafluoroborate (TBTU),[95] have been used as coupling reagents which gave a reasonable yields. TBTU has been used as the activating agent for linking the amino acid on the resorcinarene in this work.

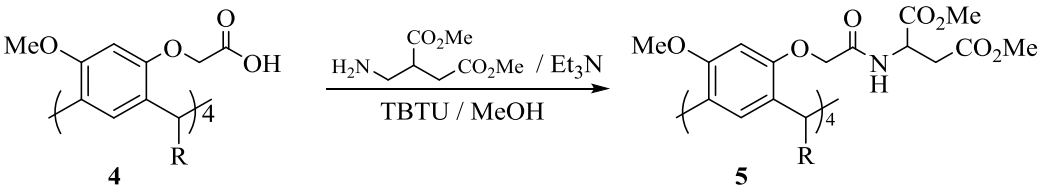

Compound	R
5a	C_3H_7
5b	C_7H_{15}
5c	$C_{11}H_{23}$

Scheme 2. 12: Coupling of dimethyl L-aspartic acid with alkyl-tetramethoxy resorcinarene derivatives.

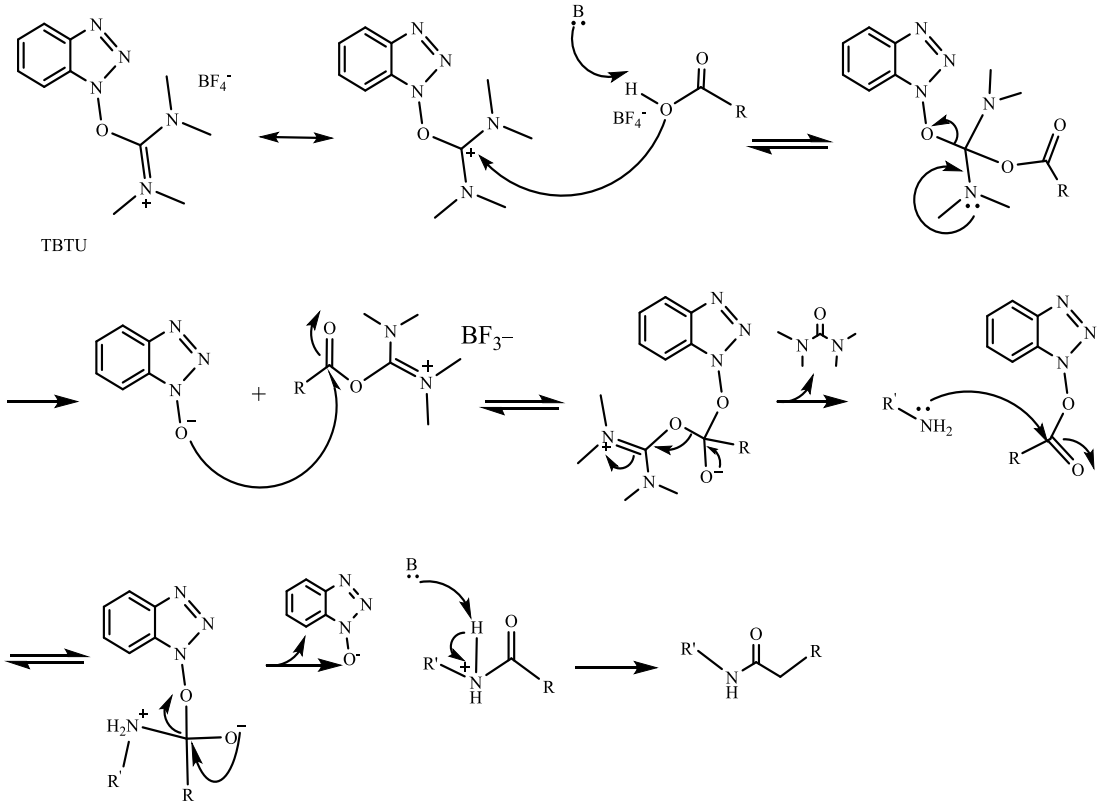

Scheme 2. 13: The suggested mechanism to form amide (**5a-c**).

Amides (**5a-c**) were synthesised from adapted literature procedures. Scheme 2.12 presents the reaction under dry, alkaline conditions in the presence of TBTU. The role of TBTU is to activate the carboxylates in the acid (**4**) in two steps; the carboxylates were firstly activated by the tetramethyluronium unit from TBTU and then reacted with the hydroxyl benzotriazole moiety to increase their reactivity. Next, the amino group of the amino acid reacts with the activated carbonyl to form the desired product as shown in Scheme 2.13.

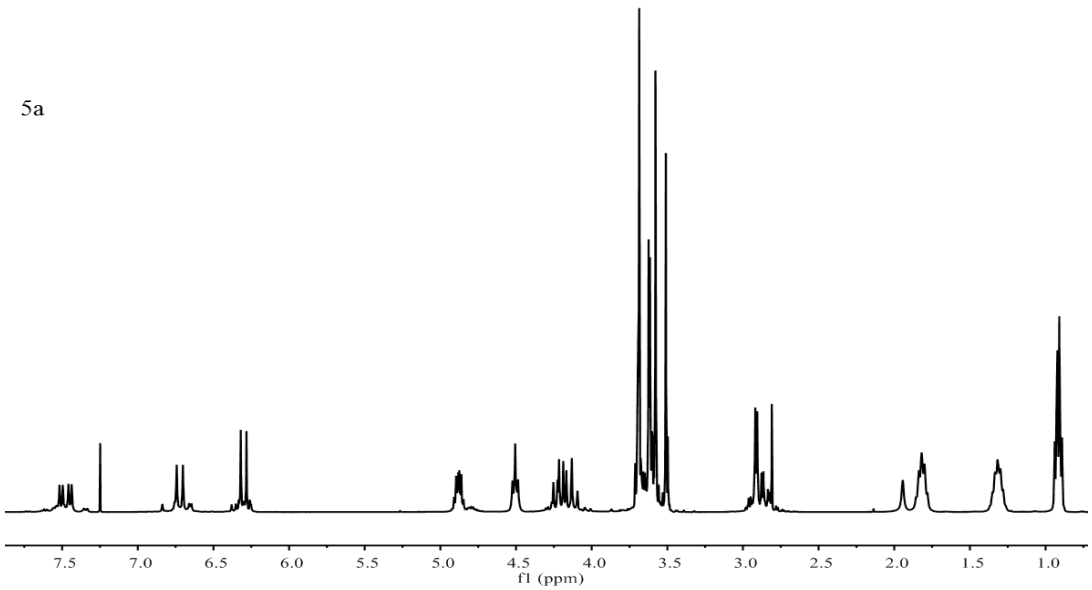

Figure 2. 17: The 1H NMR spectrum of **5a**.

The ^{1}H NMR spectrum of the amide **(5a)** clearly indicated that the desired compound was formed, but as a mixture of diastereoisomers as shown by the doubling up of the signals at 6.3, 6.7 and 7.5 ppm in Figure 2.17. Also, the multiple signals at 3.45-3.60 ppm for the methoxy groups and the mixed signal at 4.01-4.31 ppm for methylene group in the molecules are consistent with two diastereoisomers. ^{13}C NMR spectra give more evidence that the amides were formed as a diastereomeric mixture by the doubling of signals. There have been many attempts to separate the two diastereoisomers of this compound but unfortunately these attempts were unsuccessful, possibly due to the strong hydrogen bonding between these diastereoisomers, which prevented the separation process. Thus, this amide was used as a mixture of diastereoisomers.

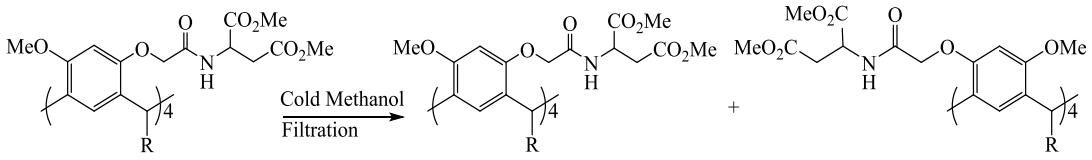

Compound	R
5b	C_7H_{15}
5c	$C_{11}H_{23}$

Compound	R
6, 7	C_7H_{15}
8, 9	$C_{11}H_{23}$

Scheme 2. 14: The isolation of (**5b**, **5c**) to diastereoisomer.

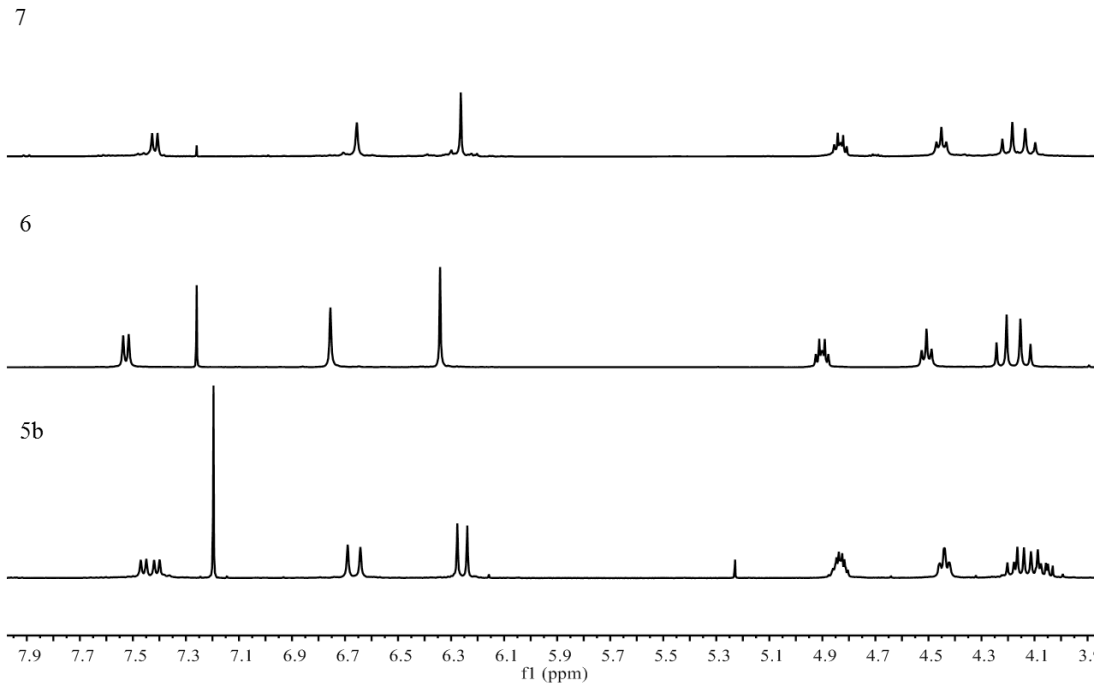

Figure 2. 18: 1H NMR spectra of **5b**, **6** and **7**.

Amide **5b** was also initially isolated as a mixture of diastereoisomers. However, unlike **5a**, these could be separated by crystallization. Addition of a minimum amount of cold methanol, up to 4°C, followed by filtration gave the first diastereomers, **6**, in 20% yield as a white powder which was pure according to the ^{1}H NMR spectrum and TLC. The second diastereomers, **7** was mixed with some of the first diastereomers, so to purify it, the first diastereoisomer was crystallized out with cold methanol until no crystals formed then the remaining oil was dissolved in DCM and washed with water (2 times) followed by brine (1 time). Finally, the organic layer was concentrated and the ^{1}H NMR spectrum in Figure 2.18 shows only a trace of the first diastereomers. Attempts to purify this by using column chromatography were not successful. The amide **5c** was treated in a similar way (Scheme 2.14) to give the first diastereomers **8** in 18 % yield as a white powder which was pure identified by the ^{1}H NMR spectrum, and the second diastereomers **9** in 60 % yield as oil which also contained a small amount of the first diastereomers.

The preparation of a series of diastereomeric tetracamphorsulfanate derivatives using (*S*)-(+)-10-camphorsulfonyl chloride in pyridine followed by isolation by flash chromatography was reported by Buckley *et al.*[108] For example, the

diastereoisomeric tetracamphorsulfanates (11a-d and 11a’-d’) were prepared and isolated from racemic resorcinarenes. They found that, the high values of optical rotation related to the *M* diastereoisomer and the *P* diastereoisomer had the lower value as shown in Figure 2.19.

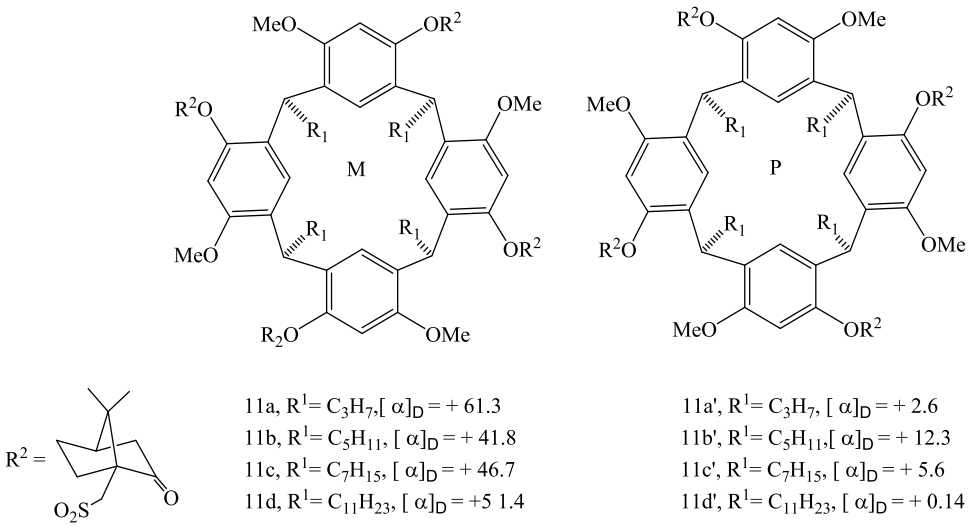

Figure 2. 19: Some examples of the formation of tetracamphorsulfanates (11a-d and 11a’-d’) from racemic resorcinarenes.

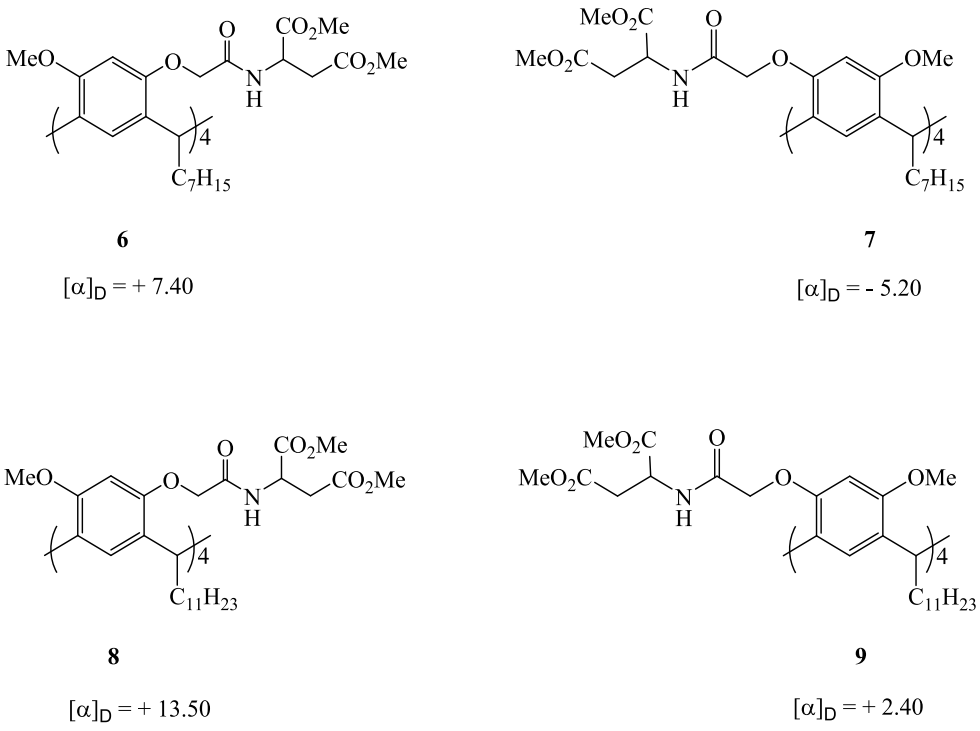

6

$[\alpha]_D$ = + 7.40

7

$[\alpha]_D$ = - 5.20

8

$[\alpha]_D$ = + 13.50

9

$[\alpha]_D$ = + 2.40

Figure 2. 20: The optical rotation value of the resorcinarenes esters.

The optical rotation of amides **5b-c** was measured. Figure 2.20 introduces the rotation values of the heptyl and the undecyl resorcinarenes derivatives. The magnitude of the rotation of the first diastereomers is significantly greater than the second one and using the trend reported by Buckley the structures have been tentatively assigned. Therefore, the amides **6** and **8** are *M* and amides **7** and **9** are *P*.

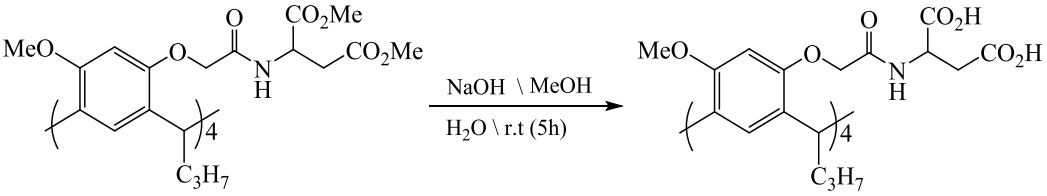

5a **10**

Scheme 2. 15: The hydrolysis of **5a** to form **10**.

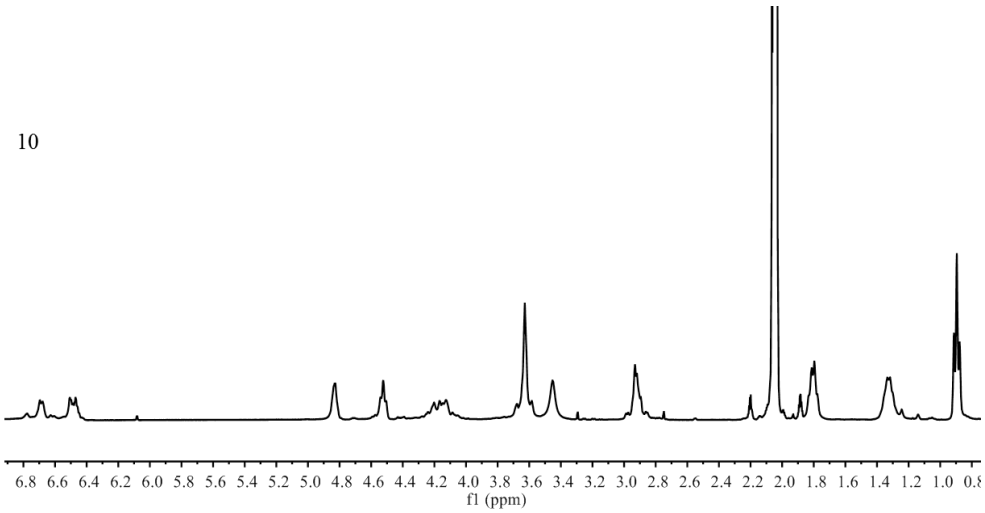

Figure 2. 21: 1H NMR spectrum of the L-aspartic acid resorcinarene (**10**).

The ester groups in the amide **5a** were hydrolysed using sodium hydroxide in refluxing aqueous methanol and then the crude was acidified by hydrochloric acid to give the acid **10** as a white powder which did not need further purification. The ^{1}H NMR spectrum of the acid **10** clearly indicated that hydrolysis was successful by the disappearance of the key signals for the methoxy groups of the *L*-aspartic acid ester (Figure 2.21). In the ^{13}C NMR spectrum the number of signals was reduced from eight to four in the region δ 55 - 70.

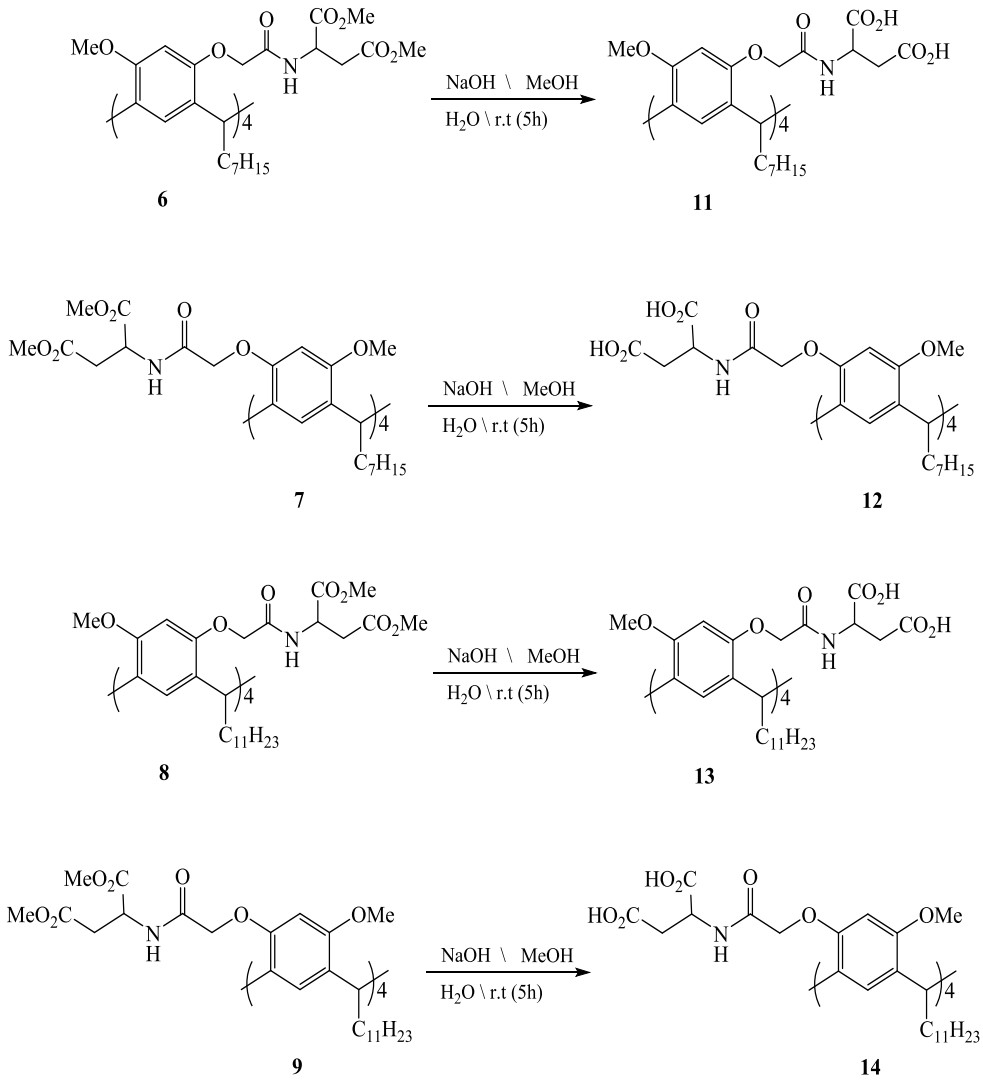

Scheme 2. 16: The hydrolysis reactions of distereoisomers.

The esters **6 - 9** were hydrolysed to give the corresponding acids **11-14** as shown in Scheme 2.16. In this step, the crude product was obtained without difficulty. The ^{1}H NMR spectra showed the disappearance of methyl groups of the amino acid esters and expected peaks of resorcinarene methoxy protons at δ 3.55. Furthermore, the ^{13}C NMR and IR spectra provided further support that the hydrolysis was successful. The ^{13}C NMR spectra of these acids were difficult to read due to the poor solubility but the key signals can be read where the four singles reduced to two in the region δ 55 - 70. Acids **11-14** were used as crystallization modifiers and corrosion inhibitors.

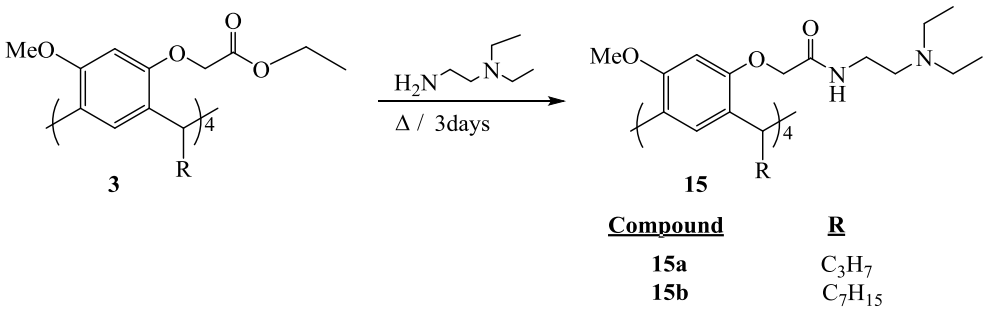

Compound	R
15a	C_3H_7
15b	C_7H_{15}

Scheme 2. 17: The synthesis of diethyldiamine or amid tetramethoxy resorcinarenes derivatives.

Scheme 2.17 presents the other types of resorcinarene derivatives that have been synthesized and investigated as corrosion inhibitors. Ester **3** was reacted with *N*,*N*-diethylethylenediamine under reflux for three days to form the amide **15**. After 3 days, the solvent was reduced and after the work up process, the desired product was obtained without the need for any further purification as shown in Figure 2.22. The ^{1}H NMR spectrum presents the disappearance of the proton signals that correspond to the ethyl ester at δ4.20 – 4.25 and new signals that corresponding to the diethyl diamine at δ0.9 -3.4 have been formed. The ^{13}C NMR spectrum gave further evidence of forming the desired product where the signals of the carbonyl group at δ170, the aromatic group at δ97–155, methoxy group at δ56, alkyl and the diethylamine groups at δ10 – 70 are observed.

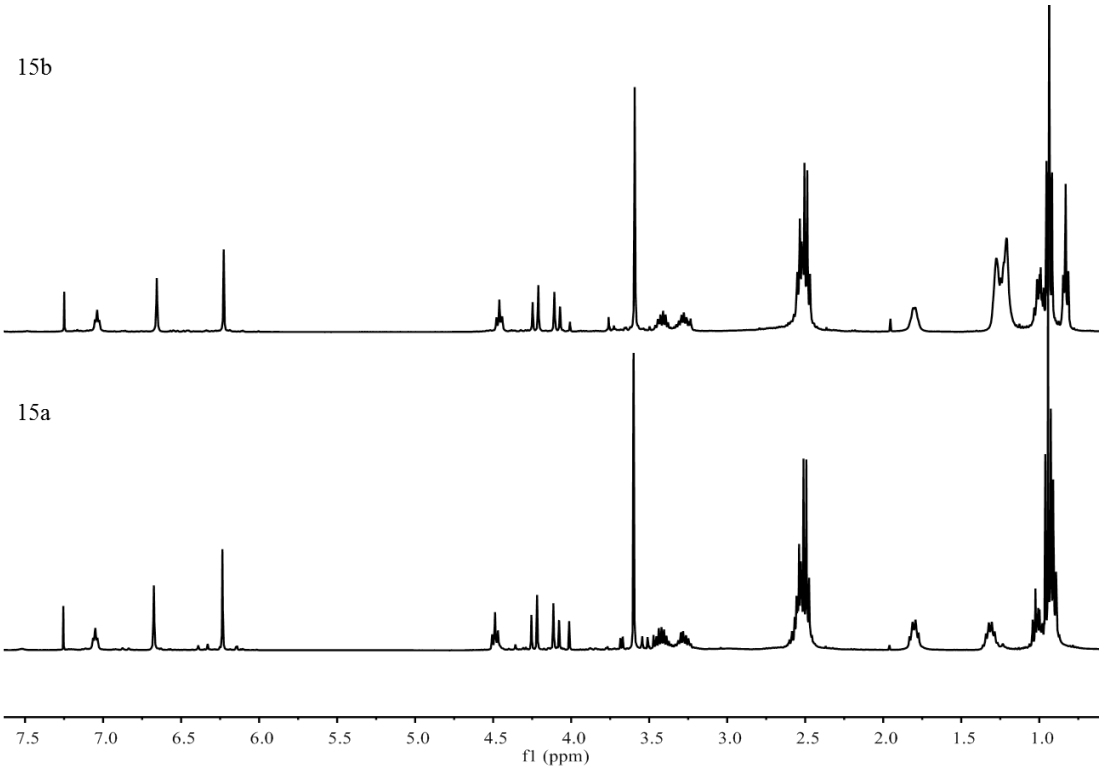

Figure 2. 22: The 1H NMR spectra of compound **15a** and **15b**.

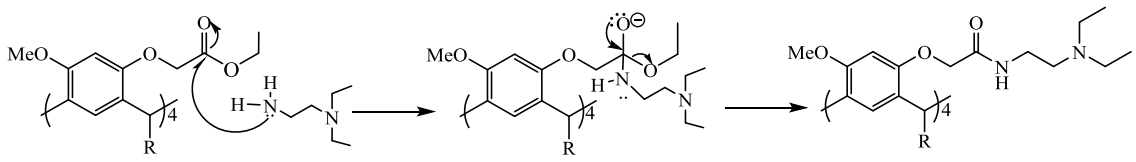

Scheme 2. 18: The suggested mechanism for the formation of **15**.

This reaction is a nucleophilic acyl substitution reaction and the suggested mechanism is introduced in Scheme 2.18. The primary amine adds to the carbonyl carbon atom in the ester to form a tetrahedral intermediate. The ethoxy group of the ester is then eliminated to produce the desired product.

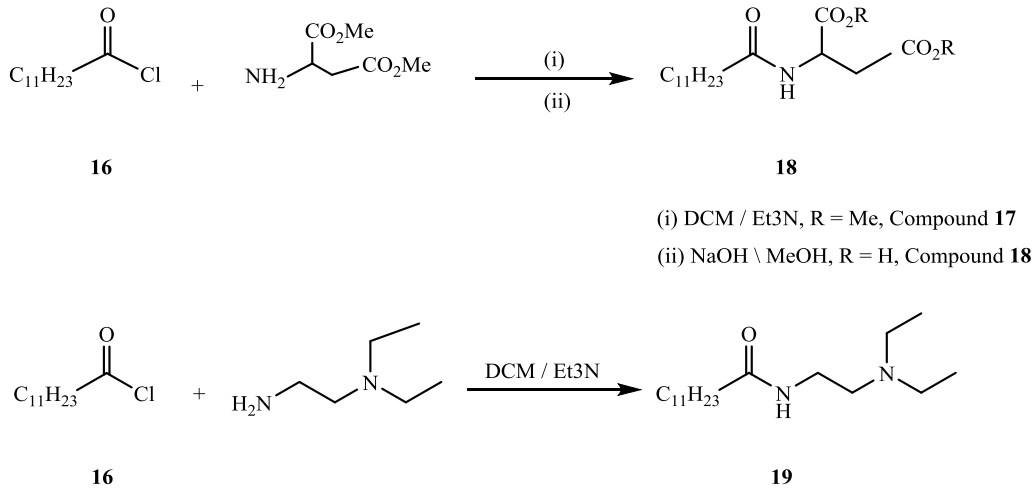

Scheme 2. 19: (a) The pathway synthesis of **18**. (b) Synthesis of **19**.

Scheme 2.19 illustrates the types of compounds that were synthesized to investigate the macrocyclic effect of the calixarene derivatives. To form compound **18**, the amide was first synthesised by reacting dodecanoyl chloride with *L*-aspartic acid dimethyl ester in dichloromethane. Workup gave the ester **17** as a white powder which did not need further purification as shown in Figure 2.22, and supported by ^{1}H COSY analysis to distinguish between the two protons that linked to the carbonyl group and the two protons that linked to the methyl ester. Following that, the hydrolysis of the ester was achieved by reacting the ester **17** with sodium hydroxide in aqueous methanol followed by acidification with hydrochloric acid (5 M). The ^{1}H NMR spectrum clearly indicates the disappearance of the methoxy signal, while maintaining signals for the amino acid and fatty acid. Similarly, compound **19** has been synthesized by reacting dodecanoyl chloride with diethylethylenediamine and the ^{1}H NMR spectrum (Figure 2.23) shows the proton signals of the diethylamide in the expected regions at δ0.8, δ2.5 and δ3.3. Also, the ^{1}H COSY analysis has been done to differentiate between the CH_2 protons linked to the carbonyl group of the dodecanoyl chain and the CH_2 protons of the aspartic acid component of compound **17**, and also to the differentiate between the CH_2 protons of the dodecanoyl group and the CH_2 protons linked to the nitrogen in the diethylethylenediamine group of compound **19**.

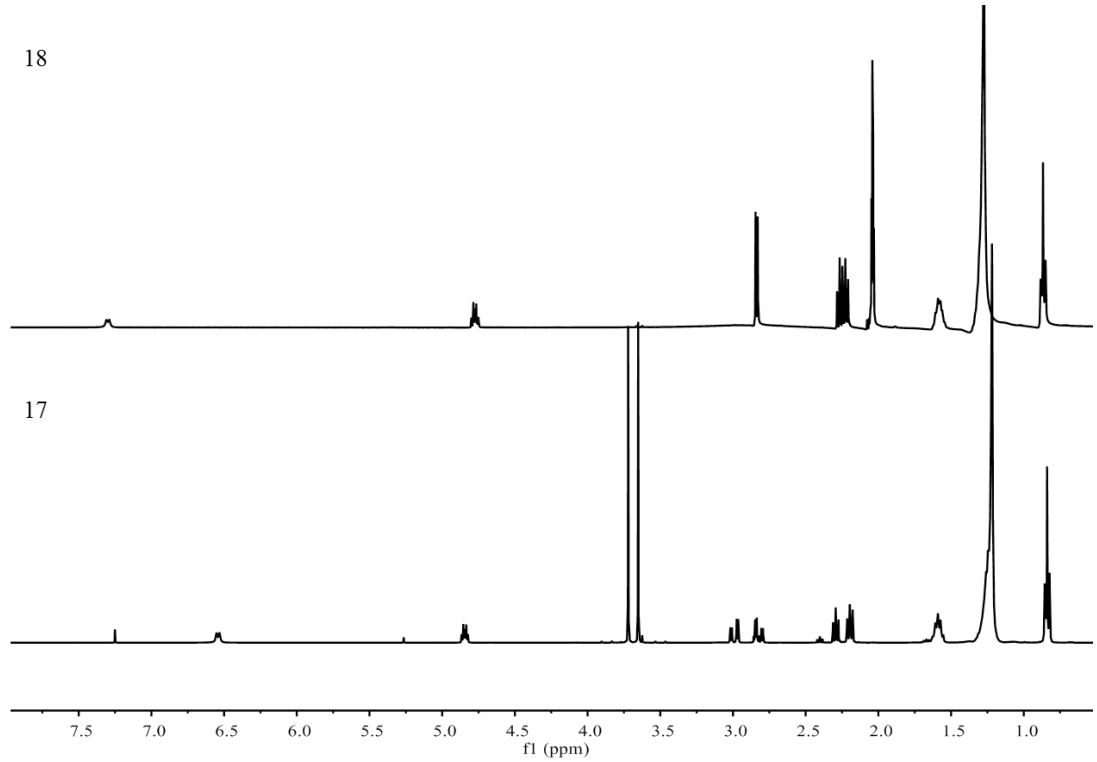

Figure 2. 23: The 1H NMR spectra of compounds **17** and **18**.

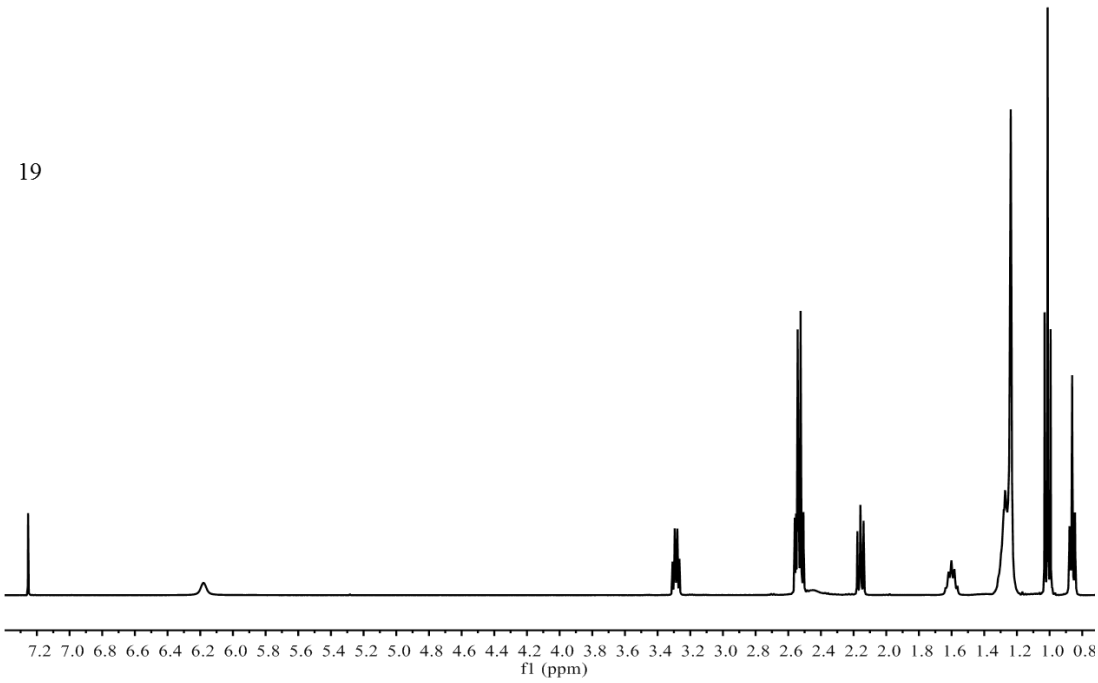

Figure 2. 24: The 1H NMR spectra of compound **19**.

2.9 Conclusion

Numerous previously unreported amino acid functionalized resorcinarene derivatives with different length hydrocarbon chains have been synthesised and characterised. Also, two reference compounds, dodecanamides of *L*-aspartic acid or diethylethylenediamine acid were successfully synthesized. These compounds will be used in studies of their inhibition efficiency for crystallization and corrosion of carbon steel in CO_2 saturated-brine at 30°C.

2.10 Experimental

2.10.1 Reagents

The chemicals were used without any further purification and were purchased from Alfa Assar and Sigma Aldrich companies. Dry acetonitrile and dichloromethane were obtained by PureSolv MD5.

2.10.2 Instrumentation

All infrared spectra were obtained on a Perkin Elmer 100 FT-IR spectrometer using a Universal ATR sampling accessory. All nuclear magnetic resonance (NMR) spectra were obtained using a Bruker AVANCEIII 400 MHz NMR spectrometer. ^{1}H spectra were recorded at 400 MHz and ^{13}C NMR at 101 MHz. All samples were dissolved in and referenced to residual chloroform or acetone-d_6. High-resolution mass spectrometry (HRMS) has been obtained using a Thermo Scientific Q-Exactive Orbitrap mass spectrometer at Edith Cowan University. Optical rotations were measured on a Rudolph Research Analytical Autopol 1 Automatic Polarimeter.

2.11 Synthesis of the resorcinarenes derivatives

General procedure for the synthesis of C-alkyl-tetramethoxy-resorcinarene derivatives (2a-c)

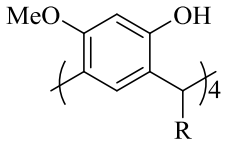

Compound	R
2a	C_3H_7
2b	C_7H_{15}
2c	$C_{11}H_{23}$

General Procedure

The procedure published by McIldowie has been followed.[65] 3-Methoxyphenol (80 mmol) was dissolved in anhydrous dichloromethane, (150 mL) then the aldehyde (80 mmol) was added and the mixture was stirred at room temperature. Boron trifluoride etherate (162 mmol) was then added dropwise and the mixture turned a red color. The reaction mixture was then left to stir at room temperature for 2.5 hours. The reaction mixture was then washed with water (1 x 150 mL), and the organic layer was dried with magnesium sulfate. Following filtration, the solvent was removed by under reduced pressure to give the crude product as dark red precipitate.

1^6,3^6,5^6,7^6-tetrahydroxy-1^4,3^4,5^4,7^4-tetramethoxy-2,4,6,8-tetrapropylresorcin[4]arene (2a). 3-Methoxyphenol (3 g, 24.16 mmol), butanal (1.74 g, 24.16 mmol) and boron trifluoride etherate (6 mL, 48.33 mmol) gave, after normal workup and crystallisation from methanol, the desired resorcinarene (**2a)** (1. 45g, 33.7%), as a white powder, m.p. 255-256°C (Lit.[59] 257-258°C), ^{1}H NMR ($CDCl_3$) δ 0.90 (t, J = 7.3 Hz, 12H, CH_2CH_3), 1.29 (apparent sxt, 8H, CH_2CH_3), 2.16-2.04 (apparent q, 8H, CH_2CH), 3.83 (s,12H, OCH_3), 4.30 (t, J = 6.1 Hz, 4H, $CHCH_2$), 6.35 (s, 4H, Ar*H*), 7.23 (s, 4H, Ar*H*), 7.50 (s, 4H, O*H*). ^{13}C NMR. ($CDCl_3$) δ 14.00 (CH_3), 21.04, 32.68 ($2CH_2$), 35.79 (*C*H), 55.89 (OCH_3), 100.01, 123.76, 124.59, 124.69, 152.97, 153.65 (CH_2-Ar).

2,4,6,8-tetraheptyl-1^6,3^6,5^6,7^6-tetrahydroxy-1^6,3^4,5^4,7^4-tetramethoxyresorcin[4]arene (2b). 3-Methoxyphenol (0.5 g, 4.02 mmol), octanal (0.52 g, 4.02 mmol) and boron trifluoride etherate (1 mL, 8.06 mmol) gave, after

normal workup and crystallisation from methanol, the desired resorcinarene (**2b)** (0.250 g, 26.5%), as a yellowish white powder, m.p. 159-160°C (Lit.[59]160°C). ^{1}H NMR ($CDCl_3$) δ 0.88 (t, J = 7.0 Hz, 12H, CH_2CH_3), 1.38-1.25 (m, 40H, $(CH_2)_5CH_3$), 2,18 (apparent q, 8H, CH_2CH), 3.82 (s, 12H, OCH_3), 4.26 (t, J = 7.0 Hz, 4H, $CHCH_2$), 6.34 (s, 4H, Ar*H*), 7.21 (s, 4H, Ar*H*), 7.50 (s, 4H, O*H*). ^{13}C NMR ($CDCl_3$) δ 14.11 (CH_3), 22.66, 28.08, 29.38, 29.68, 31.90 ($5CH_2$), 33.99 (CH), 55.88 (OCH_3), 100.02, 123.71, 124.63, 124.74, 152.95, and 153.63 (CH_2-Ar).

1^6,3^6,5^6,7^6-tetrahydroxy-1^6,3^4,5^4,7^4-tetramethoxy-2,4,6,8-tetraundecylresorcin[4]arene (2c). 3-Methoxyphenol (5 g, 40.27 mmol), dodecanal (7.42 g, 40.25 mmol) and boron trifluoride etherate (10 mL, 80.53 mmol) gave, after normal workup and crystallisation from methanol, the desired resorcinarene (**2c)** (6.95 g, 30%), as a white powder, m.p. 129-131°C. (Lit.[59] 128-130°C) ^{1}H NMR. ($CDCl_3$) δ 0.69 (t, J = 7.0 Hz, 12H, CH_2CH_3), 1.10-1.5 (m, 72H, $(CH_2)_9CH_3$), 2.10 – 1.98 (apparent q, 8H, CH_2CH), 3.59 (s, 12H, OCH_3), 3.98 (t, J = 7.7 Hz, 4H, $CHCH_2$), 6.98 (s, 4H, Ar*H*), 6.11 (s, 4H, Ar*H*). ^{13}C NMR ($CDCl_3$) δ 14.7 (CH_3), 22.71, 28.10, 29.42, 29. 63, 29.74, 29.76, 29.78, 29.79, 31.97, 31.08, 34.00 ($10CH_2$ and *C*H), 55.87 (OCH_3), 100.02, 123.71, 124.63, 124.73, 152.96, 153.62 (CH_2-Ar).

General procedure for the synthesis of ethoxycarbonyl methyleneoxy-tetramethoxyresorcinarene derivatives (3a-c)

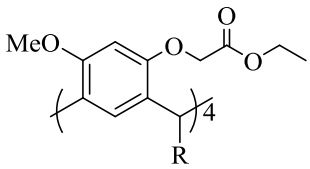

Compound	R
3a	C_3H_7
3b	C_7H_{15}
3c	$C_{11}H_{23}$

General Procedure

A mixture of the alkyl tetramethoxyresorcinarene derivatives (43.10 mmol) and of ethyl bromoacetate (4 mL, 34.48 mmol) were dissolved in dry acetonitrile (132 mL). Potassium carbonate (34. 48mmol) was then added and the reaction mixture heated at reflux for 40 h. The reaction mixture was then cooled, filtered and concentrated to

give a yellow oil. This oil was dissolved in ether (30 mL) and washed with water (3 x 30 mL) and brine (2 x 30 mL) then dried with magnesium sulfate After that, the solvent was reduced to give the crude product, brown oil.

1^6,3^6,5^6,7^6-tetra(ethoxycarbonylmethyleneoxy)-1^4,3^4,5^4,7^4-tetramethoxy-2,4,6,8-tetrapropylresorcin[4]arene (3a). The tetramethoxyresorcinarene (**2a**) (1.2 g, 1.68 mmol), ethyl bromoacetate (1.5 mL, 13.47 mmol) and potassium carbonate (1.8, 13.48 mmol) gave, after normal workup, an oil which was crystallised from a minimum amount of methanol after cooling to 4°C for 24 h compound **3a** (0.950 g, 57%) as a white powder, m.p. 133°C. ^{1}H NMR ($CDCl_3$) δ 0.91 (t, J = 7.2 Hz, 12 H, CH_2CH_3). 1.27 (t, J = 7.1 Hz, 12H, OCH_2CH_3), 1.30 – 1.39 (apparent q, 8H, CH_2CH_3), 3.60 (s, 12H, OCH_3), 3.96, 4.20. (2d, J = 15.8 Hz, 8H, CH_2CO), 4.21 - 4.26 (m, 12H, CH_2O), 4.53 (t, J = 7.4 Hz, 4H, $CHCH_2$), δ 6.28 (s, 4H, Ar *H*), 6.61 (s, 4H, Ar *H*). ^{13}C NMR ($CDCl_3$) δ 14.22, 14.30 ($2CH_3$), 21.08, 35.21, 37.00 ($2CH_2$ and *C*H), 55.56, 60.91, 68.37 (OCH_3, $COCH_2CH_3$ and CH_2CO), 99.56, 126.27, 127.47, 128.20, 154.92, 155.85 (CH_2-Ar), 169.6 (C=O). IR 1753 (CO), 2923 (CH_2), 2855 (CH_3), 1684 (C=C), 1301 cm^{-1} (C–O). HRMS *m/z* $[M+H]^+$ calculated for $C_{60}H_{81}O_{16}$ 1057.5535, found 1057.5502.

1^6,3^6,5^6,7^6-tetra(ethoxycarbonylmethyleneoxy)-2,4,6,8-tetraheptyl-1^6,3^4,5^4,7^4-tetramethoxyresorcin[4]arene (3b). The tetramethoxyresorcinarene (**2b**) (2 g, 2.13 mmol), ethyl bromoacetate (1.8 mL, 16.7 mmol) and potassium carbonate (2.4 g, 17.01 mmol) gave, after normal workup an oil which was crystallised from a minimum amount of methanol after cooling to 4°C for 24 h compound **3b** (1.5 g, 58%) as a white powder, m.p. 69.0 °C (Lit.[59] 63.5-64°C). ^{1}H NMR. ($CDCl_3$) δ, 0.84 (t, J = 6.6 Hz, 12H, CH_2CH_3), 1.20 – 1.26 (m, 40H, $(CH_2)_5CH_3$), 1.28 (t, J = 7.1 Hz, 12H, OCH_2CH_3), 1.78 – 1.86 (m, 8H, CH_2CH_3), 3.61 (s, 12H, OCH_3), 3.99 - 4.21 (2d, J = 15.8 Hz, 8H, CH_2CO), 4.22 - 4.28 (m, 12H, CH_2O), 4.51 (t, 4 H, J = 7.4 Hz, $CHCH_2$), 6.30 (s, 4H, Ar *H*), 6.61 (s, 4H, Ar *H*). ^{13}C NMR. ($CDCl_3$) δ 14.11, 14.23 ($2CH_3$), 22.70, 28.04, 29.36, 29.95, 32.03, 34.66, 35.48 ($6CH_2$ and *C*H), 55.55, 60.90, 68.38 (OCH_3, $COCH_2CH_3$ and CH_2CO), 99.58, 126.30, 127.47, 128.19, 154.94, 155.57 (CH_2-Ar), 169.63(*C*=O). IR 1753 (CO), 2923 (CH_2), 2855 (CH_3), 1684 (C=C), 1301 cm^{-1} (C–O). HRMS *m/z* $[M+H]^+$ calculated for $C_{76}H_{113}O_{16}$ 1281.8039, found 1281.8002.

$1^6,3^6,5^6,7^6$-tetra(ethoxycarbonylmethyleneoxy)-$1^6,3^4,5^4,7^4$.tetramethoxy-2,4,6,8-tetraundecylresorcin[4]arene (3c). The tetramethoxyresorcinarene (**2c**) (2.5 g, 2.15 mmol), ethyl bromoacetate (1.9 mL, 11.44 mmol) and potassium carbonate (2.4 g, 17.36 mmol) gave, after normal workup an oil which was crystalized from a minimum amount of methanol after cooling to 4 °C for 24 h compound **3c** (1.655 g, 51%), m.p. 57.0°C. ^{1}H NMR. ($CDCl_3$) δ, 0.85 (t, J = 6.7 Hz, 12H, CH_2CH_3), 1.19 – 1.25(m, 36H, $(CH_2)_9CH_3$), 1.27 (t, J = 7.1 Hz, 12H, OCH_2CH_3), 1.77-1.84 (m, 8H, CH_2CH), 3.60 (s, 12H, OCH_3), 3.98, 4.20 (2d, J = 15.8 Hz, 8H, CH_2CO), 4.21 - 4.25 (m, 12H, CH_2O), 4.50 (t, 4 H, J = 7.4 Hz, $CHCH_2$), 6.28 (s, 4H, Ar *H*), 6.59 (s, 4H, Ar *H*).^{13}C NMR. ($CDCl_3$) δ 14.10, 14.23 ($2CH_3$),), 22.69, 28.08, 29.39, 29.72, 29.75, 29.79, 29.87, 30.03, 31.94, 34.66, 35.50 ($10CH_2$ and CH), 55.55, 60.90, 68.39 (OCH_3, $COCH_2CH_3$ and CH_2CO), 99.58, 126.31, 127.47, 128.19, 154.94, 155.57 (CH_2-Ar), 169.63(C=O). IR 1759 (CO), 2920 (CH_2), 2850 (CH_3), 1612 (C=C), 1297 cm^{-1} (C–O). HRMS *m/z* $[M+H]^+$ calculated for $C_{92}H_{145}O_{16}$ 1506.0543.

General procedure for the hydrolysis of the ethyl ester in the alkyl-tetramethoxyresorcinarene derivatives (3a-c) to form (4a-c)

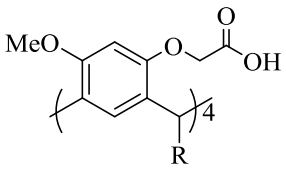

Compound	R
4a	C_3H_7
4b	C_7H_{15}
4c	$C_{11}H_{23}$

To a solution of the tetraester (1.89 mmol) in methanol (80 mL) was added sodium hydroxide (15.15 mmol) and water (4 mL) and the mixture heated at reflux for 5 hours. The solvent was removed to gain a light-yellow solid which was then acidified with 5 M of HCl, filtered and dried in a vacuum desiccator over P_2O_5 for 72 hours to gain the white solid.

$1^6,3^6,5^6,7^6$-tetra(carboxymethyleneoxy)-$1^4,3^4,5^4,7^4$-tetramethoxy-2,4,6,8-tetrapropylresorcin[4]arene (4a). The tetra-ester (**3a**) (0.51 g, 0.48 mmol) and sodium hydroxide (0.15 g, 3.86 mmol) gave, after workup and drying the desired tetra-acid (**4a**) (0.281 g, 62%) as a white solid, m.p. 272°C. ^{1}H NMR. (Acetone-d_6) δ,

0.89 (t, 12H, *J* = 7.2 Hz, CH_2CH_3), 1.78 – 1.87 (m, 8H, CH_2CH), 3.63 (s,12H, OCH_3), 4.14 - 4.42 (2d, *J* = 16 Hz, 8H, CH_2CO), 4.58 (t, *J* = 7.5, Hz, 4H, CH_2CH), 6.39 (s, 4H, Ar *H*), 6.75 (s, 4H, Ar *H*), ^{13}C NMR. (Acetone-d_6) δ14.01 (CH_3) 20.87, 34.56, 37.26 ($2CH_2$ and *C*H), 55.47, 67.04 (OCH_3 and OCH_2), 98.89, 126.01, 126.87, 126.41, 154.41, 155.47 (CH_2-Ar), 169.78 (C=O). IR 3450 (OH), 1732 (CO), 2931 (CH_2), 2869 (CH_3), 1610 (C=C), 1294 cm^{-1} (C–O). HRMS, *m/z* $[M+H]^+$ calculated for $C_{52}H_{65}O_{16}$ 945.4283, found 945.4269.

1^6,3^6,5^6,7^6-tetra(carboxymethyleneoxy)-2,4,6,8-tetraheptyl-1^6,3^4,5^4,7^4-tetramethoxyresorcin[4]arene (4b). The tetra-ester (**3b**) (0.51 g, 0.39 mmol) and sodium hydroxide (0.127 g, 3.18 mmol) gave, after workup and drying the desired tetra-acid (**4b**) (0.365 g, 78%) as a white solid, m.p. 190°C. ^{1}H NMR. (Acetone-d_6) δ, 0.88 (t, 12H, *J* = 6.5 Hz, CH_2CH_3), 1.26 -1.39 (m, 40 H, $(CH_2)_5CH_3$), 1.82 – 1.99 (m, 8H, CH_2CH), 3.70 (s,12H, OCH_3), 4.29 - 4.54 (2d, *J* = 16 Hz, 8H, CH_2CO), 4.68 (t, *J* = 7.5 Hz, 4H, CH_2CH), 6.55 (s, 4H, Ar*H*), 6.86 (s, 4H, Ar*H*). ^{13}C NMR. (Acetone-d_6) δ 13.51 (CH_3), 22.48, 27.98, 29.28, 29.75, 31.87, 34.87, 34.95 ($6CH_2$ and *C*H), 55.30, 66.68 (OCH_3 and OCH_2), 98.83, 126.02, 126.38, 126.92, 154.70, 155.76, (CH_2-Ar), 169.55 (C=O). IR 3416 (OH), 1723 (CO), 2925 (CH_2), 2854 (CH_3), 1610 (C=C), 1267 cm^{-1} (C–O). $[M+H]^+$ calculated for $C_{68}H_{97}O_{16}$, 1169.6787, found 1169.6771.

1^6,3^6,5^6,7^6-tetra(carboxymethyleneoxy)-1^6,3^4,5^4,7^4tetramethoxy-2,4,6,8-tetraundecyl-resorcin[4]arene (4c). The tetra-ester (**3c**) (1.5 g, 0.99 mmol) and sodium hydroxide (0.319 g, 7.9 mmol) gave, after workup and drying the desired tetra-acid (**4c**) (1.120 g, 80%) as a white solid, m.p. 155°C. ^{1}H NMR. (Acetone-d_6) δ, 0.41 (t, 12H, *J* = 7.0 Hz, CH_2CH_3), 0.74 – 0.92 (m, 72 H, $(CH_2)_9CH_3$), 1.32 – 1.50 (m, 8H, CH_2CH), 3.20 (s, 12H, OCH_3), 3.71- 3.99 (2dd, *J* = 16 Hz, 8H, CH_2CO), 4.14 (t, *J* = 7.4, Hz, 4H, CH_2CH), 5.97 (s, 4H, Ar*H*.), 6.31 (s, 4H, Ar*H*), ^{13}C NMR. (Acetone-d_6) δ 13.80 (CH_3), 22.54, 27.91, 29.28, 29.44, 29.60, 29.66, 29.88, 31.82, 34.87, 34.94 ($10CH_2$ and *C*H), 55.46, 67.04 (OCH_3 and OCH_2), 98.92, 126.04, 126.83, 127.36, 154.43, 155.47 (CH_2-Ar), 169.80 (C=O). IR 3880 (OH), 1721 (CO), 2920 (CH_2), 2851 (CH_3), 1611 (C=C), 1293 cm^{-1} (C–O).

General procedure for the coupling of dimethyl-L-aspartate to the carboxylic acid to form (5a-c)

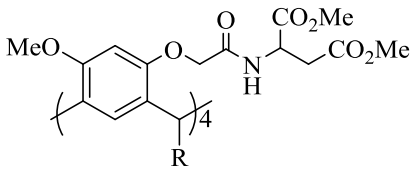

Compound	R
5a	C_3H_7
5b	C_7H_{15}
5c	$C_{11}H_{23}$

The tetramethoxyresorcinarene acid (**4**) (1.6 mmol) was dissolved in 100 mL dry dichloromethane then dimethyl *L*-aspartate hydrochloride (16.7 mmol) and trimethylamine (1.3 mL). The mixture was stirred till all the solid dissolved at room temperature. Then, 16.8 mmol of *N, N, N′, N′*-tetramethyl-*O*-(benzotriazol-1-yl) uronium tetrafluoroborate (TBTU) and a further portion of trimethylamine (1.0 mL) was added and the pH was checked during the first 30 minutes to be at 8.5. After 4 hours, the reaction was quenched by the addition of hydrochloric acid (1 M, 30 mL). The organic solution was then washed with 5% of sodium bicarbonate (3 x30 mL) and (3 x 30 mL) water, dried and concentrated under reduced pressure to give the desired amides as a mixture of diastereoisomers as oil. This was crystallised by adding a small amount of cold methanol up to 4°C for 24 h.

1^4,3^4,5^4,7^4-tetramethoxy-1^6,3^6,5^6,7^6-tetra[(dimethyl-*L*-aspartyl)-*N*-carbonylmethyleneoxy]-2,4,6,8-tetrapropylresorcin[4]arene(5a).

Tetramethoxyresorcinarene acid (**4a**) (1 g, 1.05 mmol), dimethyl *L*-aspartate hydrochloride (3.3 g, 16.7 mmol), trimethylamine (2.3 mL) and TBTU (5.4 g, 16.8 mmol) gave after workup, the desired product as a crystalline solid (0.800 g, 50%), m.p 185°C. ^{1}H NMR. ($CDCl_3$), (note a 1:1 mixture of diastereoisomer, integration values are combination of both isomers) δ 0.85 – 0.96 (m, 2 x 12H, CH_3CH$_2$), 1.24 - 1.39 (m,, 2 x 8H, CH_2CH$_3$), 1.76 - 1.88 (m, 2 x 8H, CH_2CH), 2.81 – 3.01 (m,2 x 8H, CH_2COOH), 3.45 - 3.76 (m, 2 x 12H, OCH_3), 4.07 – 4.31 (m, 2 x 8H, OCH_2CO), 4.50 (t, J = 7.4 Hz, 2 x 4H, CHCH$_2$), 4.83 - 4.95 (m, 2 x 4H, CHCH$_2$COOH), 6.28, 6.31, 6.70, 6.74 (4 s, 2 x 4H, Ar *H*). ^{13}C NMR. ($CDCl_3$) δ 14.31 (2 x CH$_3$), 21.00, 21.05, 34.79, 34.95, 35.85, 36.05, 37.42, 37.55, 48.20, 48.37(2 x 3CH$_2$ and 2CH),

51.88, 51.96, 52.75, 56.28, 56.34, 68.86, 69.16 (2 x 3O*C*H_3 and O*C*H_2), 98.70, 99.09, 126.16, 126.54, 126.77, 127.73, 127.99, 153.86, 154.08, 155.58,154.65 (2x *C*H_2-Ar), 168.84, 168.90, 170.50, 170.59, 170.81, 170.83 (*C*=O, *C*OOCH and *C*OOCH_2). IR 3415 (NH), 1737 cm^{-1} (CO), 2928 cm^{-1}(CH_2), 2868 cm^{-1} (CH_3), 1683 cm^{-1} (C=C), 1288 cm^{-1}. HRMS, *m/z* $[M+H]^+$ calculated for $C_{76}H_{101}O_{28}$, 1517.6597, found, 1517.6597.

2,4,6,8-tetraheptyl-1^4,3^4,5^4,7^4-tetramethoxy-1^6,3^6,5^6,7^6-tetra[(dimethyl-*L*-aspartyl)-*N*-carbonylmethyleneoxy]resorcin[4]arene(5b).

Tetramethoxyresorcinarene acid (**4b**) (1g, 0.85 mmol), dimethyl *L*-aspartate hydrochloride (2.70 g, 13.70 mmol), trimethylamine (1.9 mL) and TBTU (4.39 g, 13.70 mmol) gave after workup, the desired product as an oil (1. 650 g, 61%)

Separation of the diastereomers 5b to form 6 and 7

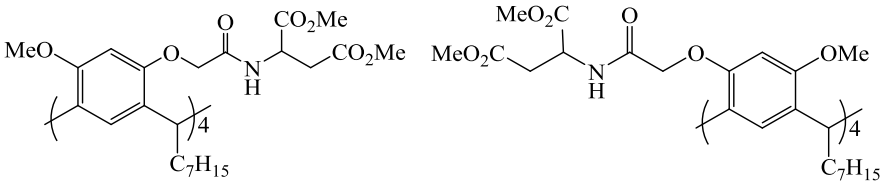

6 **7**

The compound **5b** has been isolated via addition of cold methanol (10 mL) and filtered to gain the compound **6** as a white powder (0.280 g, 20%) and the compound **7** as light yellow oil (1 g, 72%).

2(*S*),4(*S*),6(*S*),8(*S*)-tetraheptyl-1^4,3^4,5^4,7^4-tetramethoxy-1^6,3^6,5^6,7^6-tetra[(dimethyl-*L*-aspartyl)-*N*-carbonylmethyleneoxy]resorcin[4]arene(6),

m.p.149°C. ^{1}H NMR. ($CDCl_3$) δ 0.85 (t, *J* = 7.0Hz, 12H, C*H*$_3$CH$_2$), 1.17 – 1.36 (m, 40 H, C*H*$_2$CH$_3$), 1.80 – 1.90 (m, 8 H, C*H*CH$_2$), 2.82 – 3.00 (m, 8H, C*H*$_2$COO), 3.53, 3.64, 3.71 (3s, 36H, OC*H*$_3$), 4.16 – 4.25 (2d, 8H, *J* = 15.1Hz, OC*H*$_2$CO), 4.50 (t, *J* = 7.5 Hz, 4H, C*H*CH$_2$), 4.85 - 4.95 (m, 4H, C*H*COO), 6.34 (s, 4H, Ar *H*), 6.75 (s, 4H, Ar *H*), 7.55 (d, 4H, *J* =8.4 Hz, NH). ^{13}CNMR. ($CDCl_3$) δ 14.10 (*C*H$_3$), 28.00, 29.36, 29.99, 32.00, 35.09, 35.30, 36.06, 48.25, 51.88, 52.75, 56.35, 69.18, (6*C*H$_2$, 2*C*H, *C*H$_2$CO and 3*C*H$_3$O), 99.11, 126.20, 126.80, 127.99, 154.10, 154.59 (*C*H$_2$-Ar), 168.94 170.58, 170.80 (CH*C*O, CH$_2$*C*O) and *C*ONH). IR 3412 (NH), 1736 cm^{-1}

(CO), 2926 cm^{-1}(CH_2), 2854 cm^{-1} (CH_3), 1681 cm^{-1} (C=C), 1290 cm^{-1}.[M+H] $^{+}$calculated for $C_{92}H_{133}N_4O_{28}$, 1741.9115 m/z, found, 1741.9101 m/z.

2(*R*),4(*R*),6(*R*),8(*R*)-tetraheptyl-1^4,3^4,5^4,7^4-tetramethoxy-1^6,3^6,5^6,7^6-tetra[(dimethyl L-aspartyl)-*N*-carbonylmethyleneoxy]resorcin[4]arene (7). ^{1}H NMR. ($CDCl_3$) δ 0.79 (t, J = 6.4 Hz, 12H, CH_3CH$_2$), 1.15 – 1.29 (m, 40 H, CH_2CH$_3$), 1.73 – 1.84 (m, 8 H, CH_2CH), 2.87 (d, J =5.4 Hz, 8H, CH_2COO), 3.53, 3.59, 3.64 (3s, 9H, COOCH_3), 4.07 – 4.26(dd, 8H, J = 15.0 Hz, OCH_2CO), 4.45 (t, J = 7.4 Hz, 4H, CHCH$_2$), 4.78 – 4.89 (m, 4H, CHCOO), 6.26 (s, 4H, Ar *H*), 6.66 (s, 4H, Ar *H*), 7.42 (d, 4H, J =8.3 Hz, N*H*). ^{13}CNMR. ($CDCl_3$) δ 14.08 (CH_3), 22.67, 28.06, 29.31, 29.34, 30.00, 32.00, 34.97, 35.27, 35.88, 36.01, 38.64, 48.39 (7CH_2 and 2CH), 51.97, 52.77, 56.29, 68.85 (*C*H$_2$CO and 3*C*H$_3$O), 98.79, 126.14, 126.57, 127.73, 153.84, 155.63 (*C*H$_2$-Ar), 168.99, 170.43, 170.84, 170.80 (CH*C*O, CH$_2$*C*O) and *C*ONH), extra peaks notice due to the tracs of the other isomer. IR 3392 (NH), 1736 cm^{-1} (CO), 2926 cm^{-1}(CH_2), 2854 cm^{-1} (CH_3), 1672 cm^{-1} (C=C), 1291 cm^{-1} [M+H] $^{+}$calculated for $C_{92}H_{133}N_4O_{28}$, 1741.9115 m/z, found, 1741.9101 m/z.

1^4,3^4,5^4,7^4-tetramethoxy-1^6,3^6,5^6,7^6-tetra[(dimethyl-*L*-aspartyl)-*N*-carbonylmethyleneoxy]-2,4,6,8-tetraundecylresorcin[4]arene(5c).
Tetramethoxyresorcinarene acid (**4c**) (1g, 0.72 mmol), dimethyl *L*-aspartate hydrochloride (2.27g, 11.49 mmol), trimethylamine (1.mL) and TBTU (3.69 g, 11.49 mmol) gave after workup, the desired product as an oil (1. 500 g, 67%).

Separation of the diastereomers 5c to form 8 and 9

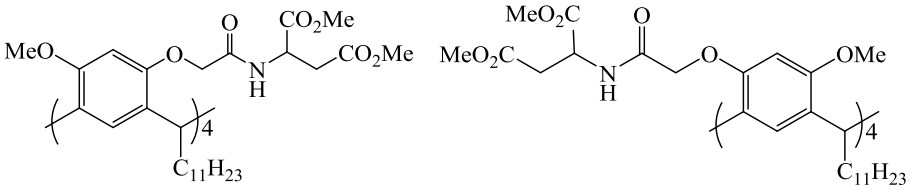

8 **9**

The methyl *L*-aspartic acid coupling dodecyltetramethoxy resorcinarene **5c** was isolated *via* addition of cold methanol (10 mL) and filtered to gain **8** as a white powder (0.200 g, 18%) and gain **9** as an oil in (0.850 g, 60%).

1^4,3^4,5^4,7^4-tetramethoxy-1^6,3^6,5^6,7^6-tetra[(dimethyl-*L*-aspartyl)-*N*-carbonylmethyleneoxy]-2(*S*),4(*S*),6(*S*),8(*S*)-tetraundecylresorcin[4]arene[58], m.p. 147°C. ^{1}H NMR. ($CDCl_3$) δ 0.85 (t, J = 6.4 Hz, 12H, CH_3CH$_2$), 1.16 – 1.40 (m, 40 H, CH_2CH$_3$), 1.79 – 1.89 (m, 8 H, CHCH$_2$), 2.80 – 3.02 (m, 8H, CH_2COO), 3.52, 3.63, 3.71 (3s, 36H, OCH_3), 4.17 – 4.26 (2d, 8H, J = 15.1Hz, OCH_2CO), 4.49 (t, J = 7.2 Hz, 4H, CHCH$_2$), 4.83 - 4.96 (m, 4H, CHCOO), 6.34 (s, 4H, Ar *H*), 6.74 (s, 4H, Ar *H*), 7.52 (d, 4H, J =8.4 Hz, NH). ^{13}CNMR. ($CDCl_3$) δ 14.10 (CH$_3$), 22.68, 28.06, 29.39, 29.73, 29.78, 29.80, 29.88, 30.11, 31.93, 35.13, 35.29, 36.06, 48.26, 51.89, 52.75, 56.35, 69.19, (6CH$_2$, 2CH, CH$_2$CO and 3CH$_3$O), 99.12, 126.21, 126.82, 127.98, 154.10, 154.59 (CH$_2$-Ar), 168.92 170.58, 170.79 (CHCO, CH$_2$$C$O) and CONH). IR 3412 (NH), 1736 cm^{-1} (CO), 2922 cm^{-1} (CH$_2$), 2852 cm^{-1} (CH$_3$), 1681 cm^{-1}, (C=C), 291 cm^{-1}. [M+H]$^+$calculated for $C_{108}H_{165}N_4O_{28}$, 1966.1619 m/z, found, 1966.1576m/z.

1^4,3^4,5^4,7^4-tetramethoxy-1^6,3^6,5^6,7^6-tetra[(dimethyl-*L*-aspartyl)-*N*-carbonylmethyleneoxy]-2(*R*),4(*R*),6(*R*),8(*R*)-tetraundecylresorcin[4]arene[58], ^{1}H NMR. ($CDCl_3$) δ 0.85 (t, J = 7.0 Hz, 12H, CH_3CH$_2$), 1.15 – 1.35 (m, 40 H, CH_2CH$_3$), 1.75 – 1.89 (m, 8 H, CHCH$_2$), 2.92 (d, 8H, CH_2COO), 3.58, 3.62, 3.69 (3s, 36H, OCH_3), 4.11 – 4.28 (2d, 8H, J = 15.0 Hz, OCH_2CO), 4.48 (t, J = 7.3 Hz, 4H, CHCH$_2$), 4.84 - 4.92 (m, 4H, CHCOO), 6.29 (s, 4H, Ar *H*), 6.68 (s, 4H, Ar *H*), 7.47 (d, 4H, J =8.2 Hz, NH). ^{13}CNMR. ($CDCl_3$) δ 14.06 (CH$_3$), 22.64, 28.09, 29.34, 29.37, 29.75, 29.85, 30.06, 30.09, 31.89, 35.30, 36.06, 48.42, 52.01, 52.82, 56.42, 69.96, (6CH$_2$, 2CH, CH$_2$CO and 3CH$_3$O), 99.84, 126.13, 126.53, 127.66, 153.84, 153.63 (CH$_2$-Ar), 168.96 170.46, 170.79 (CHCO, CH$_2$$C$O) and CONH). IR 3397 (NH), 1735 cm^{-1} (CO), 2923 cm^{-1}, (CH$_2$), 2852 cm^{-1} (CH$_3$), 1677 cm^{-1}, (C=C), 1291 cm^{-1}. [M+H]$^+$calculated for $C_{108}H_{165}N_4O_{28}$, 1966.1619 m/z, found,1966.1587m/z.

1^4,3^4,5^4,7^4-tetramethoxy-1^6,3^6,5^6,7^6-tetra[(*L*-aspartic acid)-*N*-carbonylmethyleneoxy]-2,4,6,8-tetrapropylresorcin[4]arene 10

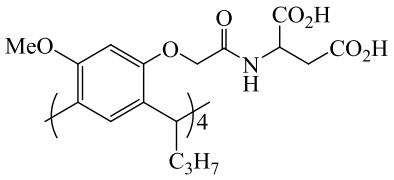

10

The dimethyl aspartate derivative (**5a**, 0.5 mmol) was dissolved in methanol (80 mL) then sodium hydroxide (4.2 mmol) and water (3 mL) were added and the reaction mixture was heated at reflux for 5 hours. Removal of the solvent gave a white solid which was acidified with HCl (30 mL of 5 M), filtered and dried in a vacuum desiccator over P_2O_5 for 72 hours to give the acid as a light brown powder, 0.550 g, 74%, m.p. 120°C. ^{1}H NMR. (Acetone-d_6) δ 0.89 (t, 2 x 12H, CH_3CH$_2$), 1.26 - 1.40 (m, 2 x 8H, CH_2CH$_3$), 1.75 - 1.86 (m, 2 x 8H, CH_2CH), 2.83 – 3.01 (m, 2 x 8H, CH_2COOH), 3.63 (s, 2 x 12H, OCH_3), 4.03 – 4.27 (m, 2 x 8H, OCH_2CO), 4.52 (t, J = 6.8 Hz, 2 x 4H, CHCH$_2$), 4.79 - 4.87 (m, 2 x 4H, CHCH$_2$COOH), 6.47, 6.50, 6.69, 6.67 (4 s, 2 x 4H, Ar *H*). ^{13}C NMR. (acetone-d_6) δ 13.98 (2 CH$_3$), 20.95, 34.94, 35.04, 35.48, 35.56, 37.14, 37.17, 48.07, 48.17, (2 x 3CH$_2$ and 2 x 2CH), 55.98, 56.04, 69.31, 69.65 (2 x OCH$_3$ and 2CH$_2$CO), 99.74, 100.12, 125.79, 125.81, 126.21, 127.79, 127.86, 153.91, 153.94, 154.51, 154.78, 155.76, 155.81 (2 x 6Ar), 169.43, 169.73, 171.27, 171.76, 171.82 (2 x 3 CO). IR 3388 (NH), 1731 cm^{-1} (CO), 2931 cm^{-1}(CH$_2$), 2869 cm^{-1} (CH$_3$), 1979 cm^{-1} (CO in COOH), 1287 cm^{-1}.

2(*S*),4(*S*),6(*S*),8(*S*)-tetraheptyl-1^4,3^4,5^4,7^4-tetramethoxy-1^6,3^6,5^6,7^6-tetra[(*L*-aspartic acid)-*N*-carbonylmethyleneoxy]resorcin[4]arene 11

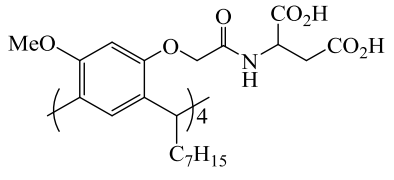

11

The dimethyl *L*-aspartic acid coupling heptyl tetramethoxy resorcinarene (**6,** 0.160 mmol) was dissolved in 40 mL methanol followed by addition of sodium hydroxide (1.28 mmol) and one millilitre of water. This was left to reflux for 5 hours. The solvent was reduced to gain a white solid. To this solid 5 mL -5 M of HCl was

added, the solid was filtered and dried it in a vacuum desiccator over P_2O_5 for 72 hours to give the acid as a white powder (0.200 g, 76%), m.p.168°C. ^{1}H NMR. (Acetone-d_6) δ 0.86 (t, J = 7.0Hz, 12H, CH_3CH$_2$), 1.20 – 1.45 (m, 40 H, CH_2CH$_3$), 1.76 – 1.95 (m, 8 H, CH_2CH), 2.86 – 3.05 (m, 8H, CH_2COO), 3.69 (s, 12H, OCH_3), 4.10 – 4.36 (m, 8H, OCH_2CO), 4.58 (t, J = 7.2 Hz, 4H, CHCH$_2$), 4,80 - 4.96 (m, 4H, CHCOO), 6.60 (s, 4H, Ar H), 6.78 (s, 4H, Ar H). ^{13}C NMR. (101MHz, $CDCl_3$) δ 13.54 (CH_3), 22.48, 27.98, 29.84, 31.89, 34.91, 35.27, 35.45, 35.52, 37.88, 48.10, 48.22 (7 CH$_2$, 2 CH) 55.91, 69.27, 69.52, (OCH_3 and CH$_2$CO), 99.84, 100.07, 125.81, 125.84, 126.58, 127.65, 127.74, 154.59, 154.81, 155.85, 155.88 (6 Ar), 169.12, 169.21, 171.19, 171.24, 171.61, 171.63 (3 C=O). IR 3396 (NH), 1737 cm^{-1} (CO), 2925 cm^{-1}. (CH_2), 2854 cm^{-1} (CH_3), 1979 cm^{-1} (CO in COOH), 1642 cm^{-1}, (C=C), 1288 cm^{-1}.

2(*R*),4(*R*),6(*R*),8(*R*)-tetraheptyl-1^4,3^4,5^4,7^4-tetramethoxy-1^6,3^6,5^6,7^6-tetra[(*L*-aspartic acid)-*N*-carbonylmethyleneoxy]resorcin[4]arene 12

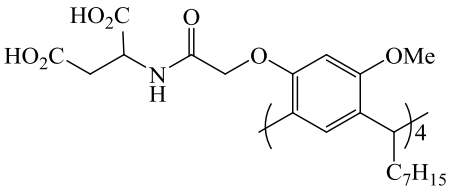

12

The dimethyl L-aspartic acid coupled heptyltetramethoxy resorcinarene **7**, (0.450 mmol) was dissolved in methanol (80 ml), then sodium hydroxide (3.65 mmol) and water (3 mL) were added. The mixture was heated at reflux for 5 hours. The solvent was then removed to gain a light yellow solid, to which was added HCl solution (10 mL, 5 M). The solid was then filtered and dried in a vacuum desiccator over P_2O_5 for 72 hours to give the acid as a light brown powder (0.450 g, 60%)**.** m.p. 150°C. ^{1}H NMR. (Acetone-d_6) δ 0.88 (t, J = 7.0 Hz, 12H, CH_3CH$_2$), 1.22 – 1.45 (m, 40 H, CH_2CH$_3$), 1.84 – 1.95 (m, 8 H, CH_2CH), 2.92 – 3.07 (m, 8H, CH_2COO), 3.72 (s, 12H, OCH_3), 4.13 – 4.32 (m, 8H, OCH_2CO), 4.62 (t, J = 7.3 Hz, 4H, CHCH$_2$), 4.86 – 4.98 (m, 4H, CHCOO), 6.61 (s, 4H, Ar H), 6.81 (s, 4H, Ar H). ^{13}C NMR. (101MHz, $CDCl_3$) δ 13.82 (CH_3), 22.55, 27.95, 28.94, 30.15, 31.92, 34.70, 35.26, 35.59, 35.60, 48.00, 48.08 (7 CH_2, 2 CH), 55.86, 55.94, 69.49, 69.79 (OCH_3, CH_2CO), 99.30, 99.58, 125.87, 125.91, 126.65, 127.83, 154.55, 154.84, 155.72 (6Ar), 169.73, 169.98,

171.04, 171.71 (3 C=O) IR 3388 (NH), 1723 cm^{-1} (CO), 2924 cm^{-1}, (CH_2), 2854 cm^{-1} (CH_3), 1980 cm^{-1} (CO in COOH), 1640 cm^{-1}, (C=C), 1288 cm^{-1}.

1^4,3^4,5^4,7^4-tetramethoxy-1^6,3^6,5^6,7^6-tetra[(*L*-aspartic acid)-*N*-carbonylmethyleneoxy]-2(*S*),4(*S*),6(*S*),8(*S*)-tetraundecylresorcin[4]arene 13.

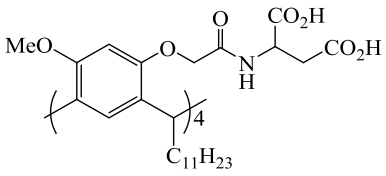

13

The dimethyl *L*-aspartic acid coupled undecylttetramethoxy resorcinarene (0.127 mmol) was dissolved in methanol (25 mL), sodium hydroxide (0.812 mmol), one millilitre of water was then added and finally 5 ml of THF was added. This was left to reflux for 5 hours. The solvent was reduced and 5 mL,5 M of HCl then added. The resulting solids was filtered and dried in a vacuum desiccator over P_2O_5 for 72 hours to gain a white powder (0.176 g, 75%), m.p. 198°C. ^{1}H NMR. (Acetone-d_6) δ 0.86 (t, J = 6.6 Hz, 12H, CH_3CH$_2$), 1.20 – 1.42 (m, 72 H, CH_2CH$_3$), 1.80 – 1.93 (m, 8 H, CH_2CH), 2.90 – 3.05 (m, 8H, CH_2COO), 3.69 (s, 12H, OCH_3), 4.10 – 4.30 (m, 8H, OCH_2CO), 4.59 (t, J = 7.2 Hz, 4H, CHCH$_2$), 4.84 – 4.96 (m, 4H, CHCOO), 6.59 (d, J = 10.2, 4H, Ar H), 6.77 (s, 4H, Ar H), 7.62 – 7.79 (m, 4H, NH). ^{13}C NMR. (Acetone-d_6) δ 13.49 (CH_3), 22.46, 27.99, 28.36, 29.25, 29.58, 29.64, 29.97, 31.79, 34.90, 35.28, 35.54, 48.03, 38.17 (11$CH_{2,}$ $_2$CH), 55.83, 69.31, 69.53(OCH_3, CH_2CO), 99.72, 99.77, 125.88, 126.52, 126.66, 127.57, 154.64, 154.81, 155.90 (6Ar), 168.97, 169.05, 171.10, 171.14, 171.48, 171.51 (C=O). IR 3390 (NH), 1727 cm^{-1} (CO), 2922 cm^{-1}, (CH_2), 2852 cm^{-1} (CH_3), 1980 cm^{-1} (CO in COOH), 1642 cm^{-1}, (C=C), 1289 cm^{-1}.

1^4,3^4,5^4,7^4-tetramethoxy-1^6,3^6,5^6,7^6-tetra[(*L*-aspartic acid)-*N*-carbonylmethyleneoxy]-2(*R*),4(*R*),6(*R*),8(*R*)-tetraundecylresorcin[4]arene 14.

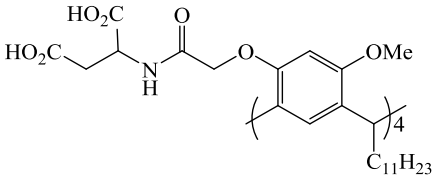

14

The methyl *L*-aspartic acid coupling undecyletramethoxy resorcinarene (0.29 mmol.) was dissolved in methanol (73 mL), sodium hydroxide (2.375 mmol), and water (3 mL) were added. This was left to reflux for 5 hours. The solvent was reduced and 10 mL, 5 M of HCl then added. The resulting solids was filtered and dried in a vacuum desiccator over P_2O_5 for 72 hours to give the acid as a light brown powder, (0.336 g, 61%), m.p. 179°C. ^{1}H NMR (400 MHz, acetone-d_6) δ 0.87 (t, J = 6.6 Hz, 12H, CH_3CH$_2$), 1.18 – 1.46 (m, 72 H, CH_2CH$_3$), 1.80 – 1.95 (m, 8 H, CH_2CH), 2.80 – 3.07 (m, 8H, CH_2COO), 3.69 (s, 12H, OCH_3), 4.01 – 4.34 (m, 8H, OCH_2CO), 4.59 (t, J = 7.2 Hz, 4H, CHCH$_2$), 4.82 – 4.99 (m, 4H, CHCOO), 6.59 (s, 4H, Ar H), 6.78 (s, 4H, Ar H), 7.62 – 7.85 (m, 4H, NH). ^{13}C NMR. ($CDCl_3$) δ 13.52 (CH_3), 22.46, 27.98, 28.42, 28.81, 29.06, 29.39, 29.63, 29.99, 31.79, 34.94, 35.49, 35.55, 37.89, 48.24(11CH$_2$, 2CH), 55.91, 55.94, 69.27, 96.55 (OCH$_3$, CH$_2$CO), 99.86, 100.17, 125.84, 126.54, 126.66, 127.56, 127.64, 154.57, 154.80, 155.89, 155.91 (6Ar), 169.17, 169.41, 171.26, 171.67, 171.71 (3 C=O). IR 3388 (NH), 1723 cm^{-1} (CO), 2922 cm^{-1}, (CH_2), 2852 cm^{-1} (CH_3), 1979 cm^{-1} (CO in COOH), 1641 cm^{-1}, (C=C), 1289 cm^{-1}.

Synthesis of (N,N-diethylamino)ethylamino-alkyl-tetramethoxy resorcinarene derivatives (15a-b)

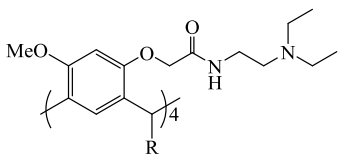

Compund no.	R
15a	C_3H_7
15b	C_7H_{15}

The tetramethyl ester derivative (**3a-b**, 0.50 mmol) was dissolved in *N*,*N*-diethylethylenediamine (9.0 g, 78 mmol) then, heated at reflux over 3 days. After that, it was concentrated to gain organic oil which was dissolved in ethyl acetate (1 x 10 mL) and washed with dilute NaOH (2 x 30 mL, 0.2 M) and brine (1 x 30 mL). The organic layer was dried *via* anhydrous sodium carbonate and the solvent removed to gain a light brown solid.

1^4,3^6,5^6,7^6-tetra(2-[(*N*,*N*-diethylamino)ethylamino]carbonylmethyleneoxy)-1^6,3^4,5^4,7^4-tetramethoxy-2,4,6,8-tetrapropylresorcin[4]arene 15a. The tetraester **3a** (0.500 g, 0.50 mmol) and *N*, *N*-diethylethyleneamine (9.0 g, 78 mmol), after workup gave the desired compound (**15a**) gain as a light brown solid (0.350 g, 55%), m.p. 162°C. ^{1}H. NMR. ($CDCl_3$) δ 1.04 – 0.85 (m, 36H, 3C*H*$_3$CH$_2$), 1.39 – 1.19 (m, 8H, CH_2CH_3), 1.86 – 1.75 (m, 8H, CH_2CH), 2.64 – 2.41 (m, 16H, 2CH_3C*H*$_2$N), 3.25 -3.27 (m, 8H, CH_2C*H*$_2$N), 3.57 – 3.35 (m, 8H, CH_2C*H*$_2$N), 3.60 (s, 12H, OCH_3), 4.10, 4.24. (2d, *J* = 14.8 Hz, 8H, CH_2CO), 4.48 (t, *J* = 5.7 Hz, 4H, $CHCH_2$), 6.24 (s, 4H, Ar), 6.67 (s, 4H, Ar), 7.05 (t, *J* = 5.6 Hz, 4H, NH). ^{13}C NMR. ($CDCl_3$) δ 11.68, 14.32 (CH_3), 21.10, 35.04, 37.09, (2CH_2, CH), 37.30, 46.96, 51.77 (CH_2N), 56.16, 68.60 (CH_2O and CH_3O), 97.75, 126.19, 126.26, 127.18, 153.84, 155.49 (Ar), 168.48, (CO). IR 3417 (NH), 1676 cm^{-1} (CO), 2925 cm^{-1}, (CH_2), 2854 cm^{-1} (CH_3), (C–N), 1297 cm^{-1}. $[M+H]^+$ calculated for $C_{76}H_{121}N_8O_{12}$, 1337.9111 m/z, found, 1337.9098 m/z.

1^4,3^6,5^6,7^6-tetra(2-[(*N*,*N*-diethylamino)ethylamino]carbonylmethyleneoxy)-1^6,3^4,5^4,7^4-tetramethoxy-2,4,6,8-tetraheptylresorcin[4]arene 15b. The tetraester **3b** (0.500 g, 0.41 mmol) and *N*, *N*-diethylethyleneamine (9.0 g, 78 mmol) gave, after workup the desired compound (**15 b**) as a light brown solid (0.400 g, 65%), m.p.178°C. ^{1}H. NMR. ($CDCl_3$) δ 1.07 – 0.77 (m, 36H, C*H*$_3$CH$_2$), 1.27 – 1.18 (m, 40H, (C*H*$_2$)$_5$CH$_3$), 1.80– 1.79 (m, 8H, C*H*$_2$CH), 2.65 – 2.42 (m, 16H, 2CH_3C*H*$_2$N), 3.35 -3.25 (m, 8H, CH_2C*H*$_2$N), 3.59 – 3.40 (m, 8H, CH_2C*H*$_2$N), 3.59 (s, 12H, OCH_3), 4.09, 4.23 (2d, *J* = 14.6 Hz, 8H, CH_2CO), 4.46 (t, *J* = 7.4 Hz, 4H, C*H*CH$_2$), 6.23 (s, 4H, Ar), 6.66 (s, 4H, Ar), 7.04 (t, *J* = 5.6 Hz, 4H, NH). ^{13}C NMR. ($CDCl_3$) δ 11.71, 14.08 (CH_3), 22.67, 28.11, 29.37, 29.98, 31.99, 35.00, 35.32, (CH_2, CH), 37.12, 46.96, 51.81 (CH_2N), 56.14, 68.58 (OCH_2, OCH_3), (3CH_3, 7CH_2, CH and OCH_3), 97.72, 126.19, 126.22, 127.18, 153.84, 155.48 (Ar), 168.48, (CO). IR 3388 (NH),

1681 cm^{-1} (CO), 2932 cm^{-1}, (CH_2), 2857 cm^{-1} (CH_3), 1352 cm^{-1} (CN), 1298 cm^{-1}. $[M+H]^+$ calculated for $C_{92}H_{153}N_8O_{12}$, 1562.1615 m/z, found, 1562.1525 m/z.

*Dimethyl N-dodecanoyl-*L*-aspartate*

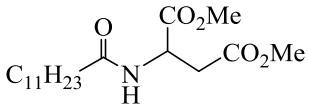

17

Dimethyl *L*-aspartic acid (1 g, 5.06 mmol) was dissolved in triethylamine (0.35 mL, 2.53 mmol) and (10 mL) of dichloromethane and cooled it to (0°C), then dodecanoyl chloride (1.2 mL, 5.06 mmol) dissolved in dichloromethane (10 mL) was added drop-wise. The mixture was allowed to warm to room temperature and left for 2 hours. Following that, water (0.5 mL) was added and stirred for 5-10 minutes. The reaction mixture was washed with 5% sodium bicarbonate (1 x 20 mL) then brine (1 x 20 mL), dried and the solvent evaporated to gain a white powder (1 g, 58 %), m.p. 58°C. ^{1}H NMR. (acetone-d6) δ 0.91 85 (t, J =6.67.0 Hz, CH_3), 1.35 21 – 1.15 29 (m, 16H, (CH_2)$_8$$CH_3$), 1.71 – 1.531.55 - 1.65 (m, 2H, CH_2), 2.18-2.23 (apparent t, 2H, CH_2CO), 2.83 (dd, J = 17.2, 4.5 Hz, 1H, CH_2COO), 3.00 (dd, J = 17.2, 4.4 Hz, 1H, CH_2COO), 3.66 (s, 3H, OCH_3), 3.72 (s, 3H, OCH_3), 4.81 - 4.87 (m, 1H, CHN), 6.55 (d, J = 7.9 Hz, 1H, NH). ^{13} C NMR. (acetone-d_6) δ 14.10 (CH_3), 22.68 24.75, 25.54, 29.09, 29.16, 29.32, 29.48, 29.60, 33.93, 36.49, 48.34 (CH_2), 50.76, 52.03, 52.81 (CHN, 2 CH_3O), 171.71, 171.32, 173.19 (CO). IR 3315 (NH), 1733 (OC=O), 1698 (NC=O), 2915 (CH_2), 2848 (CH_3), 1213 cm^{-1} (C–O). $[M+H]^+$ calculated for $C_{18}H_{34}NO_5$, 344.2446 m/z, found, 344.2430 m/z.

*N-undecanoyl-*L*-aspartic acid*

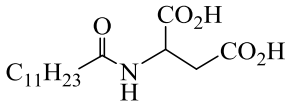

18

Dimethyl *N*-dodecanoyl-*L*-aspartate (**17**) (1 g, 2.9 mmol) was dissolved in methanol (30 mL), then sodium hydroxide (0.174 g, 4.35 mmol) and water (10 mL) were added. The reaction mixture was heated at reflux for 5 hours. The solvent was

removed and the remaining white solid was then acidified with HCl (5 mL of 5 M), filtered and dried in a vacuum desiccator over P_2O_5 for 72 hours to give a white powder (0.800 g, 87 %), m. p. 95°C. ^{1}H NMR. (acetone-d6) δ 0.87 (t, J = 6.9 Hz, CH_3CH$_2$), 1.25 - 1.35 (m, 16H, 8CH_2), 1.53 - 1.62 (m, 2H, CH_2), 2.25 (dt, J = 15.6, 7.5 Hz, 2H, CH_2), 2.84 (d, J = 5.8 Hz, 2H, CH_2COO), 4.57 - 4.80 (m, 1H, CH), 7.29 (d, J = 7.8 Hz, 1H, NH). ^{13} C NMR. (acetone-d$_6$) δ 15.43 (CH$_3$), 22.43 24.78, 28.57, 28.96, 29.15, 29.34, 29.54, 31.74, 33.35, 35.53, 35.76 (CH$_2$), 48.59, 171.74, 171.44, 173.89 (CO). IR 3338 (NH), 1697 (OC=O), 1650 (NC=O), 2914 (CH$_2$), 2849 cm^{-1} (CH$_3$). [M+H]$^+$ calculated for $C_{16}H_{30}NO_5$, 316.2133 m/z, found, 316.2122 m/z.

Synthesis of (N,N-diethylamino) undecanamide

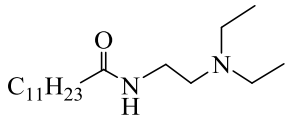

19

N,*N*-Diethylethyleneamine (**16**) (1.2 mL 8.60 mmol) was dissolved in trimethylamine (0.6 mL, 4.29 mmol.) and (10 mL) of dichloromethane then cooled to (0°C) . A solution of dodecanoyl chloride (2.04 mL, 8.60 mmol) in dichloromethane (10 mL) was added dropwise. The reaction mixture was allowed to warm to room temperature and was then left for 2 hours. Following that, water (0.5 mL) was added to the mixture and stirred for 5-10 minutes. It was then washed with 5% sodium bicarbonate (1 x 10 mL) then brine (1 x 10 mL) and evaporated to gain a white wax (1 g, 66 %). δ 0.86 (t, J = 6.6 Hz, CH_3CH$_2$), 1.01 (t, J = 7.1 Hz, 6H, 2CH_3), 1.22 - 1.32 (m, 16H, 8CH$_2$), 1.56 – 1.64 (m, 2H, CH$_2$), 2.15 (t, J = 7.4, 7.8 Hz, 2H, CH_2CO), 2.50 – 2.56 (m, 6H, 3CH_2N), 5.40 (q, J = 5.2 Hz, 2H, NCH$_2$), 6.18 (s, 1H, NH).^{13}C NMR. (CDCl$_3$) δ 11.50, 14.08, (3 CH$_3$), 22.65, 25.77, 29.30, 29.36, 29.48, 29.59, 31.88, 36.63, 36.78 (CH$_3$(CH$_2$)$_{10}$), 46.77, 50.41, 51.61 (3CH$_3$, NCH$_2$), 173.34 (CO). IR 33907 (NH), 1643 cm^{-1} (CO), 2925 cm^{-1}, (CH$_2$), 2854 cm^{-1} (CH$_3$), 1979 cm^{-1} (CO in COOH), 1642 cm^{-1}, (C=C), 1288 cm^{-1}. [M+H] $^+$ calculated for $C_{18}H_{38}N_2O$, 299.3071 m/z, found, 298.3057m/z.

3.0 Crystallization modification

3.1 Outline

This chapter will provide a brief overview of basic crystallization theory, the ways in which crystallization can be impacted, and a review on the influence of additives on the growth rate and habit modification during crystallization.

3.2 Crystallization

Crystallization is the natural or synthetic methodology that has been employed in the separation and purification of solids. Crystallization has been used in the production of a wide range of materials from a supersaturated solution by creating crystal nuclei and growing these nuclei to the desired size. The crystalline material (atoms, molecules, or ions) is formed with specific faces. The relative size of the faces of the crystal can be variable and this leads to a variety of crystal shapes, called the crystal habit. The crystal habit can be influenced by the conditions of crystallization.[109-110] This technique is important in many areas such as biomineralization (biological organisms)[111-112] and in industrial separation processes.[113] In industrial processes, unwanted deposition of crystals may result in fluid flow restrictions, which may cause process disruptions, and may prevent the equipment from operating correctly. This unwanted crystallization, is known as scale formation.[114] Mineral salts such as calcium carbonate[115-116] and barium sulfate[117] are precipitated as scale in the transportation of water through pipes. These mineral precipitations can reduce the efficiency of industrial processes and thus, crystallization control is of fundamental importance in the chemical industry, in particular, unwanted scale formation needs to be inhibited.[36, 118-119]

Nucleation and crystal growth are two steps that describe crystallization from solution. Nucleation is the moment where the new crystals are formed from solution (*i.e.* the solid is formed from the solution), while crystal growth involves the growth of the particle into a larger size. Both steps only occur if there is a driving force for this to occur, that is, when the solution is supersaturated. Unsurprisingly, both nucleation and growth is dependent on the level of supersaturation.[109]

3.3 Supersaturation

For a homogenous solution to crystallize, it must be supersaturated. Supersaturation can be reached when, at a given temperature, the solution contains more dissolved solute than given by equilibrium saturation. Supersaturation is defined mathematically by the following Equations;

$$\Delta\mu = \mu - \mu^* \qquad 3\text{-}1$$

where, μ is the chemical potential of the substance in the supersaturated state, and μ^* is the chemical potential of the same substance in the saturated solution (at equilibrium). The relation between chemical potential of a substance and the substance activity can be expressed by:

$$\mu = \mu^0 + RT\ln(a) \qquad 3\text{-}2$$

where, μ^0 is an arbitrary reference state chemical potential, R the gas constant, T the absolute temperature, and a is the substance's activity. Eq. 3.2 is applied to Eq. 3.1 and results in:[120]

$$\frac{\Delta\mu}{RT} = \ln\left(\frac{a}{a^*}\right) = \ln(S) \qquad 3.3$$

where, $\frac{\Delta\mu}{RT}$ is the dimensionless driving force for crystallization and S is the supersaturation ratio.[121]

There are four main methods to generate supersaturation in aqueous crystallization, which is: evaporation, changes in temperature (mainly cooling), changing the solvent composition and chemical reaction. The following diagram, Figure 3.1, summarizes the technique to generate supersaturation in batch crystallization. The upper dashed line is a super-solubility curve (or metastable zone limit) and denotes the temperature and concentration where spontaneous nucleation occurs. The solid line is a solubility curve. Consequently, the diagram can be divided into three zones: the first zone named stable or unsaturated zone, where crystallization is impossible and the solute can still dissolve, the second zone is known as the metastable zone, which is supersaturated but spontaneous crystallization is unlikely to happen, and finally, the unstable or supersaturated zone where spontaneous nucleation is likely to happen

(Figure 3.1a). The metastable zone is a region of supersaturated solution where nucleation may or may not occur. The probability of nucleation increases as the concentration increases towards the metastable limit. There are many features that can be impact on the metastable zone including coolant flow rate, impeller speed, solute concentration, presence of impurities, *etc*. and this zone can be determined by plotting the difference between the saturation temperature and the temperature where first crystals are formed. This temperature difference is named as the maximum undercooling and in crystallization (ΔH_{max}), knowledge of the width of this region is important because it helps to understand the nucleation behaviour in each system. Figure 3.1b shows an example of the crystallization process. In the solution, if point A is cooled to point B, then the solution is saturated. Cooling further, the solution reaches the supersaturation condition and new crystals formed (nucleation) at point C. Also, the solution concentration decreases because crystal growth begins at point C. The crystals continue to grow while the supersaturation condition can be maintained. At point D, the cooling operation stops and the solution has reached the end of the crystallization.[109]

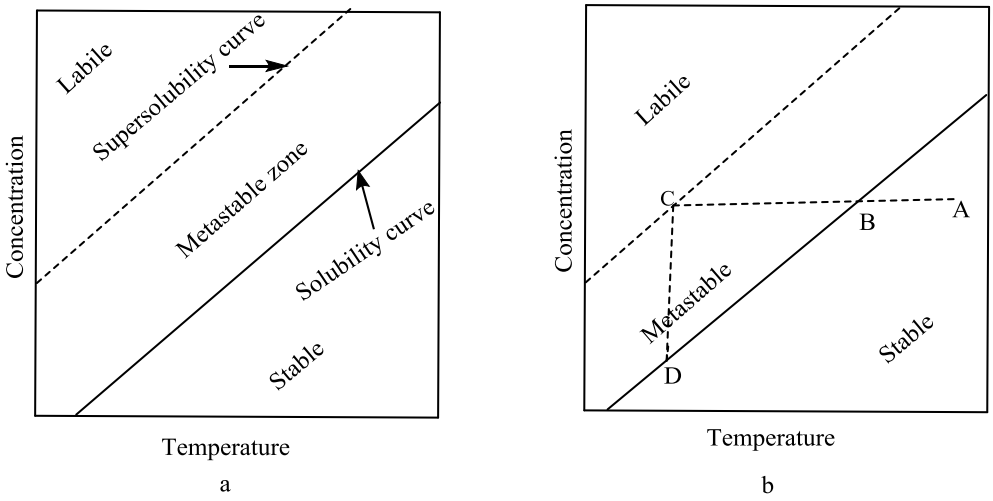

Figure 3. 1: The solubility diagram. Adapted from Mullin. [109]

3.4 Nucleation

Nucleation is the first process in crystallization and can be classified into either primary or secondary nucleation mechanisms. Primary nucleation can be subdivided into homogenous or heterogeneous mechanisms. Nucleation from a solution that does not contain crystalline matter (spontaneously) is named homogenous primary

nucleation. Heterogeneous nucleation involves the interaction of a foreign surface on which the solute can nucleate. In aqueous crystallization, heterogeneous nucleation occurs much more readily, since only a 2D nucleus is required to form on the already present surface while homogenous nucleation is less likely due to the higher driving force necessary to begin nucleation without a surface to catalyse the process.[109] In the classical theory of homogeneous nucleation the change in Gibbs free energy during nucleation of a spherical nucleus (that is made from a pure liquid phase A) with radius r under constant conditions of temperature and pressure can be expressed as the following:

$$\Delta G = 4\pi r^2 \gamma - \frac{4\pi r^3}{\nu} RTlnS \qquad 3.4$$

Where, γ is the surface free energy required to form a surface of the nucleating particle, ν is the molar volume of pure component A in the liquid state, R the gas constant, T the absolute temperature, and S is the initial supersaturation degree of component A and r the radius of the spherical nuclei.[122-124]

In nucleation, the presence of foreign particles may catalyse the nucleation process by reducing the energy barrier to nucleation. Because of that, heterogeneous nucleation can take place at low supersaturation. Therefore, under heterogeneous nucleation, the change in the overall Gibbs free energy which is associated with the formation of a critical nucleus, can be less than those required for homogeneous nucleation. It can be expressed as follows:

$$\Delta G_{hom} = \emptyset \, \Delta G_{het} \qquad 3.5$$

$$\emptyset = (2-\cos\theta)(1-\cos\theta) / 4 \qquad 3.6$$

where, ΔG_{hom}, ΔG_{het} are the Gibbs free energy for homogeneous and heterogeneous nucleation respectively, $\emptyset$ is a factor and can be less than unity if the interaction between the substrate and crystallization solute is favourable, θ is the angle of contact between the crystalline deposit and the foreign solid surface.[109, 121]

Secondary nucleation occurs in the presence of solute particles and takes place at low levels of supersaturation. It involves several possible mechanisms such as initial breeding, polycrystalline breeding, macroabrasion, dendritic, fluid shear and contact

mechanism. These mechanisms can be illustrated by following Figure 3.2.[121] The most common mechanisms are shear and contact nucleation. Shear nucleation is a result of fluid shear on growing crystal faces, while contact nucleation occurs when the crystals collide with each other, with the impeller and/or the internal surfaces of the crystallization vessel.[90, 125] The rate of secondary nucleation can be calculated by:

$$B = \frac{dN}{dt} = k_1 M_T^j (c - c^*)^b \, dt \qquad 3.7$$

here k_1 is a rate constant, M_T is the suspension density (or in alternative formulation of this equation, the surface area of seed present). The exponent *b* can range up to 5 but has a most probable value of 2. The exponent *j* ranges up to 1.5, with 1 being the most probable value.[125]

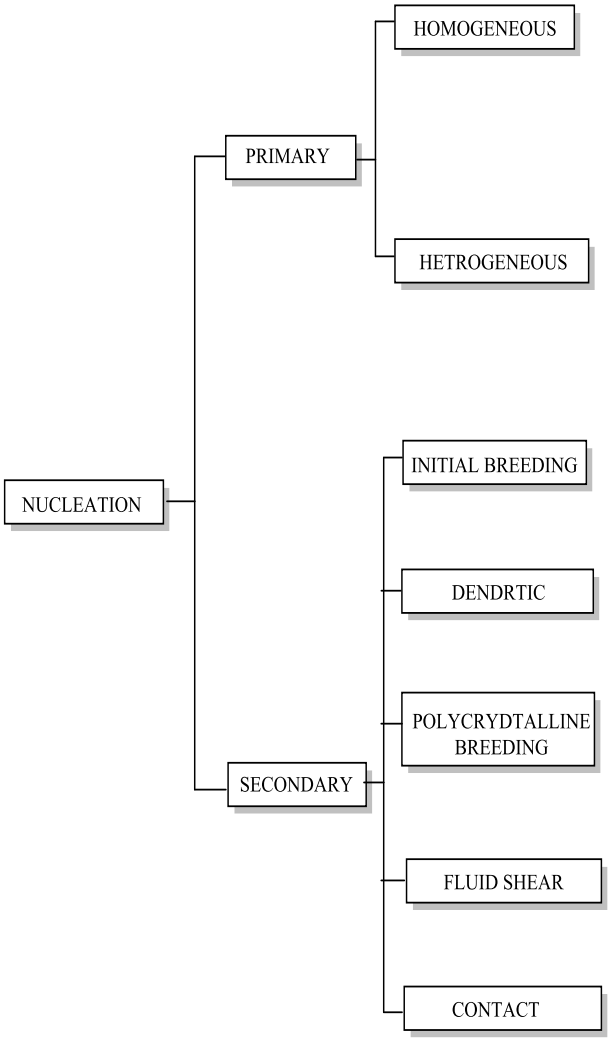

Figure 3. 2: Mechanisms of Nucleation, adapted from Myerson.[121]

3.5 Crystal growth

Crystal growth is the next stage in the crystallization process, after nucleation, where the nuclei grow into crystals of visible size.[109] Crystal growth is a diffusion and integration processes, which may occur *via* the following stages. The molecules/ions will diffuse from the bulk of the mother liquor phase to the surface and these molecules/ions then diffuse over the surface of the crystal towards a step. Finally, the ions/molecules must take their place in the lattice and this is called integration, where the absorbed molecules/ions will be incorporated into the structure.[109, 124]

There are three types of sites on a growing crystal; kink, step and terrace sites, where molecules/ions or growth units can attach to as shown in Figure 3.3. When crystal growth occurs very slowly, the kink site is the most effective site compared to other sites. However, when the supersaturation increases, the less effective sites (step and terrace) can also be integration sites. Therefore, generally, perfect crystals result from slow growth and imperfect crystals come from fast growth.[121]

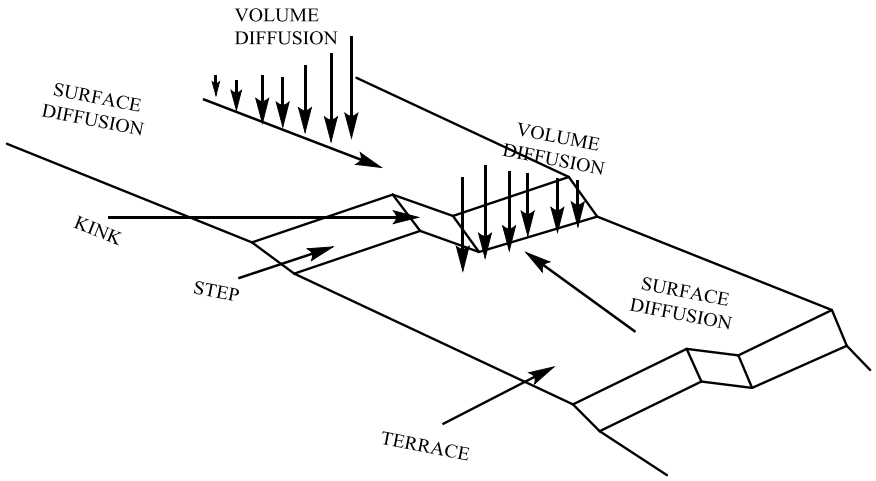

Figure 3. 3: Growth on crystal surface during diffusion process, adapted from Myerson.[121]

3.6 Crystal growth mechanisms

Several theories of crystal growth and modification by surface integration have been proposed.[121] There are three main types of crystal growth mechanisms, which are two-dimensional nucleation, the spiral growth model, and the diffusion layer model. Here, they are briefly discussed and explained.

3.6.1 Two-dimensional nucleation

On the surface, growth units will be absorbing and desorbing continually. Also, molecules/ions can collide with the adsorption layer, forming clusters and when the critical size of a surface cluster has reached a critical size, a 2-*D* nuclei will persist and growth will occur after further collisions.[121] Therefore, two-dimensional nucleation occurs at a relatively high degree of local supersaturation.[109] Within this growth mechanism there are three more specific types of models, which are mononuclear growth, polynuclear growth and "Birth and Spread". These occur at different supersaturations. They can, therefore, be summarized as follows: Myerson indicated that, in mononuclear growth, when surface nuclei are formed, these nuclei spread across the surface with no other nuclei forming until the surface layer is completed. The second model is polynuclear growth, the differences between these two growth mechanisms is the 'birth' of the nuclei. In mononuclear growth, nuclei grow quickly across the surface before the next nucleation event while in polynuclear growth, nuclei spreads are small. Thus, an infinite number of nuclei can form on a surface in the polynuclear growth model when the whole surface is covered. Moreover, Myerson stated that increasing nucleation rate leads to increasing growth rate and *vice versa* in the polynuclear growth model. Finally, the Birth and Spread model, this model allows the nuclei to spread at a finite velocity, on the growing islands as well as on incomplete layers. Also, this model predicts that, the growth rate is increasing when the supersaturation and temperature have increased.[121]

3.6.2 Spiral growth

The previous models failed to explain the crystal growth rate at low supersaturations. Frank was the first to propose that the source of new steps (layers) was a dislocation in the crystal, which would provide a way for the steps to grow continuously. One such dislocation is the screw dislocation.[121] Screw dislocations can result from stresses during crystal growth. Frank recognized the significance of the screw dislocation that presents a continuous spiral during growth, which means that the step site will be provided for the incorporation of growth units in the lattice. A new theory of crystal growth by spiral dislocation, called the BCF theory, was developed by Burton, Cabrera, and Frank. Thus, Figure 3.4 illustrates the schematic of spiral growth development..[126]

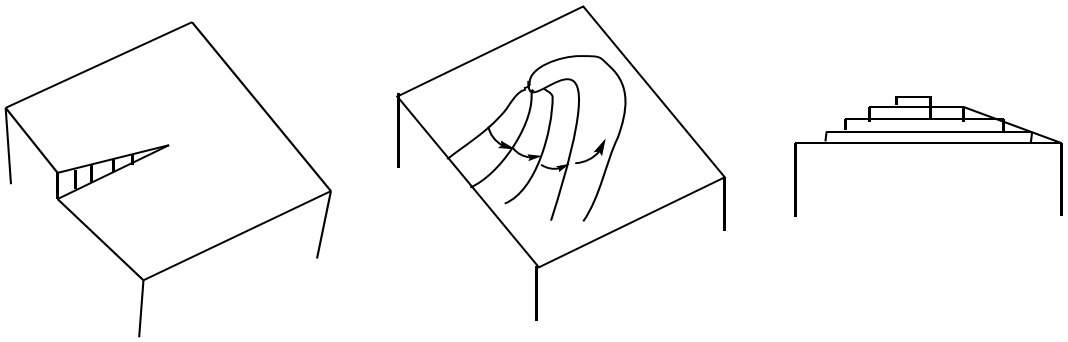

a b c

Figure 3. 4: A growth spiral development from a screw dislocation. Adapted from Myerson.[121]

Burton *et al*. developed a kinetic theory of growth. They had stated that, in the BCF model, a spiral staircase was formed during growth and this was related to the level of supersaturation and the spacing of successive turns. Moreover, they predicted kink populations by the application of Boltzmann statistics and assumed the essential step in the process was surface diffusion. So, the growth rate could be calculated at any supersaturation.[109]

3.6.3 Diffusion layer model

The solute in this model will diffuse through the liquid phase to reach the growing faces (sites) on the crystal. This theory described how the diffusion process controls when solid is deposited on the face of the growing crystal. Moreover, they assumed that crystallization was simply the reverse to the dissolution process and both can be modelled by the difference between the concentration at the solid surface and in the bulk of the solution. Mullin explained how the diffusion model was further modified and improved.[109] The growth is divided into two stages; a diffusion through the bulk of the solution to the crystal surface, followed by the growth units incorporating into the crystal, which can be illustrated by the following equations:

$$\frac{d_m}{d_t} = k_d A(c - c_i) \quad \text{diffusion} \qquad 3\text{-}8$$

$$\frac{d_m}{d_t} = k_r A(c_i - c^*) \quad \text{integration} \qquad 3\text{-}9$$

Where: m is the mass of solid deposited in time, k_d is the coefficient of mass transfer by diffusion, A is the surface area of the crystal, c is the solute concentration in

solution, c_i is the solute concentration in the solution at the crystal-solution interface, k_r is the rate constant for the surface integration, $c^*$is the equilibrium saturation concentration.[109]

In the supersaturated solution, the crystal is growing and the solute is leaving the solution at the crystal-liquid interface. So, the solute concentration will decrease in this region (crystal-liquid interface). Crystal growth is primarily a two-step process. In the first step the solute molecules diffuse towards the crystal surface and, secondly, integration of these growth units into a crystal lattice takes place. On adsorption of the growth unit to the surface, surface diffusion, spatial orientation, and the subsequent surface integration reactions can take place. The region where the concentration is changing from the bulk solution C to the surface of the crystal c^* is named the concentration boundary layer. [121]

3.7 Model systems used to study crystallization impacts

In this study three mineral systems were chosen; being calcium carbonate, barium sulfate, and calcium oxalate. Calcium carbonate and barium sulfate are two of many common minerals associated with scale formation and cause ongoing economic issue within the oil and gas industry.[58, 115, 127-128] The formation of calcium oxalate, on the other hand, is commonly found in human pathological stone formation, for example in the urinary tract, bladder or kidney.[129-130]

3.7.1 Calcium carbonate

Calcium carbonate is the most abundant mineral formed in nature and is widely studied as an attractive model mineral.[131] Calcium carbonate has five known mineral phases, which can be divided into two types; anhydrous crystalline phases (vaterite, calcite, and aragonite), and hydrated phases (mono and hexahydrate) as is shown in Fig. 3.5. In addition, amorphous calcium carbonate (ACC) is also known.[132] The thermodynamically stable form of calcium carbonate at room temperature and pressure is calcite while aragonite and vaterite are less stable forms.[133] Calcium carbonate is a common biomineral[134] and a common component of industrial scale.[135] It can be found as the calcite form in species such as fish,[136] avian egg shells[137-138] or molluscs.[139] Vaterite can be found in Herdmania momus[140] and aragonite in fish[141] or cephalopods.[142] Also, it causes a major problem as scale

formation in industrial applications such as oil fields[116, 143] and water treatment.[144-145] Thus, calcium carbonate is an important mineral in industry[146-147] and biomineralization.[148-149]

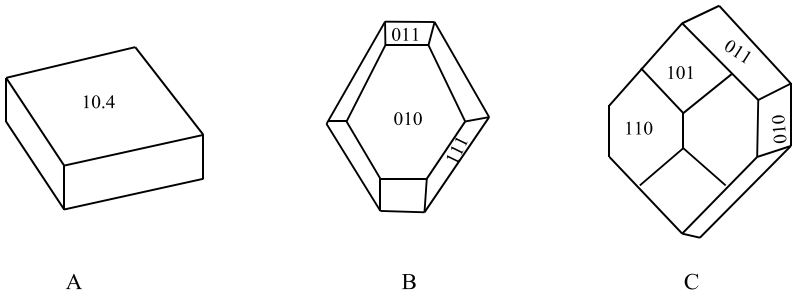

Figure 3. 5: Crystal forms of the polymorphs of calcium carbonate; (A) calcite, (B) vaterite (C) aragonite.

3.7.2 Barium sulfate

Barium sulfate is like calcium carbonate, it occurs as a biomineral[126] and as a scale in industry. Barite may be found in conjunction with both metallic and nonmetallic mineral deposits.[150] It is colorless or white, is chemically inert and insoluble (Ksp = 1.08 x 10^{-10}).[151-152] The mineral of barium sulfate is called barite and is the only known form at ordinary temperatures and pressures,[153] with no water being incorporated into the lattice. Barium sulfate is relatively simple to crystallize and, therefore, is utilized as a useful model system in crystallization studies.[154] Figure 3.6 presents the crystal morphology of barium sulfate.

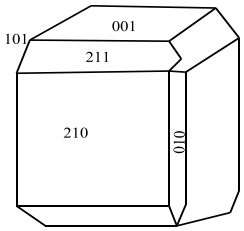

Figure 3. 6: Calculated crystal morphology of barium sulfate. Adapted from Jones and Rohl.[155]

3.7.3 Calcium oxalate

Calcium oxalate, like calcium carbonate and barium sulfate, occurs in nature where it has been reported in different genera of plants.[156] Calcium oxalate has three phases, calcium oxalate monohydrate (COM), calcium oxalate dihydrate (COD) and calcium

oxalate trihydrate[72]. COM is the thermodynamically stable form, COD is the metastable form, and COT is the unstable form and it is rarely observed. Their crystal structure are shown in Figure 3.7.[157] The presence of these hydrates in human pathological urinary stones is very high and hence it is a well studied mineral.[72, 116]

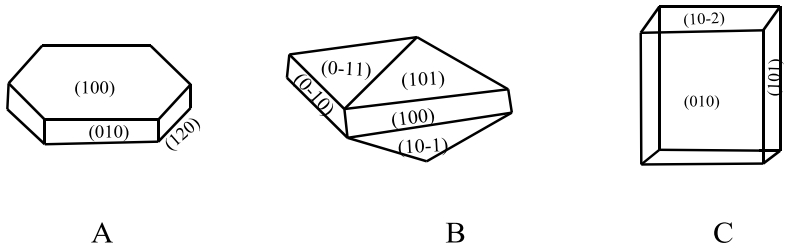

Figure 3. 7: Crystal habits of the different polymorphs of calcium oxalate hydrates; (A) COM, (B) COD, (C) COT.

3.8 Additives and their role in controlling crystallization

Additives, crystallization poison, inhibitor and admixture are some of the different terms that are used to define any foreign substance other than the solvent and the material that is crystallized (solute). They are defined as follows: the term additive is used when the impurity is intentionally added to the system of crystallization. When the impurity slows down crystal growth it is called a crystallization poison or an inhibitor. If the impurity is added in relatively enormous amounts (up to several percent) it is known as an admixture.[109, 121] Therefore, crystallization parameters such as nucleation, growth, crystal habit, agglomeration, and many other properties will be affected by the presence of these impurities.

Song and Helmut[158] pointed out that there are two types of additives, which are used for the control of crystallization. The first type is the insoluble additive, which is employed to control either the nucleation or polymorph of the nucleating crystal. Moreover, these insoluble additives can promote crystallization by heterogeneous nucleation. Different templating possibilities were reported such as Langmuir monolayers, self-assembled monolayers, latexes and colloidal crystals, these constitute a case of well-ordered and defined structures. The second type of additive is the soluble additive. In solution, the dissolved solute diffuses from the solution to the crystal surface and is integrated into the crystal lattice. However, soluble additive molecules can take the place of the solute on the crystallizing surface so the growth

rate of a face or all the faces can be affected, and the adsorption of soluble additives may cause a change in the crystal morphology.[158] Therefore, additives may adsorb upon all crystal faces, reducing the rate of crystallization to zero if present at sufficient levels, or, upon selective faces, leading to a change in morphology of the developing crystals. A mechanism of morphological change due to preferential adsorption of an additive (or solvent) is illustrated in Fig. 3.8.[159]

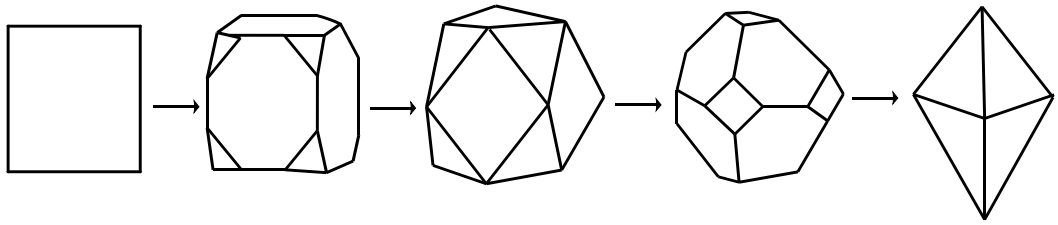

Figure 3.8: Schematic illustrating how an additive selectively adsorbing on particular faces can alter the crystal morphology. Modified from Beckmann.[110]

The role of additives has been investigated for many years by researchers. Jones and Ogden[160] have presented a brief overview about how additives impact crystallization. They summarize that the additives can inhibit or promote crystallization. For example, polymeric carboxylates and low molecular weight phosphonates were used efficiently as scale formation inhibitors in industrial processes. Moreover, they explained how these phosphonates linked with the barium sulfate lattice and changed the morphology and/or size. The additive or the inhibitor is absorbing on a selective face of the crystal surface and changes the morphology. An important mechanism for predicting the inhibition is called ‘’lattice matching’’. The anionic moieties of the inhibitor have distance that match lattice anion distances at the crystal surface.[161] Crystallization promotion is when the presence of additives increases the rate of crystallization. Inorganic ions such as potassium and sodium ions have been used as crystallization promoters of barite.[162-163] Organic crystallization promotion has also been proposed in the biomineralization field.[164] Amino acid,[165] proteins,[166] *etc*., have been employed as organic promoters of calcium carbonate. There are two mechanisms of crystallization promotion, which are desolvation of the cation where the presence of the additive increases the nucleation and growth.[167] The other mechanism is *via* an activation energy change where the kinetics of the crystallisation process changes when the additive is present and then the morphology will be changed.[168] Hence, the presence of these additives in crystallization processes

can have a major impact on the crystal growth and nucleation rate of the organic and inorganic crystals whether by inhibition or promotion.[160]

3.9 Experimental

3.9.1 Materials

Ultrapure water, with a resistance of 18.2 Ω/cm was used throughout the crystallisation experiments. Reagents barium chloride dihydrate and sodium sulfate were used as purchased from Sigma Aldrich and Alfa Assar. The resorcinarene derivatives-based additives used in these experiments were prepared by the methods described in **Chapter 2**. The macrocyclic compounds used in these studies are in the crown conformation. Table 3.1, displays additive compound's data. An additive stock solution was prepared by dissolving (0.1 g) of additives in (100 mL) ultrapure water and for the resorcinarenes ~ 10 mL of 5 % sodium hydroxide solution was also added to aid dissolution

Table 3.1: Additive compound's data

Compound Code	Compound structure	Molecular Weight (g/mol)
10	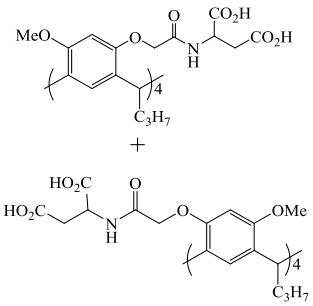	1406
11	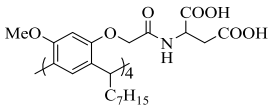	1630
12	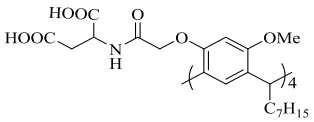	1630
13	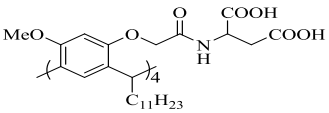	1854
14	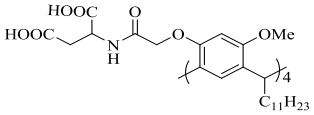	1854
18	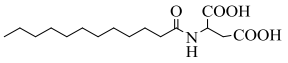	299.5

3.9.2 Crystallization procedures:

3.9.2.1 Calcium carbonate crystallization procedure

The impact on calcium carbonate crystallization by these additives was investigated by using literature methods.[36] The procedure is a static batch crystallization, which consisted of a vial containing calcium chloride solution (20 mL, 7 mM), with the appropriate concentration of additive. Cleaned microscope coverslips (11 mm diameter) were placed in the calcium chloride solutions to simplify recovery of the

crystals for microscopy. The vials were covered with laboratory film, with pinholes to allow diffusion of ammonia and carbon dioxide. The total volume of the solution was kept at 20 mL. The vials were then placed in a sealed desiccator, along with a vial of ammonium carbonate and left to stand at room temperature. After a week, the crystals were recovered, briefly washed with water, and allowed to dry. The samples were then platinum coated and the crystals were examined in a scanning electron microscope (SEM- Zeiss Evo 40XVP).

3.9.2.2 Barium sulfate crystallization procedure

Barium sulfate was also investigated through a batch crystallization process. The experiment was run at room temperature. The total volume of the solution was kept at 20 mL. The vials initially contained ultra-pure water after which the appropriate volume of additive was added, followed by barium chloride solution (50 µL, 0.1 M) and finally sodium sulfate solution (50 µL, 0.1 M) to commence crystallization. As per the carbonate experiments, cleaned microscope coverslips were placed in the vials before covering with the lid. After 3 days, the coverslips were removed and the excess solution was soaked up by tissue paper and allowed to dry. The coverslip was then prepared for imaging by SEM.

3.9.2.3 Calcium oxalate crystallization procedure

Calcium oxalate was also investigated through a batch crystallization process. The experiment was run at room temperature. The total volume of the solution was kept at 20 mL. The vials were prepared by adding ultra-pure water first, after which the appropriate volume of additive was added. Calcium chloride solution (100 µL, 0.1 M) was then added and finally sodium oxalate solution (100 µL, 0.1 M) was added to commence crystallization. Microscope coverslips were placed in the vials, covered with the lid and after 3 days, the coverslips were removed. The excess solution was soaked up by tissue paper and allowed to dry. The coverslip was then prepared for imaging by SEM.

3.9.3 Barium sulfate induction time experiments (nucleation)

Induction times were determined by a turbidity experiment at 900 nm. This wavelength was chosen to avoid the absorption of the solution and other species.[169] This was done with a UV-vis instrument and a flow through cell and reaction

chamber (the reaction chamber was temperature controlled using a recirculating water bath). The reaction chamber and flow through cell were cleaned by flushing through ethylenediaminetetraacetic acid (0.5 g) and sodium hydroxide (12 M, 2 mL) in ultrapure water (200 mL) at 60 ºC and then flushing with pure water several times. Once clean, the reaction chamber was prepared by adding barium chloride (0.1M, 500 μL) to ultrapure water then the appropriate concentration of the additive was added such that the total volume was 200 mL. After equilibration to temperature (25 °C), sodium sulfate (0.1 M, 500 μL) was added to initiate crystallisation. The reaction mixture was pumped through at 220 rpm using a peristaltic pump (Cole-Parmer Instrument Company, MASTERFLEX pump) into a quartz flow cell. The absorbance at 900 nm was recorded by a GBC UV/VIS 916 spectrometer over 20 minutes.

3.10 Results and discussion

The results from this work can be compared to the study of upper-rim acidic peptidocalixarenes as crystal growth modifiers by Goh *et al* (Figure 3.9).[36] Their study showed that an aspartic acid functionalized calixarene **A** was a more effective crystal growth modifier of calcium carbonate than **B** and **C.** Compound **C** required a higher additive level to alter the calcium carbonate morphology. Furthermore, the impact of **A** and **B** on barium sulfate morphology were similar. Therefore, the aspartic calixarene **A** and the glutamic calixarene **B** were found to have impacted on the morphology and crystallization kinetics of the model minerals investigated at low concentration (<1.2 μM) and the aspartic calixarene **A** was more potent than the glutamic calixarene **B.**

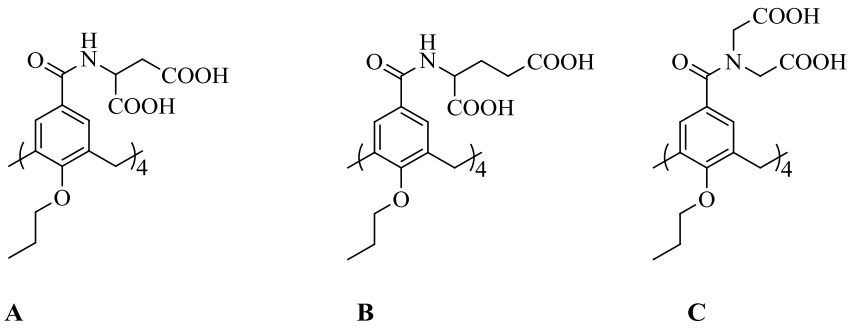

Figure 3. 9: Upper Rim functionalized calixarene investigated by Goh *et al*. for crystal growth modification properties of inorganic minerals.

3.10.1 The impact on calcium carbonate crystallization

Calcium carbonate crystallization was conducted by using the gas diffusion method.[170] In this process, ammonium carbonate decomposes to give carbon dioxide ammonia and water. Then, the ammonia and carbon dioxide dissolve into the calcium chloride solution. The increase in pH by the ammonia absorption and the conversion of carbon dioxide to carbonate results in crystallization over time. Calcium carbonate crystallization begins with the formation of vaterite or aragonite but eventually these transform to rhombohedral calcite through a dissolution re-precipitation process.[171]

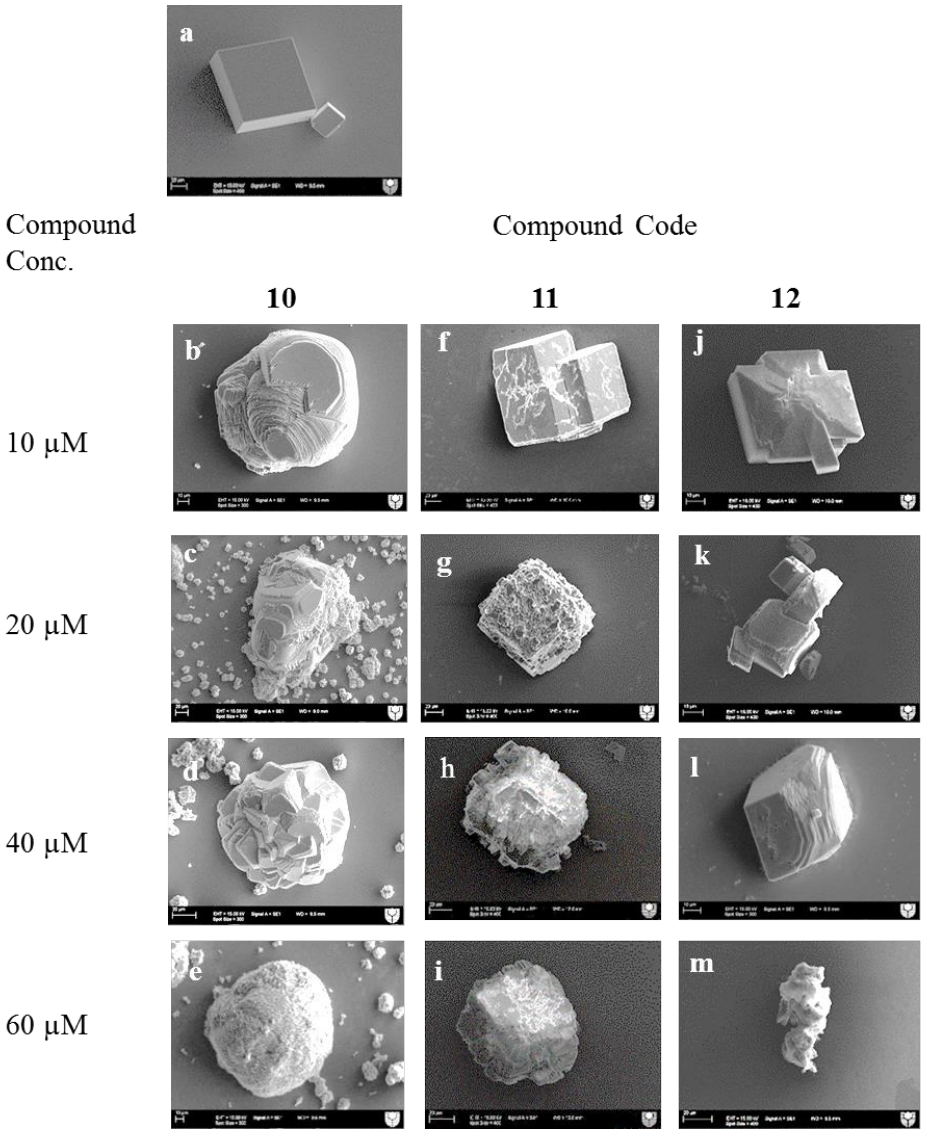

Figure 3.10: The SEM micrographs of calcium carbonate: (a) blank. Calcite morphology in the presence of **10** at; (b) 10 μM, (c) 20 μM, (d) 40 μM, (e) 60 μM. Calcite morphology in the presence of **11** at; (f) 10 μM, (g) 20 μM, (h) 40 μM, (i) 60 μM. Calcite morphology in the presence of **12** at; (j) 10 μM, (k) 20 μM, (l) 40 μM, (m) 60 μM.

Figure 3.10a presents the typical rhombohedral shape of calcite. Figures 3.10b-e shows how the presence of *L*-aspartic propyl tetramethoxy resorcinarene (**10**) has impacted the morphology of calcium carbonate even at the lowest concentrations (10 μM). At 10 μM of **10**, the steps of the calcite and the edges become more rounded. As the concentration of the additive was increased to 20 μM the rhombohedral shape of calcite was lost. Further increase in the concentration to 40 μM or 60 μM, resulted in the morphology of calcite being more rounded. Similar observations were noticed on calcium carbonate by Goh *et al*.[36] when they added the aspartic acid derivatives

A. The authors pointed out that, the irreversible adsorption of the additives at step and kink sites was the reason for the rounded morphology.

The impact of *L*-aspartic heptyl tetramethoxy resorcinarene compound **11** or its diastereoisomer compound **12** was also investigated. Figures 3.10f-i presents the impact of **11** on calcite morphology. It appeared to have an impact on the morphology of the calcite at high concentrations. The calcite morphology in the presence (10 μM) of **11** has not changed significantly but as the concentration is increased, the morphology of calcite was affected and the calcite appears to have many protrusions (a similar morphology was found by Al-Hamzah *et al*.[172] in the presences of *n*-hexyl isobutyrate-poly terminated poly(acrylic acid) (HIB-PAA)). The impact of compound **12** on calcite growth can be seen in Figures 3.10j-m. The presence of **12** appeared to have less impact on the calcite morphology than **10** or **11**. At concentrations of 10 μM, 20 μM, 40 μM and 60 μM of compound **12**, stepped faces begin to appear on calcite morphology compared to the blank calcite particle. Compounds **11** and **12** were not used by Goh *et al*., so no comparison can be made to the upper calixarene derivatives. Briefly, additive **10** altered the morphology of calcite even at low concentration (10 μM). The additive **11** had more impact on the calcite morphology than **12**.

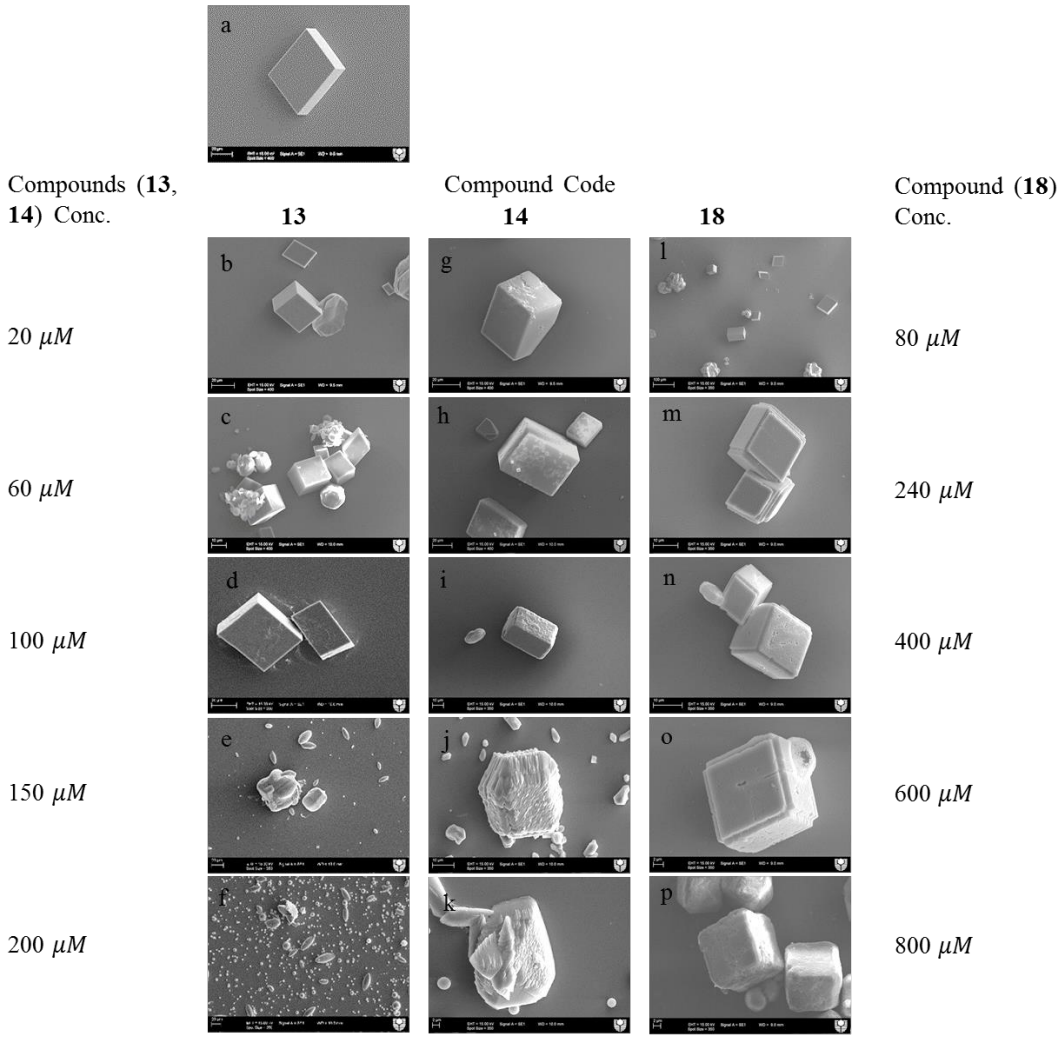

Figure 3.11: The SEM micrographs of calcium carbonate: (a) blank. Calcite morphology in the presence of **13** at; (b) 20 μM, (c) 60 μM, (d) 100 μM, (e) 150 μM, (f) 200 μM. Calcite morphology in the presence of **14** at; (g) 20 μM,; (h) 60 μM, (i) 100 μM, (j) 150 μM, (k) 200 μM. Calcite morphology in the presence of **18** at; (l) 80 μM, (m) 240 μM, (n) 400 μM, (o) 600 μM, (p) 800 μM.

Figure 3.11 displays the impact of compounds **13**, **14**, and **18** on calcite morphology. Compound **18** has been synthesized to investigate which functionality has impacted the crystallization, the resorcinarene scaffold or the alkyl chain. These compounds appear to require greater concentration to impact calcite morphology. At concentrations 20 μM, 60 μM, 100 μM of compound **13** (Figures 3.11b-d), no significant change was observed in the calcite morphology but when the concentration increased to 150 μM and 200 μM, as shown in Figures 3.11e-f, the crystals became small and the rhombohedral shape was lost. At the highest concentration rounded, 'rice' shaped particles were observed. At concentrations (20

μM, 60 μM, 100 μM) of compound **14** (Figures 3.11g-i), no significant change in calcite shape was observed as per compound **13** but the surface became rougher. Figures 3.11j-k shows the impact of compound **14** at concentrations 150 μM ,200 μM, where the calcite particle size decreases and the calcite shape changed, showing rounding and 'streaking'. The impact of compound **18** on calcite particles is shown in Figures 3.11l-p. At a concentration of 80 μM, the morphology of calcite particles was not changed. Figures 3.11m-o, shows notches along the edges of the calcite and the surface of the crystal was not smooth. Therefore, the compounds **13**, **14** have a similar effect on the calcium carbonate crystallization process and they have more of impact then the compound **18**. The results suggest that diastereoisomers of the resorcinarenes **13**, **14** were more potent in inhibiting calcium carbonate crystallization than the alkyl chain compound **18**.

3.10.2 The impact on barium sulfate crystallization

The morphology of barium sulfate was determined by batch crystallization experiments (see Experimental section). The supersaturation in the solution was created by mixing barium chloride solution and sodium sulfate solution with the appropriate additive concentration and the total volume was kept constant at 20 mL. After 3 days, the coverslips were taken then dried and prepared for imaging.

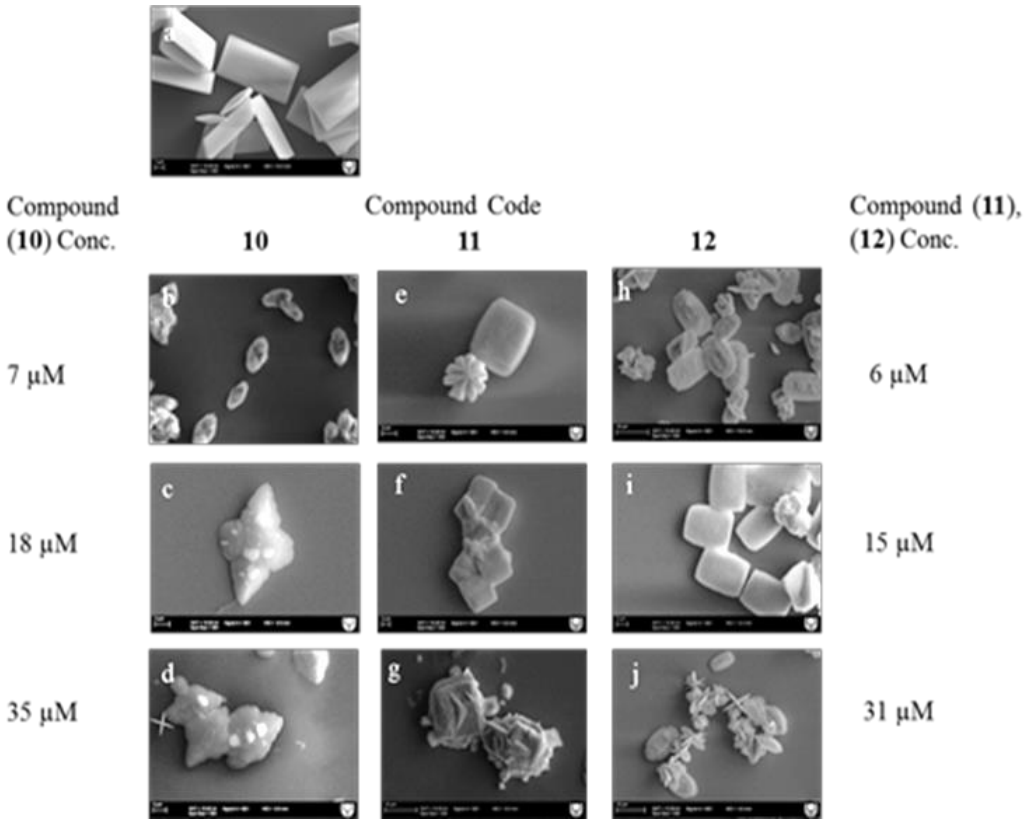

Figure 3.12: The SEM of barium sulfate; (a) blank. The SEM of BaSO4 with the compound **10** at: (b) 7 µM, (C) 18 µM, (d) 35 µM. The SEM of BaSO4 with the compound **11** at: (e) 6 µM, (f) 15 µM, (g) 31 µM. The SEM of BaSO4 with the compound **12** at: (h) 6 µM, (i) 15 µM, (j) 31 µM.

In the absence of any additives, the barium sulfate particles had the expected 'pillow' shape with (001) faces at the end and rounded (hk0) faces (Figure 3.12a). Barium sulfate in the presence of **10** was impacted and the morphology changed from 'pillow' shaped to dendritic at high concentrations. The presence of **11** at (6 µM) resulted in particles with reduced aspect ratio, the length along the c-axis being reduced relative to the other faces. Also, at 31 µM **11**, a high degree of intergrown particles was observed. At high concentrations of **11** (Figures 3.12f-g), the barium sulfate particles are short and the surface became rough, which might be attributed to the formation of nanoparticles of barium sulfate. The presence of compound **12** also impacted barium sulfate morphology (Figures 3.12h-j), the c-axis length reduced and intergrown particles of barium sulfate were also observed. At high concentrations (31 µM), thin and agglomerated crystals were observed with a somewhat rounded dendritic form. Therefore, these additives (**10**, **11**, and **12**) have impacted barium

sulfate crystallization and the additive **10** is the more effective one (based on the concentration at which impacts are observed.).

The concentrations in this study were higher than that used in the study by Goh *et al*., which showed that the *L*-aspartic calixarene compound formed small and polycrystalline barium sulfate particles at 0.04 μM. Thus, these additives are less potent modifiers for barium sulfate.

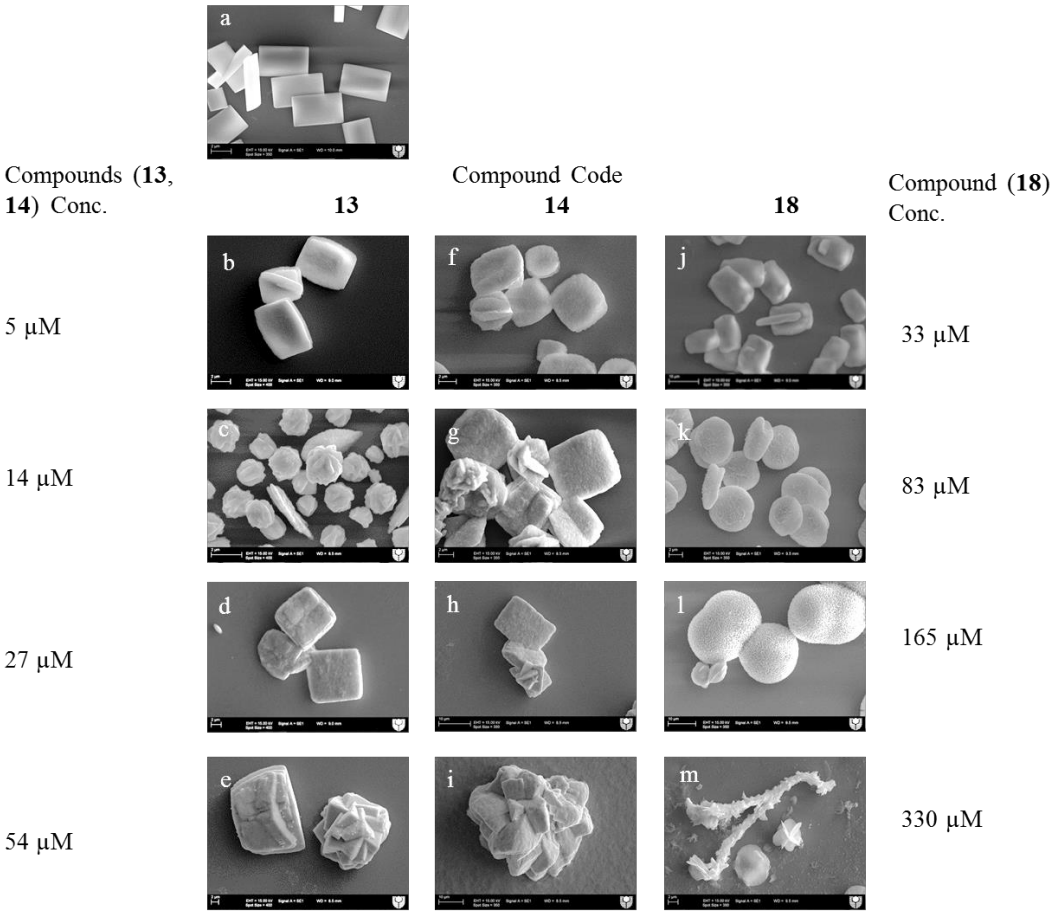

Figure 3.13: The SEM of barium sulfate; (a) blank. The SEM of BaSO4 with **13** at: (b) 5 μM, (C) 14 μM, (d) 27 μM, (e) 54 μM. The SEM of BaSO4 with **14** at:(f) 5 μM, (g) 14 μM, (h) 27 μM. (i) 54 μM. The SEM of barium sulfate; (a) blank. The SEM of BaSO4 with the **18** at; (j) 33 μM, (k) 83 μM, (l) 165 μM, (m) 330 μM.

Figure 3.13a shows the SEM images of barium sulfate in the absence of additives. The growth of barium sulfate in the presence of compound **13** is shown in Figures 3.13b-e and in the presence of **14** in Figures 3.13f-i. Their influence on barium sulfate morphology was found to be similar at the studied concentrations, where the

crystal size is reduced and crystal aggregation was observed at high concentrations of the additives. Also, the surface became rough and clusters of particles formed. Compound **18** was also investigated (Figures 3.13j-m). At low concentrations (33 μM), the length of crystal reduced in the *c* axis direction. As the concentration increased (83 μM, 165 μM) the morphology of barium sulfate became rounded. Therefore, this suggested that, the alkyl chain was more potent in inhibiting barium sulfate crystallization than the dia-stereoisomers of resorcinarenes.

3.10.3 The impact on calcium oxalate crystallization

Batch crystallization experiments were also conducted for calcium oxalate.

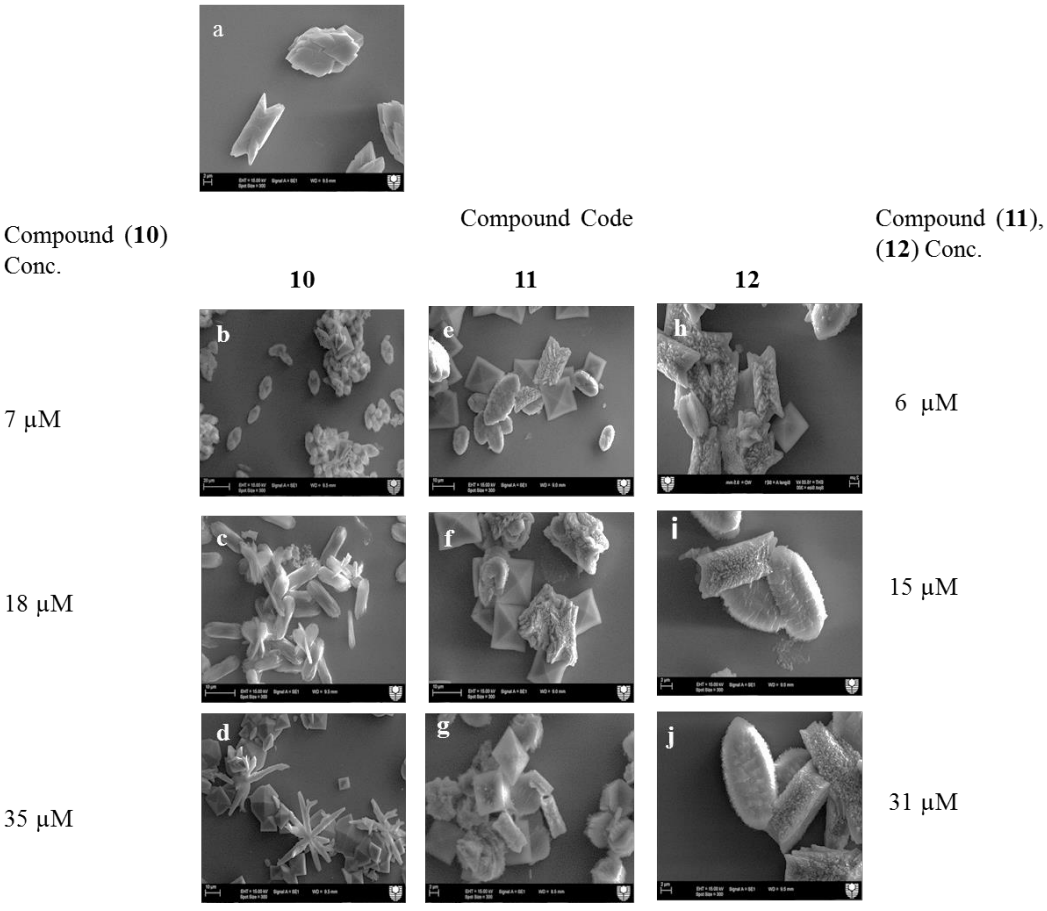

Figure 3.14: The SEM of calcium oxalate; (a) blank. The SEM of CaOX with **10**; at: (a) 7 μM, (b) 18 μM, (C) 35 μM. The SEM of CaOX with **11**; at:(e) 6 μM, (f) 15 μM, (g) 31 μM. The SEM of CaOX with **12** (h) 6 μM, (i) 15 μM, (j) 31 μM.

The morphology results for calcium oxalate in the presence of **10**, **11** and **12** can be found in Figure. 3.14. The SEM micrographs of calcium oxalate without additives is

shown in Figure 3.14a and results in particles with the typical morphology of COM crystals. The impact of **10** is shown in Figures 3.14b, where the calcium oxalate crystals formed with shortened length in the <001> direction (*c* axis). Figures 3.14c-d shows thin crystals were formed as the concentration increased with aggregates being observed at the highest concentration. This suggests that compound **10** has strongly modified the crystallization of calcium oxalate. Figures 3.14e-g presents the impact of **11** at increasing concentrations and shows the formation of both COM and COD crystals. The COM particles became more rounded with increasing concentration while the COD particles retained their bi-pyramidal shape. The impact of compound **12** was to form rough calcium oxalate particles, but these essentially retained their COM overall morphology. Thus, the three additives affected calcium oxalate crystallization and the more potent one were **10** and **11**.

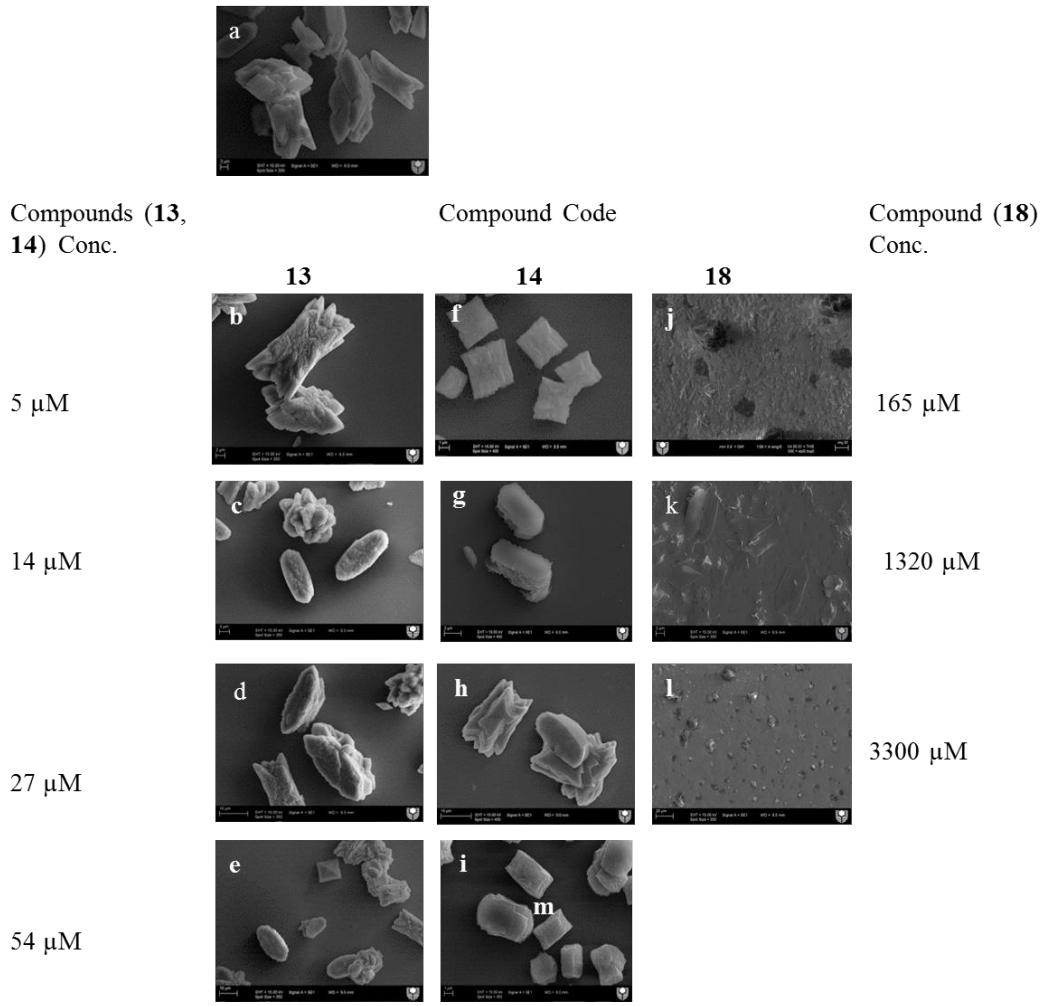

Figure 3.15: The SEM of calcium oxalate; (a) blank. The SEM of CaOX with **13**; at: (b) 5µM, (C) **14** µM, (d) 27 µM, (e) 54 µM. The SEM of CaOX with 14; at:(f) 5 µM, (g) 14 µM, (h) 27 µM. (i) 54 µM. SEM of CaOX with **18**; (j) 165 µM, (k) 1320 µM, (l) 3300 µM.

The impact of compounds **13** and **14** on calcium oxalate have been studied. At low concentrations the impact of **13** on calcium oxalate formed COM crystals with a roughened surface. At high concentrations (Figures 3.15c-e) aggregates of the particles and COD particles were observed. This means the additives have impacted the calcium oxalate crystallization. The results in the presence of **14** are shown in Figures 3.9f-i. In this case, the COM crystal's morphology has altered even at low concentrations. Initially, rough particles are formed but as the concentration is increased the particles become smoother. This suggested that the two isomers have affected the calcium oxalate morphology and **14** is more potent than the **13**. The impact of the **18** was also studied as a reference compound. The results are presented in Figures 3.15j-m. when concentrations are increased, the particle size decreases significantly to the point where distinct particles cannot be observed. At 1320 μM thin, platelets of particles similar to the COM morphology are seen but these are not observed at 3300 μM (further studies are required to better understand this altered).

3.10.4 The impact on barium sulfate nucleation

The measurement of absorbance at 900 nm can be described as a turbidity value or an optical density. It is due to the light being scattered by the particles rather than absorbed by them. The induction time is defined as the time period for the absorbance to increase above background level. Any change in induction time is related to homogenous nucleation and the surface free energy of critical nuclei. The relation between the induction time and nucleation rate is an inverse one, meaning that if the induction time increases homogenous nucleation rates are decreasing.

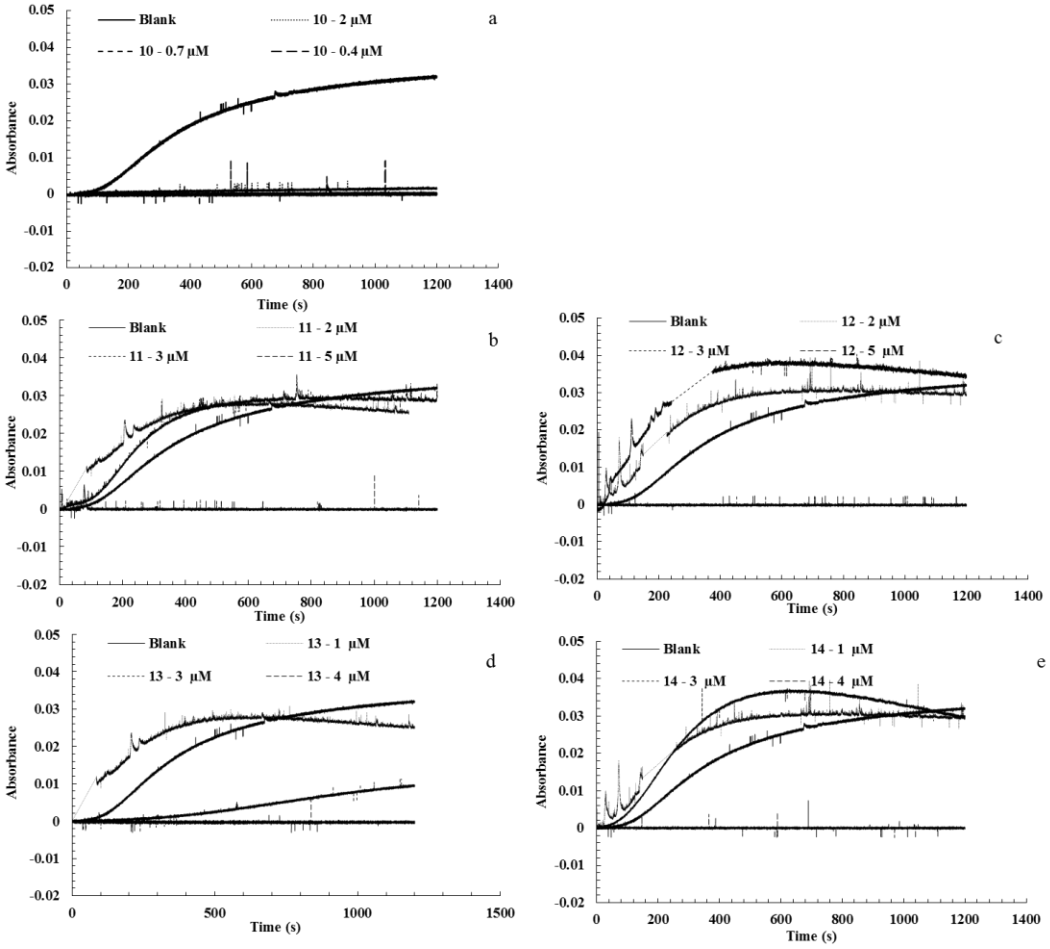

Figure 3. 16: Absorbance versus time curves for barium sulfate crystallization in the presence of different concentrations of the resorcinarenes derivatives (a) **10**, (b) **11**, (c) **12**, (d) **13**, (e) **14**.

Figure 3.16 shows the results of the impact of resorcinarene additives on barium sulfate nucleation. Figure 3.16a illustrates the induction time has increased with increasing concentrations of 10. The presence of 11, 12, 13 and 14 induce different behaviour at low concentration but the induction time increases at high concentrations of these additives. Therefore, these resorcinarene derivatives inhibit homogenous nucleation rates significantly at high concentration. At low concentration, some of these molecules appear to promote homogenous nucleation. This suggests that these molecules are interacting with the critical nuclei and changing the surface free energy of these nuclei.[173] Clearly, all the resorcinarene molecules are nucleation inhibitors at high concentrations and compound 10 appears to be the most active inhibitor at low concentrations.

3.10.5 Infrared study

The purpose of this part of the study was to investigate whether the additives adsorbed onto the barium sulfate surface using infrared spectroscopy. The results in Figure 3.17 show that the expected CH stretching peaks of the resorcinarenes molecules can be found at 2900 cm. After mixing pure barium sulfate in the presence of resorcinarenes molecules (710 μM of **10**, 610 μM of **11,12** and 540 μM of **13,14**) for 3 days, the infrared spectrum was taken. Figure 3.17a presents the IR spectrum of compound **10** and it shows that the C-H stretch bands are found at ~ 3000 cm^{-1}. After the spectrum of the barite solids was subtracted from the obtained spectrum of the barite plus obsorbed organics spectrum, a small absorption is observed in this region (~ 3000 cm^{-1}) which suggests that compound **10** is absorbed on the barium sulfate surface albeit at low levels. Also, the absorption of the diastereoisomers of heptyl resorcinarenes derivatives (**11**, **12**) on barium sulfate surface was studied and the results shown in Figures 3.17b-c. The spectra show that the isomer **11** has a tiny absorption band in the ~ 3000 cm^{-1} region, while isomer **12** has not absorption on the barium sulfate surface. This in turn means that isomer **11** is interacting with the barium sulfate surface while isomer **12** is not interacting with the barium sulfate surface strongly. Figures 3.17d-e, displays the spectra of the di- stereoisomers undecyl resorcinarenes derivatives (**13**, **14**). Both show a multiple band formed and this is suggesting that they are absorbed on the barium sulfate surface.

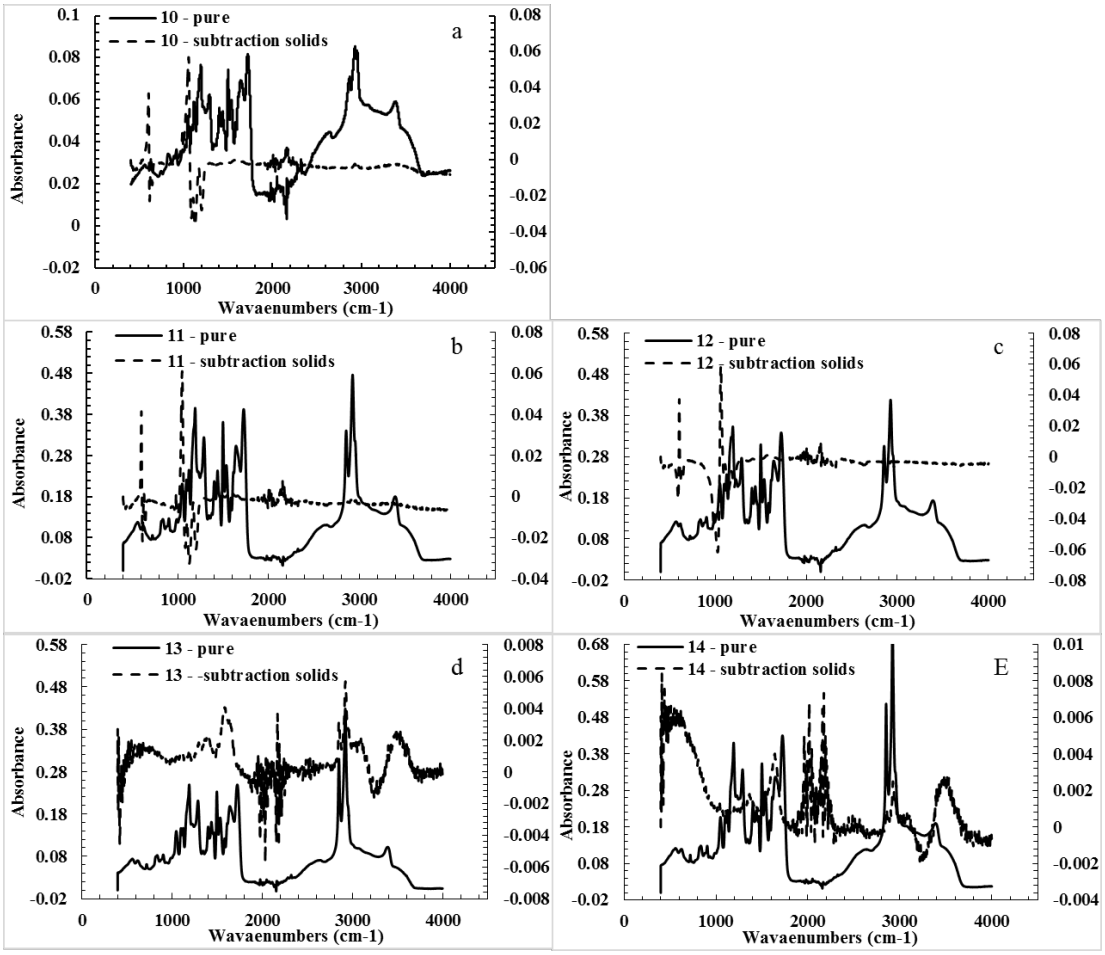

Figure 3. 17: The IR spectrum after subtraction of barium sulfate to determine any absorbed species and the spectrum of resorcinarenes derivatives (a) **10**, (b) **11**, (c) **12**, (d) **13**, (e) **14**.

3.11 Conclusions

The amino acid functionalized resorcinarenes (**10-14**) had an impact on the crystallization of model mineral systems, calcium carbonate, barium sulfate and calcium oxalate. All the amino acid functionalized resorcinarenes have affected the morphology of calcium carbonate and the mixture of diastereoisomers of propyl resorcinarenes (**10**) is appeared to be the more effective than the others. The amino acid undecyl resorcinarenes (**13**, **14**) required a higher additive level to impact on the calcium carbonate morphology. A comparative study between the stereoisomers (**13**, **14**) and the alkyl amide (**18**) resulted in the compound **13** and **14** having more effect on the calcite morphology. The growth of barium sulfate in the presence of the diferent isomers **11** and **12** gave similar effect on the barite morphology. Also, the presence of **13** and **14** gave similar effect on the barium sulfate morphology. The

comparative study between the stereoisomers (**13**, **14**) and the alkyl amide (**18**) showed that the alkyl amide **18** is more effective in impacting on the barite morphology. The aspartic acid functionalized resorcinarenes **10** affected the calcium oxalate morphology more than the others. Whilst isomer **12** has less impact on calcium oxalate morphology than isomer **11**, the isomer **14** has greater impact on calcium oxalate morphology than isomer **13** and the comparative study between them and the alkyl amide (**18)** showed that the stereoisomers have more effect on calcium oxalate morphology.

The induction time analysis of barium sulfate crystallization shows that all the amino acid resorcinarenes derivatives adsorbed onto the critical nuclei and inhibited homogenous nucleation at high concentrations. Compound **10** appeared the more potent crystal growth inhibitor.

The IR results show that the undecyl aspartic acid resorcinene (**13**, **14**) are absorbed on the barium sulfate surface more than the aspartic acid functionalized resorcinarenes (**10**-**12**).

4.0 Corrosion inhibition

4.1 Outline

This chapter will present the overview introduction of corrosion processes and focus on corrosion in a CO_2 environment. Electrochemical techniques are described and used to determine the corrosion rates and corrosion inhibition efficiency. A scoping study has also been conducted to evaluate the impact of the resorcinarene derivatives as corrosion inhibitors for carbon steel in CO_2-saturated brine.

4.2 Introduction

Corrosion is the reaction between a metal and its environment and can lead to destruction or compromise of the original characteristics of the metal.[174] Corrosion in metallic materials can be classified into two types, localized and uniform (general) corrosion. Localized corrosion occurs for example when a passive surface film breaks down in aggressive environments, such as in media containing chloride ions. Various types of localised corrosion exist, such as corrosion fatigue, stress corrosion cracking, pitting and crevice corrosion. Uniform or general corrosion is a type of corrosion where the metal exposed to the corrosive environment is uniformly corroded across its surface. This type of corrosion can be easily recognized by increased roughness of the metal surface and by the presence of corrosion products on the metal surface.[174-177] Corrosion has also been defined as an electrochemical process because of the presence of anodic and cathodic active points on the material surfaces.[178] The presence of an electrolyte is fundamental for electrochemical reactions to occur. Moreover, the bulk solution and the metallic surface present a corrosion system, involving anodic and cathodic sites at the metal. Corrosive species can be found in diferent forms, including aqueous solutions and acids or in gaseous forms such as hydrogen sulfide (sour corrosion)[179] and carbon dioxide (sweet corrosion)[180]. The extent of corrosion of the metal is dependent on the properties of the corrosive media.

There are different types of metals that have been used for industrial assets. Metallic material which is highly used as a construction material, particularly in the oil and gas industry is carbon steel. Carbon steel is preferred for engineering applications including water pipelines, cooling water systems, oil pipelines etc.[181-182] due to its

characteristics and low cost. The major elements in carbon steel are carbon and iron. Carbon steel also contains trace elements such as manganese, silicon, sulfur, and phosphorus. Carbon steel can be classified into three types, namely high carbon steels with <0.70-1.05% C, medium carbon steels with 0.25-0.70% C, and low carbon steels with <0.25% C.[183] The components in carbon steel contribute to the physical characteristics exhibited by carbon steel,[183-184] therefore, further divided into certain grades for example; grade 1008 with 0.08% C characterized by good ductility, grade 1018 with 0.18% C good for welding and is used in general applications, grade 1030 with 0.30% C is characterized by low hardness.[183]

In the oil and gas production and transportation facilities, carbon dioxide (CO_2) corrosion is a major problem. Dissolved CO_2 in aqueous solutions causes severe corrosion issues for carbon steel pipelines and equipment utilised in the production, extraction and transportation of oil and gas in the oil and gas industry.[185] CO_2 corrosion can be affected by a variety of factors including temperature, pH, CO_2 partial pressure, flow conditions, concentration of corrosion inhibitors and liquid compositions.[186-187]

4.3 CO_2 corrosion

Carbon dioxide (CO_2) corrosion or 'sweet corrosion' has been studied by numerous researchers in the past to understand its mechanism and to clarify the influential factors involved.[188-191] Aqueous CO_2 corrosion of carbon steel is an electrochemical process involving anodic dissolution of iron and cathodic evolution of hydrogen. Several processes occur simultaneously in this system, including chemical reactions in the bulk solution, electrochemical reactions at the surface and transport of species to and from the bulk solution to the steel surface.[180, 192]

4.3.1 CO_2 corrosion mechanism

Waard and Williams were first to publish the mechanism of general CO_2 corrosion, by direct reduction of carbonic acid,[193] and the understanding of CO_2 corrosion has been addressed by many researchers.[186, 189, 194-196] Nesic, *et al*.,[186, 195] studied the dissolution of steel in CO_2 saturated brine. While, Nordsveen, *et al*.,[196] studied the corrosion rate with respect of number of variables (temperature, pH, the CO_2 partial pressure). Another mechanistic model studied the effect of CO_2 diffusion, hydration,

carbonic acid (H_2CO_3) dissolution, iron carbonate ($FeCO_3$) precipitation on CO_2 corrosion.[189]

Carbon steel is the most widely used material in oil and gas production. Carbon steel can be rapidly corroded when exposed to CO_2 in aqueous environments. The overall reaction is present in the following equation:[197]

$$Fe_{(s)} + CO_{2(aq)} + H_2O_{(l)} \rightleftharpoons FeCO_{3(s)} + H_{2\,(g)} \qquad 4.1$$

This overall reaction can be described by the following equations:[180, 186]

$$CO_2 \rightleftharpoons CO_{2(aq)} \qquad 4.2$$

$$CO_{2(aq)} + H_2O_{(l)} \rightleftharpoons H_2CO_{3(aq)} \qquad 4.3$$

$$H_2CO_{3(aq)} \rightleftharpoons H^+_{(aq)} + HCO_3^-{}_{(aq)} \qquad 4.4$$

$$HCO_3^-{}_{(aq)} \rightleftharpoons H^+_{(aq)} + CO_3^{2-}{}_{(aq)} \qquad 4.5$$

Carbon dioxide (CO_2) is dissolved in water (eq. 4.2), and then is hydrated to form carbonic acid (eq. 4.3). The carbonic acid then dissociates partly into bicarbonate and carbonate in two steps (eqs. 4.4 and 4.5).[198] Aqueous CO_2 corrosion is considered as acid corrosion type due to the formation of carbonic acid.[199]

Anode is a positively charged electrode, therefore, the anodic corrosion reaction is oxidation reaction where the metal is being oxidized and loses electrons.[200] The anodic reaction is the dissolution of iron (eq. 4.6):

$$Fe_{(s)} \rightleftharpoons Fe^{2+}_{(aq)} + 2e^- \qquad 4.6$$

Bockris[201] pointed out that the anodic dissolution of iron in CO_2 aqueous solution is a pH-dependent process. During these corrosion processes, the presence of carbonates in the electrolyte and ferrous ions can form a scale on the carbon steel surface and reduce the corrosion rate.[190, 202] The following equation represents the formation of corrosion product layer of iron carbonate:

$$Fe^{2+}_{(aq)} + CO_3^{2-}{}_{(aq)} \rightleftharpoons FeCO_{3(s)} \qquad 4.7$$

Based on the reaction above (eq. 4.7), the precipitation of $FeCO_3$ will occur if its solubility limit is exceeded. The $FeCO_3$ corrosion product layer is formed on the steel surface and is acting as a barrier to prevent corrosive species reaching the steel surface.

Cathode is a negatively charged electrode where a reduction reaction occurs. Electrons produced in an oxidation reaction are consumed in reduction reaction.[203-204] The main cathodic reaction that occurs in CO_2 corrosion at pH<7, involves reduction of hydrogen ions (eq. 4.8) and carbonic acid (eq. 4.9).[204]

$$2H^+_{(aq)} + 2e^- \rightleftharpoons H_{2(ads)} \qquad 4.8$$

$$2H_2CO_{3(ads)} + 2e^- \rightleftharpoons H_{2(ads)} + 2HCO_3^-{}_{(ads)} \qquad 4.9$$

In cathodic reactions, hydrogen evolution is generated and is dependent on pH. Bicarbonate (HCO_3^-) undergoes reduction at pH>7 and forms carbonate (eq.4.10). This reaction is accepted to be slow compared to other cathodic reactions (eq. 4.8 and eq. 4.9).[205-206]

$$2HCO_3^-{}_{(ads)} + 2e^- \rightleftharpoons H_{2(ads)} + 2CO_3^{-2}{}_{(ads)} \qquad 4.10$$

CO_2 corrosion can be affected by several parameters such as temperature or pH. Changes in the temperature and pH affect the solubility and the kinetics of the formation of iron carbonate ($FeCO_3$) and the corrosion rate.[207-210] For example, Sun, *et al*.[211] found that the solubility of $FeCO_3$ as corrosion product decreased with temperature in temperature range of 20°C - 80°C and the corrosion rate decreased. Waard and Lotz pointed out that at temperatures between 70°C - 80°C, dense precipitation of iron carbonate ($FeCO_3$) occurs and reduces corrosion.[212] Solution pH can also affect the kinetics of formation of the protective $FeCO_3$ layer. At low pH, the concentration of corrosive species (H^+) and the corrosion rate increased, as the kinetics of precipitation of the protective layer reduced.[213] Changes in pH also affect the concentration of species (H_2CO_3, HCO^{3-}, CO_3^{2-}) in an electrolyte.[196] Therefore, the CO_2 corrosion process can be significantly affected by temperature and solution pH.

To conclude, carbon dioxide corrosion significantly affects oil and gas pipelines. For this reason, numerus studies have been conducted to understand the mechanisms of CO_2 corrosion. There are many factors that can impact CO_2 corrosion process such as the temperature and solution pH. In oil and gas industry, CO_2 corrosion is one of the challenging concerns due to the hydration of CO_2 in the liquid phase (water) that can lead to an internal corrosion in the pipeline.[214] To prevent destruction or degradation of metal surface various strategies have been applied. Chemical corrosion inhibition is one of the most applied strategies in the industry due to its the low cost and practical application.[215-217]

4.3.2 CO_2 corrosion inhibition

Corrosion processes can be reduced by addition of small amounts of chemicals to a corrosive environment. This is a preventative process known as chemical inhibition and the chemicals used to reduce the corrosion process are called corrosion inhibitors. These inhibitors can adsorb at the metal surface and form a protective film. Therefore, corrosion inhibitors can affect the anodic or cathodic reactions and increase the electrical resistance of the metallic surface.[218-220] There are many factors that influence the adsorption of the inhibitor molecule such as the solution chemistry, state of the metal surface, chemical structure of the inhibitor molecule, and the electrochemical potential at the interface.[221] Inhibitors can be classified as anodic inhibitors (reducing anodic reactions), cathodic inhibitors (reducing cathodic reactions), and mixed inhibitors (reducing both anodic and cathodic reactions).[222] Corrosion inhibitors can also be classified according to their chemical nature as organic and inorganic substances. Organic inhibitors have electron delocalization and amphiphilic characteristics. The electron delocalization characteristics mean that the organic compound has π electrons whether in double, triple bounds, aromatic ring or has electronegative groups. The amphiphilic characteristics mean the organic compound has both the hydrophobic and hydrophilic parts in its molecule.[223-225] Numerous compounds with these chemical structures have been widely used as CO_2 corrosion inhibitors. These include imidazoline derivatives,[226-231] quaternary ammonium compounds[232-234] and sodium thiosulfate as a corrosion inhibition enhancer.[235-238] Imidazoline derivatives and quaternary ammonium compounds are surfactant molecules that typically have two functionalities: a head group is hydrophilic and a tail group which is hydrophobic (Figure 4.1).[239-241] In aqueous

solutions, the inhibition efficiency of these molecules increased with increasing the length of the alkyl chain.[231, 242]

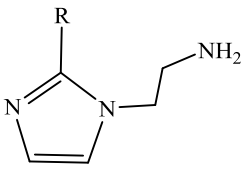

R = C_{16}-C_{18} chain

a

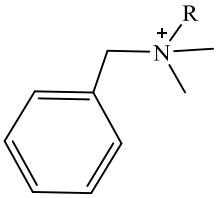

R = C_{10} - C_{18} chain

b

Figure 4.1: Sturcture of some organic inhibitors: (a) imidazoline.[230] (b) quaternary ammonium compound.[238]

In oil and gas production lines, CO_2 corrosion has been mitigated by using film forming corrosion inhibitors (FFCls). These inhibitors are organic compounds and usually contain nitrogen, oxygen and sulfur atoms in their structure.[243-245] The performance of organic inhibitors is related to the magnitude to which they adsorb and cover the metal surface. They are linked with the metallic surface through two common types of binding interactions: physical adsorption or chemisorption. The physical adsorption or physisorption process is a weak interaction between the molecules and the surface. For instance, van der Waals forces of interaction between gas or liquid molecules and electrically charged metal surface.[246] The chemical adsorption or chemisorption can occur in two ways: ionic interaction due to a charge transfer, where the adsorbed species must have a dipole in the molecule.[221] Covalent bonds form due to electrons transfer between atoms. For example, molecules with functional groups that contain atoms such as O, N, S, P can donate electrons from the binding species to the vacant d-orbital of the transition metals (substrate), or π-electrons in aromatic rings.[247] When the inhibitor molecules adsorb on the steel surface, a stable film can be formed that protects the steel surface against corrosion.

Calixarenes and resorcinarenes are macrocyclic compounds that can be readily functionalized on the upper or lower rims, thus, they are used in different fields (see **Chapter 2** for more details). There are examples in the published literature involving calixarenes and resorcinarenes as corrosion inhibitors.[49-50, 248-251] Kaddouri *et al.*[250] synthesized calix[8]arene derivatives which are shown in Figure 4.2, and tested as

corrosion inhibitors at concentrations (10^{-3} – 10^{-6} M) in HCl solution at 308 K by weight loss method and electrochemical measurements. They found that the efficiency of the calixarene derivatives was higher at low concentrations. The corrosion inhibitors were shown to reduce anodic dissolution of the metal and retarded the hydrogen evolution reaction.

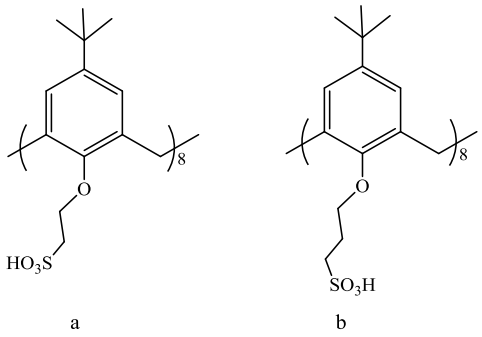

a b

Figure 4.2: An example of calix[8]arene derivatives used as a corrosion inhibitors.[250]

Tan *et al*.,[49] used wire beam electrode (WBE) to investigate the corrosion inhibition properties of resorcinarene acid (Figure 4.3). They found that it was an effective corrosion inhibitor which minimized localized corrosion by promoting a random distribution of insignificant anodic currents. Also, this study of Tan *et al*. showed that the resorcinarene acid effectively inhibited steel exposed to CO_2 saturated brine solution.

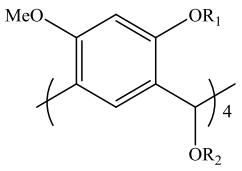

R_1 = CH_2COOH, H, CH_2COOEt.
R_2 = C_3H_7

Figure 4. 3: An example of resorcinarene derivatives used as a corrosion inhibitors.[49]

This chapter aims to investigate corrosion inhibition efficiency of resorcinarene derivatives that contain nitrogen and oxygen atoms in their chemical structures, but differ by the length of their aliphatic chains. All compounds are studied in CO_2-saturated brine that simulates conditions encountered in the oil and gas operations.

4.4 Electrochemical techniques

In corrosion science, the application of electrochemical techniques makes it possible to measure the parameters of corrosion processes, particularly the corrosion rates. Electrochemical techniques can provide information about instantaneous corrosion rates and advance our understanding about corrosion reaction mechanisms. In corrosion inhibition studies, the corrosion rate measurements allow for comparison and ranking of corrosion inhibitor compounds for their efficiency to inhibit corrosion processes. The next section explains the electrochemical methods applied in this study.

4.4.1 Liner polarization resistance (LPR)

Linear polarization resistance technique is a common corrosion monitoring technique used in assessment of CO_2 corrosion of carbon steel. Linear polarization resistance technique has proven to be a rapid response technique that determines the general corrosion rates of steel by measuring polarization resistance [105].[252] The measurements in this work were conducted according to the ASTM G59 standard.[253]

In this method, the test setup comprises a test cell fitted with three electrodes that are electrically isolated from each other. The electrodes are a working electrode (tested steel sample), a counter electrode and a reference electrode. A small potential is applied in a range of ±5 mV to ±20 mV (±10 mV used in this work) from the open circuit potential (OCP) between the counter and working electrode. The current response is measured and it is assumed to be linear in the given narrow potential range. A typical plot showing current density vs. potential is shown in Figure 4.4.[253] It shows that the current density is linearly proportional to the applied potential.

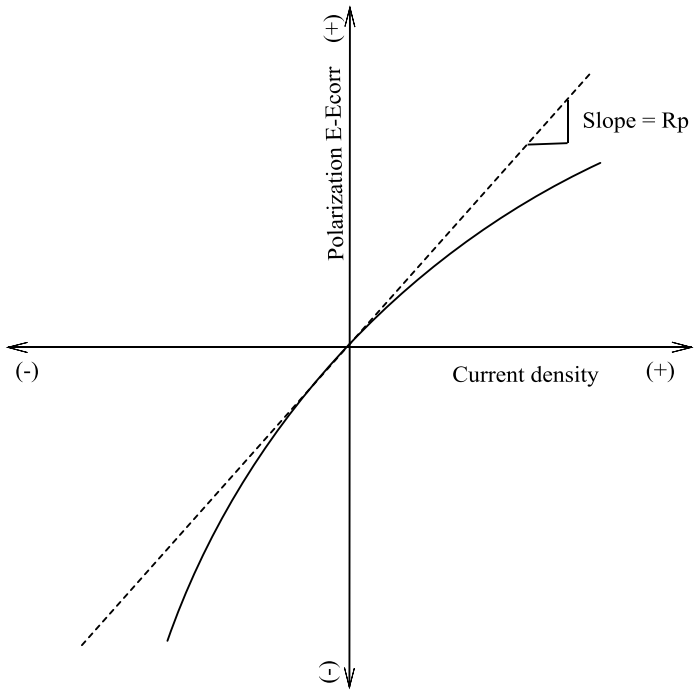

Figure 4.4: Hypothetical linear polarization resistance plot.[253]

The ratio (ΔE/Δi) which forms the basis of the linear polarization theory, is the ratio of the applied potential to the produced current density. This ratio is known as the polarization resistance (*R*p, unit ohm) at a free corrosion potential (open circuit potential). According to the Stern–Geary equation, the curve defines the slope polarization resistance *R*p as follows:[254]

$$i_{\text{corr}} = \frac{B}{R\text{p}} \qquad 4.11$$

where, i_{corr} is corrosion current density in A/cm^2, B is the Stern-Geary coefficient or empirical polarization resistance constant in *V*, *R*p is polarization resistance of the corroding electrode in ohm.cm^2.

The constant *B* value can be determined by the following equation:

$$B = \frac{b_a b_c}{2.303\,(b_a + b_c)} \qquad 4.12$$

where b_a and b_c are the anodic and cathodic Tafel constants.

The corrosion rate can be calculated by the following equation:

$$CR = K_1\, i_{\text{corr}} \frac{EW}{\rho} \qquad 4.13$$

where, CR is the corrosion rate in mm/y, K_1 is a constant with the value of 3.27 x 10^{-3} in mm.g/μA.cm, and i_{corr} is current density in μA/cm^2, ρ is steel density in g/cm^3, and EW is the equivalent weight of carbon steel.[253]

4.4.2 Potentiodynamic polarization (Tafel extrapolation)

Potentiodynamic polarization is a commonly used technique applied to measure corrosion current i_{corr} and to calculate corrosion rate of metals. This technique is based on the relationship between the logarithm of the current density and the applied over potential. The relationship can be linear at large potential scale.[255] An example of potentiodynamic measurement is presented in Figure 4.5. This plot is known as Tafel plot.[256]

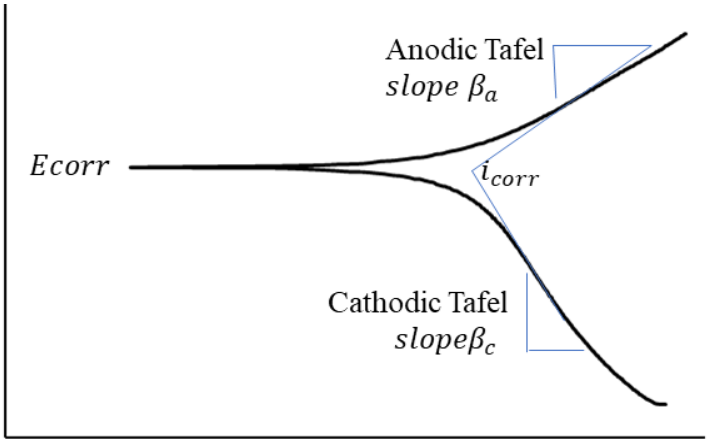

Figure 4.5: Typical potentiodynamic polarization scan.[256]

The electrochemical polarization can be mathematically expressed as follows:[256]

$$i = i_{corr}\left[\left(\exp\left\{\frac{2.303\ (E-E_{corr})}{\beta_a}\right\} - \exp\left\{-\frac{2.303\ (E-E_{corr})}{\beta_c}\right\}\right]\right] \qquad 4.14$$

where, i is the current in μA/cm^2, i_{corr} is the corrosion current in μA/cm^2, E_{corr} is the corrosion potential in mV, β_a is the anodic Tafel slope constant in V/decade, β_c is the cathodic Tafel slope constant in V/decade. The value of (E – E_{corr}) is named overpotential and is symbolized by η. So, the rearranged equation 4.14 becomes:

$$\eta_a = \beta_a \log\frac{i}{i_{corr}} \qquad 4.15$$

$$\eta_c = \beta_c \log\frac{i}{i_{corr}} \qquad 4.16$$

where, η_a and η_c is sufficiently larger values of η in the anodic or cathodic direction respectively.[256] The Stern-Geary constant (B) is calculated from the Tafel slope constants (β_a , β_c). The corrosion current density (i_{corr}) is determined from the Stern-Geary constant (B) and the polarization resistance [105].[253]

The inhibition efficiency (IE %) can be calculated from the i_{corr} values obtained from potentiodynamic measurements using the following equation:

$$\text{IE } \% = \left(\frac{i_{\text{corr(brine)}} - i_{\text{corr(inhibitor)}}}{i_{\text{corr(brine)}}}\right) \qquad 4.17$$

where $i_{corr(brine)}$ is the corrosion current density in μA/cm^2 from the non-inhibited test solution, $i_{corr(inhibitor)}$ is the corrosion current density in μA/cm^2 from the inhibited test solution.

4.4.3 Electrochemical impedance spectroscopy (EIS)

Electrochemical Impedance Spectroscopy (EIS) was applied to evaluate the corrosion inhibition efficiency of the corrosion inhibitors. It is an alternating current (AC) electrochemical technique that has been used to evaluate corrosion rates. It has been used to investigate the mechanisms of electrochemical reactions, to measure the dielectric and transport properties of materials, to explore the properties of porous electrodes, and to investigate passive surfaces.[257]

The impedance result can be presented in a graphical format as Nyquist, Bode phase or Bode magnitude plots (Fig. 4.6), which are typically used to report the electrochemical impedance data. In this thesis will report the electrochemical impedance data in the form of Nyquist plot. The Nyquist plots display the impedance in the form of semicircle with an in-phase (real $Z_{(t)}$) in positive values at x-axis and out-of-phase (imaginary j $Z_{(t)}$) in negative values at y-axis. Bode plots report the corresponding phase angle and impedance magnitude vs. the frequency of the applied signal as is shown in Figs.4.4a-b.[255-256]

The inhibition efficiency (IE%) can be calculated from the EIS data using the following equation:

$$\text{IE\%} = \left(\frac{R_{\text{ct(inhibitor)}} - R_{\text{ct(brine)}}}{R_{\text{ct(inhibitor)}}}\right) \qquad 4.18$$

where $R_{\text{ct(brine)}}$ is the charge transfer resistance in Ω cm^2 from the non-inhibited test solution, $R_{\text{ct(inhibitor)}}$ is the charge transfer resistance in Ω cm^2 from the inhibited test solution.

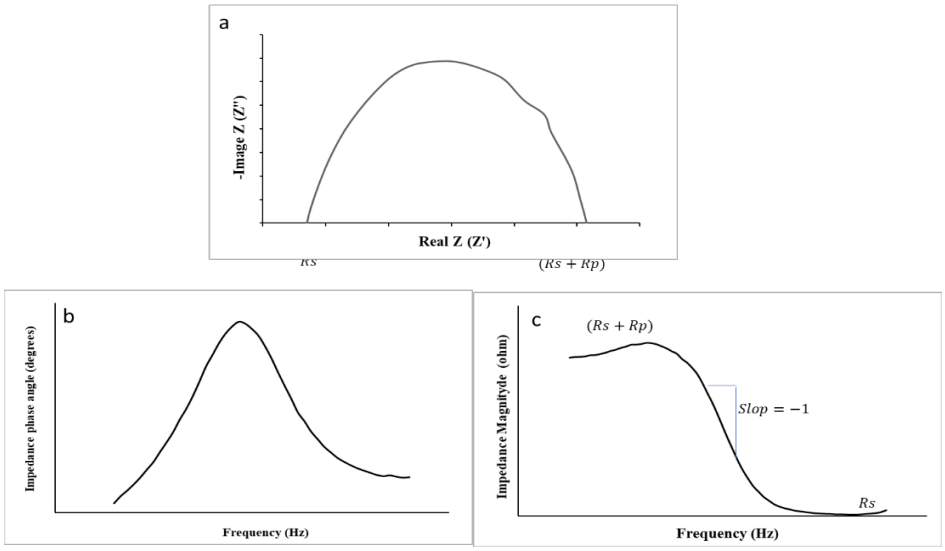

Figure 4.6:The three graphical formats commonly used to report electrochemical impedance spectroscopy data; (a) Nyquist plot, (b) Bode phase plot, (c) Bode magnitude plot.[255]

To evaluate the rate of the corrosion an electronic equivalent circuit model needs to be used. The equivalent circuit consists of resistors including charge transfer resistance (R_{ct}) and solution resistance (R_{s}), capacitors (a constant phase element).[258] The values of these parameters are calculated from the fitting data. Figure 4.7 shows the two types of the electrical equivalent circuit that are used to analyse the impedance data in this work.

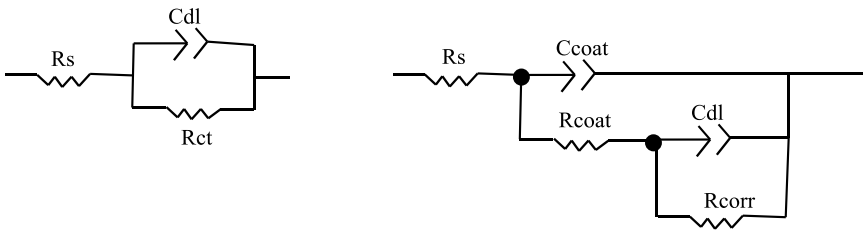

Figure 4. 7: The electrical equivalent circuits used to fit the impedance spectra.

Figure 4.7a shows the first type of the equivalent circuit and it is named a Randles circuit model. This model is composed of the solution resistance (*R*s), the charge transfer resistance (*R*ct), and the pure double layer capacitance (C_{dl}). The impedance of the CPE (Z_{CPE}) is defined as:

$$Z_{CPE} = [Y(j\omega)^n]^{-1} \qquad 4.19$$

where, *Y* is the CPE constant proportional to the C_{dl} of the system, *j* is the imaginary number ($j^2 = -1$), ω is the angular frequency and n is the coefficient which reflects the extent of phase shift.[259]

The double layer capacitor (C_{dl}) is calculated as follows:

$$C_{dl} = Y_0 (2\pi f_{max})^{n-1} \qquad 4.20$$

where, f_{max} is the frequency at which the imaginary component of the impedance is maximal.[260]

Figure 4.7b shows the second type of the equivalent circuit used in this thesis. This model is composed of the solution resistance (R_s), the charge transfer resistance (R_{coat}), the capacitance of double electric layer (C_{coat}), the pure double layer capacitor (C_{dl}), and the capacitance of adsorbed layer (R_{corr}).[261]

In this thesis, the resistance value (*R*) is extracted after the impedance data is fitted with the equivalent circuit model. When the first type is used (Figure 4.7a), the R value is referring to the charge transfer resistance value (R_{ct}), while when the second type model is used (Figure 4.7b), the resistance value (*R*) is equal to summation of the values of R_{coat} and R_{corr}.

4.5 Experimental

4.5.1 Materials

The test material is a 1030 carbon steel with the following composition (wt.%): C (0.30%), Si (0.25%), Mn (0.75%), P (0.04%), S (0.04%) and Fe balance. The sample was gradually wet polished with silicon carbide abrasive paper up to 600 grit, cleaned with ethanol and rinsed with DI water (18.2 MΩ cm), then dried with high-purity (99.9%) nitrogen gas.

A standard brine was used as the test solution to which corrosion inhibitors were added in specific tests. The standard brine was prepared by dilution of 3 wt.% sodium chloride (NaCl; Ajax Finechem, analytical reagent, 99.9%) and 0.01 wt.% sodium bicarbonate ($NaHCO_3$; Merck, 99.5%) in ultra-pure water (Milli-Q system) with a resistivity of 18.2 MΩ cm.

Table 4.1 shows chemical data of the organic synthetic compounds that were used in this study and they are the crown conformation. These compounds are tetramethoxy resorcinarene derivatives with different aliphatic chains, compounds **10** and **20** are used as mixture of diastereoisomers. These organic compounds contain heteroatoms such as N and O in their molecules, which can adsorb on the metal surface. These organic compounds have both polar functional groups (methoxy with amino acid) and a non-polar group (alkyl chain). The effectiveness of these molecules can be ascribed to the presence of the polar groups, which are the reaction centres for the adsorption process, and the length of the aliphatic chain that can affect the corrosion inhibitor performance.

Table 4.1: Chemicals Data.

Compound group	Compound code	Chemical structure	Molecular weight (g /mol)	Concentration	
				Molar (M)	Part per million (ppm)
I	10	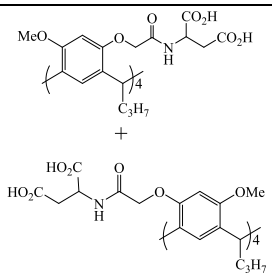	1406	3.5×10^{-3}	5
				5.6×10^{-2}	80
	20	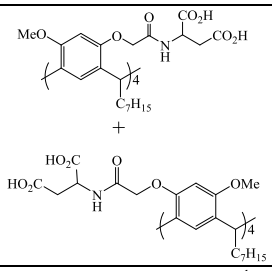	1630	3.0×10^{-3}	5
				4.9×10^{-2}	80
II	15 a	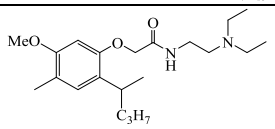	1340	3.7×10^{-3}	5
				5.9×10^{-2}	80
	15 b	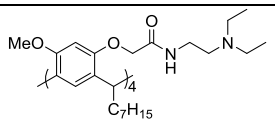	1564	3.1×10^{-3}	5
				5.1×10^{-2}	80
III	18	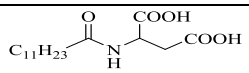	315.5	0.25	80
	19	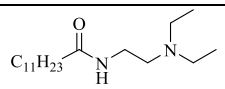	299	0.26	80

4.5.2 Electrochemical measurements

The electrochemical measurements were performed using a three-electrode test setup. The working electrode (WE) was the 1030 carbon steel cylindrical electrode that was rotated at 1000 rpm during the test. Hastelloy C was used as counter electrode (CE) and a double junction silver-silver chloride electrode was used as reference electrode (RE). The glass cell (1L) was filled with standard brine test solution (700 mL) and the test solution was sparged with high-purity CO_2 gas (99.99%) to remove oxygen and saturate the solution with CO_2. The CO_2 sparging was started at least two hours prior to the immersion of the WE into the test solution and continued for the duration of the experiment. The sample was immersed in the

test solution and the open circuit potential (OCP) was recorded for 1 h followed by the other electrochemical measurements. Linear polarization resistance (LPR) was conducted at a potential range of ± 10 mV vs OCP. Electrochemical impedance spectroscopy (EIS) measurements were performed within the frequency range from 10 kHz to 0.01 Hz. The Nyquist representations of the impedance data were analysed with Z-View software (Scribner Associates). The polarization resistance [105] was obtained from fitting the Nyquist plot using the software. Finally, potentiodynamic polarization measurements (PD) were conducted over the potential range from -0.250 V to +0.250 V vs. OCP at scan rate of 0.1667 mV/s. All the electrochemical measurements have been conducted by potentiostat that controlled by EC-Lab software. All tests were performed at 30°C. The LPR and EIS data were recorded every hour for 24 hours followed by potentiodynamic polarization measurement. Each electrochemical experiment was repeated at least two times to ensure that reproducible results were obtained. Figure 4.8 shows examples of the software fitting for the three types of the electrochemical measurements (LPR, EIS, and PD) that were used to determine the corrosion rates and efficiency of the corrosion inhibitors.

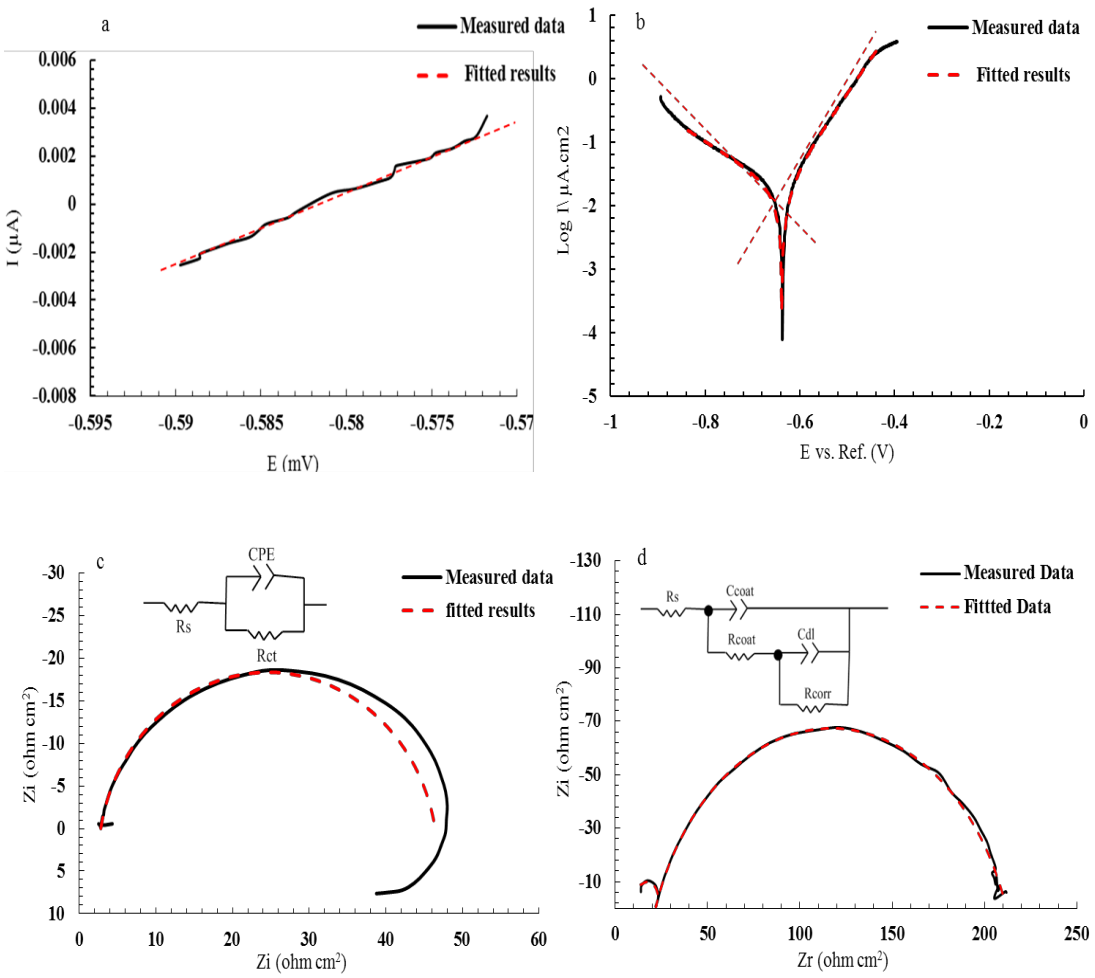

Figure 4.8: The fitting for analysing the results of: (a) LPR, (b) PD, (c) EIS data and the fitted data with the equivalent circuit model a (Figure 4.7a), and (d) EIS data and fitted data with the equivalent circuit model b (Figure 4.7b).

4.6 Results and discussion

Chemical compounds that have been studied as corrosion inhibitors in this thesis are presented in Table 4.1. In this section, the inhibition performance of these resorcinarenes derivatives (see Table 4.1) to mitigate corrosion of carbon steel in CO_2-saturated brine has been investigated. The compounds were tested at concentrations of 5 and 80 ppm at 30°C. The target was to compare the effectiveness of the different alkyl resorcinarenes under corrosive conditions simulating oil and gas corrosion system.

4.6.1 Comparison between L-aspartic acid tetramethoxy resorcinarenes derivatives

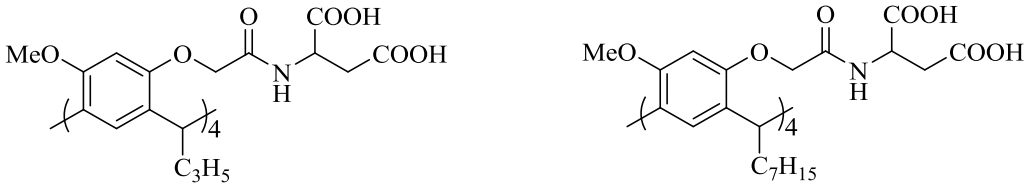

10 **20**

Figure 4.9: Compound **10** is the diasteromeric mixture of the propyl-L-aspartic acid resorcinarene derivatives. Compound **20** is the diasteromeric mixture of the heptyl-L-aspartic acid resorcinarene derivatives.

The first group of compounds the *L*-aspartic acid derivative of alkyl tetramethoxy resorcinarenes, were synthesised for a preliminary investigation of their effectiveness in the corrosion inhibition process related to the length of the aliphatic chains in their structures. The electrochemical methods described earlier in this chapter, namely LPR, EIS and PD were applied and the two compounds were used at two concentrations.

4.6.1.1 Corrosion inhibitor evaluation at concentration of 5 ppm

Figure 4.10 shows corrosion rates obtained from LPR measurements of carbon steels exposed to tetramethoxy resorcinarenes derivatives at 5 ppm at 30°C during 24 h. The corrosion rates from the inhibited steels are compared to corrosion rates from the brine solution (non-inhibited), under the same experimental conditions. The results show that the corrosion rate of the blank solution increases to 3.11 mm y^{-1} at 24 h. In the presence of compound **10**, the corrosion rate decreased to 0.92 mm y^{-1} after 24 h. In the presence of compound **20**, the corrosion rate dropped to 0.76 mm y^{-1} at the time of 24 h immersion. This suggested that both the tetramethoxy resorcinarenes derivatives can reduce the corrosion rate and that the efficiency of compound **20** to inhibit corrosion is higher than of compound **10**. The observed corrosion mitigation is likely due to formation of a surface inhibitor film which covered the steel surface.[262-263]

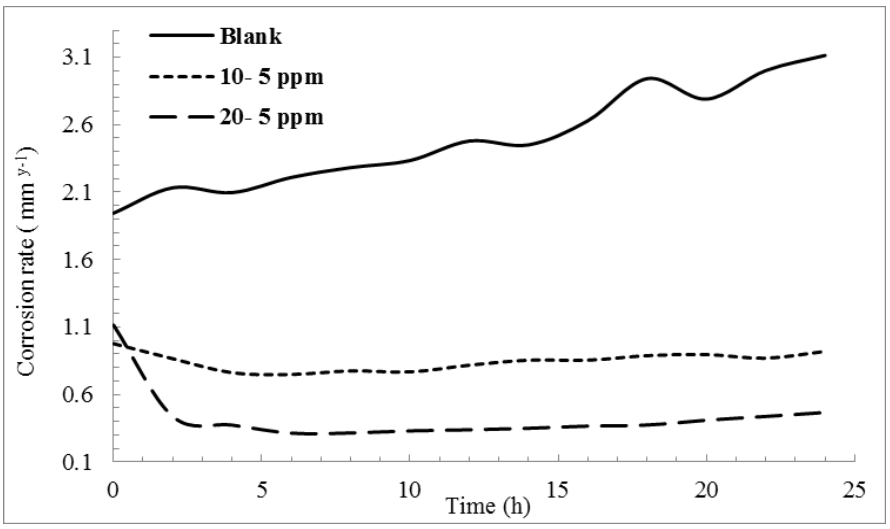

Figure 4.10: Corrosion rates derived from linear polarization resistance (LPR) measurements for 24 h, at steels surface without and with 5 ppm of the L-aspartic acid tetramethoxy resorcinarenes derivatives in CO**2** - saturated brine solution at 30°C.

Figure 4.11 illustrates the Nyquist plots from electrochemical impedance spectroscopy (EIS) from mild steel in CO_2 saturated brine without and with 5 ppm of the *L*-aspartic acid tetramethoxy resorcinarenes derivatives after 24 h. Each EIS spectrum shows two loops, a small capacitive loop at high frequency region followed by a larger capacitive loop at low frequency region which could be attributed to the double layer capacitance and the charge transfer resistance at the corroding surface in the corrosion process.[264] The EIS measurements were fitted to equivalent circuits presented in Figure 4.7. The derived EIS parameters are shown in table 4.2. The impedance data were fitted with the equivalent circuit model a (Figure 4.7a) when analysing the non-inhibited solution data, and with the equivalent circuit model b (Figure 4.7b) when analysing the data from inhibited solution. The table 4.2 contains the following elements: (R_s) is the solution resistance, (R) is the resistance, (i_{corr}) is the corrosion current density calculated by eq.4.11, (CR) is the corrosion rate calculated by eq.4.13, and (IE) is the inhibition efficiency calculated by eq.4.18. It is observed from Table 4.2 that adding an inhibitor (**10** or **20**) into solution increases the resistance (R) and solution resistance (R_s) values resulting in decrease of corrosion rates compared to the blank solution. The EIS data are in good agreement with the relevant LPR measurements. In the presence of the inhibitor (**10** or **20**), the corrosion rate has dropped from 2.46 mm y^{-1} of the non-inhibited solution to 1.02 or

0.06 mm y^{-1} for the inhibited solution that contains the compounds **10** and **20,** respectively. These data are in agreement with those obtained from the LPR results where the corrosion rate had decreased from 3.11 mm y^{-1} of the non-inhibited solution to 0.92 or 0.76 mm y^{-1} of the inhibited solution containing the compounds **10** and **20** respectively.

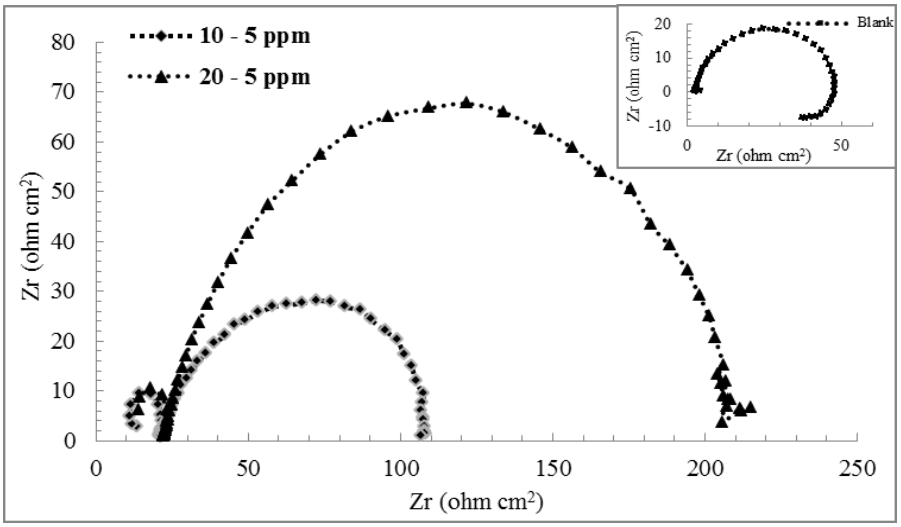

Figure 4.11: Nyquist plots for mild steel in CO_2 saturated brine solution at 30°C with 5 ppm of tetramethoxy resorcinarenes **10** and **20** after 24 h.

Table 4.1: EIS parameters obtained from Nyquist plot fitting with equivalent circuits after 24 h.

Test solution	**C ppm**	R_S **Ωcm²**	R **Ωcm²**	$i_{corr.}$ μ**Acm^{-2}**	CR **mm.y^{-1}**	**Err %**	**IE %**
Blank	-	2.74	44.61	2.12×10^{-4}	2.46	1.48	-
10	5	12.06	100.19	8.84×10^{-5}	1.02	0.23	55.47
20	5	12.49	199.35	5.59×10^{-6}	0.06	2.03	77.62

Figure 4.12 shows the potentiodynamic polarisation curves of carbon steel in brine solution containing CO_2 at 30°C without or with 5 ppm of two different tetramethoxy resorcinarenes derivatives (**10** and **20**). Electrochemical parameters such as corrosion potential (E_{corr}), corrosion current density (i_{corr}), Tafel slope constants (β_a , β_c), corrosion rate (CR), and inhibition efficiency (IE) were calculated and are listed in Table 4.3. It can be seen that the addition of inhibitors reduces the corrosion potential E_{corr} which was shifted towards more positive values in respect to the brine solution, indicating that the inhibition of corrosion of carbon steel was under anodic

control. Also, the value of i_{corr} was reduced when the compound **10** or **20** was added into the solution compared to the blank solution, meaning that the steel was inhibited by these resorcinarenes compounds. From the inhibition efficiency data, it is apparent that the compound **20** is more effected than the compound **10**. This trend is consistent with the results obtained by the LPR and EIS methods.

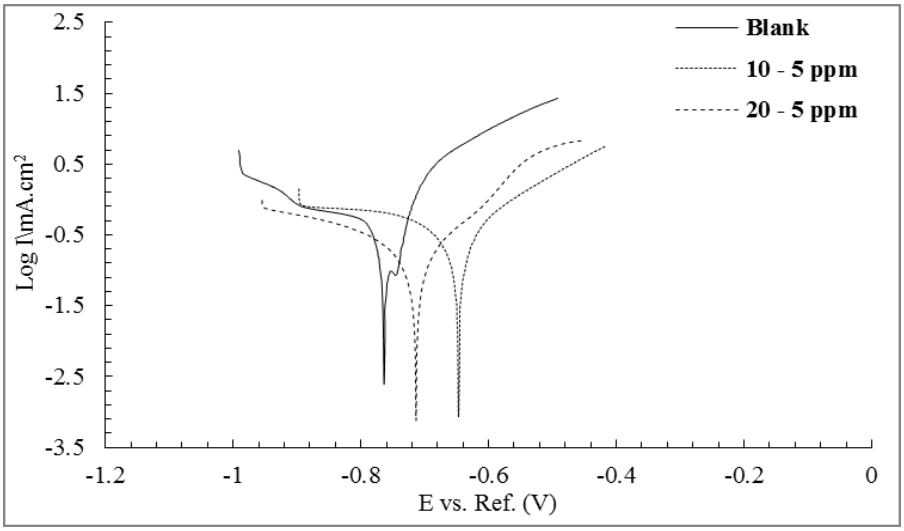

Figure 4.12: Potentiodynamic polarisation curves measured for mild steel in CO_2 saturated without and with 5 ppm of L-aspartic acid tetramethoxy resorcinarenes **10** and **20** at 30°C after 24 h.

Table 4.2: Electrochemical parameters and inhibition efficiency obtained from potentiodynamic polarization measurements at steel surface in brine with and without corrosion inhibitors.

Test Solution	**C Ppm**	**$-E_{corr.}$ mV**	**$i_{corr.}$ μAcm^{-2}**	**β_a V decade^{-1}**	**β_b V decade^{-1}**	***CR*** **mm y^{-1}**	**Err %**	**IE %**
Blank	-	837.13	5.07	185.5	220.8	2.14	0.23	-
10	5	658.32	3.30	193.6	332.7	1.31	0.01	34.91
20	5	708.96	1.38	128.7	233.8	0.55	0.01	72.62

4.6.1.2 Corrosion inhibitor evaluation at concentration of 80 ppm

The *L*-aspartic acid tetramethoxy resorcinarenes derivatives have been evaluated as corrosion inhibitors at concentrations of 80 ppm by LPR method compared to the blank solution (Figure 4.10). The results of the LPR measurements of compounds **10** and **20** at 80 ppm are shown in Figure 4.13. The corrosion rate decreased to 0.08 mm y^{-1} in the presence of the inhibitor **10** and to 1.29 mm y^{-1} in the presence of inhibitor

20 at 24 h. This decrease in corrosion rates can be attributed to the inhibitor molecules forming a film on the steel surface and have affected the corrosion process.[263] It can be seen that both compounds inhibited the corrosion process and that compound **10** is more protective to the steel than compound **20** at 80 ppm.

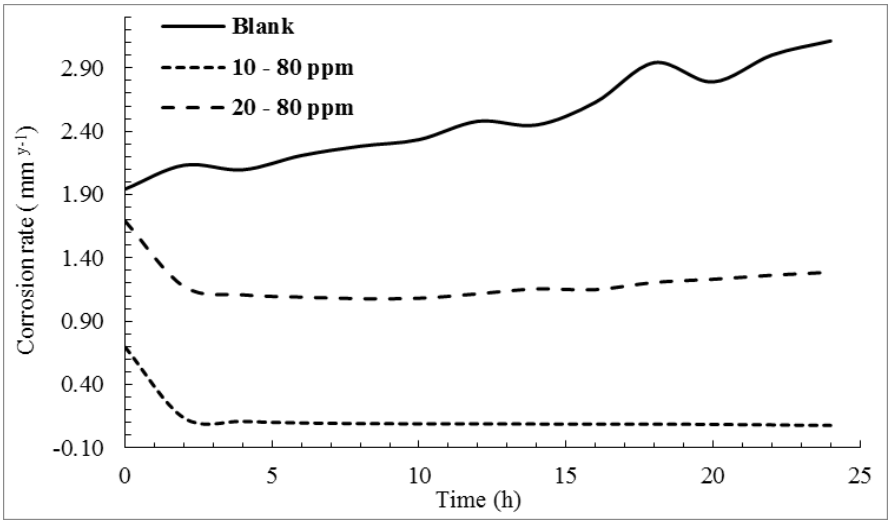

Figure 4.13: Corrosion rates derived from linear polarization resistance (LPR) measurements for 24 h, at the steel surface without and with 80 ppm of the L-aspartic acid tetramethoxy resorcinarene derivatives in CO_2-saturated brine solution at 30°C.

Figure 4.14 shows the EIS spectra for these tetramethoxy resorcinarenes compared to the blank solution. The EIS data show increase in resistivity after adding inhibitors in the test solution compared to the blank solution. The calculated parameters which resulted from fitting the EIS data to Randle's circuit, for both measurements from the non-inhibited and inhibited solutions. The measured parameters are shown in Table 4.4. The results show that adding the inhibitor into the solution causes a significant increase in R to 111.4 Ωcm^2 in the presence of (**10**) and increase to 62.21 Ωcm^2 in the presence of (**20**). Also, the i_{corr} value decreases to 7.45 $x10^{-5}$ μAcm^{-2} in the presence of compound **10** and to 1.38 $x10^{-4}$ μAcm^{-2} in the presence compound **20** at 24 h. This indicates that these inhibitors can retard the corrosion process in the corrosive system with compound **10** being the more effective corrosion inhibitor compared to compound **20** at the studied concentrations. Results obtained from the EIS measurements are in good agreement with those obtained from the LPR measurements.

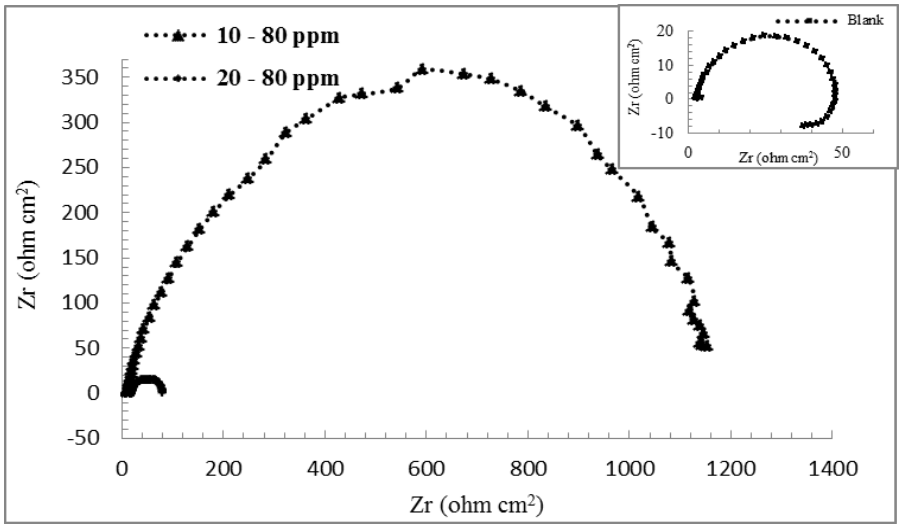

Figure 4.14: Nyquist plots for mild steel in CO_2 saturated brine solution at 30°C with 80 ppm of tetramethoxy resorcinarenes **10** and **20** after 24 h.

Table 4.3: EIS parameters obtained from Nyquist plot fitting with equivalent circuit after 24 h.

Test solution	**C ppm**	R_S **Ωcm²**	R **Ωcm²**	$i_{corr.}$ **μAcm⁻²**	CR **mm.y⁻¹**	**Err %**	**IE %**
Blank	-	2.74	44.61	2.12×10^{-4}	2.46	1.48	-
10	80	20.11	111.4	7.45×10^{-5}	0.86	1.75	59.95
20	80	18.73	62.21	1.38×10^{-4}	1.61	1.05	28.29

The potentiodynamic polarization curves from carbon steel in brine solution containing CO_2 at 30°C without or with the *L*-aspartic acid resorcinarenes derivatives at 80 ppm and after 24 h are presented in Figure 4.15. Table 4.5 summaries the electrochemical parameters derived from the potentiodynamic measurements. The results show increase in E_{corr} values towards positive values in the presence of the corrosion inhibitors **10** and **20** compared to the blank solution. Also, the values of i_{corr} decrease in the presence of compound **10** to 1.73 μAcm^{-2} and to 4.55 μAcm^{-2} in the presence of compound **20** in respect of the non-inhibited solution. This suggests that compound **10** has a more significant effect on the corrosion process due to the high decrease in i_{corr} value compared to compound **20**. This trend is similar to those obtained from LPR and EIS measurements.

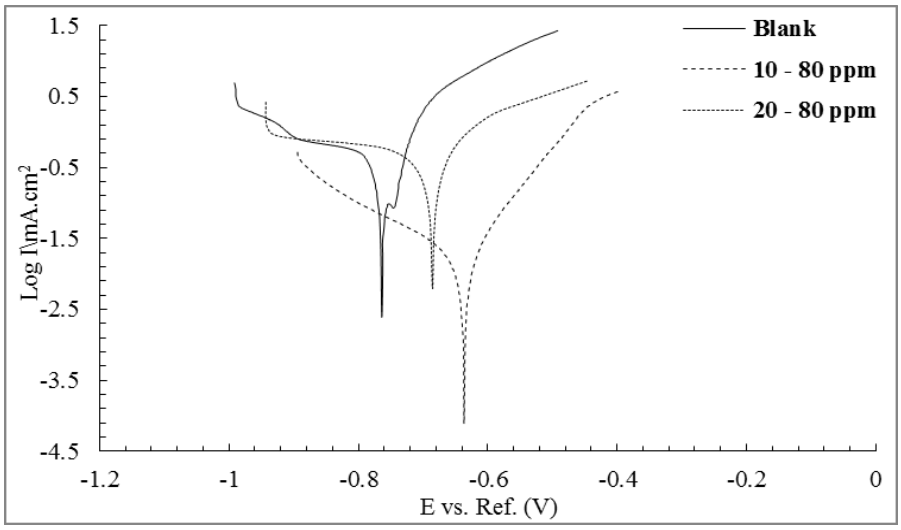

Figure 4.15: Potentiodynamic polarisation curves measured for mild steel in CO_2 saturated without and with 80 ppm of L-aspartic acid tetramethoxy resorcinarenes **10** and **20** at 30°C after 24 h.

Table 4.4**:** Electrochemical parameters and inhibition efficiency obtained from potentiodynamic polarization measurements at steel surface in brine with and without corrosion inhibitors.

Test Solution	**C** **ppm**	**$-E_{corr.}$** **mV**	**$i_{corr.}$** **μAcm^{-2}**	**β_a** **V decade^{-1}**	**β_b** **V decade^{-1}**	***CR*** **mm y^{-1}**	**Err** **%**	**IE** **%**
Blank	-	837.13	5.07	185.5	220.8	2.14	0.23	-
10	80	638.36	1.73	138.2	223.5	0.45	0.17	65.87
20	80	686.51	4.55	161.2	664.3	1.75	0.26	10.25

4.6.2 Comparison between diethyl diamine tetramethoxy resorcinarenes derivatives

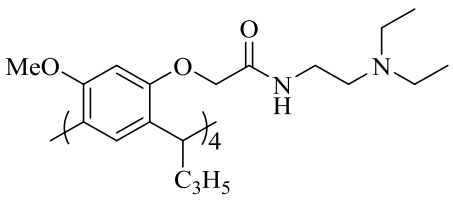

15 a

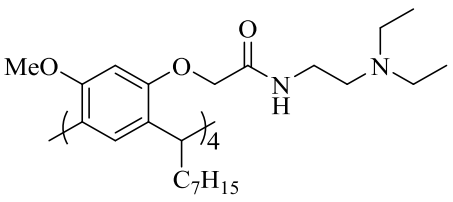

15 b

Figure 4.16**:** Chemical structures of propyl (**15a**) and heptyl (**15b**) diethyl diamine tetramethoxy resorcinarenes derivatives**.**

This second group of compounds studied as corrosion inhibitors is similar to that studied in the previous section (compounds **10** and **20**) except that the aspartic acid

has been replaced with an *N*, *N*-diethylethyleneamine group. The capacity of these compounds, **15a** and **15b**, to act as corrosion inhibitors has been studied and the results are discussed below.

4.6.2.1 Corrosion inhibitor evaluation at concentration of 5 ppm

Figure 4.17 shows corrosion rates of carbon steel in brine saturated solution without and with 5 ppm of the diethyl diamine resorcinarenes derivatives (**15a**) or (**15b**) at 30°C obtained from LPR measurements. The corrosion rate values in the presence of compound **15a** or **15b** were lower than those measured in the blank solution over 24 h. After the addition of 5 ppm of **15a,** the corrosion rate dropped and remained relatively constant over the 24 h period with an average rate of approximately 1.1 mm y^{-1}. The presence of inhibitor **15b** decreased the corrosion rate to 2.23 mm y^{-1} after 24 h and the results show that compound **15a** is a more effective corrosion inhibitor compared to compound **15b**. However, the overall decrease in corrosion rates in the presence of these compounds is not significant, compared to the brine solution, and the corrosion rates remain high.

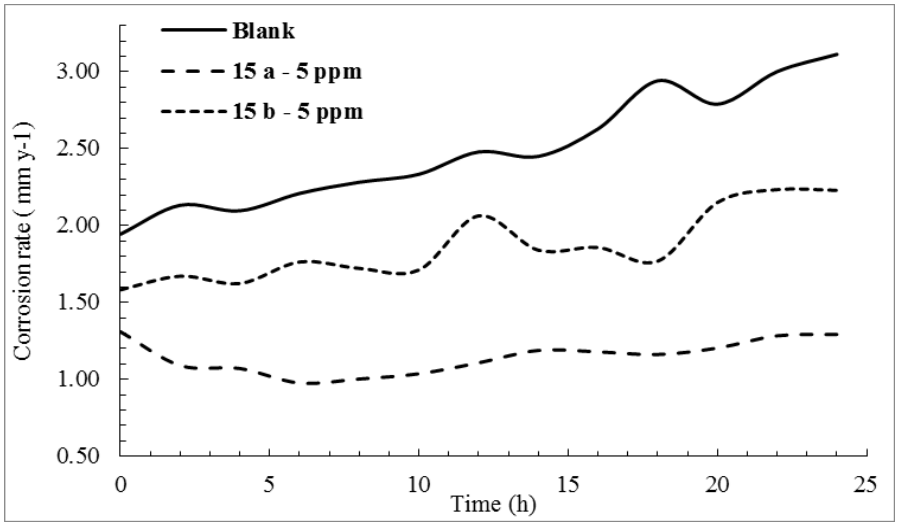

Figure 4.17: Corrosion rates derived from linear polarization resistance (LPR) measurements for 24 h, at the steel surface without and with 5 ppm of diethyl diamine tetramethoxy resorcinarene derivatives in CO_2-saturated brine solution at 30°C.

Figure 4.18 presents the Nyquist plots recorded in the presence of compounds **15a** and **15b** in the test solutions, and in brine solution. Table 4.6 summarizes the EIS parameters that resulted from the fitting with the equivalent circuit

model a (Figure 4.7a) for analysing the non-inhibited solution data and the equivalent circuit model b (Figure 4.7b) for analysing the inhibited solution data. The increase in R and the decrease in i_{corr} when compounds **15 a** and **15 b** were added showed that both inhibitors **15a** and **15b** can affect the corrosion process, with compound **15a** being more effective. This trend is in agreement with that obtained from LPR measurements.

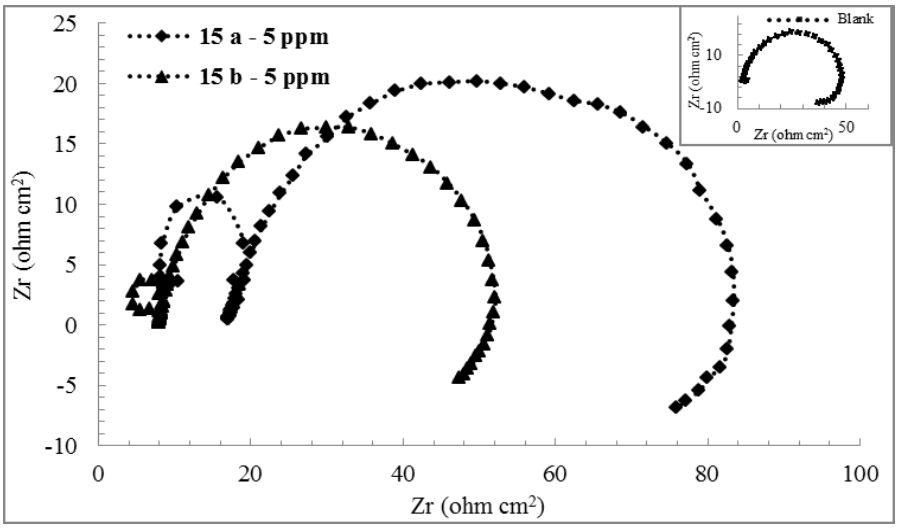

Figure 4.18: Nyquist plots for mild steel in CO_2 saturated brine solution at 30°C with 5 ppm of diethyldiethylenediamine tetramethoxy resorcinarenes 15a and 15b after 24 h.

Table 4.5 Table 4.6: EIS parameters obtained from Nyquist plot fitting with equivalent circuit after 24 h.

Test Solution	**C ppm**	R_S **Ωcm²**	R **Ωcm²**	$i_{corr.}$ **μAcm⁻²**	CR **mm.y⁻¹**	**Err %**	**IE %**
Blank	-	2.74	44.61	2.12×10^{-4}	2.46	1.48	-
15 a	5	8.72	73.24	1.16×10^{-4}	1.35	2.03	39.09
15 b	5	5.17	46.21	1.94×10^{-4}	2.25	1.04	3.46

Figure 4.19 and Table 4.7 introduce the potentiodynamic polarization curves and the electrochemical parameters respectively without and with **15a** or **15b** at 30°C after 24 h. The table shows decrease in both E_{corr} and i_{corr} values in the presence of corrosion inhibitors compared to the blank solution. Accordingly, the corrosion rates decreased in the presence of the inhibitors (**15a, 15b**) showing their inhibiting properties. Results obtained from PD measurements are in good agreement with those obtained from LPR and EIS measurements.

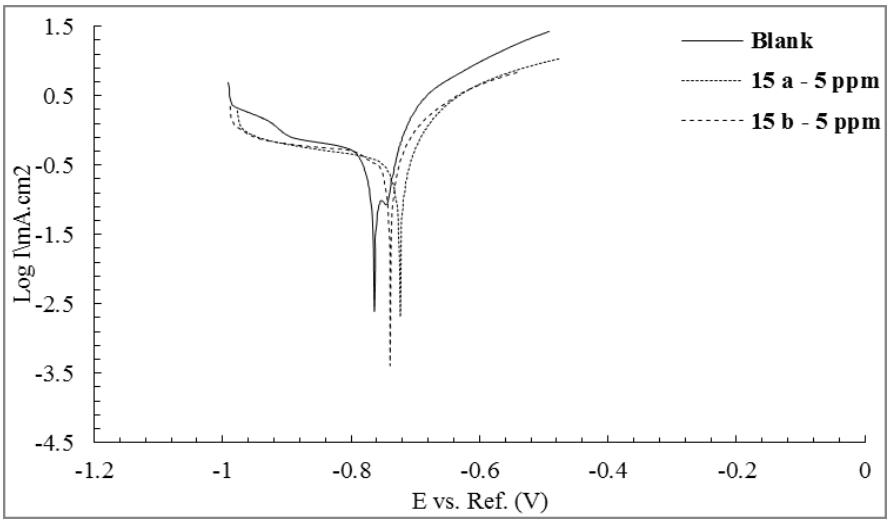

Figure 4.19: Potentiodynamic polarisation curves measured for mild steel in CO_2 saturated without and with 5 ppm of diethyldiethylenediamine tetramethoxyresorcinarenes (**15a**, **15b**) at 30°C after 24 h.

Table 4.6: Electrochemical parameters and inhibition efficiency obtained from potentiodynamic polarization measurements at steel surface in brine with and without corrosion inhibitors.

Test Solution	**C ppm**	**$-E_{corr.}$ mV**	**$i_{corr.}$ μAcm^{-2}**	**β_a V decade^{-1}**	**β_b V decade^{-1}**	***CR*** **mm y^{-1}**	**Err %**	**IE %**
Blank	-	837.13	5.07	185.5	220.8	2.14	0.23	-
15 a	5	729.04	3.54	96.0	673.3	1.35	0.01	30.18
15 b	5	738.61	4.30	106.7	888.7	1.72	0.26	15.19

4.6.2.2 Corrosion inhibitor evaluation at concentration of 80 ppm

The LPR measurements were conducted at carbon steel over 24 h in the presence of 80 ppm of propyl (**15a**) and heptyl diethyl (**15b**) diethylethylenediamine resorcinarene derivatives. The results are shown in Figure 4.20. At 80 ppm, compared to corrosion rate value of the blank solution, the corrosion rate in the presence of compound **15a** decreased to 0.90 mm y^{-1}. The corrosion rate in the presence of compound **15b** decreased to 1.76 mm y^{-1} after 24 h. The corrosion rates were found to decrease with increasing inhibitor concentration, which might be attributed to the increase in the adsorption and surface coverage.[265] It should however be pointed out that the corrosion rates remain high and do not provide adequate corrosion inhibition to the carbon steel.

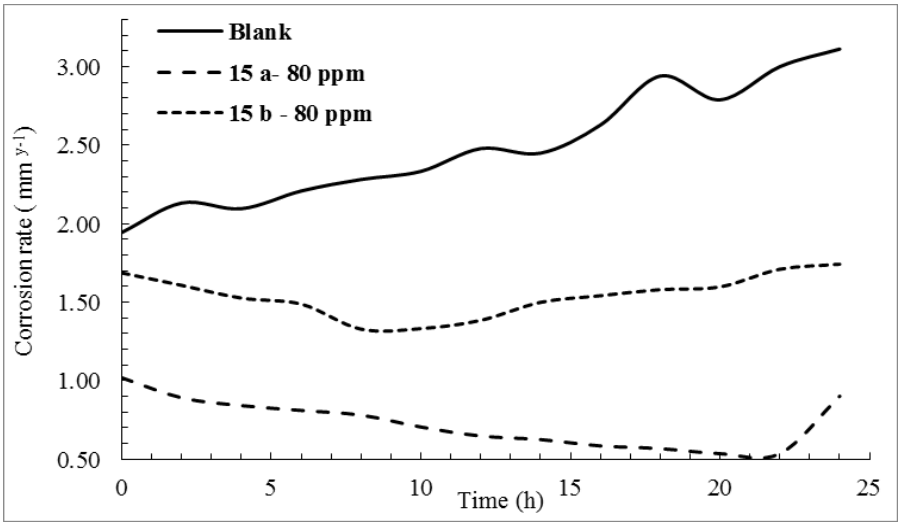

Figure 4.20: Corrosion rates derived from linear polarization resistance (LPR) measurements for 24 h, at the steel surface without and with 80 ppm of diethylethylenediamine tetramethoxyresorcinarene derivatives in CO**2**-saturated brine solution at 30°C.

The Nyquist plots from corrosion measurements with inhibitors **15a** and **15b** are shown in Figure 4.21. Table 4.8 summarises the EIS parameters determined from fitting the impedance data with the equivalent circuit model a (Figure 4.7a) for the non-inhibited solution and equivalent circuit model b (Figure 4.7b) for the inhibited solution. The presence of compound **15a** increased the *R* values and the i_{corr} values, the corrosion rate decreased to 0.51 mm y^{-1}. The presence of **15b** resulted in increased *R* value compared to the blank solution and decreased i_{corr}, the corrosion rate decreased to 1.81 mm y^{-1}. It can be seen that the two inhibitors have only moderately impacted on the corrosion process with the compound **15a** being the more effective one. The trend is in agreement with the results obtained from LPR measurements.

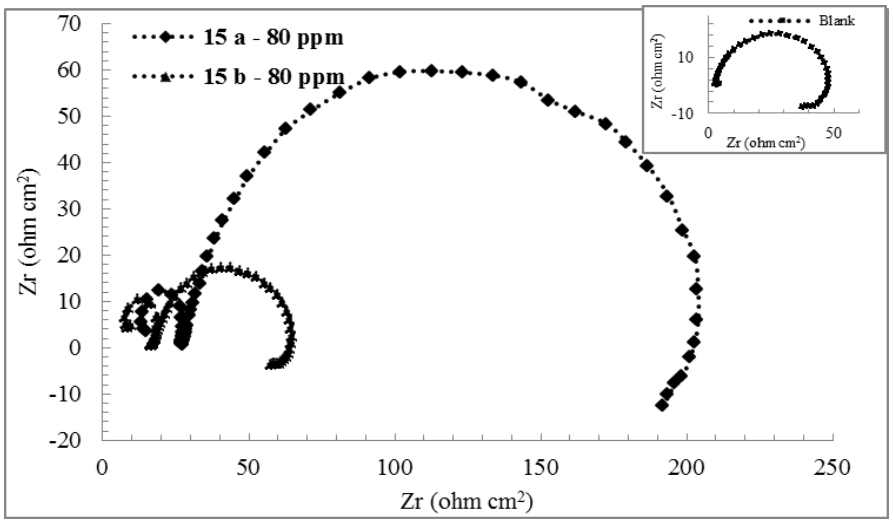

Figure 4.21: Nyquist plots for mild steel in CO**2** saturated brine solution at 30°C with 80 ppm of the diethylethylenediamine tetramethoxyresorcinarene **15a** and **15b** after 24 h.

Table 4.7: EIS parameters obtained from Nyquist plot fitting with equivalent circuit after 24 h.

Test solution	**C ppm**	R_S **Ωcm²**	R **Ωcm²**	$i_{corr.}$ **μAcm⁻²**	CR **mm.y⁻¹**	**Err %**	**IE %**
Blank	-	2.74	44.61	2.12×10^{-4}	2.46	1.48	-
15 a	80	14.29	189.91	4.41×10^{-5}	0.51	0.81	76.51
15 b	80	8.45	55.21	1.56×10^{-4}	1.81	1.57	19.19

The potentiodynamic polarisation measurements were conducted in the absence or presence of compounds (**15a** or **15b**) at 80 ppm in brine solution saturated with CO_2 at 30°C after 24 h (Figure 4.22). Table 4.9 summarises the electrochemical parameters estimated from potentiodynamic measurements. It shows that there is a decrease in i_{corr} and E_{corr} compared to the blank solution, and the associated decrease in corrosion rates. The anodic and cathodic Tafel slopes (β_a and β_c) respectively have been increased compared to the blank solution after adding the inhibitors to solution and the corrosion rate has decreased, meaning that the steel corrosion is affected by these compounds. The corrosion rate value of compound **15a** is less than that of compound **15b** which means that compound **15a** inhibits the corrosion process more effectively. Slightly higher corrosion efficiency is achieved with increasing concentration of the inhibitors (**15a**, **15b**) and compound **15a** is more effective than

compound **15b**. This trend is in good agreement with those obtained from LPR and EIS measurements.

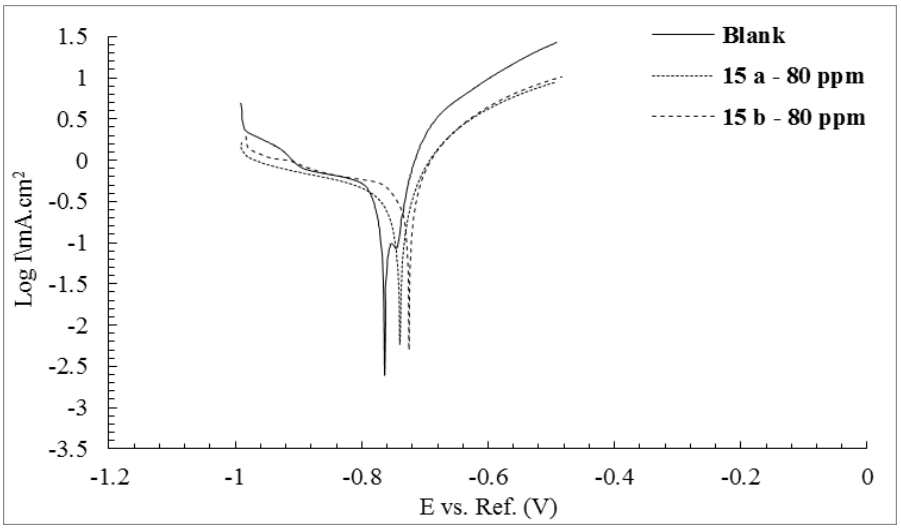

Figure 4.22: Potentiodynamic polarisation curves measured for mild steel in CO_2 saturated without and with 80 ppm different diethyldiethylenediamine tetramethoxy resorcinarenes (**15a**, **15b**) at 30°C.

Table 4.8: Electrochemical parameters and inhibition efficiency obtained from potentiodynamic polarization measurements at steel surface in brine with and without corrosion inhibitors.

Test Solution	**C Ppm**	**$-E_{corr.}$ mV**	**$i_{corr.}$ μAcm^{-2}**	**β_a V decade^{-1}**	**β_b V decade^{-1}**	***CR*** **mm y^{-1}**	**Err %**	**IE %**
Blank	-	837.13	5.07	185.5	220.8	2.14	0.23	-
15 a	80	735.86	1.96	61.6	168.1	0.73	0.01	61.34
15 b	80	765.31	4.58	165.5	466.5	1.76	0.26	9.66

4.6.3 Comparison between the undecyl L-aspartic acid and the undecyl diethyl diamine derivatives

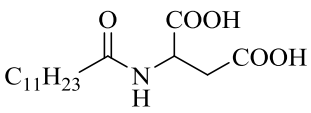

18

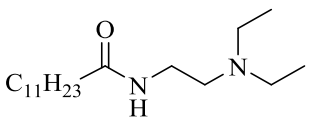

19

Figure 4.23: Chemical structures of two model compounds, the undecyl amide derivatives of L-aspartic acid 18 and of N, N- diethylethylenediamine tetramethoxy **19**.

The third group of compounds used in the corrosion study was synthesised to investigate the effect of the macrocycle present in the previous set of compounds. These are the dodecyl amide derivatives of *L*-aspartic acid or diethylethylenediamine. The efficiency of these compounds (**18** and **19**) to inhibit carbon steel corrosion is discussed below. To compare compounds (**18** and **19**) with those used in the previous sections, the concentration of 80 ppm was selected as it corresponds with the higher corrosion inhibition efficiencies obtained from measurements in the previous section.

4.6.3.1 Corrosion inhibition at concentration of 80 ppm

Figure 4.24 shows the corrosion rates from steel surfaces with and without inhibitors **18** or **19** in CO_2 saturated brine solution at 30°C. The addition of compound **18** to the brine solution decreased the corrosion rate to below 0.01 mm y^{-1} after 24 h. The addition of compound **19** decreased the corrosion rate to 0.10 mm y^{-1} after 24 h compared to non-inhibited solution. This can be attributed to the formation of a film on the steel surface by the inhibitor molecules.[263] A rapid decrease in corrosion rate was observed upon the addition of the inhibitors (**18** or **19**) at the concentration of 80 ppm. This suggests that 1 h and 2 h are sufficient times for significant deposition of the respective compounds **18** and **19** on the steel surface and formation of a protective layer.

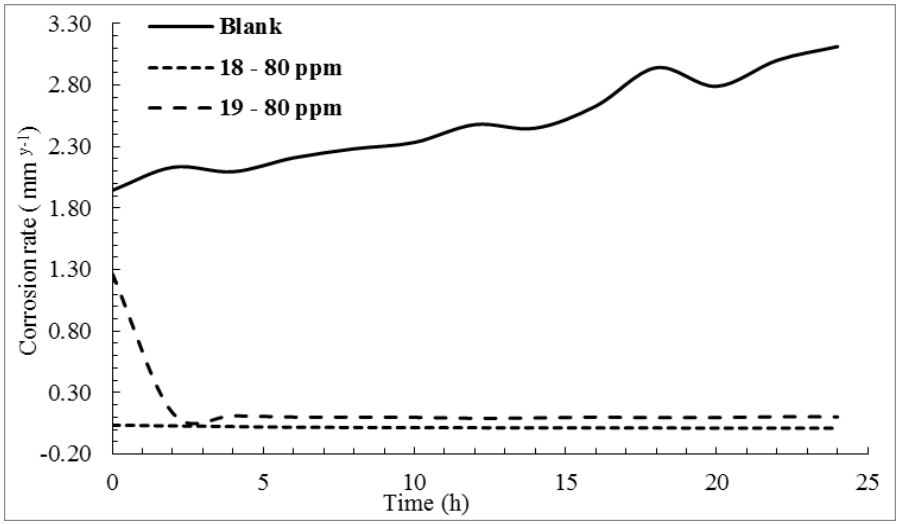

Figure 4.24: Corrosion rates derived from linear polarization resistance (LPR) measurements for 24 h, at steels surface without and with 80 ppm of undecyl L-aspartic acid and undecyl diethylethyleneamine derivatives in CO_2- saturated brine solution at 30 °C.

EIS measurements were recorded without and with 80 ppm of inhibitors **18** or **19** at the steel sample in CO_2 saturated brine solution at 30°C after 24 h. Figure 4.25 shows the Nyquist plots from carbon steel without inhibitor that fits the equivalent circuit model a (Figure 4.7a) and the Nyquist plots from carbon steel with the inhibitors (**18**, **19**) that fit the equivalent circuit model b (Figure 4.7b), the double depressed semicircle equivalent to charge transfer resistance (R_{ct}) has been observed. This indicates that the corrosion processes in the non-inhibited and inhibited solutions are charge transfer controlled. Table 4.10 shows the calculated parameters from the fitted EIS data. It can be seen that the solution resistance (R_s) and (R) increased in the presence of corrosion inhibitors compared to the non-inhibited solution. Consequently, the corrosion current (i_{corr}) decreased dramatically compared to the non-inhibited solution. The results show high efficiency of the corrosion inhibitors (**18**, **19**) at the studied concentration.

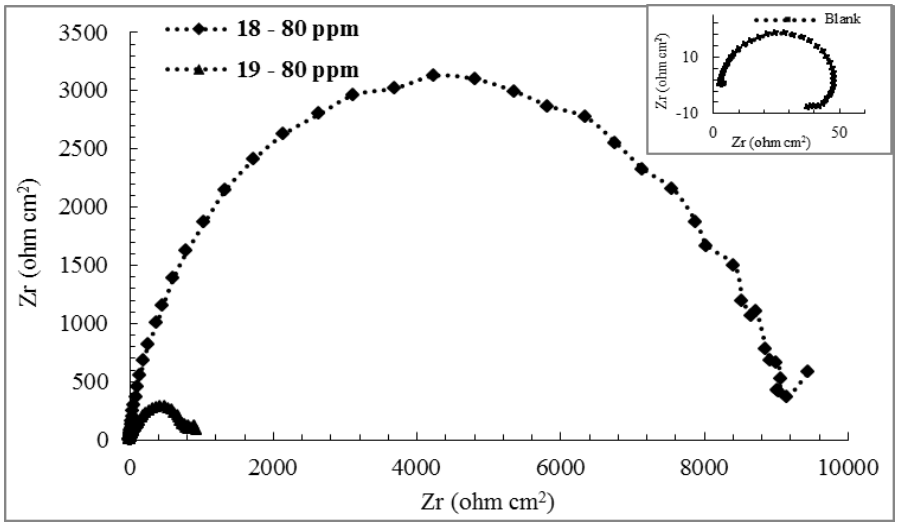

Figure 4.25: Nyquist plots for mild steel in CO_2 saturated brine solution at 30°C without and with 80 ppm of undecyl L-aspartic acid **18** and undecyl diethylethyleneamine **19** after 24 h.

Table 4.9: EIS parameters obtained from Nyquist plot fitting with equivalent circuit after 24 h.

Test Solution	**C Ppm**	**R_S Ωcm^2**	**R Ωcm^2**	**$i_{corr.}$ μAcm^{-2}**	**CR mm.y^{-1}**	**Err %**	**IE %**
Blank	-	2.74	44.61	2.12×10^{-4}	2.46	1.48	-
18	80	9.77	8581.52	8.64×10^{-7}	0.01	1.11	99.48
19	80	1091	189.6	4.53×10^{-5}	0.53	1.45	76.52

The potentiodynamic polarization curves from carbon steel without and with 80 ppm of inhibitors (**18** or **19**) in CO_2-saturated brine solution at 30°C and at 80 ppm after 24 h are shown in Figure 4.26. Table 4.11 shows the values of the associated electrochemical parameters. From the results, it can be concluded that the corrosion potential (E_{corr}) value shifts toward more positive values and the values of current density (i_{corr}) decrease sharply in the presence of the inhibitors (**18** or **19**) in respect to the non-inhibited solution showing that these inhibitors mitigate the corrosion process. The trend is in good agreement with the results obtained from the LPR and EIS measurements.

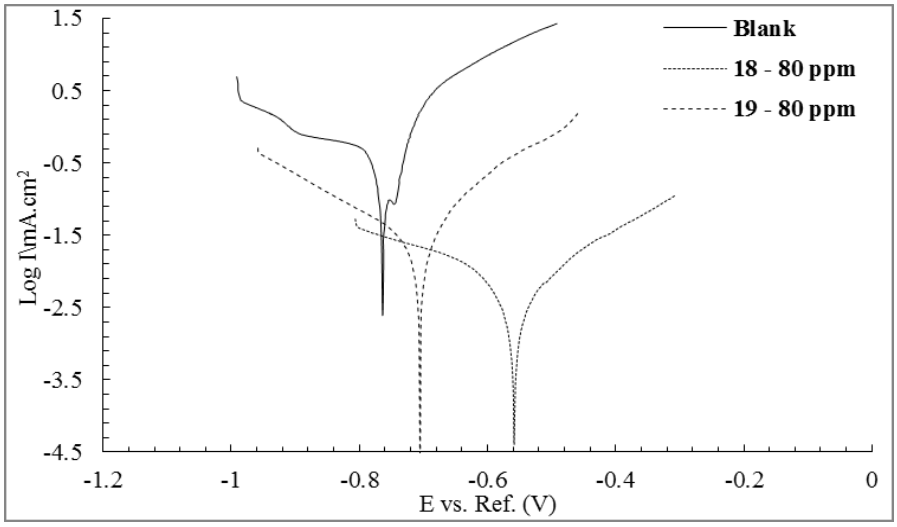

Figure 4. 26: Potentiodynamic polarisation curves measured for mild steel in CO_2 saturated without and with 80 ppm of undecyl L-aspartic acid **18** and undecyl diethylethyleneamine **19** at 30°C.

Table 4.10: Electrochemical parameters and inhibition efficiency obtained from potentiodynamic polarization measurements at steel surface in brine with and without corrosion inhibitors.

Test Solution	**C ppm**	**$-E_{corr.}$ mV**	**$i_{corr.}$ μAcm^{-2}**	**β_a V decade^{-1}**	**β_b V decade^{-1}**	***CR*** **mm y^{-1}**	**Err %**	**IE %**
Blank	-	837.13	5.07	185.5	220.8	2.14	0.23	-
18	80	554.95	0.06	197.3	252.4	0.03	0.01	98.81
19	80	749.51	0.39	191.1	198.3	0.15	0.26	81.65

4.7 Conclusions

The inhibition performance of the studied compounds at steel surface exposed to CO_2 saturated brine solution at concentration of 5 ppm is in sequence **20** > **10** > **15a** > **15b**, and at 80 ppm is in sequence **18** > **19** > **10** > **20** > **15a** > **15b**. The comparison of the three corrosion inhibitor groups of synthesized compounds shows that the resistance offered by group III (dodecyl amide derivatives of *L*-aspartic acid **18** and of *N*, *N*- diethyldiamine tetramethoxy **19**) is significantly higher than that obtained from the other groups. It can be concluded that the synthesized compounds (**18, 19**) provide sufficient corrosion inhibition to carbon steel (CS1030) in CO_2 environment at the tested concentration.

The trends in corrosion rates obtained from the variety of corrosion measurements, namely LPR, EIS and PD, provided good agreement and allowed for evaluation of the synthesized compounds as corrosion inhibitors.

5.0 Summary and future work

In conclusion, this research is concerned with the synthesis of novel tetramethoxy resorcinarenes derivatives and these compounds were investigated for crystal growth modification and corrosion inhibition. Several compounds were successfully synthesized. *L*-aspartic acid and diethylethylenediamine were attached to resorcinarenes by an amide linkage. For the desired compounds first step was synthesis resorcinarene skeleton by reaction of 3-methoxyphenol with an aldehyde (butanal, octanal or dodecanal) in the system DCM/BF_3Et_2O. This resorcinarene was alkylated with ethyl bromoacetate to give the resorcinarene ester derivatives. This ester was hydrolysed by reaction with sodium hydroxide in methanol then acidified with hydrochloric acid to give resorcinarene acid. The acid coupling with the amino acid (dimethyl *L*-aspartate hydrochloride) in presence of triethylamine and *N, N, N′, N′*-Tetramethyl-*O*-(benzotriazol-1-yl) uronium tetrafluoroborate (TBTU) gave the amino acid resorcinarenes derivatives. These amino acid resorcinarenes were isolated by fractional crystallization. The first isomer was pure while the second isomer has trace of the first isomer and the optical rotation was measured of these amides to distinguish between the absolute C_4 dissymmetric resorcinarene enantiomers. However, the propyl amino acid resorcinarenes (**10**) could not separate and were used as a diasteroisomeric mixture in the applications. Alkyl amino acid ester resorcinarenes were hydrolysed to give tetra-*L*-aspartic acid tetramethoxyresorcinarenes. Also, the resorcinarene acid was reacted with *N*-*N*- diethylethylenediamine to give tetraalkyl tetra-diethylethylenediamine tetramethoxyresorcinarenes.

Novel alkyl amino acid amide was also synthesised by reaction of dimethyl *L*-aspartic acid with dodecanoyl chloride in the presence of triethylamine to give the dimethyl N-dodecanoyl-*L*-aspartate which, after hydrolysis with sodium hydroxide, gave N-dodecanoyl-*L*-aspartic acid (**18**). Also, *N*-*N*-diethylethylenediamine was reacted with dodecanoyl chloride to give *N*-(2-diethylaminoethyl)dodecanamide. These compounds were prepared to

compare their impact on the crystallization or corrosion process with the amino acid functionalized resorcinarenes.

These compounds have been investigated as inhibitors on calcium carbonate, barium sulfate and calcium oxalate crystallization and carbon steel corrosion in CO_2 saturated brine media. The resulted showed that all the amino acid functionalized resorcinarenes could alter the morphology of the model systems (calcium carbonate, barium sulfate and calcium oxalate) and resorcinarene **10** appears to be the most effective. Moreover, these resorcinarenes derivatives were able to influence the growth kinetic of barium sulfate. The comparative study showed that alkyl amino acid amid **18** has less impact on the calcium carbonate and calcium oxalate morphology and high impact on barium sulfate morphology**.** The initial investigation of these derivatives as corrosion inhibitors showed that they inhibited the CO_2 corrosion in brine media by reducing the corrosion rate compared to the non-inhibited solution and the comparative study showed the alkyl amide *L*-aspartic acid (**18)** inhibited the carbon steel corrosion better than the resorcinarene derivatives.

This research can be further extended. Isolation of the two diastereoisomers of the propyl *L*-aspartic acid resorcinene (**10**) should be attempted. This could be performed by the using amino acid with different esters and this may allow easier separation. Also, it would be useful to determine the absolute configuration of the diastereoisomers. The application of amino acid functionalized resorcinarenes as crystallization modification can be extended by using the atomic force microscopy (AFM) technique to study the growth process. In addition, kinetic studies would be useful and determination of the critical micelle concentration would aid in the understanding of their impact. Amino acid functionalized resorcinarenes can also be further investigated as corrosion inhibitors by using more concentration ranges and it would be useful to conduct a comparison study between dodecyl amide **19** with undecyl resorcinarene. Moreover, an AFM study to investigate any surface coating that forms would aid in the mechanistic understanding of how the resorcinarene protects against corrosion.

6.0 References

1. Steed, J., W.; Atwood, J., L., *Supramolecular Chemistry*. John Wiley & Sons,Ltd: West Sussex-England, 2000.

2. Steed, J., W.; Turner, D., R.; Wallace, K., J., *Core Concepts in Supramolecular Chemistry and Nanochemistry*. John Wiley & Sons, Ltd: West Sussex-England, 2007.

3. Desiraju, G., R., Crystal engineering; solid dtate supramolecular synthesis. *Current Opininon in Solid State and Materials Science* **1997,** *2* (4), 451-454.

4. Desiraju, G., R., Crystal engineering. from molecules to materials. *Journal of Molecular Structure* **2003,** *656* (1), 5-15.

5. Zhang, S., Fabrication of novel biomaterials through molecular self-assembly. *Nature Biotechnology* **2003,** *21* (10).

6. Ariga, K.; Hill, J., P.; Lee, M., V.; Vinu, A.; Charvet, R.; Acharya, S., Challenges and breakthroughs in recent research on self-assembly. *Science & Technology of Advanced Materials* **2008,** *9*, 1-96.

7. van Veggel, F., C,J,M.; Verboom, W.; Reinhoudt, D., N., Metallomacrocycles: Supramolecular Chemistry with Hard and Soft Metal Cations in Action. *American Chemical Society* **1994,** *94* (2), 1-21.

8. Lehn, J. M., Perspectives in Supramolecular Chemistry-From Molecular Recognition towards Molecular Information Processing and Self-organization. *Angew Chem. lnr. Ed. EngI.* **1990,** *29*, 1304-1319.

9. Kurth, D., G., Metallo-supramolecular modules as a paradigm for materials science. *Science and TTechnology of Advanced Materials* **2008,** *9*, 1-26.

10. Bureekaew, S.; Shimomura, S.; Kitagawa, S., Chemistry and application of flexible porous coordination polymers. *Science & Technology of Advanced Materials* **2008,** *9*, 1-12.

11. Balzani, V.; Gomes-Lopez, M.; Stoddart, J. F., Molecular Machines. *Accounts of Chemical Research* **1998,** *31* (7), 405-414.

12. Elber, R.; Kimizialtin, S., Molecular Machines. *Current Opinion in Structural Biology* **2013,** *23* (2), 206-211.

13. Böhmer, V., Calixarenes, Macrocycles with (Almost) Unlimited Possibilities. *Angewandte Chemie International Edition in English* **1995,** *34* (7), 713-745.

14. Saluja, V.; Sekhon, B. S., Calixarenes and cucurbiturils: Pharmaceutial and biomedical applications. *Journal of Pharmaceutical Education and Research* **2013,** *4* (1), 16-25.

15. Roundhill, D. M., Calixarenes. In *Comprehensive Coordination Chemistry ll*, 491 ed.; 2004; Vol. 1, pp 485-491.

16. Parker, D., *Macrocyclie Synthesis*. *A practical approach* Oxford university press 1996.

17. Böhmer, V.; Vicens, J., *Calixarenes: A versatile class of macrocyclic compounds* Dordrecht ; Boston : Kluwer Academic Publishers 1991.

18. Lumetta, G. J.; Rogers, R. D.; Gopalan, A. S., *Calixarene for separations*. American chemical society: 2000.

19. Jain, V. K.; Ksnaiya, P. H., Chemistry of calix[4]resorcinarenes. *Russian Chemical Reviews* **2011,** *80* (1), 75-102.

20. Alam, I.; Gutsche, D., Calixarene. *The Journal of Organic Chemistry* **1990,** *55* (14), 4487-4489.

21. De Fátima, A.; Fernandes, S. A.; Sabino, A., Calixarenes as new platforms drug design. *Current Drug Discovery Technologies* **2009,** *3* (6), 1-17.

22. Högberg, A. G. S., Stereoselective Synthesis and DNMR Study of Two 1,8,15,22-Tetraphenyl[14]metacyclophan- 3,5,10,12,17,19,24,26-octols. *Journal of American Chemical Society* **1980,** *102* (19), 6046-6050.

23. Hogberg, A. G. S., Two Stereoisomeric Macrocyclic Resorcinol-Acetaldehyde Condensation Products. *Journal of Organic Chemistry*. **1980,** *45* (22), 4498-4500.

24. Timmerman, P.; Verboom, W.; Reinhoudt, D. N., Resorcinarenes. *Tetrahedron* **1996,** *52* (8), 2663-2704.

25. Dondoni, A.; Marra, A., Calixarene and calixresorcarene glycosides: their synthesis and biological applications. *Chemical reviews* **2010,** *110* (9), 4949–4977.

26. Böhmer, V.; Vicens, J., *Calixarenes: A versatile class of macrocyclic compounds Dordrecht* Kluwer Academic Publishers Boston 1991.

27. Kamboh, M. A.; Ibrahim, W.-A. W.; Nodeh, H. R.; Sanagi, M. M.; Sherazi, S. T. H., The removal of organophosphorus pesticides from water using a new amino-substituted calixarene-based magnetic sporopollenin. *New Journal of Chemistry* **2016,** *40* (4), 3130-3138.

28. Nimse, S. B.; Kim, T., Biological applications of functionalized calixarenes. *Chemical Society Reviews,* **2012,** *42* (1), 366-386.

29. Wang, F.; Wu, Y.; Lu, K.; Ye, B., A simple but highly sensitive and selective calixarene-based voltammetric sensor for serotonin. *Electrochimica Acta* **2013,** *87* (756-762).

30. Jose, P.; Menon, S., Lower-rim substituted calixarenes and their applications. *Bioinorganic chemistry and applications* **2007,** *2007*, 1-17.

31. Couton, D.; Mocerino, M.; Rapley, C.; Kitamura, C.; Yoneda, A.; M., O., Silver and thallium ion complexation with allyloxycalix[4]arenes. *Australian Journal of Chemistry* **1999,** *52* (3), 227-229.

32. Kimura, K.; Tatsumi, K.; Yokoyama, M.; Ouchi, M.; Mocerino, M., Remarkable thallium(I) selectivity for ion sensors based on π-coordination of calix[4]arene neutral carriers. *Analytical communications* **1999,** *36* (6), 229-230.

33. Katsu, T.; Ido, K.; Takaishi, K.; Yokosu, H. T., Thallium(I)-selective membrane electrodes based on calix[6]arene or calix[5]arene derivatives. *Sensors and Actuators B: Chemical* **2002,** *87* (2), 331-335.

34. Dietzsch, M.; Barz, M.; Schüler, T.; Klassen, S.; Schreiber, M.; Susewind, M.; Loges, N.; Lang, M.; Hellmann, N.; Fritz, M.; Fischer, K.; Theato, P.; Kühnle, A.; Schmidt, M.; Zentel, R.; Tremel, W., PAA-PAMPS copolymers as an efficient tool to control $CaCO_3$ scale formation. *Langmuir : the ACS journal of surfaces and colloids* **2013,** *29* (9), 3080-3088.

35. Taylor, S. M.; Sanz, S.; Mcintosh, R. D.; Beavers, C. M.; Teat, S. J.; Brechin, E. K.; Dalgarno, S. J., p - tert -Butylcalix[8]arene: An Extremely Versatile Platform for Cluster Formation. *Chemistry – A European Journal* **2012,** *18* (50), 16014-16022.

36. Goh, C. Y.; Baldini, L.; Casnati, A.; Jones, F.; Mocerino, M.; Ogden, M. I.; Sansone, F.; Ungaro, R., Upper-rim acidic peptidocalixarenes as crystal growth modifiers. *Supramolecular Chemistry* **2014,** *26* (7), 488-499.

37. Addadi, L.; Joester, D.; Nudelman, F.; Weiner, S., Mollusk Shell Formation: A Source of new concepts for understanding biomineralization processes. *Chemistry - A European Journal* **2006,** *12* (4), 980-987.

38. Checa, A. G.; Cartwright, J. H. E.; Willinger, M. G., The key role of surface membranein why gastropod nacre grows in towers. *Proceedings of the National Academy of Sciences of the United States of America.USA* **2009,** *106* (1), 38-43.

39. He, G.; Gajjeraman, S.; Schultz, D.; Cookson, D.; Qin, C.; Butler, W. T.; Hao, J.; George, A., Spatially and temporally controlled biomineralization is facilitated by interaction between self-assembled dentin matrix protein 1 and calcium phosphate nuclei in solution. *Biochemistry* **2005,** *44* (49), 16140-16148.

40. Marie, B.; Marin, F.; Marie, A.; Bedouet, L.; Dubost, L.; Alcaraz, G.; Milet, C.; Luquet, G., Evolution of nacre: biochemistry and proteomics of the shell organic matrix of the cephalopod nautilus macromphalus. *ChemBioChem* **2009,** *10* (9), 1495-1506.

41. Marin, F.; Luquet, G.; Marie, B.; Medakovic, D., Molluscan shell proteins: primary structure, origin, and evolution. *Current Topics in Developmental Biology* **2007,** *80*, 209-276.

42. Gotliv, B. A.; Kessler, N.; Sumerel, J. L.; Morse, D. E.; uross, N.; Addadi, L.; Weiner, S., Asprich: a Novel aspartic acid-rich protein family from the prismatic shell matrix of the bivalve atrina rigida. *ChemBioChem* **2005,** *6* (2), 304-314.

43. Sigel, A.; H., S.; Sigel, R. K. O., *Sulfate-containing biominerals*. *In biomineralization: from nature to application*. John Wiley and sons, Ltd: England; Chichester, 2010; Vol. 4.

44. Jones, F.; Mocerino, M.; Ogden, M. I.; Oliveira, A.; Parkinson, G. M., Bio-inspired calix[4]arene additives for crystal growth modification of inorganic materials. *Crystal growth & Design* **2005,** *5* (6), 2336-2343.

45. Jones, F.; Rohl, A. L.; Ogden, M.; Parkinson, G. M., Scale Formation and Inhibition. Materials Forum2001, 25, 116-135. *Materials Forum* **2001,** *25*, 116-135.

46. Volkmer, D.; Fricke, M., Growth of calcite single crystals underneath monolayers of 5,11,17,23-tetra-t-butyl-25,26,27,28-tetrakis(carboxymethoxy)calix[4]arene. *Zeitschrift für anorganische und allgemeine Chemie* **2003,** *629* (12-13), 2381-2390.

47. Volkmer, D.; Fricke, M.; Agena, C.; Mattay, J., Oriented crystallization of calcite single crystals grown underneath monolayers of tetracarboxyresorc[4]arenes. *CrystEngComm* **2002,** *4* (52), 288-295.

48. Fricke, M.; Volkmer, D.; Krill, C. E.; Kellermann, M.; Hirsch, A. V., Vaterite polymorph switching controlled by surface charge density of an amphiphilic dendron-calix[4]arene. *Crystal Growth and Design* **2006,** *6* (5), 1120-1123.

49. Tan, Y.; Mocerino, M.; Paterson, T., Organic molecules showing the characteristics of localised corrosion aggravation and inhibition. *Corrosion Science* **2011,** *53* (5), 2041-2045.

50. Benabdellah, M.; Souana, R.; Cheriaa, N.; Abidi, R.; Hammouti, B.; Vicens, J., Synthesis of calixarene derivatives and their anticorrosive effect on steel in 1 M HCl. *Pigment & Resin Technology* **2007,** *36* (6), 373-381.

51. Moran, J. R.; Karbach, S.; Cram, D. J., Cavitands: synthetic molecular vessels. *Journal of the American Chemical Society* **1982,** *104* (21), 5826-5828.

52. Wieser, C.; Dieleman, C. B.; Matt, D., Calixarene and resorcinarene ligands in transition metal chemistry. *Coordination Chemistry Reviews* **1997,** *165*, 93-161.

53. Szumna, A., Water co-encapsulation in an inverted molecular capsule. *Chemical Communications* **2009,** (28), 4191-4193.

54. BinMerdhah, A. B., Inhibition of barium sulfate scale at high-barium formation water. *Journal of Petroleum Science and Engineering* **2012,** *90–91*, 124.

55. MacGillivray, L. R.; Atwood, J. L., Cavity-Containing Materials Based Upon Resorcin[4]arenes by Discovery and Design . *Journal of Solid State Chemistry*. **2000,** *152* (1), 199-210.

56. Tunstad, L. M.; Tucker, J. A.; Dalcanale, E.; Weiser, J.; Bryant, J. A.; Sherman, J. C.; Helgeson, R. C.; Knobler, C. B.; Cram, D. J., Host-Guest Complexation. 48. Octo1 Building Blocks for Cavitands and Carcerands. *Journal of Organic Chemistry*. **1989,** *54* (6), 1305-1312.

57. Favre, H. A.; Hellwinkel, D.; Powell, W. H.; Smith, H. A.; Tsay, S. S.-C., Phane nomenclature. Part II. Modification of the degree of hydrogenation and substitution derivatives of phane parent hydrides (IUPAC Recommendation 2002). *Pure and Applied Chemistry* **2002,** *74* (5), 809-834.

58. Benton, W. J.; Collins, I. R.; Grimsey, I. M.; Parkinson, G. M.; Rodger, S. a., 281., Nucleation, growth and inhibition of barium sulfate-controlled modification with or- ganic and inorganic additives. *Faraday Discuss*. **1993,** *95*, 281-297.

59. McIldowie, M. J. The synthesis and structure of C_4 symmetric resorcinarenes. Curtin Universty, Perth, 2007.

60. Kuberski, B.; Szumna, A., A self-assembled chiral capsule with polar interior. *Chemical Communications* **2009,** (15), 1959-1961.

61. Salorinne, K.; Nauha, E.; Nissinen, M.; Ropponen, J., Synthesis and Characterization of the *O*-Alkylation Products of Resorcinarene. *European Journal of Organic Chemistry* **2013,** *2013* (8), 1591–1598.

62. Hisatoshi, K.; Takashi, T.; Hiromichi, O.; Kazuhiro, K.; Osamu, M., Synthesis of Chiral Calix[4]resorcinarenes via Mono-*O*-henzylation. Complexation Behavior with a Chiral Trimethylammonium Compound. *Chemistry Letters* **1996,** *25* (8), 685-686.

63. Shivanyuk, A.; Schmidt, C.; Bohmer, V.; Paulus, E. F.; Lukin, O.; Vogt, W., Selective Derivatization of Resorcarenes. 3. C_2 -Symmetrical and Transcavity Bridged Bis-Benzoxazines Derived from C_{2v} -Symmetrical Tetratosylates. *Journal of the American Chemical Society* **1998,** *120* (4319-4326).

64. Arnecke, R.; Böhmer, V.; Friebe, S.; Gebauer, S.; Krauss, G. J.; Thondorf, I.; Vogt, W., Regio- and Diastereoselective Condensation of Resorcarenes with Primary Amines and Formaldehyde. *Tetrahedron Letters* **1995,** *36* (35), 6221-6224.

65. McIldowie, M. J.; Mocerino, M.; Skelton, B. W.; White, A. H., Facile Lewis Acid Catalyzed Synthesis of C_4 Synthesis Resorciarenes. *Organic Letters* **2000,** *2* (24), 3869-3871.

66. McIldowie, M. J.; Mocerino, M.; Ogden, M., A brief review of *C*n - symmetric calixarenes and resorcinarenes. *Supramolecular Chemistry* **2010,** *22* (1), 13-39.

67. Sun, J.; Zhang, L.-L.; Yao, Y.; Yan, C. G., Synthesis, crystal structures and complexing properties of tetramethoxyresorcinarene functionalized tetraacylhydrazones . *Journal of Inclusion Phenomena and Macrocyclic Chemistry*. **2014,** *79* (3), 485-494.

68. Cram, D. J.; Karbach, S.; Kim, H. E.; Knobler, C. B.; Maverick, E. F.; Ericson, J. L.; Helgeson, R. C., Host-Guest Complexation. 46. Cavitands as Open Molecular Vessels Form Solvent. . *Journal of American Chemical Society* **1988,** *110* (7), 2229-2237.

69. Egberink, R. M. J.; Cobben, P. L. H. M.; Verboom, W.; Harkema, S.; Reinhoudt, D. N. J., Högberg Compounds with a Functionalized Box-Like Cavity. *Journal of Inclusion Phenomena and Macrocyclic Chemistry*. **1992,** *12* (1-4), 151-158.

70. Aoyama, Y.; Tanaka, Y.; Sugahara, S., Molecular Recognition. 5. Molecular Recognition of Sugars *via* Hydrogen-Bonding Interaction with a Synthetic Polyhydroxy Macrocycle. . *Journal of the American Society*. **1989,** *11* (14), 5397-5404.

71. Iwanek, W.; syzdo'l, B., Lewis acid-induced synthesis of octamethoxyresorcanes. *Synthetic Communications*. **1999,** *29* (7), 1209-1216.

72. Roberts, B. A.; Cave, G. W. V.; Raston, C. L.; Scott, J. L., Solvent-free synthesis of calix[4]resorcinarenes. . *Green chemistry*. **2001,** *3*, 280-284.

73. Morikawa, O.; Iyama, E.; Oikawa, T.; Kobayashi, K.; Konishi, H., Conformational properties of C2v-symmetricalresorcin[4]arene tetraethers. *Journal of Physical Organic Chemistry* **2006,** *19* (3), 214-218.

74. Weinelt, F.; Schneider, H. J., Mechanisms of Macrocycle Genesis. The Condensation of Resorcinol with Aldehydes. 1991.56(19). *Journal of Organic Chemistry* **1991,** *56* (19), 5527-5535.

75. Konishi, H.; Yamaguchi, H.; Miyashiro, M.; Kobayashi, K.; Morikawa, O., Functionalization at the Extraannular Positions of Calix[4]resorcinarene Using a Mannich-type Thiomethylation. . *Tetrahedron Letters*. **1996,** *37* (47), 8547-8548.

76. Matsushita, Y.; Matsui, T., Synthesis of Aminomethylated Calix[4]resorcinarenes. . *Tetrahedron Letters*. **1993,** *34* (47), 7433-7436.

77. Page, P. C. B.; Heaney, H.; McGrath, M. J.; Sampler, E. P.; Wilkins, R. F., Retro-Mannich reactions of 3-alkyl-3,4-dihydro-2H-1,3-benz[e]oxazines and the synthesis of axially chiral resorcinarenes. *Terahedron Letters*. **2003,** *44* (14), 2965-2970.

78. Buckley, B. R.; Page, P. C. B.; Heaney, H.; P., S. E.; Carley, S.; Brockeb, C.; Brimbleb, M. A., Use of bis-(aminol) ethers derived from *N*-(*S*)-(*K*)-a-methylbenzylamine in reactions with resorcinarenes and double Mannich reactions. *Tetrahedron* **2005,** *61* (24), 5876-5888.

79. Arnott, G.; Hunter, R., Enantioselective addition of diethylzinc to benzaldehyde catalysed by chiral, bridged resorcinarenes- a stereoselectivity model based on chirality transfer Gareth *Tetrahedron* **2006,** *62* (5), 992-1000.

80. Bourgeois, J.-M.; Stoeckli-Evansb, H., Synthesis of New Resorcinarenes Under Alkaline Conditions. *Helvetica chimica acta*. **2005,** *88* (10), 2722-2730.

81. Moore, D.; Matthews, S. E., *O*-alkyl resorcarenes- where are we now?. *Journal of Phenom Macrocycl Chem* **2009,** *65* (1-2), 137-155.

82. Nummelin, S.; Falabu, D.; Shivanyuk, A.; Rissanen, K., Alkoxy-, Acyloxy-, and Bromomethylation of Resorcinarenes. *Organic Letters* **2004,** *6* (17), 2869-2872.

83. Biros, S. M.; Jr, J. R., Structure and binding properties of water-soluble cavitands and capsules. *Chemical Society Reviews* **2007,** *36*, 96-104.

84. Zheng, A.; Xue, Y.; Wei, D.; Guan, Y.; Xiao, H., Amphiphilic star block copolymers as gene carrier Part I: Synthesis via ATRP using calix[4]resorcinarene-based initiators and characterization. *Materials Science and Engineering C* **2013,** *33* (1), 519-526.

85. Pirondini, L.; Melegari, M.; Pinalli, R.; Dalcanale, E., Introduction of Water-Solubilizing Groups at the Lower Rim of Tolylpyridine-Bridged Cavitands. *Supramolecular Chemistry* **2007,** *19* (1–2), 67–74.

86. Hooley, R. J.; Jr, J. R., Chemistry and Catalysis in Functional Cavitands. *Chemistry and Biology* **2009,** *16* (3), 255-264.

87. Ghaedia, M.; Karamia, B.; Ehsanib, S.; Marahelb, F.; Soylakc, M., Preconcentration–separation of Co2+, Ni2+, Cu2+ and Cd2+ in real samples by solid phase extraction of a calix[4] resorcinarene modified Amberlite XAD-16 resin. *Journal of Hazardous Materials* **2009,** *172* (2), 802–808.

88. Darvish, F.; Khazraee, S., Molecular iodine: An efficient and environment-friendly catalyst for the synthesis of calix[4]resorcinarenes. *Comptes Rendus Chimie* **2014,** *17*, 890-893.

89. Karami, B.; Hoseini, J.; Nikoseresht, S.; Khodabakhshi, S., Fe3O4 nanoparticles: A powerful and magnetically recoverable catalyst for the synthesis of novel calix[4]resorcinarenes. *Chinese Chemical Letters* **2012,** *23*, 173-176.

90. Kresta, S. M.; Etchells III, A. W.; Dickey, D. S.; Atiemo-Obeng, V. A., Mixing Issues in Crystallization and Precipitation Operations. In *Advance in Industrial Mixing*. *A companion to The Handbook of Industrial Mixing*., Nienow, A. W.; Paul, E. L., Eds. John Wiley & Sons, Inc.: Canada., 2016.

91. Peterson, K. E.; Smith, R. C.; Mohan, R. S., Bismuth compounds in organic synthesis. Synthesis of resorcinarenes using bismuth triflate. *Tetrahedron Letters* **2003,** *44* (42), 7723–7725.

92. Parac-Vogt, T. N.; Binnemans, K., Lanthanide(III) nosylates as new nitration catalysts. *Tetrahedron Letters* **2004,** *45*, 3137–3139.

93. Vuano, B.; Pieroni, O. I., A One-Step Synthesis of *O*-Functionalized Resorcinarene under Heterogeneous Catalysis Conditions. *Synthesis* **1999,** (1), 72-73.

94. Han, J.; Cai, Y. H.; Liu, L.; Yana, C. G.; Lib, Q., Syntheses, crystal structures, and electrochemical properties of multi-ferrocenyl resorcinarenes. *Terahedron* **2007,** *63* (10), 2275-2282.

95. Sansonea, F.; Barbosoa, S.; Casnatia, A.; Fabbia, M.; Pochinia, A.; Ugozzolib, F.; Ungaro, R., Synthesis and Structure of Chiral Cone Calix[4]arenes Functionalized at the Upper Rim with L-Alanine Units. *European Journal of Organic Chemistry* **1998**, 8972905.

96. McIldowie, M. J.; Mocerino, M.; Ogden, M. I.; Skelton, B. W.; White, A. H., C_4 Dissymmetric resorcinarene derivatives: synthesis, crystal structure and micelle formation. *J Incl Phenom Macrocycl Chem* **2015,** *82*, 47–51.

97. Moridi, N.; Elend, D.; Danylyuk, O.; Suwinska, K.; Shahgaldian, P., Amidophenol-Modified Amphiphilic Calixarenes: Synthesis, Interfacial Self-Assembly, and Acetaminophen Crystal Nucleation Properties. *Langmuir* **2011,** *27* (15), 9116–9121.

98. Tsou, L. K.; Dutschman, G. E.; Gullen, E. A.; elpoukhovskaia, M.; Cheng, Y.-C.; Hamilton, A. D., Discovery of a synthetic dual inhibitor of HIV and HCV infection based on a tetrabutoxy-calix[4]arene scaffold. *Bioorganic & Medicinal Chemistry Letters* **2010,** *20* (7), 2137–2139.

99. Sasine, J. S.; Brewster, R. E.; Caran, K. L.; Bentley, A. M.; Shuker, S. B., Heterodimerization Studies of Calix[4]arene Derivatives in Polar Solvents. *Organic Letters* **2006,** *8* (14), 2913–2915.

100. Mai, J. H.; Liu, J. M.; Li, S. Y.; Jiang, H. F., A fluorescent probe for fluoride ion based on 2-aminopyridyl-bridged calix[6]arene. *Chinese Chemical Letters* **2009,** *20* (10), 1191–1194.

101. Miao, R.; Zheng, Q.-Y.; Chen, C.-F.; Huang, Z.-T., A Novel N-linked Peptidocalix[4]arene Receptor for Anions. *Supramolecular Chemistry* **2007,** *19* (7), 531-535.

102. Kubo, M.; Mollberg, W. C.; Padias, A. B.; Hall, H. k.; Calvert, P., Solubilization of Peptides in Water and Hexane: Synthesis of Peptide-Terminated PolyOerf-butyl acrylate) and Poly(acrylic acid) via Living Anionic Polymerization. *Macromolecules* **1995,** *28* (4), 838-843.

103. Anderson, G. W.; Callahan, F. M., Racemization By The Dicyclohexylcarbo-Dimide Methode Of Peptide Synthesis. *Journal of the American Chemical Society* **1958,** *80* (11), 2902-2903.

104. Chinchilla, R.; Dodsworth, D. J.; Nájera, C.; Soriano, J. M., Polymer-bound *N*-hydroxysuccinimide as a solid-supported additive for DCC-mediated peptide synthesis. *Tetrahedron Letters* **2001,** *42* (27), 4487-4489.

105. Carpino, L. A.; El-Faham, A., Tetramethylfluoroformamidinium Hexafluorophosphate: A Rapid-Acting Peptide Coupling Reagent for Solution and Solid Phase Peptide Synthesis. *Journal of the American Chemical Society* **1995,** *117* (19), 5401-5402.

106. Huang, Y.; Feng, W. H., *N*,*O*-Bis(trimethylsilyl)acetamide/N-hydroxysuccinimide ester (BSA/NHS) as coupling agents for dipeptide synthesis. *Chinese Chemical Letters* **2016,** *27* (3), 357-360.

107. Baldini, L.; Sansone, F.; Faimani, G.; Massera, C.; Casnati, A.; Ungaro, R., Self-Assembled Chiral Dimeric Capsules from Difunctionalized *N*,*C*-LinkedPeptidocalix[4]arenes: Scope and Limitations. *European journal of organic chemistry* **2008,** *2008* (5), 869-886.

108. Buckley, B. R.; Page, P. C. B.; Chan, Y.; Heaney, H.; Klaes, M.; Mcildowie, M. J.; Mckee, V.; Mattay, J.; Mocerino, M.; Moreno, E.; Skelton, B. W.; White, A. H., The Preparation and Absolute Configurations of Enantiomerically Pure C4-Symmetric Tetraalkoxyresorcin[4]arenes Obtained from Camphorsulfonate Derivatives. *European journal of organic chemistry* **2006,** *2006* (22), 5135-5151.

109. Mullin, J. W., *Crystallisation*. 3 ed.; Butterworth-Heinemann: 1993.

110. Beckmann, W., The Influence of Additives and Impurities on Crystallization. In *Crystallisation: basic concepts and industrial application* Schmidt, C.; Jones, M. J.; Ulrich, J., Eds. Wiley-VCH Verlag GmbH & Co. : Germany, 2013; p 111.

111. Mann, S., *in Biomineralization: Principles and Concepts in Bioinorganic Materials Chemistry*. Oxford University Press: 2001.

112. Weiner, S.; Addadi, L., Design strategies in mineralized biological materials. *Journal of Materials Chemistry* **1997,** *7* (5), 689-702.

113. Wibowo, C.; Ng, K. M., Unified approach for synthesizing crystallization-based separaton processes. *American Institute of Chemical Engineers* **2000,** *46* (7), 1400-1421.

114. Jones, F.; Stanley, A.; Oliveira, A.; Rohl, A. L.; Reyhani, M. M.; Parkinson, G. M.; Ogden, M. I., The role of phosphonate speciation on the inhibition of barium sulfate precipitation. *Crystal growth* **2003,** *249* (3-4), 584-593.

115. Reddy, M. M.; Hoch, A. R., Calcite crystal growth rate inhibition by polycarboxylic acids. *Journal of Colloid and Interface Science* **2001,** *235* (2), 365-370.

116. Amjad, Z., *Mineral scales in biological and industrial systems*. aylor & Francis Group: 2014.

117. Boerlage, S. F. E.; Kennedy, M. D.; Bremere, I.; Witkamp, G. J.; Van Der Hoek, J. P., The scaling potential of barium sulphate in reverse osmosis systems. *Journal of Membrane Science* **2002,** *197* (1-2), 251–268.

118. Kelland, M. A., Effect of Various Cations on the Formation of Calcium Carbonate and Barium Sulfate Scale with and without Scale Inhibitors. *Industrial & Engineering Chemistry Research* **2011,** *50* (9), 5852–5861.

119. Amjad, Z., Evaluating Biopolymer Phosphonate Blends as Gypsum Scale Inhibitors for Industrial Waters. *Materials Performance* **2015,** *54* (3), 62-66.

120. Jancic, S. J.; Grootscholten, P. A. M., *Industrial Crystallization*. Delft University Press: 1984.

121. Myerson, A. S., *Handbook of Industrial Crystallization*. 3 ed.; Butterworth-Heinemann: 1993.

122. Brujan, E. A., *Cavitation in Non-Newtonian Fluids With Biomedical and Bioengineering Applications*. *Emil-Alexandru Brujan*. *2011*. Springer, 2011.

123. Kwon, S. G.; Hyeon, T., Formation Mechanisms of Uniform Nanocrystals via Hot-Injection and Heat-Up Methods. *Small* **2011,** *7* (19), 2685-2702.

124. Mullin, J. W., *Crystallization*. , ed.; Butterworth-Heinemann: Oxford, 2001.

125. Harrison, R. G.; Todd, P. W.; Rudge, S. R.; Petrides, D. P., Crystallisation. In *Bioseparations Science and Engineering*, 2 nd ed.; Oxford University Press: New York, 2015.

126. R., D.; Garside, J., *From Molecules to Crystallizers; An Introduction to Crystallization*. Oxford University Press: 2000.

127. Jones, F.; Radomirovic, T.; Ogden, M. I., Effect of solution silicate on the precipitation of barium sulfate. *Crystal growth & design* **2012,** *12* (6), 3057–3065.

128. Isopescu, R.; Mateescu, C.; Mihai, M.; Dabija, G., The effects of organic additives on induction time and characteristics of precipitated calcium carbonate. *chemical engineering research and design* **2010,** *88* (11), 1450-1454.

129. Shiraga, H.; Min, W.; Vandusen, W. J.; Clayman, M. D.; Miner, D.; Terrell, C. H.; Sherbotie, J. R.; Foreman, J. W.; Przysiecki, C.; Neilson, E. G.; Hoyer, J. R., Inhibition of calcium oxalate crystal growth in vitro by uropontin: Another member of the aspartic acid-rich protein superfamily. *Proceedings of the National Academy of Sciences of the United States of America.USA* **1992,** *89* (1), 426-430.

130. Frackowiak, A.; Kozlecki, T.; Skibinski, P.; Zaczynska, E.; Czarny, A.; Piekarska, K.; Gancarz, R., Solubility, inhibition of crystallization and microscopic analysis of calcium oxalate crystals in the presence of fractions from Humulus lupulus L. *Journal of Crystal Growth* **2010,** *312* (1), 3525-3532.

131. Nyvlt, J.; Ulrich, J., *Admixtures in Crystallization,*. VCH, Weinheim,: 1995.

132. Malkaj, P.; Dalas, E., Calcium carbonte crystallization in the presence of Aspartic Acid. *Crystal growth design*. **2004,** *4* (40), 721-723.

133. Liu, Y.; Cui, Y.; Mao, H.; Guo, R., Calcium carbonate Crystallisation in the Ptrsence of Casein. *Crystal growth design*. **2012,** *12* (10), 4720-4726.

134. Dhami, N. K.; Reddy, M.; Mukherjee, A., Biomineralization of calcium carbonates and their engineered applications: a review. *Frontiers in Microbiology* **2013,** *4*, 1-14.

135. Yang, Q.; Liu, Y.; Gu, A.; Ding, J.; Shen, Z., Investigation of calcium carbonate scaling inhibition and scale morphology by AFM. *Journal of Colloid and Interface Science* **2001,** *240* (2), 608–621.

136. Ren, D.; Li, Z.; Gao, Y.; Feng, Q., Effects of functional groups and soluble matrices in fish otolith on calcium carbonate mineralization. *Biomedical Materials* **2010,** *5* (5), 1-11.

137. Chiena, Y.-C.; Hincke, M. T.; Mckee, M. D., Avian Eggshell Structure and Osteopontin. *Cells Tissues Organs* **2009,** *189* (1-2), 38-43.

138. Tavangar, A.; Tan, B.; Venkatakrishnan, K., Synthesis of three-dimensional calcium carbonate nanofibrous structure from eggshell using femtosecond laser ablation. *Journal of Nanobiotechnology* **2011,** *9* (1-6).

139. Khalifa, G. M.; Weiner, S.; Addadi, L., Mineral and Matrix Components of the Operculum and Shell of the Barnacle Balanus amphitrite: Calcite Crystal Growth in a Hydrogel. *Crystal Growth & Design* **2011,** *11* (11), 5122-5130.

140. Kabalah-Amitai, L.; Mayzel, B.; Zaslansky, P.; Kauffmann, Y.; Clotens, P.; Pokroy, B., Unique crystallographic pattern in the macro to atomic structure of Herdmania momus vateritic spicules. *Journal of Structural Biology* **2013,** *183* (2), 191–198.

141. Doubleday, Z. A.; Harris, H. H.; Izzo, C.; Gillanders, B. M., Strontium randomly substituting for calcium in fish otolith aragonite. *Analytical chemistry* **2014,** *86* (1), 865-869.

142. De Baets, K.; Munnecke, A., Evidence for Palaeozoic orthoconic cephalopods with bimineralic shells. *Palaeontology* **2018,** *61* (2), 173-181.

143. Luo, H.; Chen, D.; Yang, X.; Zhao, X.; Feng, H.; Li, M.; Wang, J., Synthesis and performance of a polymeric scale inhibitor for oilfield application. *Journal of Petroleum Exploration and Production Technology* **2015,** *5* (2), 177–187.

144. Neveux, T.; Bretaud, M.; Chhim, N.; Shakourzadeh, K.; Rapenne, S., Pilot plant experiments and modeling of CaCO*3* growth inhibition by the use of antiscalant polymers in recirculating cooling circuits. *Desalination* **2016,** *397*, 43–52.

145. Rahmani, K. h.; Jadidian, R.; Haghtalab, S., Evaluation of inhibitors and biocides on the corrosion, scaling and biofouling control of carbon steel and copper–nickel alloys in a power plant cooling water system. *Desalination* **2016,** *393*, 174–185.

146. Erez, J., The Source of Ions for Biomineralization in Foraminifera and Their Implicationa for Paleoceanographic Proxies. *Reviews in Mineralogy and Geochemistry* **2003,** *54* (1), 115–149.

147. Teir, S.; Eloneva, S.; Zevenhoven, R., Production of precipitated calcium carbonate from calcium silicates and carbon dioxide. *Energy Conversion and Management* **2005,** *46*, 2954-2979.

148. Kamba, A., S.; smail, M.; brahim, T. A. T.; Zakaria, Z. A., Synthesis and Characterisation of Calcium Carbonate Aragonite Nanocrystals from Cockle Shell Powder (Anadara granosa). *Journal of Nanomaterials* **2013,** *2013*, 9.

149. Preisig, D.; Haid, D.; J.O. Varum, F.; Bravo, R.; Alles, R.; Huwyler, J.; Puchkov, M., Drug loading into porous calcium carbonate microparticles by solvent evaporation. *European Journal of Pharmaceutics and Biopharmaceutics* **2014,** *87* (3), 548–558.

150. Sifontes, A. B.; Cañizales, E.; Mendoza, J. T.; Ávila, E.; Hernández, P.; Delgado, B. A.; Gutiérrez, B. G.; Díaz, Y.; Cruz-Barrios, E., Obtaining Highly Crystalline Barium Sulphate Nanoparticles via Chemical Precipitation and Quenching in Absence of Polymer Stabilizers. *Journal of Nanomaterials* **2015,** *2015*, 8.

151. Fernandez-Gonzalez, A.; Martın-Dıaz, R.; Prieto, M., Crystallisation of Ba(SO , CrO) solid solutions from aqueous solutions. *Journal of Crystal Growth* **1999,** *200* (1-2), 227—235.

152. Jones, F.; Oliveira, A.; Rohl, A. L.; Parkinson, G. M.; Ogden, M. I.; Reyhani, M. M., Investigation into the effect of phosphonate inhibitors on barium sulfate precipitation. *Journal of Crystal Growth* **2002,** *237–239*, 424–429.

153. Baynton, A.; Ogden, M. I.; Raston, C. L.; Jones, F., Barium sulfate crystallization dependence on upper rim calix[4]arene functional groups. *CrystEngComm* **2012,** *14* (3), 1057-1062.

154. Boon, M.; Freeman, S.; I., O. M.; Oliveira, A.; Richmond, W. R.; Skelton, B. W.; Jones, F., The many roles of mellitic acid during barium sulfate crystallization. *The Royal Society of Chemistry*. **2015,** *179*, 343-357.

155. Jones, F.; Rohl, A. L., Empirical molecular modelling of crystal growth modifiers. *Molecular Simulation* **2005,** *31* (6-7), 393–398.

156. Franceschi, V. R.; Nakata, P., Calcium Oxalate in Plants: Formation and Function. *Annual Review of Plant Biology; Palo Alto* **2005,** *56*, 41-71.

157. Amjad, Z.; Demadis, K. D., *Mineral Scales and Deposits Scientific and Technological Approaches*. 2015.

158. Song, R. Q.; Colfen, H., Additive controlled crystallization. *CrystEngComm* **2011,** *13* (5), 1249-1276.

159. Weissbuch, I.; Addadi, L.; LAHAV, M.; Leiserowitz, L., Molecular recognition at crystal interfaces. *Science* **1991,** *253* (5020), 637–645.

160. Jones, F.; Ogden, M. I., Controlling crystal growth with modifiers. *CrystEngComm* **2010,** *12* (4), 1016-1023.

161. Ruiz-Agudo, E.; Putnis, C. V.; Rodriguez-Navarro, C., Interaction between Epsomite Crystals and Organic Additives. *Crystal growth & design* **2008,** *8* (8), 2665–2673.

162. Liu, S. T.; Nancollas, G. H.; Gasieck, E. A., Scanning Electron Microscopic and Kinetic Stusieds of The Crystallization and Disso;ution of Barium Sulfate Crystals. *Journal of Crystal Growth* **1976,** *33* (1), 11-20.

163. He, S.; Oddo, J. E.; Tomson, M. B., The Nucleation Kinetics of Barium Sulfate in NaCl Solutions up to 6 M and 90°C. *Journal of Colloid and Interface Science* **1995,** *174* (2), 319-326.

164. Garside, J.; Davey, R.; Jones, A. G., *Advances in industrial crystallization*. Oxford : Butterworth Heinemann Ltd: 1991.

165. Kim, I. W.; Collino, S.; Morse, D. E.; Evans, J. S., A Crystal Modulating Protein from Molluscan Nacre That Limits the Growth of Calcite in Vitro. *Crystal Growth & Design* **2006,** *6* (5), 1078-1082.

166. Gower, L. B., Biomimetic Model Systems for Investigating the Amorphous Precursor Pathway and Its Role in Biomineralization. *Chemical reviews* **2008,** *108* (11), 4551-4627.

167. Kowacz, M.; Putnis, C. V.; Putnis, A., The effect of cation:anion ratio in solution on the mechanism of barite growth at constant supersaturation: Role of the desolvation process on the growth kinetics. *Geochimica et Cosmochimica Acta* **2007,** *71* (21), 5168–5179.

168. Benson, S. W., *Thermodynamical Kinetics*. 2nd ed.; John Wiley: New York, 1976.

169. Yang, K. C.; Hogg, R., Estimation of Particle Size Distributions from Turbidimetric Measurements. *Analytical Chemistry* **1979,** *51* (6), 758-763.

170. Gower, L. A.; Tirrell, D. A., Calcium carbonate films and helices grown in solutions of poly(aspartate). *Journal of Crystal Growth* **1998,** *191* (1-2), 153—160.

171. Gehrke, N.; Colfen, H.; Pinna, N.; Antonietti, M.; Nassif, N., Superstructures of Calcium Carbonate Crystals by Oriented Attachment. *Crystal growth & Design* **2005,** *5* (4), 1317-1319.

172. Al-Hamzah, A. A.; East, C. P.; S., D. W. O.; Fellows, C. M., Inhibition of homogenous formation of calcium carbonate by poly (acrylic acid). The effect of molar mass and end-group functionality. *Desalination* **2014,** *338*, 93–105.

173. Niederberger, M.; Colfen, H., Oriented attachment and mesocrystals: Non-classical crystallization mechanisms based on nanoparticle assembly. *Physical Chemistry Chemical Physics* **2006,** *8* (28), 3271-3287.

174. Uhlig, H. H.; Revie, R. W., *Corrosion and corrosion control : an introduction to corrosion science and engineering*. 3rd ed.; New York : Wiley: 1985.

175. Kaesche, H., *Corrosion of Metals: Physicochemcial Principles and Current Problems*. Springer-Verlag: Berlin/Heidelberg: Germany, 2003.

176. Frankel, G. S.; Sridhar, N., Understanding localized corrosion. *Materials Today* **2008,** *11* (10), 38-44.

177. Schweitzer, P. A., *Corrosion engineering handbook , Fundamentals of metallic corrosion : atmospheric and media corrosion of metals*. 2 ed.; Boca Raton : CRC Press: 2007; Vol. Schweitzer, P. A.

178. Farelas, F.; Galicia, M.; Brown, B.; Nesic, S.; Castaneda, H., Evolution of dissolution processes at the interface of carbon steel corroding in a CO_2 environment studied by EIS. *Corrosion Science* **2010,** *52* (2), 509-517.

179. Robertson, J. O.; Chilingar, G. V., Corrosion. In *Environmental Aspects of Oil and Gas Production*, John Wiley & Sons and Scrivener Publishing LLC: New jersy, 2017.

180. Kermani, M. B.; Morshed, A., Carbon dioxide corrosion in oil and gas production-a compendium. *Corrosion Science* **2003,** *59* (8), 659-683.

181. Chilana, L.; Bhatt, A. H.; Najafi, M.; Sattler, M., Comparison of carbon footprints of steel versus concrete pipelines for water transmission. *Journal of The Air and Waste Management Association* **2016,** *66* (5), 518–527.

182. Otakar, J.; Joyce, M.; Andrew, M., SCC of Carbon Steel in Nuclear Component Cooling Water Systems. Part 1. *Materials Performance* **2005,** *44* (5), 52-56.

183. Dwivedi, D., D.; Kateina, L.; Thomas, B., Carbon steel corrosion: a review of key surface properties and characterization methods. *RSC Advances* **2017,** *7* (8), 4580-4610.

184. Alsabagh, A. M.; Migahed, M. A.; Awad, H. S., Reactivity of polyester aliphatic amine surfactants as corrosion inhibitors for carbon steel in formation water (deep well water). *Corrosion Science* **2006,** *48* (4), 813-828.

185. Wang, Z. M.; Han, X.; Zhang, J.; Wang, Z. L., In situ observation of CO_2 corrosion under high pressure. *Corrosion Engineering, Science and Technology* **2014,** *49* (5), 352-356.

186. Nesic, S.; Postlethwaite, J.; Olsen, S., An Electrochemical Model for Prediction of Corrosion of Mild Steel in Aqueous Carbon Dioxide Solutions. *Corrosion* **1996,** *52* (4), 280-294.

187. Roberge, P. R., *Corrosion engineering : principles and practice* New York : McGraw-Hill: 2008.

188. De Waard, C.; Lotz, U.; Milliams, D. E., Predictive Model for CO_2 Corrosion Engineering in Wet Natural Gas Pipelines. *Corrosion Journal* **1991,** *47* (12), 976-985.

189. Song, F. M.; Kirk, D. W.; Graydon, J. W.; Cormack, D. E., Predicting carbon dioxide corrosion of bare steel under an aqueous boundary layer. *Corrosion* **2004,** *60* (8), 736-748.

190. Srdjan, N., Key issues related to modelling of internal corrosion of oil and gas pipelines – A review. *Corrosion Science* **2007,** *49* (12), 4308-4338.

191. Popoola, L. T.; Grema, A. S.; Latinwo, G. K.; Gutti, B.; Balogun, A. S., Corrosion problems during oil and gas production and its mitigation. *International Journal of Industrial Chemistry* **2013,** *4* (1), 1-15.

192. Jiang, X.; Zheng, Y. G.; Qu, D. R.; Ke, W., Effect of calcium ions on pitting corrosion and inhibition performance in CO_2 corrosion of N80 steel. *Corrosion science* **2006,** *48* (10), 3091-3108.

193. De Waard, C.; Williams, D. E., Prediction of carbonic acid corrosion in natural gas pipelines. *Ind. Finish. Surf. Coatings,* **1976,** *28* (340), 24-26.

194. Linter, B. R.; Burstein, G. T., Reactions of pipeline steels in carbon dioxide solutions. *Corrosion Science* **1999,** *41* (1), 117-139.

195. Nesic, S.; Pots, B.; Postlethwaite, J.; Thevenot, N., Superposition of diffusion and chemical reaction controlled limiting currents - Application to Corrosion. *Journal of Corrosion Science & Engineering* **1995,** *1*, 1-14.

196. Nordsveen, M.; Nešic, S.; Nyborg, R.; Stangeland, A., A Mechanistic Model for Carbon Dioxide Corrosion of Mild Steel in the Presence of Protective Iron Carbonate Films-Part 1: Theory and Verification. *Corrosion Journal* **2003,** *59* (5), 443-456.

197. Revie, R. W., Carbon Dioxide Corrosion of Mild Steel In *Uhlig's corrosion handbook* 3 rd ed.; Nesic, S., Ed. John Wiley & Sons, Inc.: New Jersey-Canada, 2011; p 229.

198. Nesic, S.; Lee, L., A Mechanistic Model for CO_2 Corrosion with Protective Iron Carbonate Films. *Corrosion* **2003,** *59*, 616-628.

199. Moiseeva, L. S., Carbon dioxide corrosion of oil and gas field equipment. *Protection of Metals* **2005,** *41* (1), 76-83.

200. Callister, W. D., *Materials science and engineering : an introduction*. 7th ed.; Hoboken, NJ : John Wiley & Sons: 2007.

201. Bockris, J. M.; Drazic, D.; Despic, A. R., The electrode kinetics of the deposition and dissolution of iron. *Electrochimica Acta* **1961,** *4* (2), 325-361.

202. Perez, T. E., Corrosion in the Oil and Gas Industry: An Increasing Challenge for Materials. *The Journal of Minerals, Metals and Materials Society (TMS),* **2013,** *65* (8), 033-1041.

203. van Hunnik, E. W. J.; Pots, B. F. M.; Hendriksen, E. L. J. A., The Formation of Protective $FeCO_3$ Corrosion Product Layers in CO_2 Corrosion. *corrosion (Houston, TX: NACE)* **1996**.

204. Tanupabrungsun, T.; Brown, B.; Nešić, S., Effect of CO_2 Corrosion of Mild Steel at Elevated Temperatures. *Corrosion* **2013**.

205. Nesic, S.; Lunde, L., Carbon Dioxide Corrosion of Carbon Steel in Two-Phase Flow. *Corrosion* **1994,** *54*, 717–727 (

206. Lopeza, D. A.; Perezb, T.; Simisona, S. N., The influence of microstructure and chemical composition of carbon and low alloy steelsin CO_2 corrosion.Astate-of-the-artappraisal. *Materials and Design* **2003,** *24* (8), 561–575.

207. Ingham, B.; Ko, M.; Kear, C.; Kappen, P.; Laycock, N.; Kimpton, J. A.; Williams, D. E., In situ synchrotron X-ray diffraction study of surface scale formation during CO_2 corrosion of carbon steel at temperatures up to 90 °C. *Corrosion Science* **2010,** *52* (9), 3052–3061.

208. Sk, M. H.; Abdullah, A. M.; Ko, M.; Ingham, B.; Laycock, N.; Arul, R.; Williams, D. E., Local supersaturation and the growth of protective scales during CO_2 corrosion of steel: Effect of pH and solution flow. *Corrosion Science,* **2017,** *126*, 26-36.

209. Das, G. S., Precipitation and Kinetics of Ferrous Carbonate in Simulated Brine Solution and Its Impact on CO_2 Corrosion of Steel. *International Journal of Advances in Engineering & Technology* **2014,** *7* (3), 790-797.

210. Schmitt, G.; Horstemeier, M., Fundamental aspects of CO_2 metal loss corrosion- Part II: Influence of different parameters on CO_2 corrosion mechanisms. *Corrosion - NACE International,* **2006,** *6*.

211. Sun, W.; Nesic, S.; Woollam, R. C., The effect of temperature and ionic strength on iron carbonate ($FeCO_3$) solubility limit. *Corrosion Science* **2009,** *51* (6), 1273-1276.

212. De Waard, C.; Lotz, U., Prediction of CO_2 Corrosion of Carbon Steel. *Corrosion (NACE International,)* **1993**.

213. De Waard, C.; Lotz, U.; Milliams, D. E., Predictive Model for CO_2 Corrosion Engineering in Wet Natural Gas Pipelines. *Corrosion* **1991,** *47* (12), 976-985.

214. Honarvar Nazari, M.; Allahkaram, S. R.; Kermani, M. B., The effects of temperature and pH on the characteristics of corrosion product in CO_2 corrosion of grade X70 steel. *Materials & Design* **2010,** *31* (7), 3559-3563.

215. Al-Otaibi, M. S.; Al-Mayouf, A. M.; Khan, M.; Mousa, A. A.; Al-Mazroa, S. A.; Alkhathlan, H. Z., Corrosion inhibitory action of some plant extracts on the corrosion of mild steel in acidic media. *Arabian Journal of Chemistry* **2014,** *7* (3), 340-346.

216. Obot, I. B.; Obi-Egbedi, N. O.; Umoren, S. A., Antifungal drugs as corrosion inhibitors for aluminium in 0.1 M HCl. *Corrosion Science* **2009,** *51* (8), 1868-1875.

217. Yıldırım, A.; Çetin, M., Synthesis and evaluation of new long alkyl side chain acet- amide, isoxazolidine and isoxazoline derivatives as corrosion inhibitors. *Corrosion Science* **2008,** *50* (1), 155-165.

218. Byars, H. G., *Corrosion Control in Petroleum Production*. 2nd ed.; NACE International: 1999.

219. Molland, A. F., *The Maritime Engineering Reference Book*. *A Guide to Ship Design, Construction and Operation*. Elsevier Ltd.: 2008.

220. Cū, C. V., *Corrosion inhibitors : principles and applications*. Wiley Chichester ; New York 1998.

221. Durnie, W.; De Marco, R.; Kinsella, B.; Jefferson, A.; Pejcica, B., Predicting the Adsorption Properties of Carbon Dioxide Corrosion Inhibitors Using a Structure-Activity Relationship. *Journal of The Electrochemical Society* **2005,** *152* (1), B1-B11.

222. Revie, R. W., Corrosion Inhibitors. In *Uhlig's corrosion handbook*,, 3 rd ed.; Papavinasm, S., Ed. John Wiley & Sons, Inc.: New Jersey-Canada, 2011; pp 1021-1023.

223. Chilingar, G. V.; Mourhatch, R.; Al-Qahtani, G. D., *The Fundamentals of Corrosion and Scaling for Petroleum and Environmental Engineers*. Gulf Publishing Company, Houston: Texas, 2008.

224. Orazem, M. E., *Underground pipeline corrosion Detection, analysis and prevention*. Woodhead Publishing Limited: 2014.

225. Desimone, M. P.; Grundmeier, G.; Gordillo, G.; Simison, S. N., Amphiphilic amido-amine as an effective corrosion inhibitor for mild steel exposed to CO_2 saturated solution: Polarization, EIS and PM-IRRAS studies. *Electrochimica Acta* **2011,** *56* (8), 2990-2998.

226. Liu, X.; Okafor, P. C.; Zheng, Y. G., The inhibition of CO_2 corrosion of N80 mild steel in single liquid phase and liquid/particle two-phase flow by aminoethyl imidazoline derivatives. *Corrosion Science,* **2009,** *51* (4), 744-751.

227. Liua, J.; Yub, W.; Zhanga, J.; Hua, S.; Youa, L.; Qiao, G., Molecular modeling study on inhibition performance of imidazolines for mild steel in CO_2 corrosion. *Applied Surface Science* **2010,** *256* (14), 4729-4733.

228. Porcayo-Calderon, J.; Martínez de La Escalera, L. M.; Canto, J.; Casales-Diaz, M., Imidazoline Derivatives Based on Coffee Oil as CO_2 Corrosion Inhibitor. *International Journal Of Electrochemical Science* **2015,** *10* (4), 3160-3176.

229. Liu, H.; Du, D.-M., Recent Advances in the Synthesis of 2-Imidazolines and TheirApplications in Homogeneous Catalysis. *Advance Synthesis & Catalysis* **2009,** *351* (18), 489–519.

230. Cheng, Y.; Haisheng Bi, Z.-L.; Song, Y., Research on the CO_2 Corrosion Inhibitor Technology in Oil and Gas Fields. *Advanced Materials Research* **2013,** *734-737*, 1240-1245.

231. Ramachandran, S.; Tsai, B.; Blanco, M., Self-Assembled Monolayer Mechanism for Corrosion Inhibition of Iron by Imidazolines. *Langmuir* **1996,** *6419–6428* (26), 12.

232. Bereket, G.; Yurt, A., S., Inhibition of the corrosion of low carbon steel in acidic solution by selected quaternary ammonium compounds. *Anti-Corrosion Methods and Materials* **2002,** *49* (3), 210-220.

233. Zhao, J.; Duan, H.; Jiang, R., Synergistic corrosion inhibition effect of quinoline quaternary ammonium salt and Gemini surfactant in H_2S and CO_2 saturated brine solution. *Corrosion Science* **2015,** *91*, 108-119.

234. Ren, Y.; Zhang, J.; Du, M.; Niu, L., The synergistic inhibition effect between imidazoline- based dissymmetric bis-quaternary ammonium salts and thiourea on Q235 steel in CO_2 corrosion process. *Research on Chemical Intermediates* **2016,** *42* (2), 641-657.

235. Ezuber, H. M., Influence of temperature and thiosulfate on the corrosion behavior of steel in chloride solutions saturated in CO_2. *Materials and Design* **2009,** *30* (9), 3420-3427.

236. Kappes, M.; Frankel, G. S.; Sridhar, N.; Carranza, R. M., Corrosion Behavior of Carbon Steel in Acidified, Thiosulfate-Containing Brines. *Corrosion* **2012,** *68* (10), 872-884.

237. Emori, W.; Jiang, S. l.; Duan, D. L.; Zheng, Y. g., Effects of Sodium Thiosulfate and Sodium Sulfide on the Corrosion Behavior of Carbon Steel in an

MDEA-Based CO_2 Capture Process. *Journal of Materials Engineering And Performance* **2017,** *26* (1), 335-342.

238. Zvauya, R.; Dawson, J., Zvauya, R.; Dawson, J., Inhibition studies in sweet corrosion systems by a quaternary ammonium compound. *Journal of Applied Electrochemistry* **1994,** *24* (9), 943-94.

239. Ramachandran, S.; Tsai, B.; Blanco, M., Atomistic Simulations of Oleic Imidazolines Bound to Ferric Clusters. *Journal of Physical Chemistry A,* **1997,** *101* (1), 83–89.

240. Ramachandran, S.; Jovancicevic, V., Molecular modeling of the inhibition of mild steel carbon dioxide corrosion by imidazolines. *Corrosion* **1999,** *55* (3), 259–267

241. Aljourani, J.; Raeissi, K.; Golozar, M. A., Benzimidazole and its derivatives as corrosion inhibitors for mild steel in 1M HCl solution. *Corrosion Science* **2009,** *51* (8), 1836-1843.

242. Malik, M. A.; Hashim , M. A.; Nabi, F.; Al-Thabaiti, S. A.; Khan, Z., Anti-corrosion ability of sur- factants: A review. *International Journal of Electrochemical Science* **2011,** *6* (6), 1927-1948.

243. Zheng, X.; Zhang, S.; Li, W.; Yin, L.; He, J.; Wu, J., Investigation of 1-butyl-3-methyl-1H-benzimidazolium iodide as inhibitor for mild steel in sulfuric acid solution. *Corrosion Science* **2014,** *80*, 383-392.

244. Amin, M. A.; Khaled, K. F.; Mohsen, Q.; Arida, H. A., A study of the inhibition of iron corrosion in HCl solutions by some amino acids. *Corrosion Science* **2010,** *52* (5), 1684-1695.

245. Hegazy, M. A.; El-Tabei, A. S.; Bedair, A. H.; Sadeq, M. A., An investigation of three novel nonionic surfactants as corrosion inhibitor for carbon steel in 0.5 M H_2SO_4,. *Corrosion Science* **2012,** *54*, 219-230.

246. Abd El-lateef, H. M.; Abbasov, V. M.; Aliyeva, L. I.; Ismayilov, T. A., Corrosion protection of steel pipelines against CO_2 corrosion-a review. *Chemistry journal* **2012,** *2*, 52.63.

247. Luo, H.; Guan, Y. C.; Han, K. N., Inhibition of mild steel corrosion by sodium dodecyl benzene sulfonate and sodium oleate in acidic solutions. *Corrosion* **1998,** *54* (8), 619-627.

248. Ju, H.; Kai, Z. P.; Li, Y., Aminic nitrogen-bearing polydentate Schiff base compounds as corrosion inhibitors for iron in acidic media: A quantum chemical calculation. *Corrosion Science* **2008,** *50* (3), 865–871.

249. Ahamad, I.; Prasad, R.; Quraishi, M. A., Thermodynamic, electrochemical and quantum chemical investigation of some Schiff bases as corrosion inhibitors for mild steel in hydrochloric acid solutions. *Corrosion Science* **2010,** *52* (3), 933–942.

250. Kaddouri, M.; Bouklah, M.; Rekkab, S.; Touzani, R.; Al-Deyab, S. S.; Hammouti, B.; Aouniti, A.; Kabouche, Z., Thermodynamic, Chemical and Electrochemical Investigations of Calixarene Derivatives as Corrosion Inhibitor for Mild Steel in Hydrochloric Acid Solution. *International Journal of Electrochemical Science* **2012,** *7* (9), 9004-9023.

251. Kaddouri, M.; Rekkab, S.; Bouklah, M.; Hammouti, B.; Aouniti, A.; Kabouche, Z., Experimental study of inhibition of corrosion of mild steel in 1 M HCl solution by two newly synthesized calixarene derivatives. *Research on Chemical Intermediates* **2013,** *39* (8), 3649-3667.

252. Faritov, A.; Rozhdestvenskii, Y. G.; Yamshchikova, S.; Minnikhanova, E.; Tyusenkov, A., Improvement of the linear polarization resistance method for testing steel corrosion inhibitors. *Russian Metallurgy (Metally)* **2016,** *2016* (11), 1035-1041.

253. International., A., Standard Practice for Calculation of Corrosion Rates and Related Information from Electrochemical Measurements. In *G102-89*, Weat Conshohocken, 2010.

254. Cuevas-Arteaga, C.; Porcayo-Calderon, J.; Izquierdo, G.; Martinez-Villafane, A.; Gonzalez-Rodriguez, J. G., Study of hot corrosion of alloy 800 using linear polarisation resistance and weight loss measurement. *Materials Science and Technology* **2001,** *17*.

255. Stansbury, E. E.; Buchanan, R. A., *Fundamentals of Electrochemical Corrosion*. ASM International: 2000.

256. Baboian, R., Corrosion Tests and Standards: Application and Interpretation. 2nd ed.; ASTM manual: 2005.

257. Macdonald, D. D., Reflections on the history of electrochemical impedance spectroscopy. *Electrochimica Acta* **2006,** *51* (8), 1376–1388.

258. Benedetti, A. V.; Sumodjo, P. T. A.; Nobe, K.; Cabot, P. L.; Proud, W. G., Electrochemical studies of copper, copper-aluminium and copper-aluminium-silver alloys- Impedance results in 0.5 M NaCl. *Electrochim*. *Acta*. **1995,** *40* (16), 2657-2668.

259. Hassan, H. H., Inhibition of mild steel corrosion in hydrochloric acid solution by triazole derivatives Part II- Time and temperature effects and thermodynamic treatments. *Electrochim*. *Acta*. **2007,** *53* (4), 1722-1730.

260. Azghandi, M. V.; Davoodi, A.; Farzi, G. A.; Kosari, A., Water-base acrylic terpolymer as a corrosion inhibitor for SAE1018 in simulated sour petroleum solution in stagnant and hydrodynamic conditions. *Corrosion Science*. **2012,** *64*, 44-54.

261. Tiginyanu, I.; Ursaki, V.; Topala, P., The Study of Films by Electrochemical Impedance Spectroscopy. In *Nanostructures and Thin Films for Multifunctional Applications:Technology, Properties and Devices*, Cesiulis, H.; Tsyntsaru, A.; Ramanavicius, A.; Ragoisha, G., Eds. Springer International: Springer International, 2016; pp 8-10.

262. Cao, C., On Electrochemical Techniques for Interface Inhibitor Research. *Corrosion Science* **1996,** *38* (12), 2073-2082.

263. Pandarinathan, V.; Lepkova, K.; Bailey, S.; Gubner, R., Impact of mineral deposits on CO_2 corrosion of carbon steel. In *Proceedings of the Corrosion Conference & expo*, NACE - International Corrosion Conference Series: Orlando, Florida, USA: NACE., 2013; pp 5118-5132.

264. Okafor, P. C.; Liu, C. B.; Liu, X.; Zheng, Y. G., Inhibition of CO_2 corrosion of N80 carbon steel by carboxylic quaternary imidazoline and halide ions additives. *Journal of applied electrochemistry* **2009,** *39*, 2535-2543.

265. El-Sayed, A.; Shaker, A. M.; Abd El-lateef, H. M., Corrosion inhibition of tin, indium and tin–indium alloys by adenine or adenosine in hydrochloric acid solution. *Corrosion Science* **2010,** *52* (1), 72–81.

APPENDICES

The nuclear magnetic resonance (^{1}HNMR, ^{13}CNMR) and Infrared (IR) spectroscopies of (3a-c)

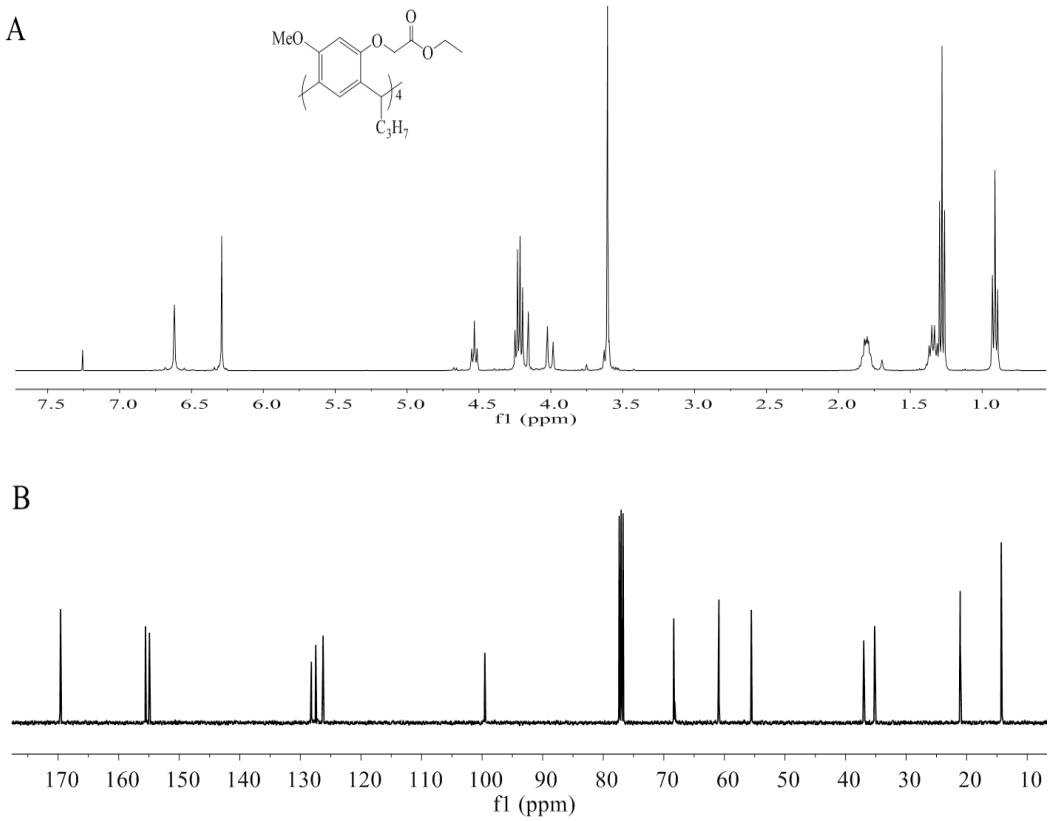

Appendix A1. 1: ^{1}HNMR (A), ^{13}CNMR (B) and IR (C) of **3a**.

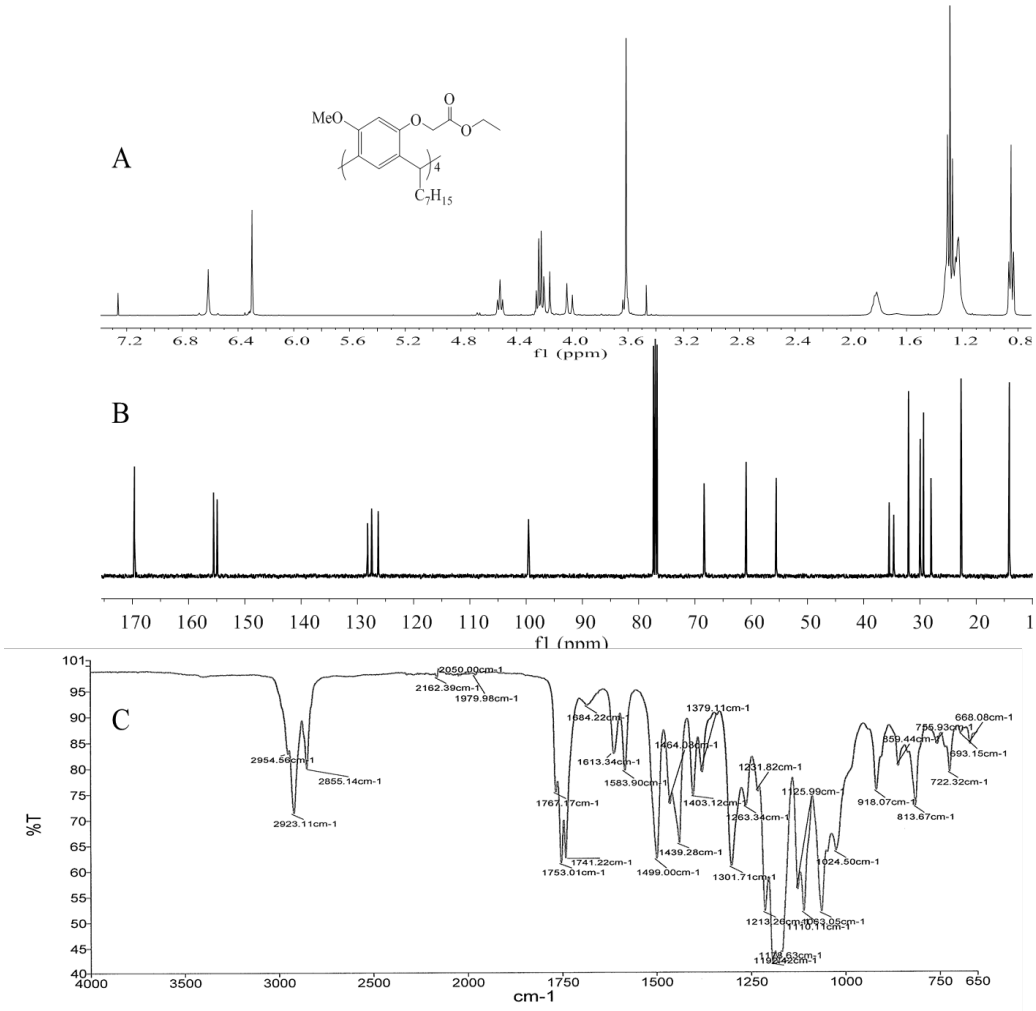

Appendix A1. 2: ^{1}HNMR (A), ^{13}CNMR (B) and IR (C) of **3b.**

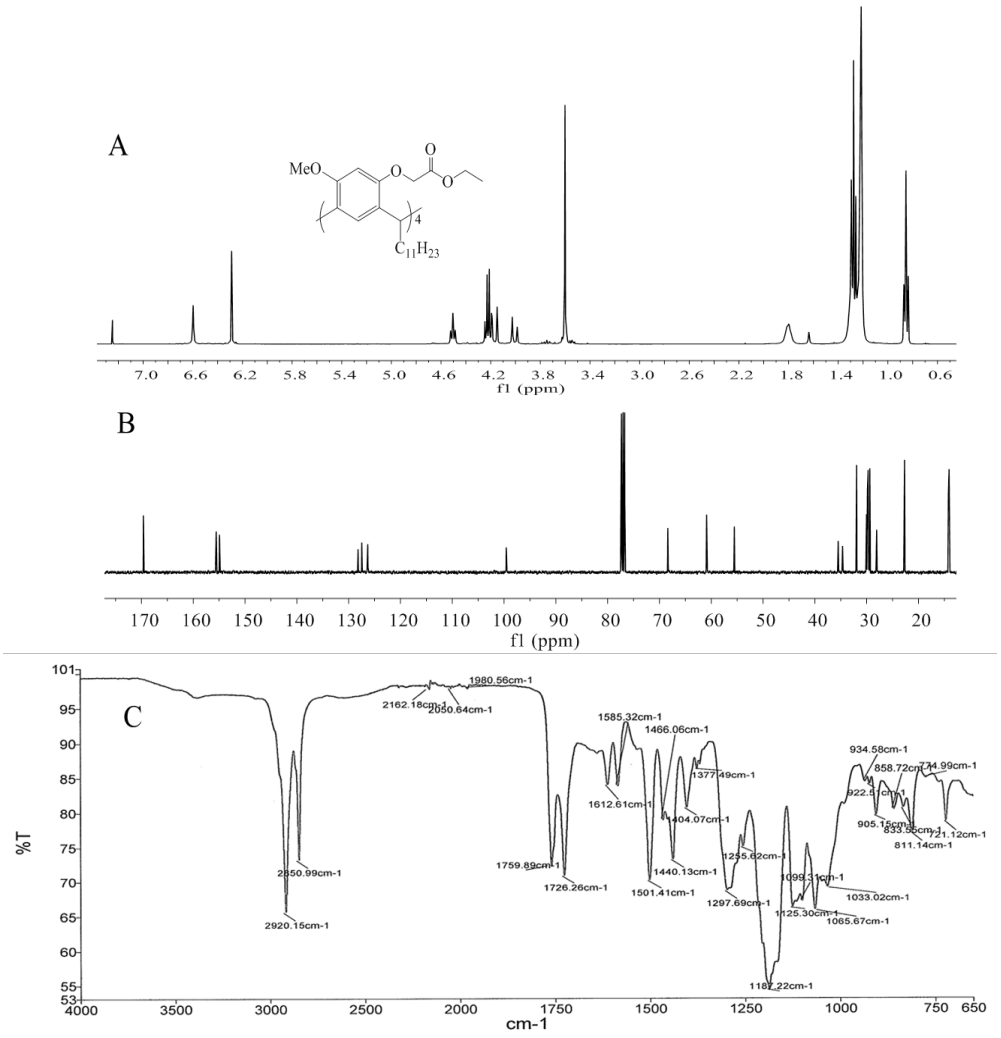

Appendix A1. 3: ^{1}HNMR (A), ^{13}CNMR (B) and IR (C) of **3c.**

The nuclear magnetic resonance (^{1}HNMR, ^{13}CNMR) and Infrared (IR) spectroscopies of (4a-c)

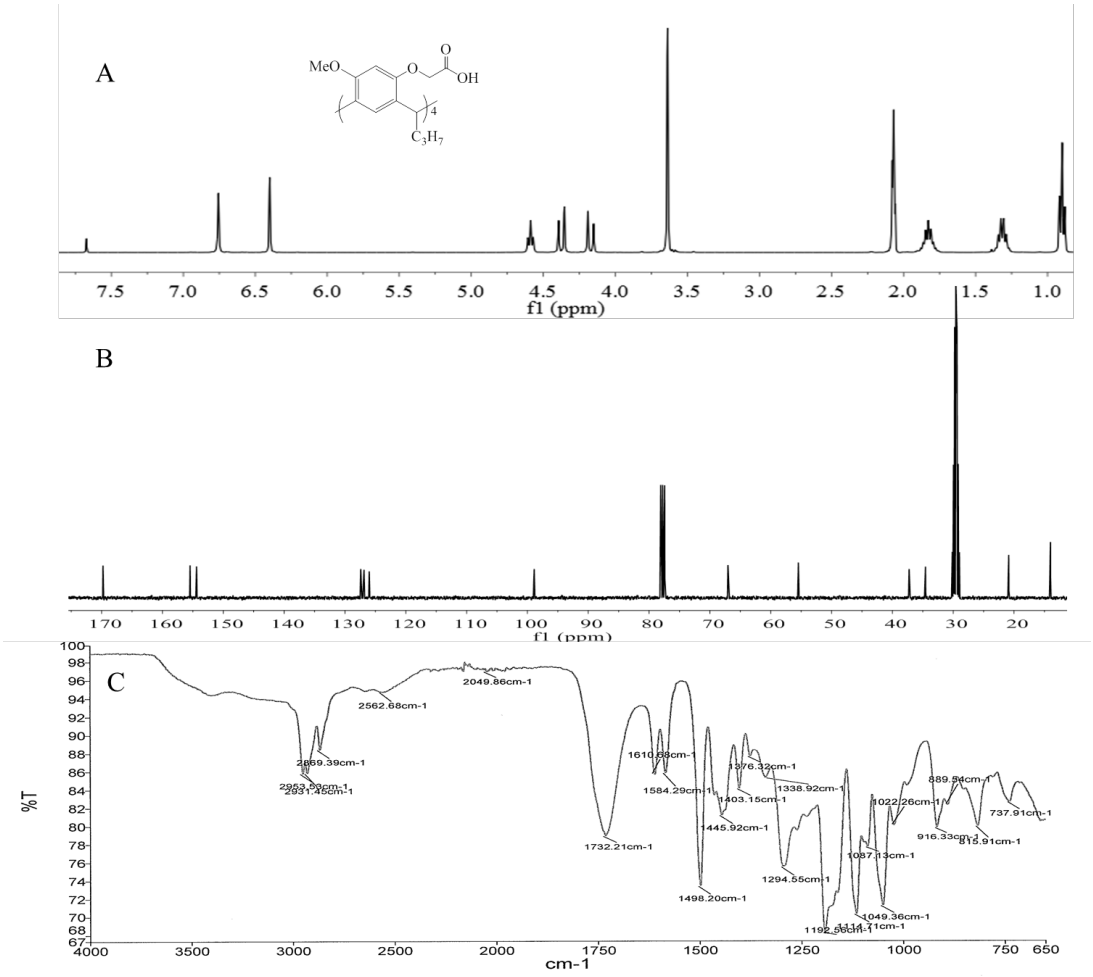

Appendix A2. 1: ^{1}HNMR (A), ^{13}CNMR (B) and IR (C) of **4a.**

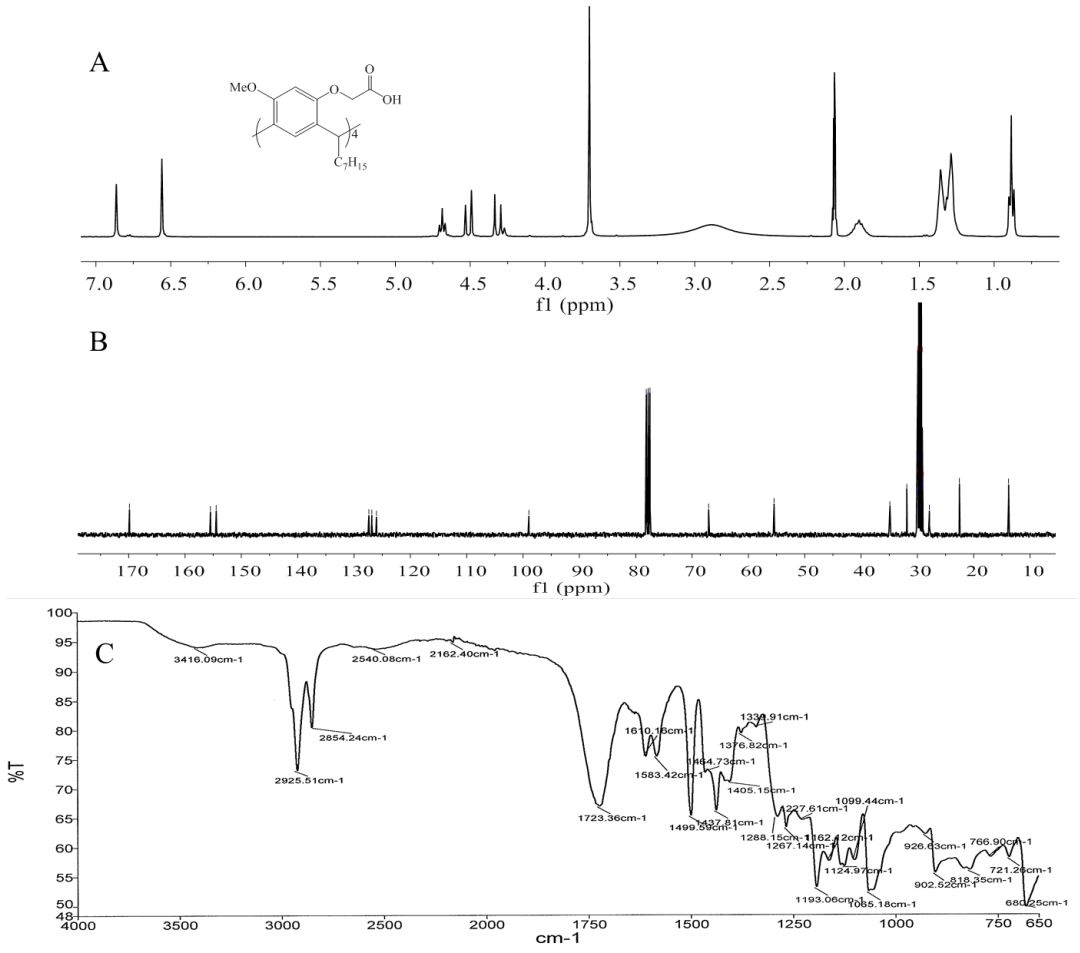

Appendix A2. 2: ^{1}HNMR (A), ^{13}CNMR (B) and IR (C) of **4b.**

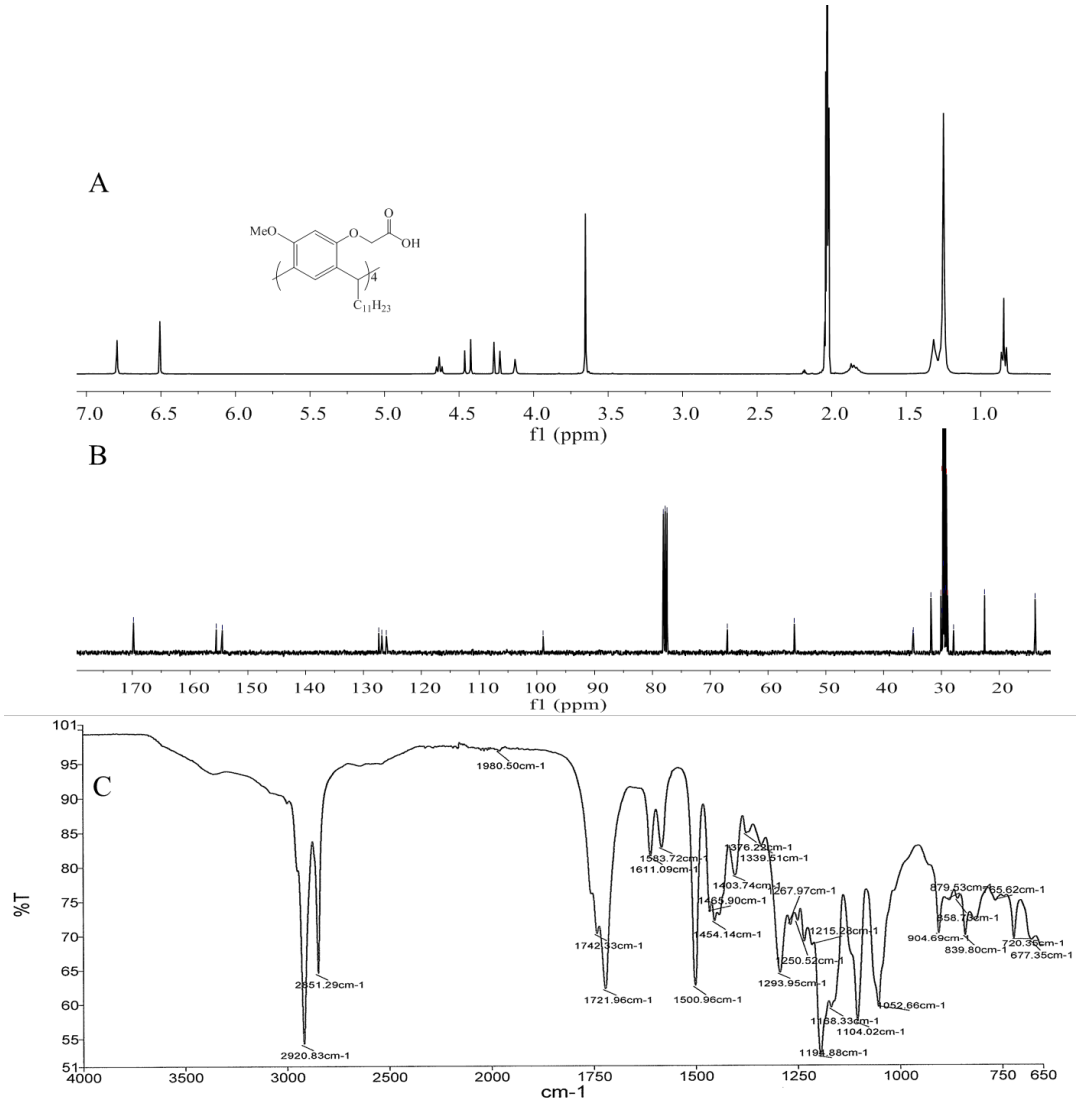

Appendix A2. 3: ^{1}HNMR (A), ^{13}CNMR (B) and IR (C) of **4c.**

The nuclear magnetic resonance (^{1}HNMR, ^{13}CNMR) and Infrared (IR) spectroscopies of (5a,6-9)

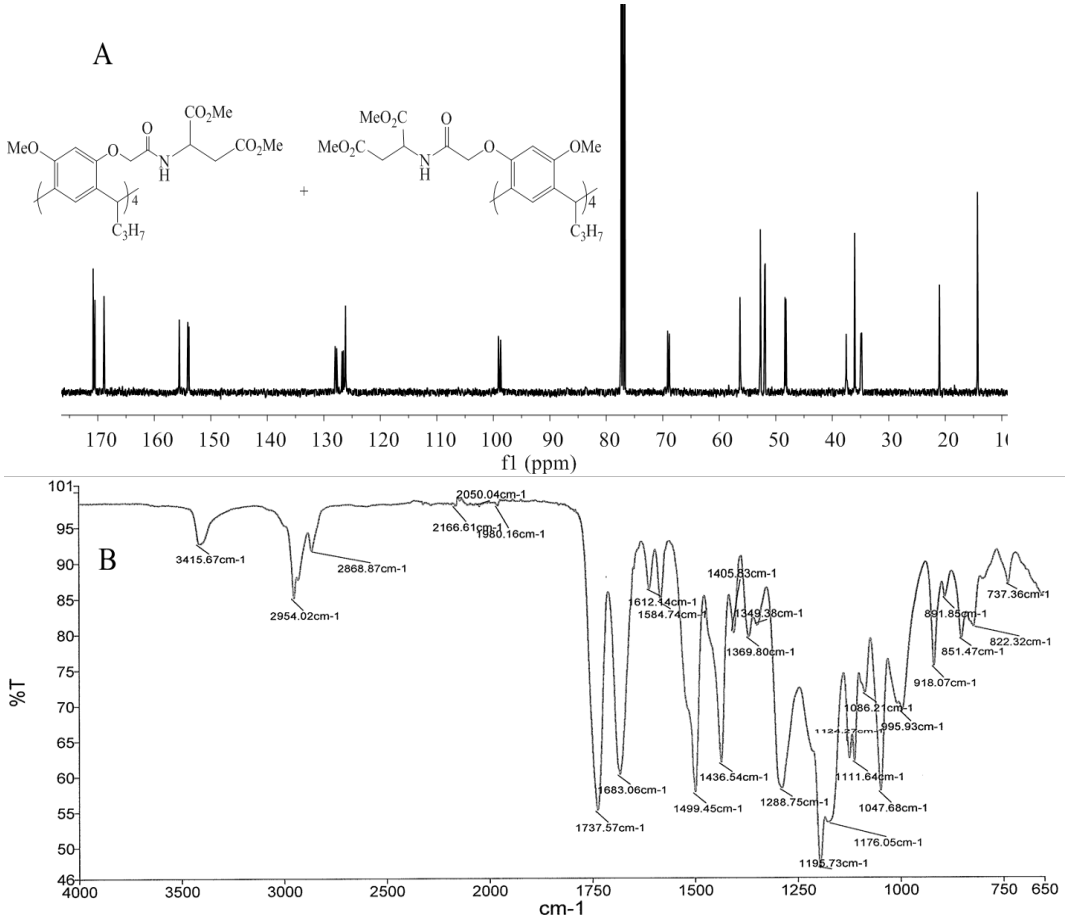

Appendix A3. 1: ^{13}CNMR (A) and IR (B) of **5a**.

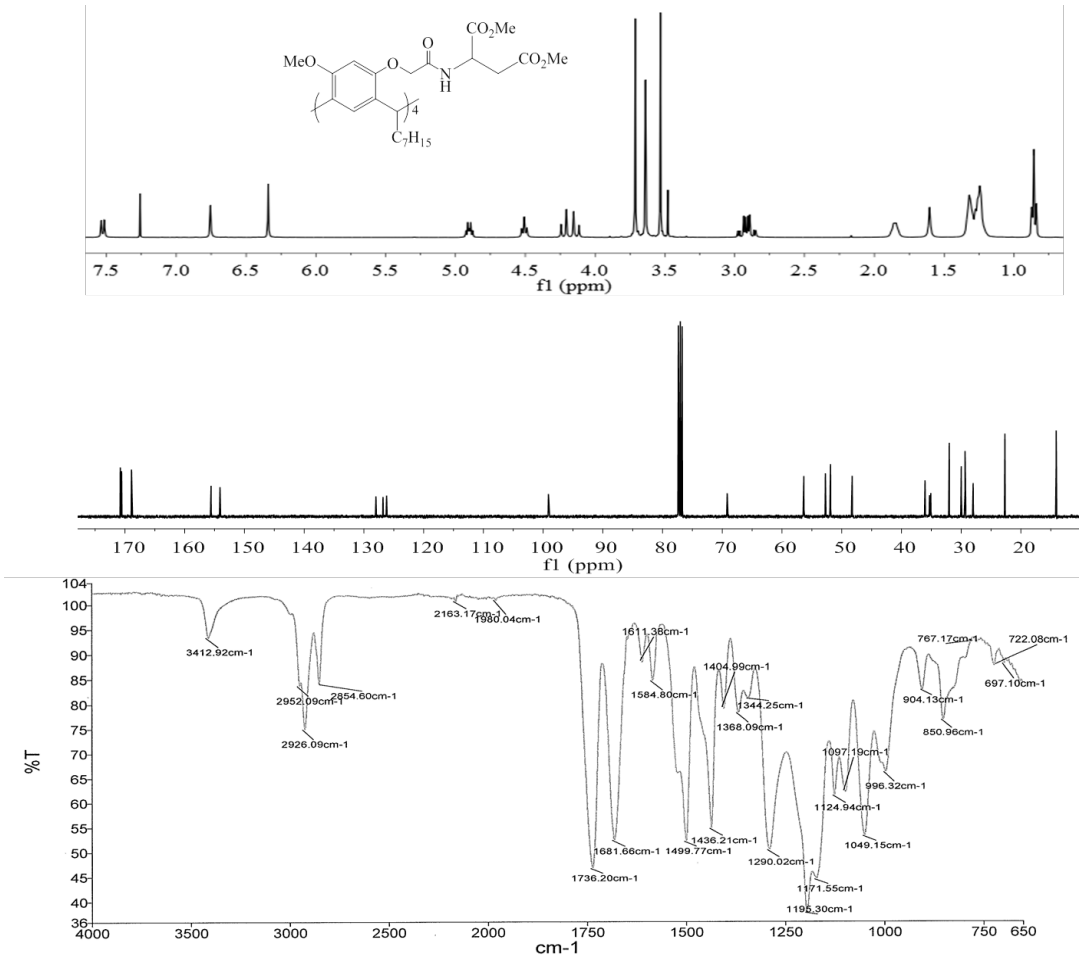

Appendix A3. 2: ^{1}HNMR (A) ^{13}CNMR (B) and IR (C) of **6**.

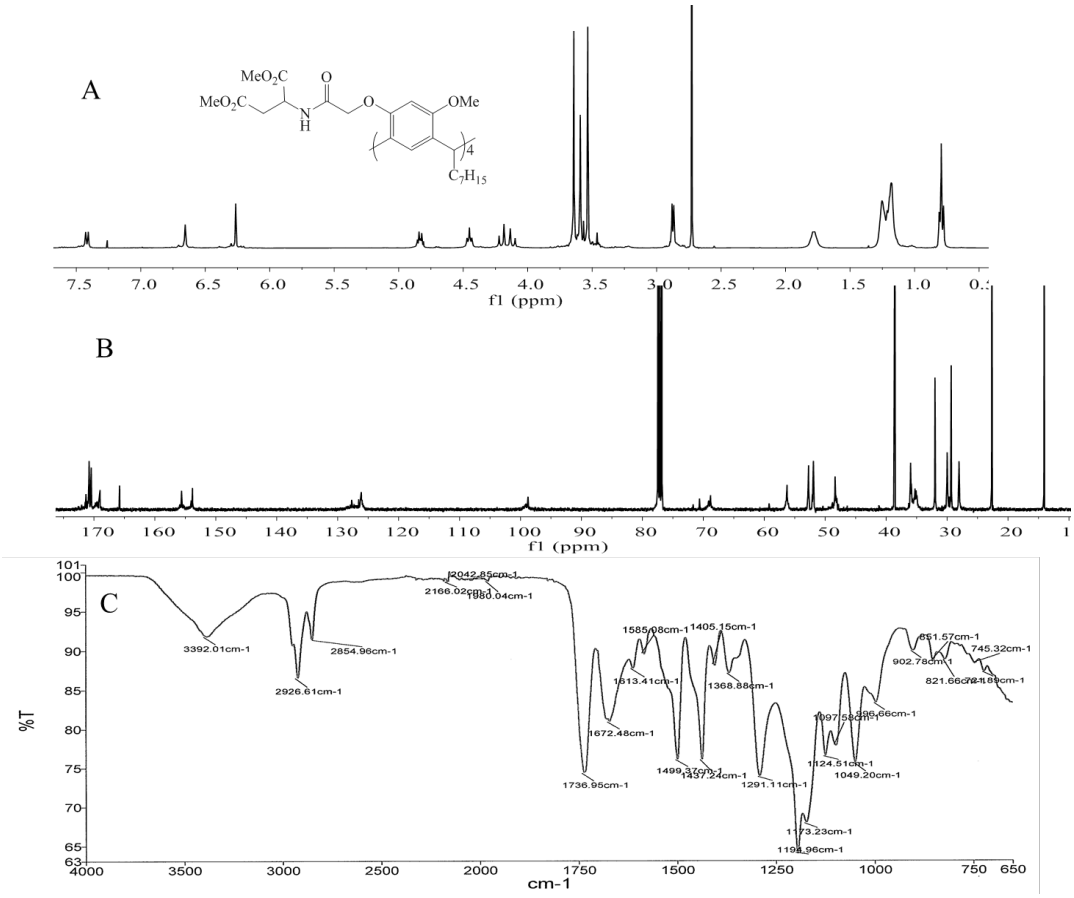

Appendix A3. 3: ^{1}HNMR (A) ^{13}CNMR (B) and IR (C) of **7**.

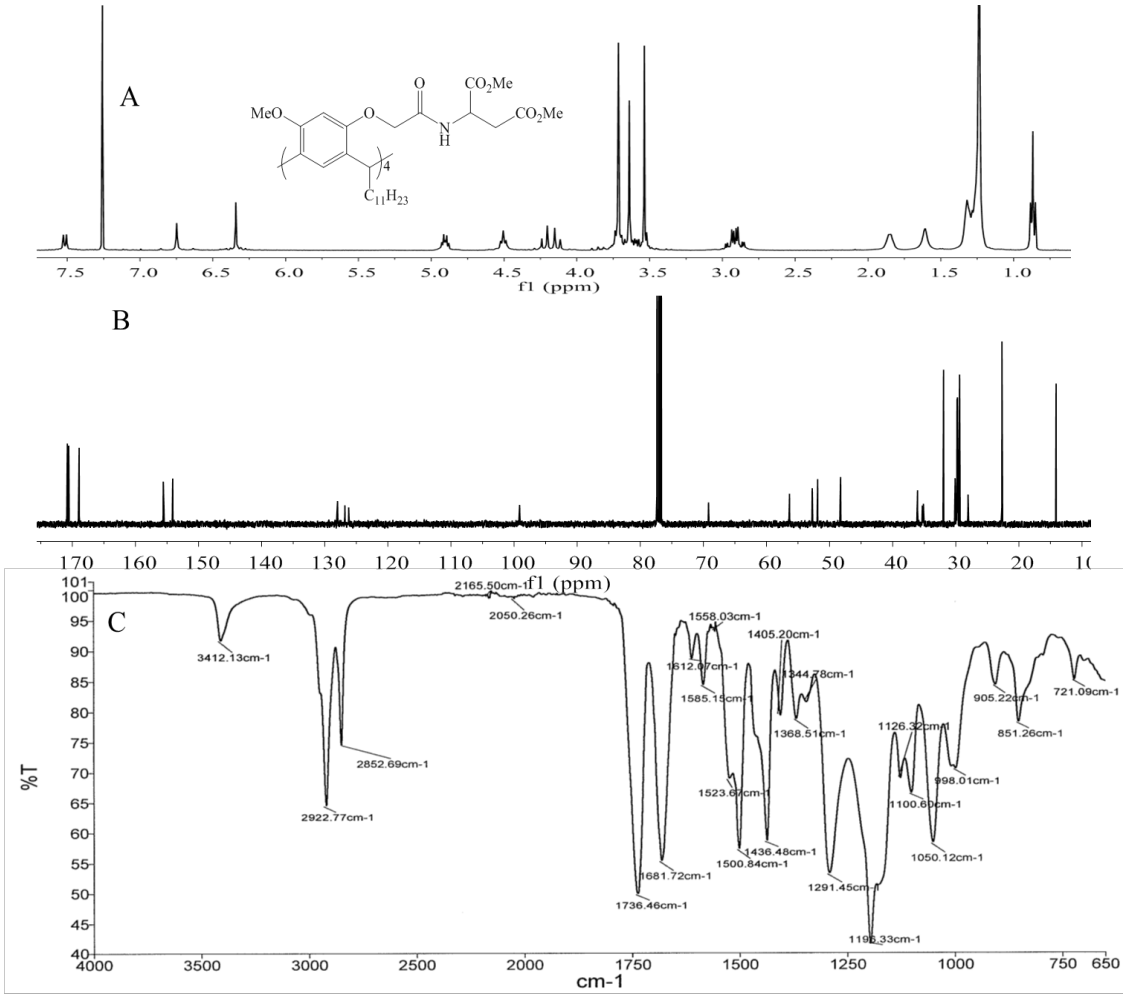

Appendix A3. 4: ^{1}HNMR (A) ^{13}CNMR (B) and IR (C) of **8**.

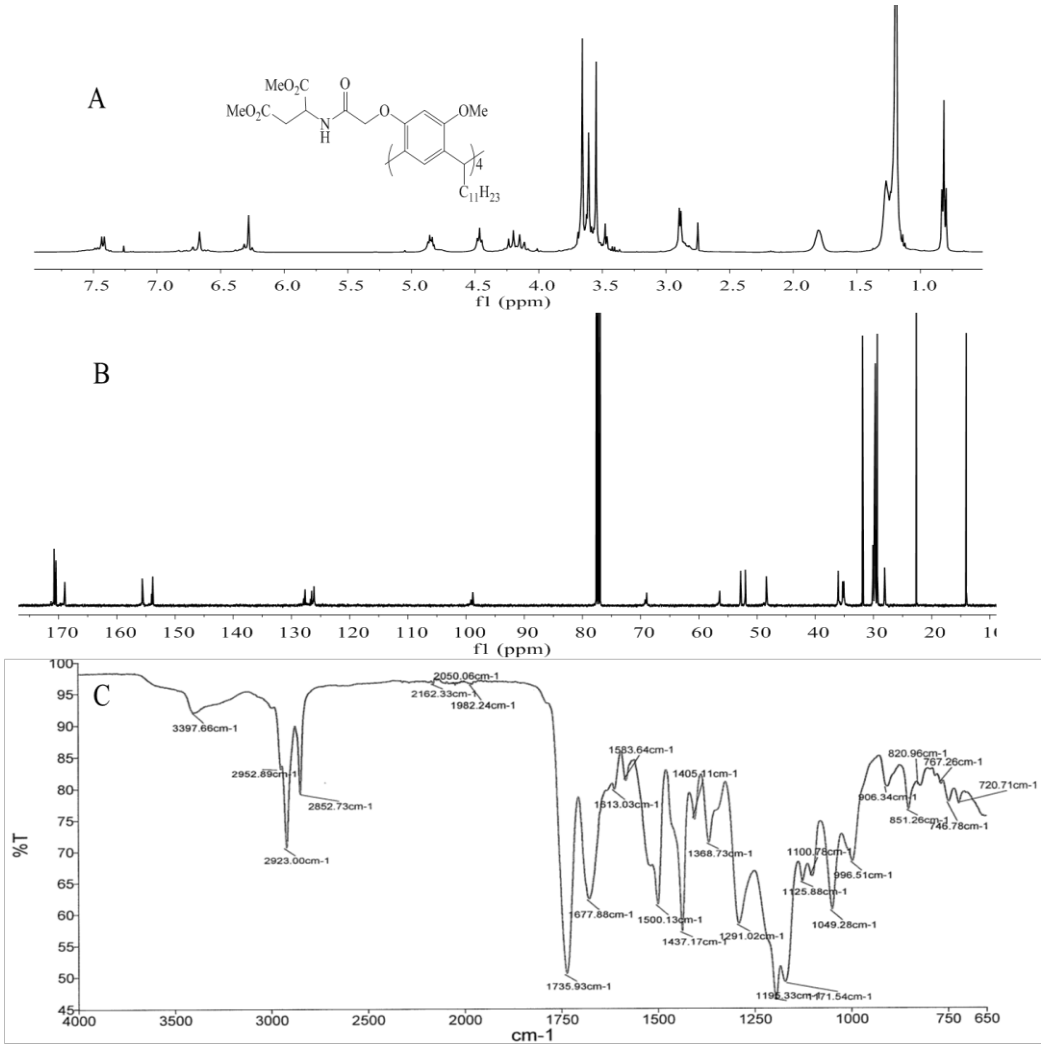

Appendix A3. 5: ^{1}HNMR (A) ^{13}CNMR (B) and IR (C) of **9**.

The nuclear magnetic resonance (^{1}HNMR, ^{13}CNMR) and Infrared (IR) spectroscopies of (10-14)

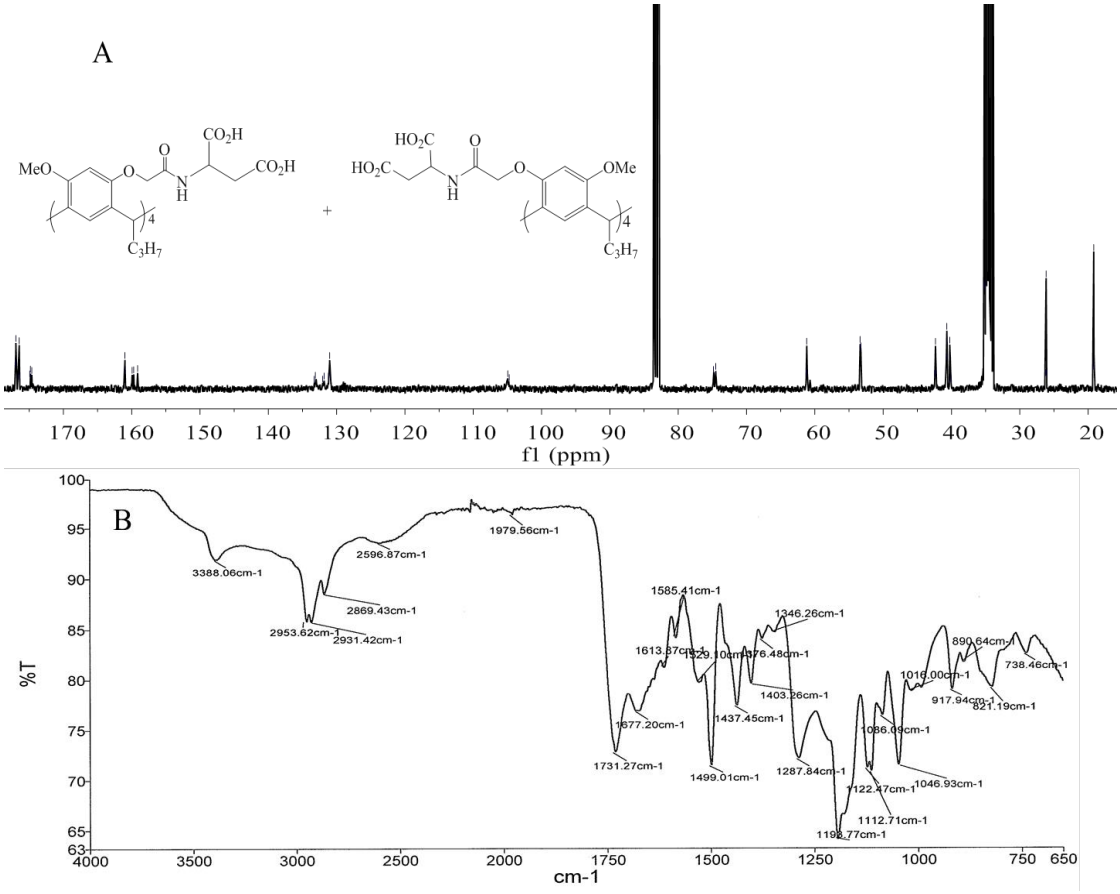

Appendix A4. 1: ^{13}CNMR (A) and IR (B) of **10**.

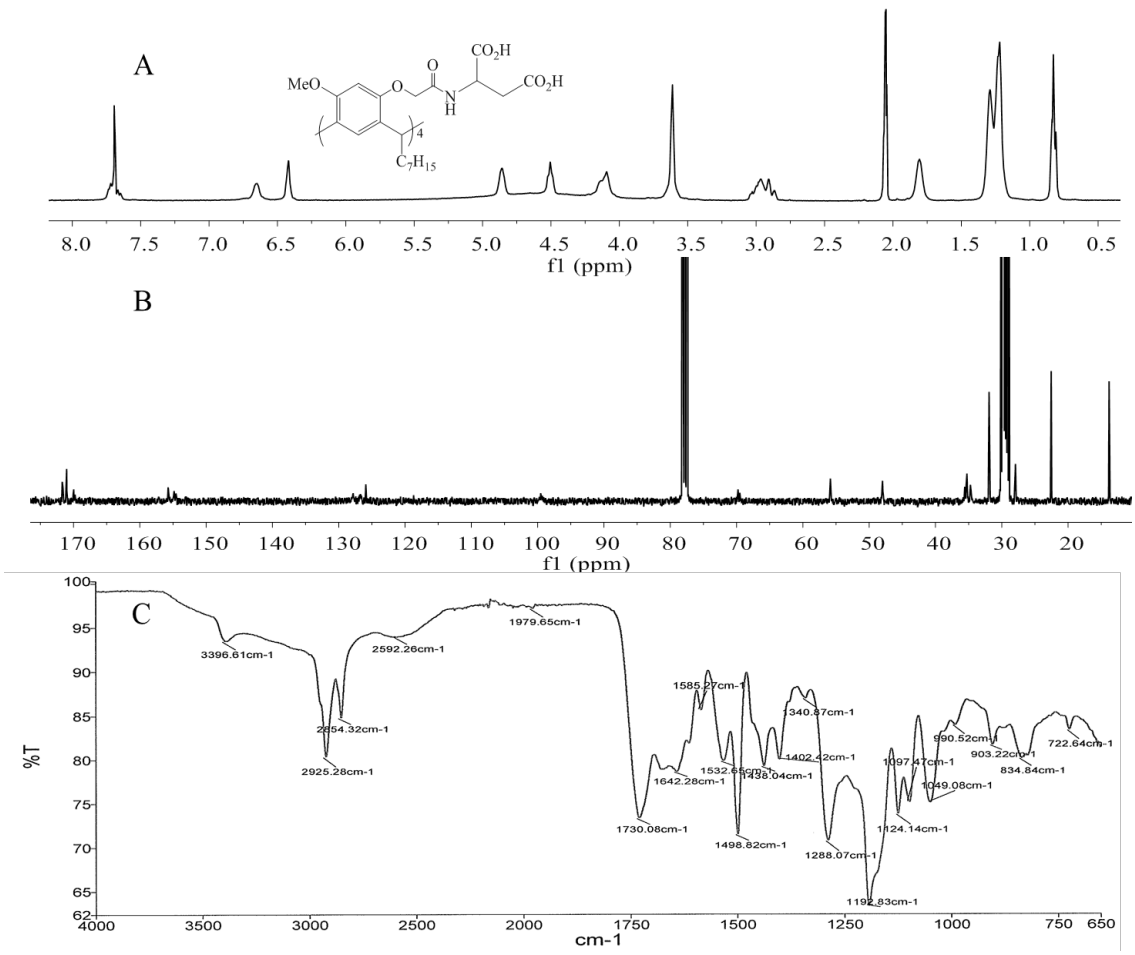

Appendix A4. 2: ^{1}HNMR (A) ^{13}CNMR (B) and IR (C) of **11.**

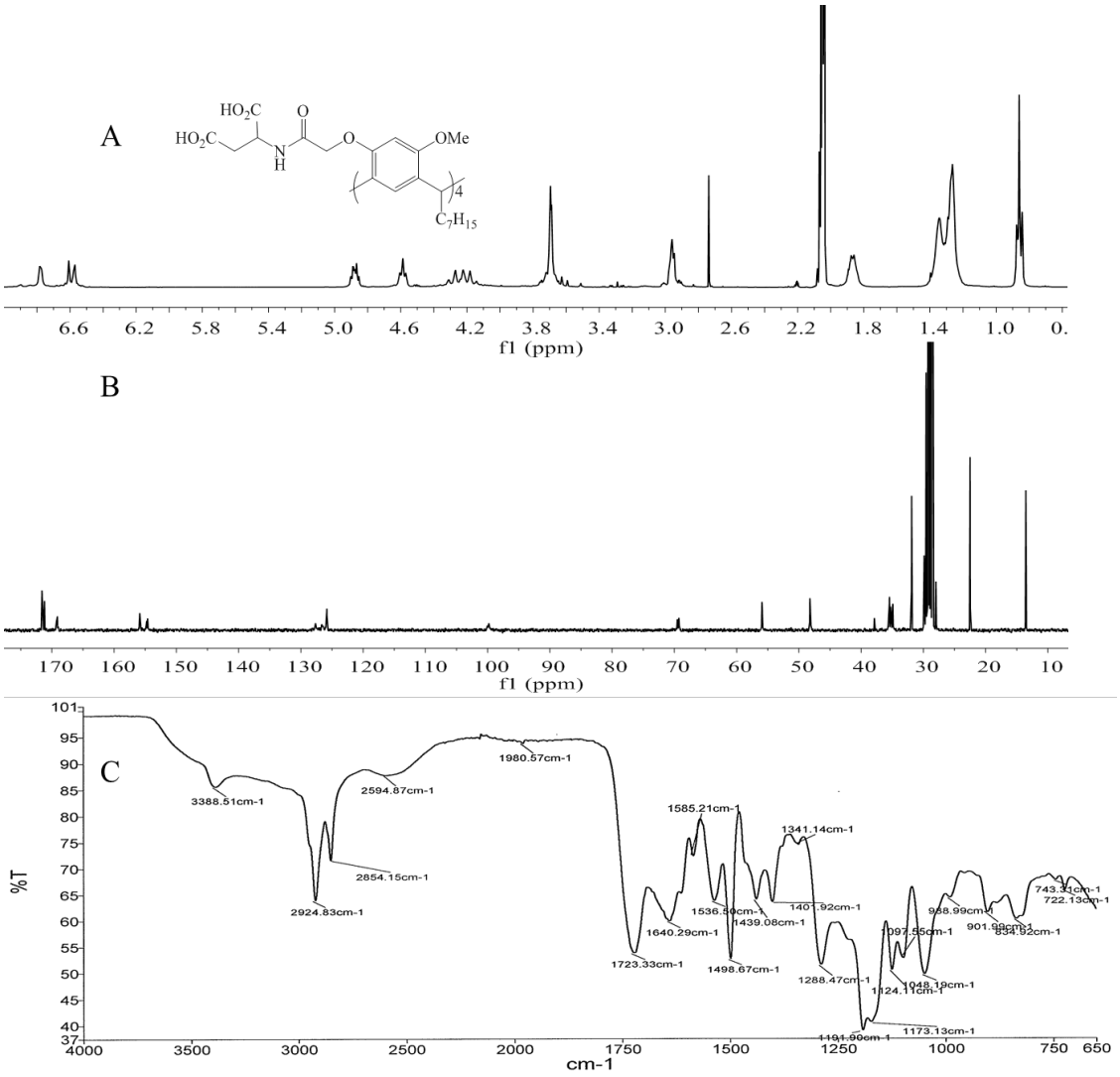

Appendix A4. 3: ^{1}HNMR (A) ^{13}CNMR (B) and IR (C) of **12.**

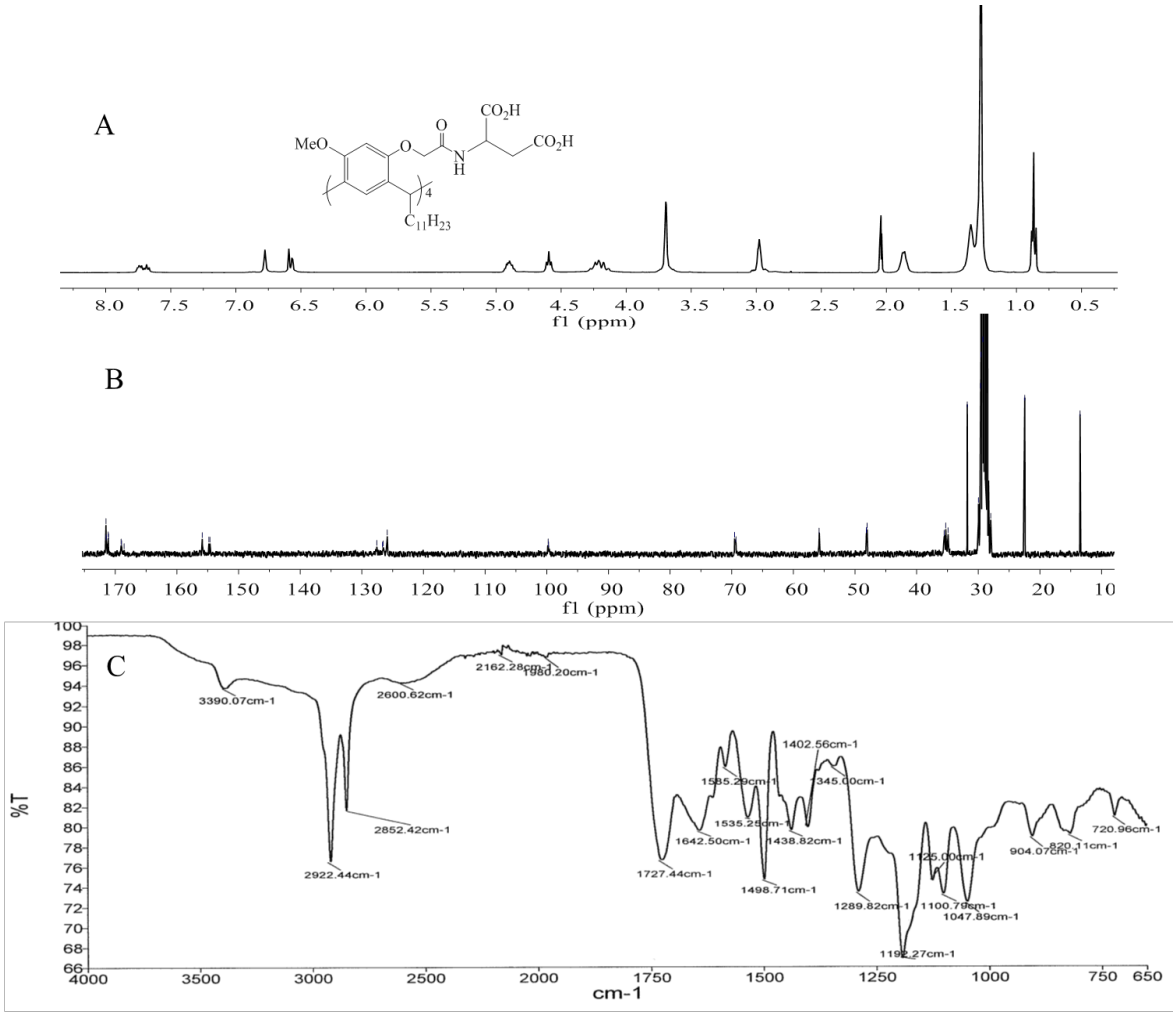

Appendix A4. 4: ^{1}HNMR (A) ^{13}CNMR (B) and IR (C) of **13.**

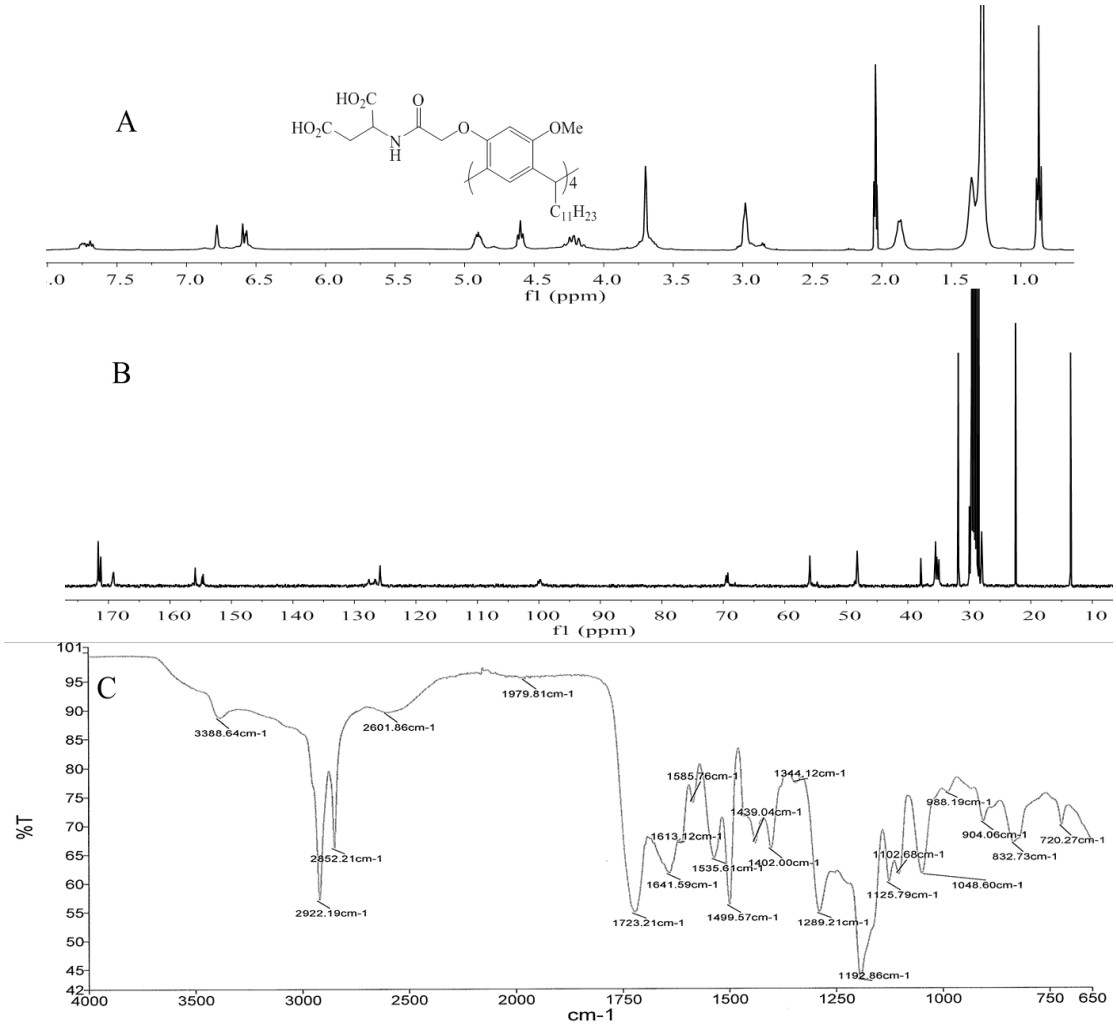

Appendix A4. 5: ^{1}HNMR (A) ^{13}CNMR (B) and IR (C) of **14.**

The nuclear magnetic resonance (^{1}HNMR, ^{13}CNMR) and Infrared (IR) spectroscopies of (15a-b)

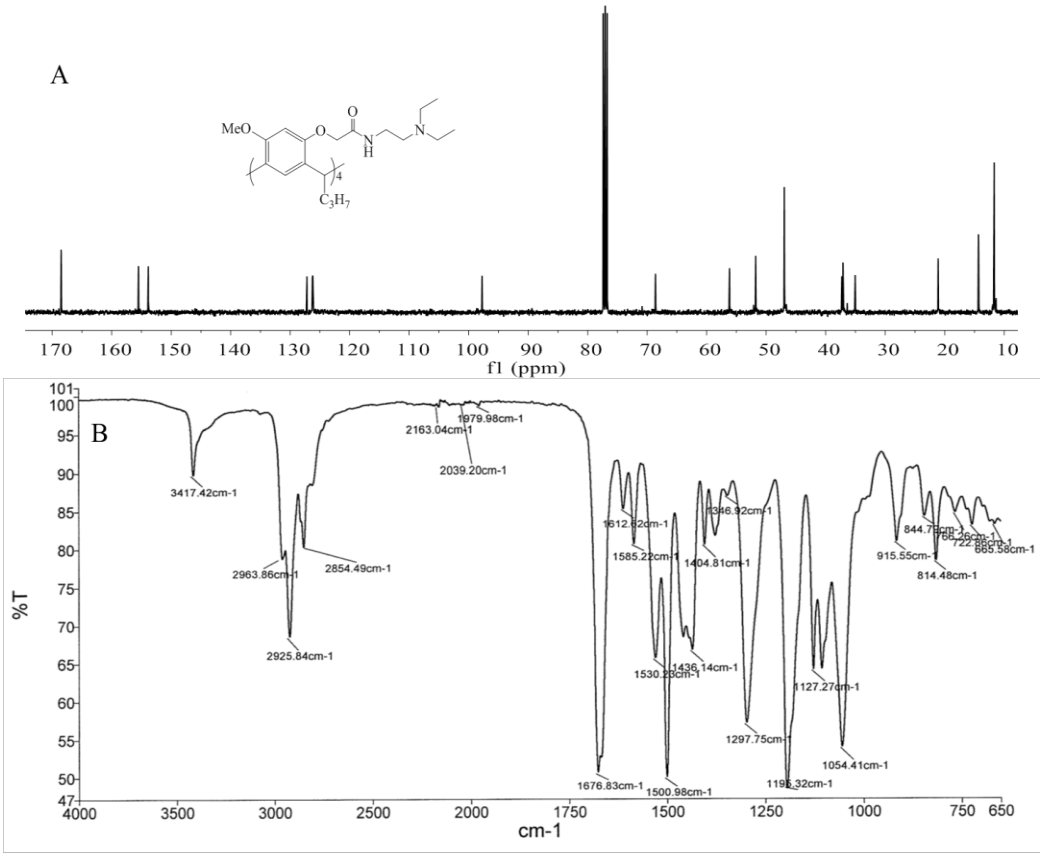

AppendixA5. 1: ^{13}CNMR (A) and IR (B) of **15a.**

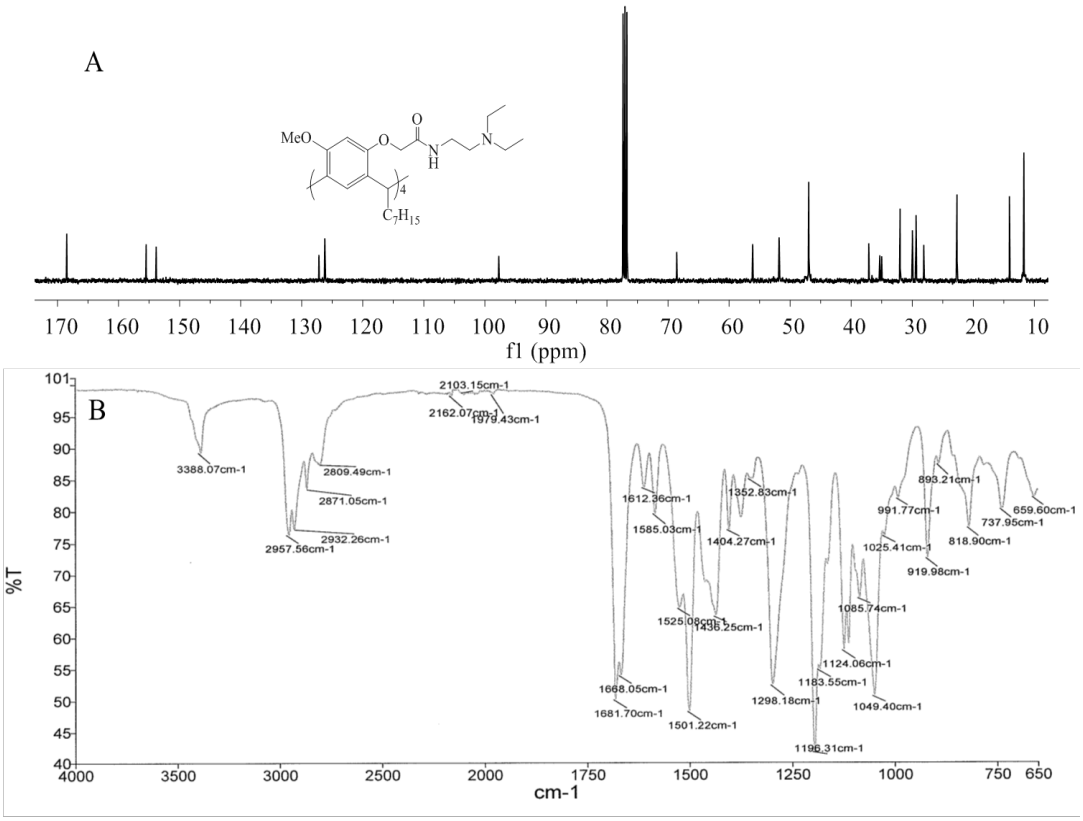

AppendixA5. 2: ^{13}CNMR (A) and IR (B) of **15b.**

The nuclear magnetic resonance (^{1}HNMR, ^{13}CNMR) and Infrared (IR) spectroscopies of (17-18)

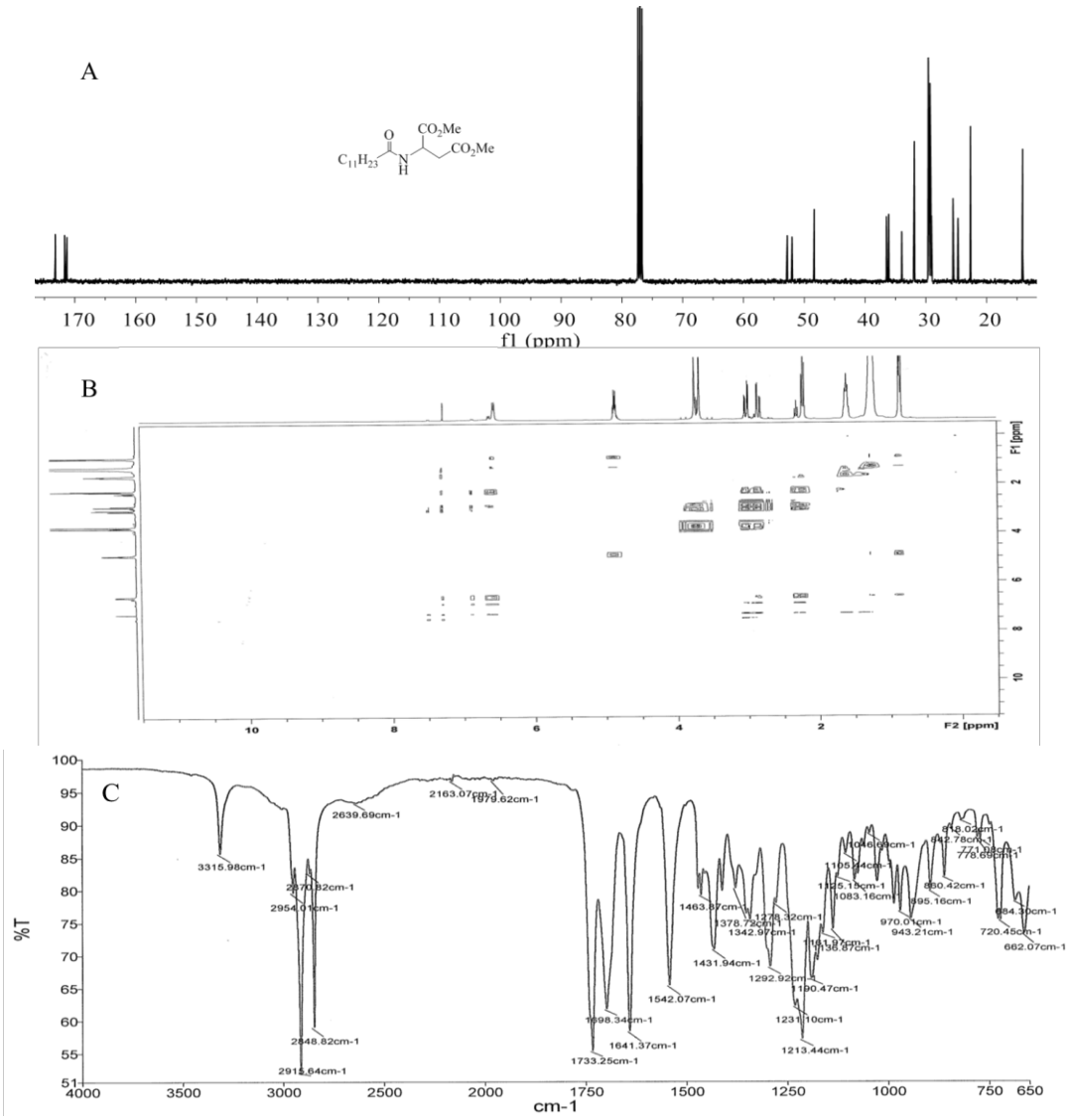

AppendixA6. 1: ^{1}HNMR (A) ^{13}CNMR (B) and IR (C) of **17.**

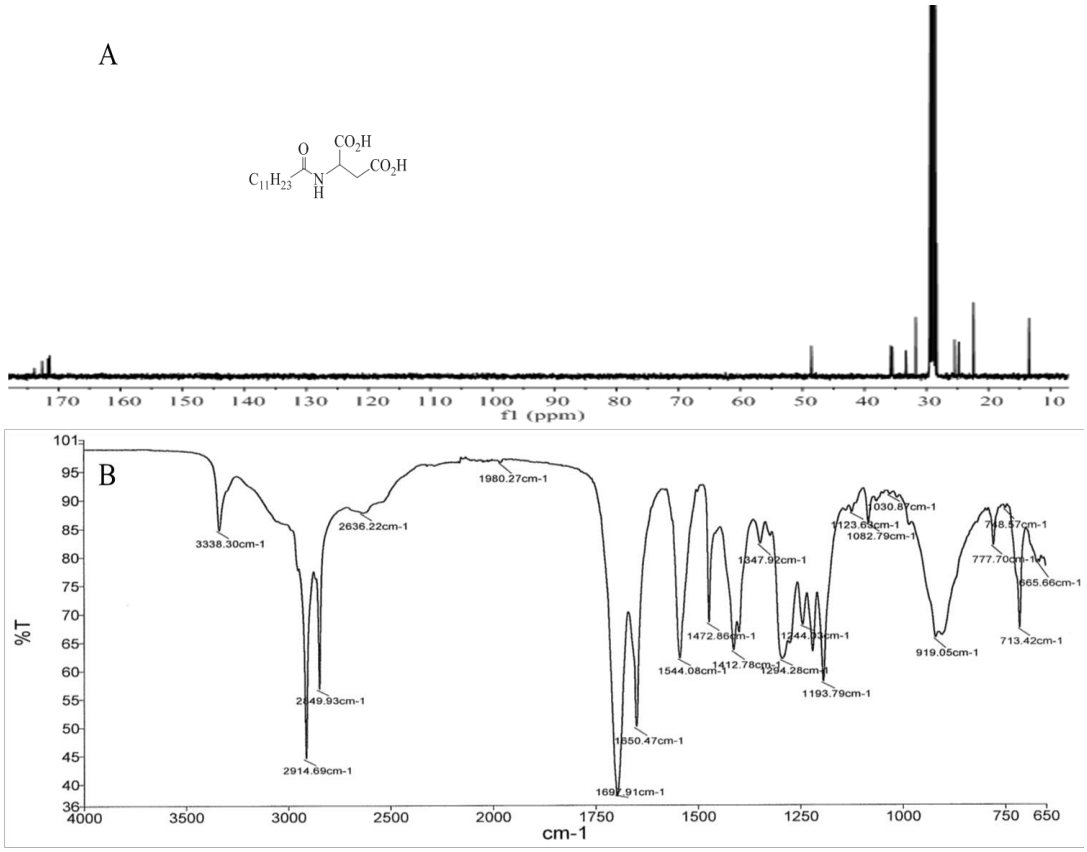

AppendixA6. 2: ^{13}CNMR (A) and IR (B) of **18.**

The nuclear magnetic resonance (^{1}HNMR, ^{13}CNMR) and Infrared (IR) spectroscopies of 19

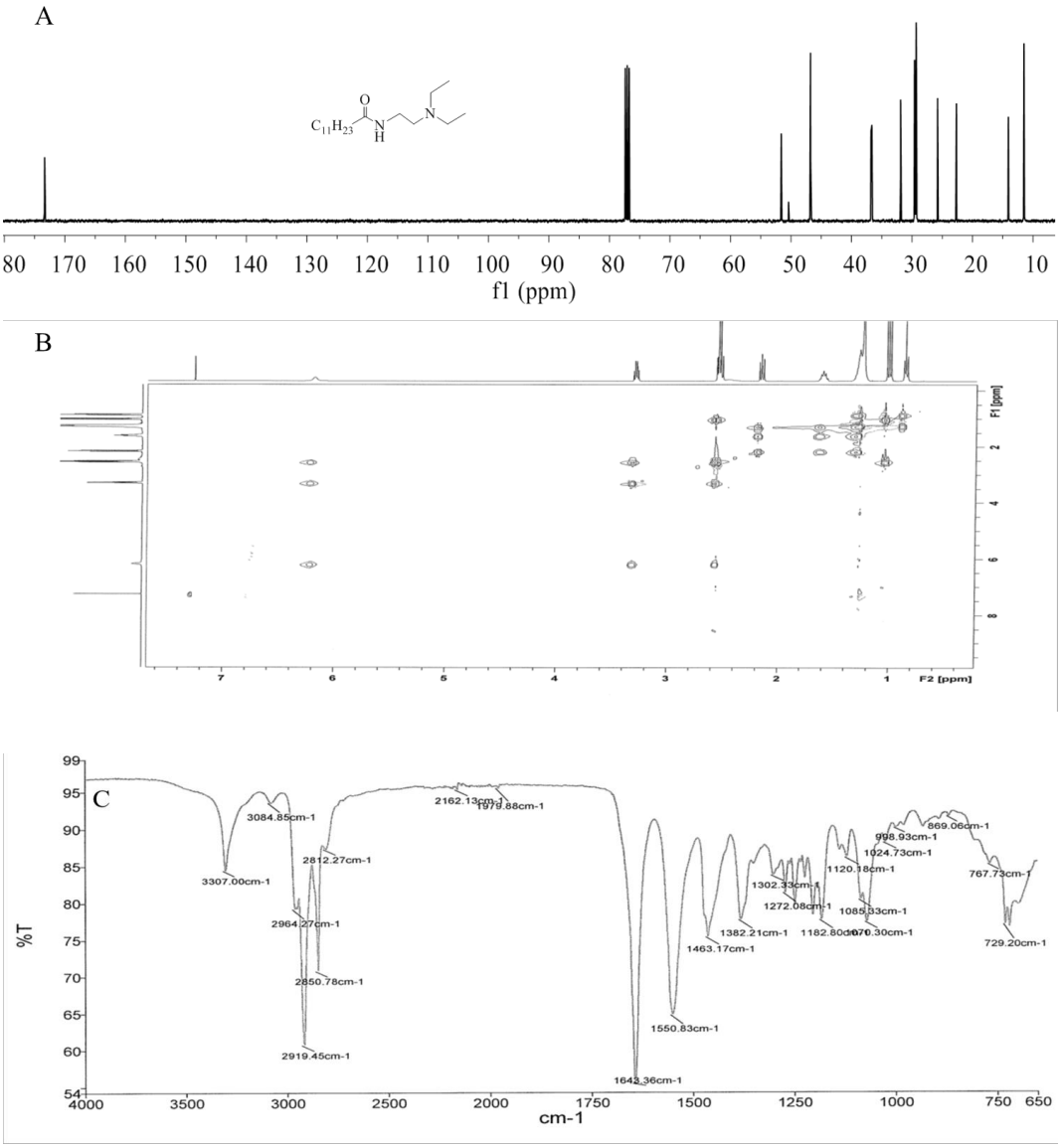

Appendix 7. 1: ^{1}HNMR (A) ^{13}CNMR (B) and IR (C) of **19**.